Simulating the formation and evolution of disc galaxies in a ΛCDM universe

Michael Aumer

SIGILL · UNIVERSITAT · LUDOVIC · MAXIM

München, im Oktober 2013 AD

Simulating the formation and evolution of disc galaxies in a ΛCDM universe

Michael Aumer

Dissertation
an der Fakultät für Physik
der Ludwig–Maximilians–Universität
München

vorgelegt von
Michael Aumer
aus Roding

München, den 29.10.2013 AD

Erstgutachter: Prof. Dr. Simon D.M. White
Zweitgutachter: Prof. Dr. Joseph Mohr
Tag der mündlichen Prüfung: 29.01.2014 AD

The Force is what gives a Jedi his power.
It's an energy field created by all living things.
It surrounds us and penetrates us.
It binds the galaxy together.

Obi-Wan Kenobi

Contents

List of Figures

List of Tables

Abstract

The majority of stars in the universe has formed in disc galaxies with masses similar to that of the Milky Way. Ab-initio cosmological hydrodynamical simulations of the formation and evolution of galaxies in a Λ Cold Dark Matter universe have long suffered from serious problems in correctly modelling the star-formation history and structure of disc galaxies.

We first use idealized semi-cosmological simulations to gain a better understanding of processes leading to problems in disc formation simulations. We add rotating spheres of hot gas to cosmological dark-matter-only simulations of individual haloes and follow the formation and evolution of galaxy discs from the cooling gas. The initial orientation of the baryonic angular momentum with respect to the halo has a major effect on disc formation. Despite the coherently rotating initial conditions, the orientations of the disc and the outer gas and the relative angle between the components can all change by more than 90 degrees over several billion years. Dominant discs with realistic structural and kinematical properties form preferentially if slow cooling times shift disc formation to later times, if the initial angular momentum is aligned with the halo minor axis and if there is little reorientation of the disc.

We then present a new set of fully cosmological simulations with an updated multiphase smoothed particle hydrodynamics galaxy formation code. The update includes improved treatment of metal-line cooling, metal production, turbulent diffusion of metals, kinetic and thermal supernova feedback and radiation pressure from massive young stars. We compare the models to a variety of observations at high and low redshifts and find good agreement for morphologies, stellar-to-dark-matter mass ratios, star formation rates, gas fractions and heavy element abundances. Agreement is better at redshift $z = 1$ than at present day as discrepancies in star formation histories for the lowest and highest simulated galaxy masses become apparent at late times. 18 out of 19 of our model galaxies at $z = 0$ contain stellar discs with kinematic disc fractions up to 65 %, higher than in any previous simulations.

We finally compare our model galaxies in detail with recent observations of the structural evolution of stellar galactic discs and the structure of $z = 0$ gas discs. Stellar surface density profiles agree well with observations at $z > 1$, but reveal too little central growth afterwards. This is likely connected to a lack of bars in our simulations resulting from overly strong feedback. Discs at $z = 0$ are too extended by a factor ~ 2. The discs have diverse formation histories ranging from pure inside-out growth in systems with quiescent merger histories to continuous mass growth at all radii. Central mass growth in our models is driven by mergers and misaligned infall events, which leave signatures in the present day distributions of radii and element abundances as functions of stellar age. Gas discs agree well with observations in terms of sizes and profile shapes, but on average have overly high gas-to-stellar mass ratios. Our models agree well with the observed neutral hydrogen mass-size relation.

Despite significant progress, our models continue to suffer from various problems illustrating that we are still far away from capturing all relevant physical processes accurately.

Zusammenfassung

Die meisten Sterne im Universum sind in Scheibengalaxien enstanden, die ähnliche Massen wie die Milchstraße haben. Kosmologische, hydrodynamische Ab-inititio-Simulationen der Enstehung und Entwicklung von Galaxien in einem Λ-Kalte-Dunkle-Materie Universum haben seit langer Zeit ernsthafte Probleme damit, die Sternentstehungsgeschichten und Strukturen von solchen Scheibengalaxien korrekt wiederzugeben.

In dieser Arbeit verwenden wir zuerst idealisierte, semi-kosmologische Simulationen, um ein besseres Verständnis für die Prozesse zu gewinnen, die zu Problemen in den Simulationen von Scheibengalaxien führen. Wir benützen kosmologische Simulationen von einzelnen Dunkle-Materie-Halos ohne baryonische Physik und fügen heiße, rotierende, kugelförmige Gaswolken hinzu, um die Entstehung und Entwicklung von galaktischen Scheiben aus dem kühlenden Gas zu verfolgen. Es zeigt sich, dass die anfängliche Ausrichtung des baryonischen Drehimpulsvektors im Vergleich zur Struktur der Dunklen Materie große Auswirkungen auf die Entstehung von Scheiben hat. Trotz der anfänglich koherenten Rotation der Gaswolke können sich sowohl die Ausrichtungen der Drehimpulsvektoren der galaktischen Scheibe und der äußeren Gasschichten, als auch der Winkel zwischen den Komponenten über mehrere Milliarden Jahre hinweg um mehr als 90 Grad verändern. Galaxien, die überwiegend aus einer Scheibenkomponente bestehen und realistische strukturelle und kinematische Eigenschaften besitzen, entstehen vorzugsweise, wenn langsame Kühlungsprozesse die Entstehung der Scheiben hinauszögern, wenn der Drehimpulsvektor anfänglich entlang der kurzen Halbachse des Dunkle-Materie-Halos ausgerichtet ist und wenn sich die Orientierung des Drehimpulsvektors der Scheibe über die Entstehungsgeschichte hinweg nur wenig ändert.

Anschließend beschreiben wir eine Reihe neuer, voll-kosmologischer Simulationen, die mit einem verbesserten Galaxiensimulationsprogramm durchgeführt wurden, dass sich der Smoothed-Particle-Hydrodynamics Methode bedient und eine explizite Modellierung von multiplen Gasphasen beinhaltet. Die Verbesserungen betreffen die Gas-Kühlung durch Metall-Linienübergänge, die Elemententstehung in Sternen und Supernovae, die Diffusion von Elementen in turbulenter Umgebung, kinetische und thermische Feedback-Prozesse durch Supernova-Explosionen und den Strahlungsdruck in der Umgebung massereicher, junger Sterne. Wir vergleichen unsere Modelle mit einer Vielzahl von Beobachtungen bei hohen und niedrigen Rotverschiebungen und zeigen gute Übereinstimmung bezüglich Morphologien, Massenverhältnissen von Sternen und Dunkler Materie, Sternentstehungsraten, Gas-Massenanteilen und Elementhäufigkeiten auf. Die Übereinstimmungen sind bei Rotverschiebung $z = 1$ besser ausgeprägt als in der Gegenwart, da die Sternentstehungsraten in den Modellgalaxien mit den höchsten und niedrigsten Massen in den späten Entwicklungsstadien von den Beobachtungen abweichen. 18 von unseren 19 Modellgalaxien zeigen bei $z = 0$ ausgeprägte Scheibenkomponenten, deren Massenanteil, nach kinematischen Kri-

terien bestimmt, bis zu 65 % beträgt, höher als in allen vorherigen Simulationen.

Schließlich vergleichen wir unsere Modellgalaxien im Detail mit neuesten Beobachtungen zur strukturellen Entwicklung von galaktischen Sternscheiben und zur Struktur von Gasscheiben bei $z = 0$. Die stellaren Massen-Profile unserer Galaxien stimmen gut mit Beobachtungen bei $z > 1$ überein, zeigen aber anschließend zu geringes Anwachsen im Zentrum. Dies hängt wohl damit zusammen, dass sich in unseren Sternscheiben zu wenige Balkenstrukturen bilden, was übermäßig starkem Feedback in den Modellen geschuldet ist. Die Scheiben sind bei $z = 0$ um einen Faktor ~ 2 zu ausgedehnt. Unsere Scheibengalaxien-Modelle durchlaufen vielfältige Enstehungsgeschichten. Galaxien, die bei $z < 2$ keinen Verschmelzungen mit ähnlich schweren Galaxien ausgesetzt sind, wachsen von innen nach außen. Andere Galaxien gewinnen kontinuierlich in den inneren und äußerern Regionen an Sternmasse hinzu. Das Wachstum im Zentrum rührt von Verschmelzungen mit anderen Galaxien und vom Einfall von Gas, dessen Drehimpulsvektor eine deutlich von der Scheibennormale abweichende Ausrichtung besitzt, her. Diese Ereignisse hinterlassen in den gegenwärtigen Verteilungung von radialen Positionen und Elementhäufigkeiten als Funktionen des stellaren Alters ausgeprägte Signaturen. Die Gasscheiben in unseren Modellen stimmen, was ihre Größen und Massenprofile betrifft, gut mit Beobachtungen überein, sie sind aber im Mittel zu massereich im Vergleich zu den Sternscheiben. Die beobachtete Relation zwischen Masse und Ausdehnung von neutralem Wasserstoff in Galaxien reproduzieren die Modelle sehr gut.

Trotz des beachtlichen Fortschritts, den wir erzielt haben, leiden unsere Modelle noch an vielfältigen Problemen. Dies zeigt uns, dass wir immer noch weit davon entfernt sind, alle relevanten physikalischen Prozesse korrekt zu berücksichtigen.

1 | Motivation

Galaxies in our universe come in many flavours. They can be dwarfs or giants, ellipticals, discs, lenticulars, irregulars or spheroidals. They can be active, star-bursting, interacting, merging or quenched. They can have spirals, bulges, bars, satellites, haloes, warps and rings. They can live in clusters, groups or the field. And there is a lot more they can be.

Our own galaxy, the Milky Way, is a medium-sized galaxy (neither a dwarf nor a giant) that harbours $\sim 6 \times 10^{10}$ solar masses ($M_\odot$, $1\ M_\odot = 1.989 \times 10^{30}\ \mathrm{kg}$) of stars. At least 80 % of these stars live in a disc, which is often divided into an older thick disc and a younger thin disc, although these components are not distinct. The stars in the central parts of the galaxy form a peanut-shaped 'pseudo'-bulge, in the centre of which a super-massive black hole has been found. The disc is barred and warped and surrounded by a spheroidal halo of stars with a total mass $\sim 1 \times 10^{9} M_\odot$ and a population of dwarf satellite galaxies of which currently ~ 25 are known. All these galaxies are part of the Local Group of galaxies, which also contains the Andromeda galaxy (M31), the Triangulum galaxy (M33) and their satellites. The oldest stars in the Milky Way have ages consistent with formation within the first billion years (Gyr) after the Big Bang. Stars have likely been forming ever since. Currently, the Galactic gas disc contains several $10^{9} M_\odot$ of gas, from which stars form with a rate $\sim 1 M_\odot/\mathrm{yr}$. The Galaxy is surrounded by circumgalactic gas, which is likely responsible for the replenishing of the gas reservoir for star formation. It is also thought to be surrounded by a dark matter (sub-)halo and to live in a universe currently dominated by dark energy and dark matter.

Most galaxies with masses similar to that of the Milky Way are dominated by discs. Moreover, galaxies at this or a slightly lower mass have been shown to be most efficient in turning gas into stars. This has likely been the case for most of the history of our universe. Star forming galaxies at high and low redshift have also been shown to have disc dominated morphologies. Consequently, most stars in the universe have formed in disc galaxies with masses similar to that of the Milky Way.

The population of disc galaxies in the local universe is diverse, as visualized in Fig. 1.1. The population has also changed strongly during the last ~ 10 Gyr. Gas-fractions, star formation rates, heavy element abundances, disc sizes and gas velocity dispersions are among the quantities known to have been very different in high-redshift discs.

Understanding the formation and evolution of galaxies requires knowledge about a variety of physical processes on a multitude of scales. Models, for example, require input about cosmology, the inter-galactic medium, the inter-stellar medium, star formation, stellar evolution, stellar and galactic dynamics and black holes.

So apparently each disc galaxy is a complex system with a complex formation history that is part of a complex population. This makes the formation and evolution of disc galaxies not only a key question in astrophysics but also a topic that offers new questions to be answered no matter how many are thought to have been answered already.

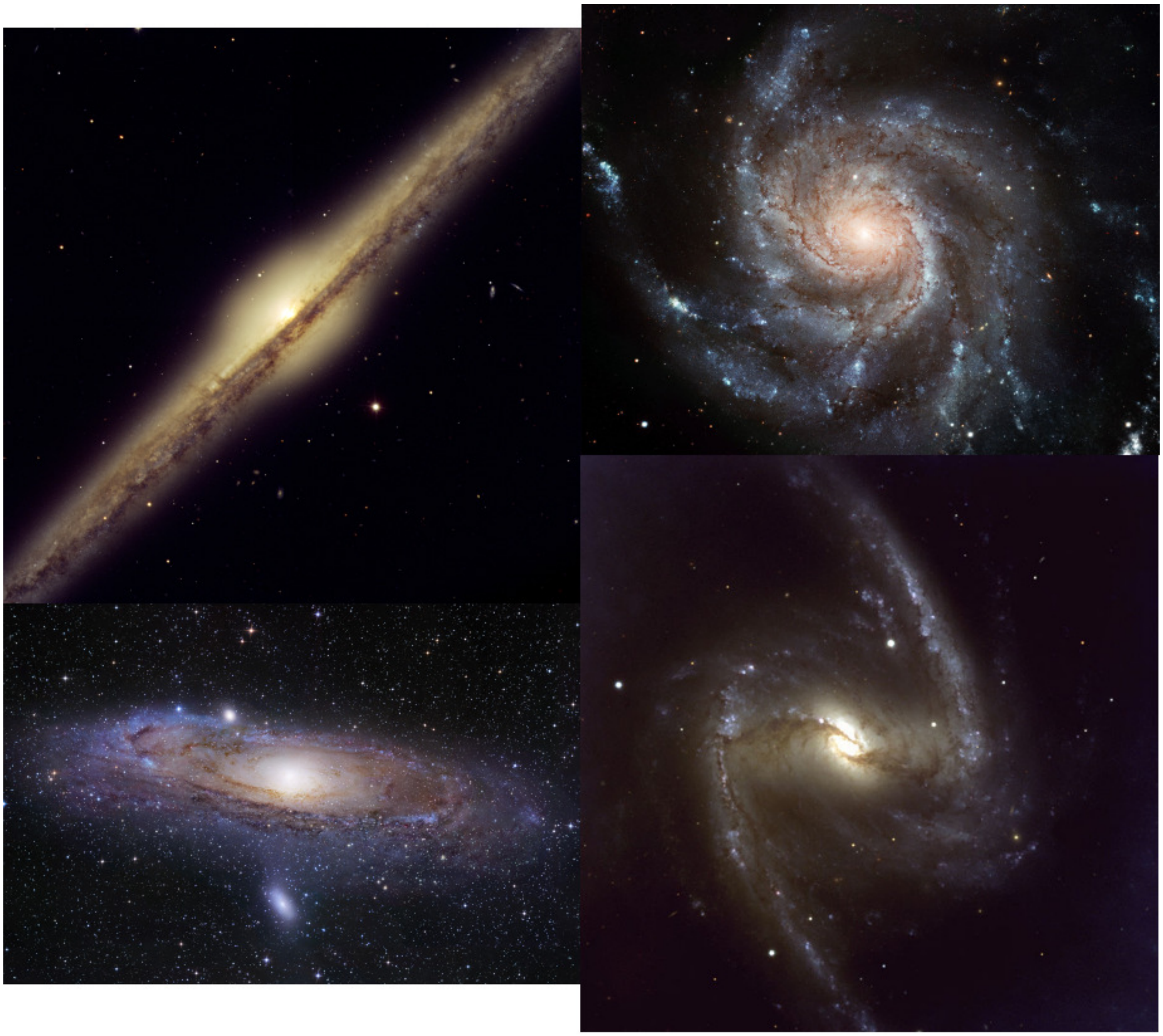

Figure 1.1: Four images of modern day disc galaxies. Top Left: NGC4565, an edge-on type Sb spiral (from the ESO Very Large Telescope (VLT)); Top right: M101 (*Pinwheel Galaxy*), a type Sc spiral (from the NASA/ESA Hubble Space Telescope); Bottom left: the Andromeda galaxy (M31), a type Sb spiral (image by John Lanoue); Bottom right: NGC1365, a type SBb barred-spiral (from the ESO VLT). This figure compilation was first presented in Aumer (2010).

2 | Introduction

In this chapter we try to present a brief introduction to the field of galaxy formation by giving an overview on observational facts, theoretical concepts and numerical methods. We refer to books by Peebles (1993) on physical cosmology, by Mo et al. (2010) on galaxy formation and evolution in a cosmological context and by Binney & Tremaine (2008) on galactic dynamics for thorough treatments of the field.

2.1 | (Disc) Galaxies in the real universe

2.1.1 | The galaxy population

Galaxies are gravitationally bound objects that contain a large number of stars. The most massive galaxies known live in the centres of galaxy clusters and contain a stellar mass of $\sim 10^{12} M_\odot$. At the low mass end, the distinction between galaxies and star clusters has been a matter of debate (see e.g. Willman & Strader, 2012). The lowest mass satellite galaxies of the Milky Way contain $10^{3-4} M_\odot$ of stars, less than many star clusters.

Galaxies with stellar masses $M_\star \lesssim 10^9 M_\odot$ are usually referred to as *dwarf* galaxies. The vast majority of galaxies are dwarfs. The number density of galaxies as a function of stellar mass drops sharply above $\sim 10^{11} M_\odot$. The stellar mass of the Milky Way (MW), $M_\star \sim 10^{10.8} M_\odot$, is only slightly lower. The contribution to the total stellar mass in the universe is highest for galaxies with $M_\star$ similar to that of the MW (Kauffmann et al., 2003a).

A clear morphological bimodality in the galaxy population was first classified by Hubble (1926). His morphological classification scheme, the *Hubble Sequence*, divided regularly shaped galaxies into *ellipticals* (confusingly also referred to as *early type* galaxies) and *spirals* (*late type* galaxies). Elliptical galaxies are flattened ellipsoidal systems that are mainly supported by the random motions of their stars, whereas spirals show a spiral pattern (see Fig. 1.1) and are strongly flattened by rotation. Spirals are thus *disc* galaxies.

However, there is no strict bimodality as most ellipticals contain disc components (Emsellem et al., 2011) and most discs contain central spheroidal components that are referred as *bulges*. Therefore, it is common to sub-divide spirals and ellipticals into morphological sub-types reflecting the mixture of components. The morphological sequence is completed by *Lenticular* (or *S0*) galaxies which are intermediate-type objects that contain a disc but no spiral arms. A recent morphological classification scheme is presented in Fig. 2.1 (Cappellari et al., 2011).

Disc galaxies have significant gas components and are actively star-forming, whereas ellipticals are gas-poor and hardly forming any stars. For dwarf galaxies, gas-rich systems have *irregular*, patchy morphologies and gas poor systems are diffuse and *spheroidal*. Finally, there are *peculiar* galaxies, which show tidal tails, rings or multiple components and

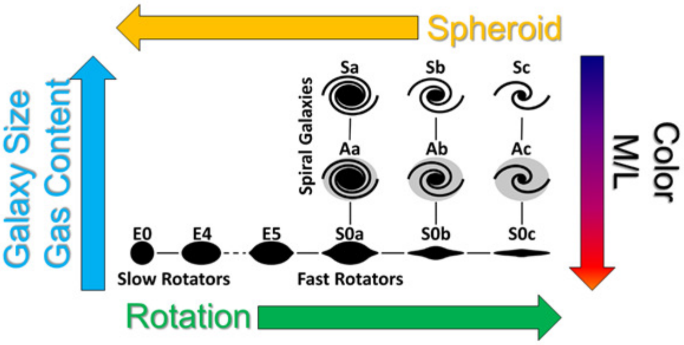

Figure 2.1: The *Atlas3D comb*, a morphological classification scheme for galaxies put forward by the ATLAS3D survey collaboration. Spiral galaxies (types S and A) are shown by face-on pictograms, whereas lenticulars (S0) and ellipticals (E) are shown edge-on. The figure was adapted from Cappellari et al. (2011).

are often made up of merging or interacting systems.

At a given stellar mass, spiral galaxies are brighter and bluer than ellipticals, i.e. they emit a higher fraction of blue light. Ellipticals are correspondingly red. Colour reflects the age of a stellar population, as massive stars are luminous and blue, but live only for several Myr. Moreover, a higher metal content (*metallicity*), i.e. fraction of all elements except H and He, and a higher dust content, can also lead to redder colours. Due to the young stars, star-forming galaxies also have a lower mass-to-light ratio M/L. As gas-poor galaxies have (almost) stopped forming stars, they are also referred to as *quenched* galaxies.

A small fraction of all galaxies contains a small, bright central region called *Active Galactic Nucleus* (AGN), which emits light with a spectral energy distribution which cannot be explained by gas and stars alone. AGN can be brighter than their host galaxies and are believed to be powered by the accretion of material onto super-massive black holes (SMBHs).

Modern spectroscopic surveys, such as the *Sloan Digital Sky Survey*, have allowed a detailed inventory of the local galaxy population by collecting data on $\gtrsim 10^5$ systems. They revealed two distinct families of galaxies, divided at a stellar mass $M_\star \sim 3 \times 10^{10} M_\odot$. The division is diffuse in stellar mass, the populations are best separated as a function of surface mass density (Kauffmann et al., 2003b; Baldry et al., 2004). The lower-mass *blue cloud* of galaxies contains blue, young, star-forming, gas-rich, extended galaxies, most of which are discs. The higher-mass *red sequence* contains red, old, dead, gas-poor, more concentrated systems, most of which are ellipticals.

Apart from the dependence on mass, there is also a clear dependence of galaxy properties on environment. High density environments, such as galaxy clusters, on average host galaxies that are redder, more concentrated, less gas-rich and have lower star formation rates (SFRs) and lower disc fractions (Kauffmann et al., 2004). Fig. 2.2 (Peng et al., 2010) gives an overview on the the galaxy bimodality by showing the fraction of red galaxies as a function of environment and stellar mass.

The focus in this thesis will be on disc galaxies with masses $10^9 \lesssim M_\star/M_\odot \lesssim 10^{11} M_\odot$, which live in low density environments (the *field*).

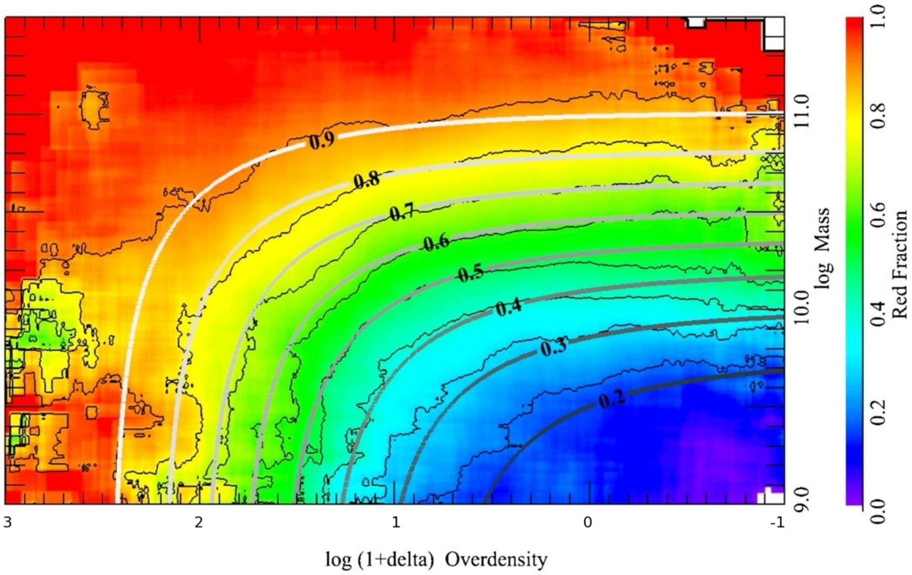

Figure 2.2: The fraction of red galaxies as a function of stellar galactic mass and environment as measured by overdensity. The figure was adapted from Peng et al. (2010).

2.1.2 | Scaling relations for disc galaxies

Disc galaxies follow several *scaling relations*. Tully & Fisher (1977) showed that there is a well-defined relation between the luminosity of a galaxy and the maximum rotation velocity of the disc and thus between the luminous and the dynamical mass. The relation is quantified as $L \propto V_{\mathrm{max}}^{\alpha}$ with $\alpha = 2.5 - 4.0$. A more modern version of this relation, the *baryonic Tully-Fisher* relation, uses stellar plus gas mass instead of luminosity. This has been claimed to yield a tighter relation (McGaugh, 2012).

The *mass-metallicity* relation of galaxies reveals that more massive galaxies have higher mass fractions of heavy elements. This relation exists for the gas (Tremonti et al., 2004) and for the stars in galaxies (Gallazzi et al., 2005). The relation for gas-phase metals shows little scatter and a steady increase of metallicity up to $M_\star \sim 10^{10.5} M_\odot$, where bulges become dominant and the relation flattens. The typical metallicity of a MW-like galaxy is close to the solar one.

The *mass-size* relation reveals that the half-light radii of lower mass disc galaxies only increase mildly with stellar mass as $R_{50} \propto M_\star^{0.15}$ (Shen et al., 2003). Again, at masses above $10^{10.5} M_\odot$ the slope of the relation becomes steeper due to the influence of bulges. The typical half-light radius of a MW-like galaxy is ~ 4 kpc ($1\ \mathrm{pc} = 1\ \mathrm{parsec} = 3.086 \times 10^{16}\ \mathrm{m}$).

The fraction of *cold gas* in neutral and molecular phases in $z = 0$ disc galaxies decreases strongly with increasing stellar mass (Haynes & Giovanelli, 1984). At $M_\star \sim 10^9 M_\odot$, discs contain slightly more gas than stars, whereas in massive discs, such as the MW, the gas fraction is ~ 10 per cent (e.g. Peeples & Shankar, 2011).

The specific star formation rate, i.e. the SFR per stellar mass, is almost constant as a function of stellar mass for blue cloud galaxies (e.g. Elbaz et al., 2007). This relation is sometimes referred to as the *main sequence of star forming galaxies*. There is a fraction of ~ 1 per cent of galaxies which have significantly higher specific SFRs, they are referred to as *star-bursts*.

2.1.3 | The structure(s) of disc galaxies

Disc galaxies at $z = 0$ show a variety of morphologies as depicted in Fig. 1.1. Traditionally they are classified according to their morphology as Sa, Sb or Sc. From Sa to Sc the bulge fraction decreases, the spiral arms become more loosely wound, the gas fraction increases and the spiral structure becomes clumpier. Type Sa galaxies often show *grand-design* spiral structure, i.e. usually two spiral arms which are distinct over a large radial range. Type Sc spirals more often show *flocculent* spiral structure, which consists of a multitude of arm segments. The classification of Fig. 2.1 reflects this and also includes *anemic* (A type) spirals (van den Bergh, 1976). This additional type attempts to classify the transition from spirals to lenticulars.

Hubble's tuning fork morphological classification of galaxies splits spirals into barred and unbarred. A bar is a rotating, elongated, triaxial structure in the centre of a disc galaxy (see lower right panel in Fig. 1.1). More than 50 per cent of disc and lenticular galaxies contain bars, independent of mass or spiral morphology (Eskridge et al., 2000). The MW is usually regarded as a fairly typical barred Sb/Sc type spiral.

The surface brightness profiles of galaxies are often fitted with *Sersic profiles* (Sersic, 1968) of the form

$$I(R) = I_0 \exp\left[-\kappa R^{\frac{1}{n_s}}\right], \tag{2.1}$$

where n_s is called the *Sersic index* and I_0 and κ are parameters governing the level of surface brightness and the radial extent of the profile.

Disc galaxies often have two-component profiles, which are generally attributed to the contributions of the bulge and the disc (Freeman, 1970). The disc profile typically is similar to an exponential profile, i.e. $n_s = 1$. Typical exponential scale-lengths of disc galaxies are of the order $R_d \sim 2 - 6$ kpc (Courteau et al., 2007). For the MW, $R_d \sim 3\,\mathrm{kpc}$ is found (e.g. Bovy et al., 2012). If disc galaxy profiles are approximated by one-component Sersic fits, the Sersic index on average increases with disc mass due to a stronger influence of the bulge, which is apparent as a central excess.

According to the structure of their light profiles, bulges are usually divided into *pseudo-bulges* with $n_s \lesssim 1$ and *classical bulges* with $n_s \sim 4$. The latter thus have profiles similar to the ones of elliptical galaxies (de Vaucouleurs, 1958). Pseudo-bulges are connected to bars and are sometimes peanut shaped, as is the bulge of the MW (Wegg & Gerhard, 2013). The MW bulge contains stars with metallicities spanning three orders of magnitudes from strongly sub-solar to super-solar (Ness et al., 2013). It is likely made up of various components and is thought to have had a complex formation history.

The exponential disc profile usually extends over several exponential scale-lengths. Outside, most profiles are down-bending, but some are up-bending or show more complex behaviour (e.g. Martín-Navarro et al., 2012). The disc outskirts are often found to be bluer (Wang et al., 2011b) and the metallicity in the disc component typically decreases outwards (Zaritsky et al., 1994). All these phenomena can be connected to an inside-out disc formation process.

The vertical density distribution of the MW disc and many other disc galaxies has a double-exponential shape, with components being referred to as *thin disc* and *thick disc* (Yoachim & Dalcanton, 2006). The ratio of scale-heights is often $\sim 1 : 2 - 3$ and for MW-like galaxies the thin disc dominates in mass. In the MW, the scale heights are ~ 300 pc and ~ 1000 pc. The MW thick disc contains stars that are $\gtrsim 10$ Gyr old, metal poor, have a higher fraction of α elements such as C and Mg and lower rotation velocities compared to thin disc stars. Recent studies have shown that the components are not distinct, but rather the outcome of a continuous formation process (Schönrich & Binney, 2009b; Bovy et al., 2012).

The MW is surrounded by a spheroidal distribution of stars, the *stellar halo*, which contains $\sim 10^9 M_\odot$ of stars. The density profile is similar to $\rho \propto r^{-3}$, but the halo is highly substructured with stellar streams which were stripped from satellite galaxies and globular star clusters (e.g. Helmi et al., 1999). There is hardly any ordered rotation in the stellar halo (Fermani & Schönrich, 2013).

2.1.4 | Gas in and around disc galaxies

The gas in disc galaxies lives in discs with a smaller vertical extent than that of the stellar counterparts. The mass is dominated by a neutral and a molecular component. The gas and dust (small solid particles) in galaxies are together referred to as the *Inter-Stellar Medium* (ISM).

Neutral hydrogen (HI) discs are often more extended than stellar discs (e.g. Walter et al., 2008) and frequently show complex morphology, such as warps (Sancisi, 1976) or lopsidedness (Baldwin et al., 1980). The HI mass of a galaxy and the diameter of the HI disc are tightly correlated as $M_{\rm HI} \propto D_{HI}^2$ (Broeils & Rhee, 1997) implying that there is a typical surface density of HI gas in disc galaxies.

Above gas mass surface densities of $\Sigma \sim 5\ M_\odot {\rm pc}^{-2}$, molecular gas becomes dominant. It is thus preferentially detected in spiral arms and other substructures of higher density. The molecular component is confined to *Giant Molecular Clouds* (GMCs) with average densities of order $n \sim 100\ {\rm cm}^{-3}$. Molecular cloud complexes in $z = 0$ galaxies typically have masses in the range $\sim 10^5 - 10^7 M_\odot$.

The cold gas in discs moves on nearly circular orbits and can thus be used to determine the circular velocity curve $V_{\rm circ}(R)$, from which the dynamical mass distribution in galaxies can be inferred. The circular velocities in disc galaxies usually rise steeply in the centre because of the centrally concentrated bulge. The lower the bulge fraction, the shallower the increase. The outer parts of the circular velocity curves can be determined from neutral hydrogen and are found to be flat out to radii far beyond the edges of stellar discs (Rubin et al., 1978). Typical rotation velocities of disc galaxies are in the range $100 - 300\ {\rm kms}^{-1}$ (Courteau et al., 2007). Schönrich (2012) finds $V_{\rm circ} = 238 \pm 9\ {\rm kms}^{-1}$ for the solar neighbourhood, at a distance $R \sim 8\ {\rm kpc}$ from the centre of the MW.

Star formation (SF) in disc galaxies occurs in molecular clouds. The SFR surface density is observed to increase linearly with the molecular gas mass surface density (Bigiel et al., 2008) implying a constant efficiency of SF from molecular gas. The corresponding depletion time of gas due to SF is a few Gyr and thus significantly lower than the age of the universe.

The UV radiation emitted from massive young stars can create bubbles of ionized gas which are called *HII regions*. A large volume fraction of galactic gas discs is filled with hot gas with temperatures $T \sim 10^6\ {\rm K}$ and densities $n \sim 10^{-4}{\rm cm}^{-3}$. The thermal energy density of the ISM is dominated by this hot gas phase. Cosmic rays (relativistic protons and electrons) and galactic magnetic fields both contain similar energy densities.

Gas in the universe is not only found within galaxies, but also in the regions surrounding galaxies (the *Circumgalactic Medium*, CGM) and in the space between galaxies (the *Intergalactic Medium*, IGM). The IGM contains the majority of ordinary (*baryonic*) matter in the universe and at present day is highly ionized (see e.g. Davé et al., 2001). Interestingly, the IGM is enriched with metals down to densities that are clearly unassociated with galaxies (e.g. Schaye et al., 2003).

The metal enrichment of the IGM is likely connected to *galactic winds*, i.e. gas flows out of galaxies. Such winds have been detected for star-forming galaxies of various masses and contain gas at various temperatures and densities. The wind velocities can be as high as several hundred kms^{-1} and thus higher than the escape speed of typical spiral galaxies (see Veilleux et al., 2005 for a review).

Apart from winds, circumgalactic gas has been detected in neutral and ionized phases. There is evidence for significant masses of HI surrounding some disc galaxies (Fraternali et al., 2002). Around the MW, infalling high-velocity clouds of HI have been observed (e.g. Peek et al., 2008). Moreover, observations of hot X-ray emitting gas around galaxies show that galaxies can be surrounded by extended hot gas haloes with masses of at least several $10^9 M_\odot$ (Anderson et al., 2013).

2.1.5 | The observed evolution of galaxies

During the last years, a variety of new and improved space- and ground-based observatories have enabled observers to probe the galaxy population at ever greater distances and thus at earlier times. These observations provide important insights into the evolution of galaxies.

The cosmic SFR density was highest ~ 10 Gyr ago, at cosmological redshifts $z \sim 2-3$ (Hopkins et al., 2006). Until today ($z = 0$), it has dropped by roughly an order of magnitude. Star-forming galaxies at all times $z = 0-3$ have been observed to form an evolving main sequence of star formation with a specific SFR that varies only mildly with galaxy mass (e.g. Karim et al., 2011). For galaxies of a fixed stellar mass, the typical SFR drops by an order of magnitude from $z = 3$ to $z = 0$, similar to the cosmic SF history.

Wuyts et al. (2011) combined data on SFRs and stellar masses of galaxies with data on the structure of the surface brightness profiles as quantified by the Sersic index n_s. We show their results in Fig. 2.3. They reveal that at all times $0 < z < 2.5$ star-forming galaxies have profiles with $n_s \sim 1$, i.e. exponential disc profiles. Rodighiero et al. (2011) showed that, as at $z = 0$, star-bursting galaxies with higher than average SFRs, at $z = 2$ also contribute only ~ 10 per cent to the cosmic SFR density. Combining these observations, one can infer that SF during (at least) the last 10 Gyr has been dominated by disc galaxies. Fig. 2.3 also reveals that at all z the most massive star-forming galaxies have $M_\star \sim 10^{11} M_\odot$.

As indicated by the evolution of specific SFRs, galaxies were different at higher z. Discs with stellar masses of several $10^{10} M_\odot$ at $z = 2$ contain turbulent gas with velocity dispersions exceeding $50\ \mathrm{kms}^{-1}$, several times higher than at $z = 0$, and giant star forming clumps with masses $\sim 10^9 M_\odot$ (Genzel et al., 2008). At a fixed stellar mass, gas fractions are a factor of a few to several higher at $z = 2$ than at $z = 0$ (Tacconi et al., 2010) and gas-phase metallicities have increased with time (Maiolino et al., 2008). Due to the high SFRs, high-z disc galaxies are driving strong, metal-enriched galactic winds (e.g. Steidel et al., 2010).

By combining observations at various redshifts, the typical evolution of a population of galaxies of a certain $z = 0$ mass can be attempted to be traced throughout its evolution. Evolutionary samples can e.g. be constructed by observing galaxies at various z but constant comoving number density (van Dokkum et al., 2013) or by inferring a mass evolution history from the evolution of specific SFRs (Patel et al., 2013b). For a MW-like $z = 0$ mass, van Dokkum et al. (2013) e.g. find that from $z = 2.5$ until today, colours continuously become

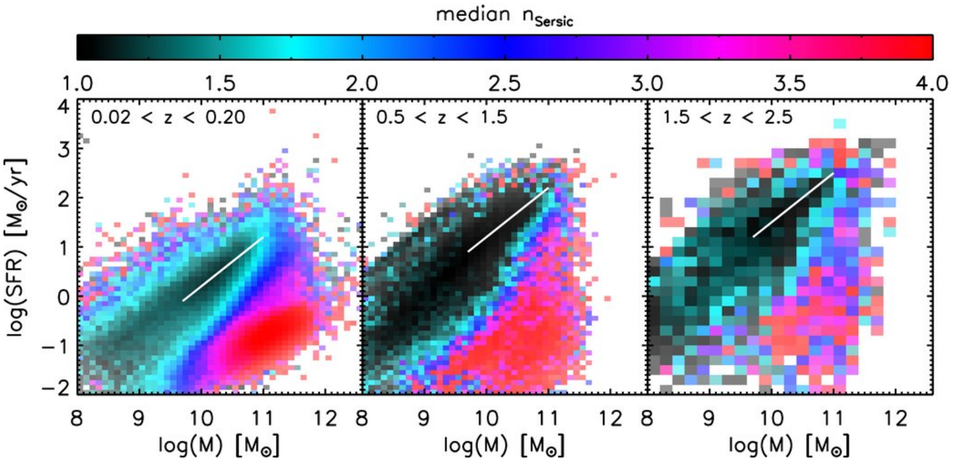

Figure 2.3: Surface brightness profile shape as measured by Sersic index in the SFR-mass diagram at $0.02 < z < 0.20$ (left), $0.5 < z < 1.5$ (middle) and $1.5 < z < 2.5$ (right). The white lines indicate the *main sequence of star forming galaxies*. The figure was adapted from Wuyts et al. (2011).

redder, Sersic indices on average increase from $n_s \sim 1$ to $n_s \sim 3$, half-light radii double until $z \sim 1$ and then remain constant and the stellar mass grows continuously at inner and outer radii.

2.2 | The ΛCDM paradigm of structure formation

Over the last decades, the ΛCDM cosmological model has emerged as the standard model of cosmogony. It is named after the two components which are thought to currently dominate the energy budget of the universe, the *cosmological constant* Λ and *cold dark matter* (CDM).

2.2.1 | The homogeneous universe

Physical cosmology is based on the *Cosmological Principle*, which states that the universe is homogeneous and isotropic on large scales. In such a universe, any large distance r between two arbitrary points can only evolve as

$$r(t) = a(t)r_0, \tag{2.2}$$

where r_0 is constant in time and called the *comoving distance* between these points, and $a(t)$ is called the *scale factor* and encodes all information about the large scale evolution of the universe. In the absence of *peculiar velocities*, the change in physical distance between points is determined by the change in scale factor. Hubble (1929) discovered that galaxies on large scales are drifting apart, i.e. the scale factor is increasing with time. The *Hubble parameter* $H(t)$ is defined as

$$\frac{dr}{dt} = \dot{a}(t)r_0 = \frac{\dot{a}(t)}{a(t)}r(t) \equiv H(t)r(t) \tag{2.3}$$

and the present-day value is referred to as *Hubble Constant* H_0. Large distances in this context means on scales $\gtrsim 100$ Mpc. In comparison, the characteristic size of the visible universe is $H_0/c \sim 4.3$ Gpc. The expansion of space results in a change of the wavelength of photons from λ_i at time of emission t_i to λ_0 at present-day t_0 quantified by the *cosmological redshift* $z(t)$ as

$$\frac{\lambda_0}{\lambda_i} = \frac{1}{a(t_i)} \equiv 1 + z(t), \tag{2.4}$$

where $a(t_0)$ is set to 1.

General Relativity (Einstein, 1916) relates the space-time structure of the universe to its energy content. In its context, a homogeneous and isotropic universe is described by the equations of Friedmann (1922). It is illustrative to consider the following form of the first of Friedmann's equations:

$$H^2 = \frac{\dot{a}^2}{a^2} = H_0^2 \left[\Omega_r(1+z)^4 + \Omega_m(1+z)^3 + \Omega_k(1+z)^2 + \Omega_\Lambda\right]. \tag{2.5}$$

Here the density parameters $\Omega_i = \rho_i/\rho_{\rm crit}$ denote the present-day densities ρ_i in units of the critical density of the universe

$$\rho_{\rm crit}(t) = \frac{3H^2(t)}{8\pi G}, \tag{2.6}$$

for which the geometry of the universe is Euclidian. In this case, the contribution of curvature, $\Omega_k = 1 - \Omega_r - \Omega_m - \Omega_\Lambda$, is zero. Current observations indicate that this is the case, our universe is *flat*.

Ω_r denotes the density of radiation and other massless or highly relativistic particles, Ω_m the density of non-relativistic matter and Ω_Λ the contribution of a cosmological constant.

The observed expansion of the universe led to the idea, that the universe started from an extremely hot and dense state, the *Hot Big Bang* (Lemaître, 1931; Gamow, 1946), which explains the formation of the light elements in the universe (Gamow, 1946) and the existence of a *Cosmic Microwave Background* (CMB, Alpher & Herman, 1948), which was later discovered by Penzias & Wilson (1965). The radiation energy density in the current universe is $\Omega_r \sim 10^{-4}$, but according to equation 2.5 it was the dominant component in the early universe ($z \gtrsim 3000$). At $z \sim 1100$ ($\sim 3 \times 10^5$ years after the Big Bang) , ρ_r became too low to keep the primordial gas of hydrogen and helium fully ionized and radiation and matter *decoupled*. The CMB is the relic radiation from this epoch.

The CMB is remarkably isotropic, but shows fractional anisotropies of the order 10^{-5}. The corresponding density perturbations at $z \sim 1100$ are believed to be the seeds for structure formation in the universe. They are thought to originate from quantum fluctuations, which were blown up to macroscopic scales during *Inflation* (Guth, 1981; Mukhanov & Chibisov, 1981), a phase of extremely rapid expansion within the first 10^{-32} seconds of the universe.

Ω_m is thought to be dominated by non-baryonic *dark matter* (DM) consisting of elementary particles yet to be detected. Among the candidates are *Weakly Interacting Massive Particles* (WIMPs), as for example predicted by supersymmetry, *sterile neutrinos* and *axions* (see Feng, 2010 for a review). The idea of DM dates back to Zwicky (1933), who argued that the motions of the galaxies in the Coma cluster required a much higher gravitating mass than that inferred from star light. Although the observed baryonic mass in clusters has since increased due to the detection of gaseous components, the argument still holds. Similar arguments were later made because of the kinematics of satellite galaxies around the MW and other local galaxies (Ostriker et al., 1974) and flat rotation curves of gas in the very outskirts of disc galaxies (Rubin et al., 1978).

Moreover, the density fluctuations inferred from the CMB are too small to explain the growth of the vast density contrasts observed in the universe today. Before recombination, Thomson scattering locked the ionized plasma to the photons, allowing the growth of baryonic structures only after $z \sim 1100$. Due to the absence of radiation pressure, for a DM component, which decouples at earlier times, fluctuations could already have reached a significantly higher density contrast at recombination.

Ω_Λ is thought to be currently dominating the energy budget of the universe. This conclusion was first drawn by Efstathiou et al. (1990), who showed that observations of large scale galaxy clustering favoured a flat universe with Ω_m significantly smaller than unity. White et al. (1993) presented a similar conclusion based on the baryon content of galaxy clusters. The idea became widely accepted when high-redshift type Ia supernovae (SNIa) were used as standard candles to test the expansion history of the universe, and accelerated expansion was found (e.g. Riess et al., 1998).

Equation 2.5 illustrates that Λ was unimportant in the early universe, but will become the only relevant part of the energy budget in the future. Λ can be interpreted as a *vacuum energy*. It is accompanied by a negative pressure $P = -\rho_\Lambda c^2$, has the peculiar feature of exerting repulsive gravitational forces and thus accelerates the expansion of the universe. The nature of this *dark energy* is not well understood and a multitude of models exist (e.g. Peebles & Ratra, 2003). The data is still consistent with a simple cosmological constant (Planck Collaboration, 2013).

The idea that the universe is dominated by DM and a dark energy has been confirmed by a variety of independent types of observations, which include the anisotropies in the CMB (e.g. Planck Collaboration, 2013), the distances to high-redshift SNIa (e.g. Riess et al., 1998), the large scale clustering of galaxies (e.g. Cole et al., 2005), light element abundances predicted by Big Bang nucleosynthesis (e.g. Yang et al., 1984), weak gravitational lensing (e.g. Hoekstra & Jain, 2008), baryonic acoustic oscillations as displayed by the large scale galaxy distribution (e.g. Percival et al., 2010) and the Lyman-alpha-forest power-spectrum (e.g. Seljak et al., 2006). It should be noted that all these lines of evidence come from scales larger than that of galaxies.

The following values for the age of the universe τ_H and other cosmological parameters were recently presented by the Planck Collaboration (2013):

$$\begin{aligned}
\tau_H &= 13.798 \pm 0.037\ \mathrm{Gyr} \\
H_0 &= 67.80 \pm 0.77\ \mathrm{kms^{-1}Mpc^{-1}} \\
\Omega_{\text{dark matter}} &= 0.262 \pm 0.0038 \\
\Omega_{\text{baryons}} &= 0.0489 \pm 0.00053 \\
\Omega_\Lambda &= 0.692 \pm 0.010. \qquad (2.7)
\end{aligned}$$

2.2.2 | Structures in the universe

All structures in the universe, whether satellite galaxies, galaxies, groups and clusters of galaxies, superclusters or voids are thought to have grown from small density perturbations in the early universe. The perturbations are visible in the CMB as fluctuations of the black-body temperature T_{cmb} on the order of $10^{-5}T_{\mathrm{cmb}}$. According to current knowledge, the perturbations were Gaussian with an almost scale invariant perturbation power spectrum ($n_s \sim 0.96$ for $P(k) \propto k^{n_s}$)(Planck Collaboration, 2013), as first predicted by Harrison (1970) and Zel'dovich (1972).

As the universe evolved, the perturbations were amplified by gravitational instability (Jeans, 1902). In an evolving and expanding universe perturbations $\delta = (\rho - \bar{\rho})/\bar{\rho}$ grow as $\delta(t) \propto t^{\alpha}$ with $\alpha > 0$ (Gamow & Teller, 1939). When perturbations have grown to $\delta > 1$, the evolution decouples from cosmic expansion and enters a highly non-linear regime of collapse (e.g. Zel'dovich, 1970) producing the typical structures of the *Cosmic Web* with sheets, filaments and voids and a characteristic mass function of collapsed objects (Press & Schechter, 1974). As DM dominates the gravitating mass and perturbations in baryons can only grow after recombination, the growth of perturbations is determined by the properties of DM.

To allow structure formation in the universe as observed, DM is required to be *cold*, i.e. its velocities at decoupling have to be non-relativistic (Davis et al., 1985). Model universes dominated by other forms of DM with relativistic velocities at decoupling (*hot* DM), such as neutrinos, cannot reproduce the large scale clustering of galaxies, as small scale perturbations are suppressed in the early universe (White et al., 1984). *Warm* DM (WDM) models are intermediate and predict the suppression of structure formation on scales below a mass-scale similar to the dynamical masses of the smallest MW satellite galaxies (e.g. Lovell et al., 2012). CDM allows the formation of structures down to much smaller mass scales and predicts that small structures form first and larger structures assemble later through the *hierarchical clustering* of smaller objects (Peebles, 1965).

Collapsed objects undergo violent relaxation to a quasi-equilibrium state (Gunn & Gott, 1972). The virialized regions are referred to as DM *haloes* and have an average density ρ_h that is Δ_h times higher than the cosmic mean density. Δ_h depends on the cosmological model parameters, $\Delta_h = 200$ is commonly used to determine the *virial radius* $r_{\rm vir}$ and the enclosed *virial mass* $M_{\rm vir}$, which characterize the halo. The mass of the MW halo is inferred to be $M_{\rm vir} \sim 1 \times 10^{12} M_{\odot}$ (e.g. Barber et al., 2013). The corresponding size is $r_{\rm vir} \sim 200\,{\rm kpc}$.

DM haloes show mass and phase space profiles which are basically independent of the mass of the halo (Navarro et al., 1997). The shape of the mass distribution of the halo is usually triaxial with a tendency towards a prolate shape (Frenk et al., 1988). Haloes are supported mainly by random motions, rather than by rotation. The energy in rotation is only a few 10^{-3} of the total energy of the system. The angular momentum is acquired due to tidal torques in interactions with neighbouring systems (Peebles, 1969).

Due to the hierarchical nature of CDM, haloes are constantly evolving and growing in mass due to mergers with other haloes. *Major mergers* with mass ratios $\eta = M_{>}/M_{<} \lesssim 3$, however on average contribute little ($\sim 20\%$) to the mass growth. Accretion of material is dominated by mergers with much higher values for η, which can be thought of as smooth accretion (Genel et al., 2010; Wang et al., 2011a). Haloes on average grow inside-out, as only major mergers affect the central regions.

Since the survival time of infalling haloes increases with η (see Section 2.3), haloes are highly substructured (Moore et al., 1999). Haloes that fall into a bigger halo are referred to as *sub-haloes* as long as they remain bound objects. On these sub-halo scales, ΛCDM is currently facing its most severe problems. The population of satellite galaxies in the Local Group of galaxies has been claimed to be inconsistent with ΛCDM predictions in terms of, among others, numbers (Moore et al., 1999), central density profiles (e.g. Goerdt et al., 2006) or anisotropic spatial distribution (Pawlowski et al., 2012).

WDM models have been proposed as a possibility to attenuate some of the problems (Lovell et al., 2012), but constraints on the cutoff-mass-scale from the Lyman-alpha forest leave little room for models that differ significantly from CDM on scales relevant for galaxy formation (Viel et al., 2013). In the context of these problems, *Modified Newtonian Dynamics*

(MOND, Milgrom, 1983) is also often cited as capable of explaining galactic and circumgalactic phenomena without having to invoke DM. However, baryonic physical processes (see Section 2.3) are important on these scales and have been proposed as solutions to some of the problems within the ΛCDM paradigm (Bullock et al., 2000; Zolotov et al., 2012).

2.3 | The physics of Galaxy Formation

2.3.1 | Accretion, Cooling and Condensation

In the framework of ΛCDM, the formation of galaxies is supposed to be a two-stage process, as first described by White & Rees (1978). The hierarchical formation of DM dominated structures leads to the formation of virialized (sub-)haloes (see Section 2.2) within which baryons cool and condense to form a galaxy. The processes relevant for the second stage of this scenario are discussed in this Section.

Fig. 2.4 gives an overview on the different baryonic components that are involved and on the processes that lead to interactions between the components. Note that this sketch is certainly incomplete and over-simplified. The components are the *Intergalactic Medium* (IGM) representing the gas outside the virialized halo, the *Circumgalactic Medium* (CGM) representing the gas surrounding the galaxy on scales smaller than $r_{\rm vir}$, the *Interstellar Medium* (ISM) representing the gas within the galaxy, the stars in the galaxy and the *Supermassive Black Hole* (SMBH) in the centre of the galaxy.

The IGM has at all times been the component harbouring the majority of baryonic mass in the universe. All the baryons in the other components at some earlier time were also part of the IGM. Unlike collisionless DM, gas falling into the halo will undergo strong compression and shock heating to the virial temperature of the halo (e.g. Rees & Ostriker, 1977), turning kinetic into thermal energy. Dissipation of internal energy due to radiative cooling is counteracting and depending on the efficiencies of the processes gas will rapidly cool to the centre of the halo and feed the ISM, or it will form a hot corona in hydrostatic equilibrium with the gravity of the halo, so that material is added to the CGM. The hot CGM can subsequently cool on timescales that are long compared to the dynamical timescale of the halo. In Fig. 2.4 these processes are represented by three corresponding arrows for *cold* and *hot mode* accretion and cooling. Cooling leads to a segregation of baryons from DM, allowing the formation of galaxies in the centres of haloes.

The most important radiative cooling processes are the emission of Bremsstrahlung, collisional excitation and the subsequent radiative decay, and collisional ionization followed by recombination and photon emission. These are all two-body processes and consequently the cooling times decrease with increasing density. At redshifts $z \gtrsim 6$, inverse Compton scattering of CMB photons by electrons in hot gas also contributes to cooling. The cooling rates depend sensitively on chemical composition and on temperature (see e.g. Fig. 8.8 in Mo et al., 2010). At $T > 10^6 K$, Bremsstrahlung dominates as gas is fully ionized. At $10^4 < T/K < 10^6$, excitation and ionization processes dominate and cooling rates are highest. For neutral gas at $T < 10^4 K$, collisional excitation/de-excitation of fine and hyper-fine structure lines in heavy elements and of vibrational or rotational lines in molecules provide the most efficient cooling channels. For optically thin, extragalactic gas, photo-ionization by UV or X-rays can have an important effect on cooling rates (Wiersma et al., 2009b). Such short wavelength radiation is also supposed to prevent any efficient cooling and condensation of gas in dwarf-galaxy-scale haloes during the epoch of reionization ($z \sim 6 - 10$, Bullock et al.,

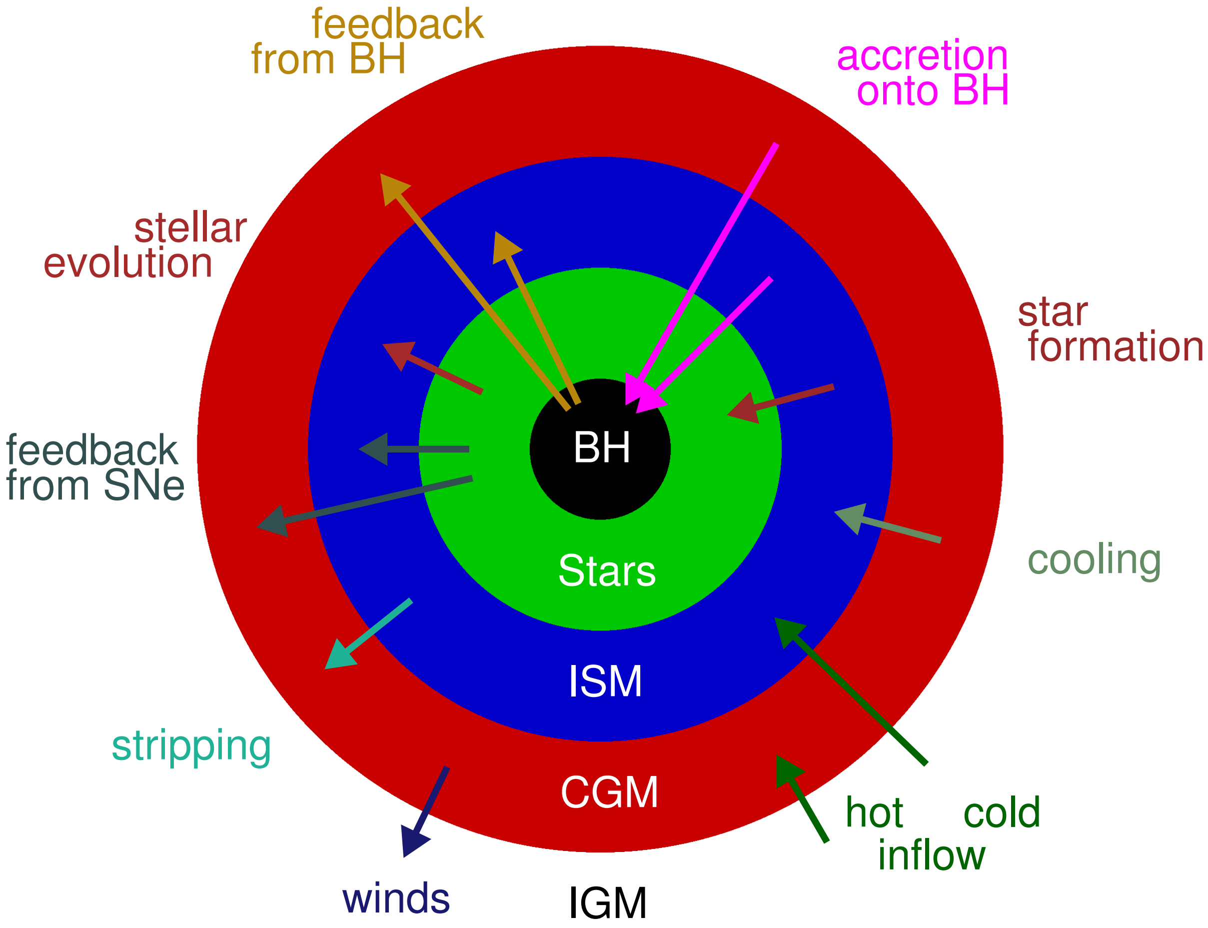

Figure 2.4: A sketch of the different baryonic components involved in galaxy formation and of processes that lead to interactions among the components. For a different interpretation see Fig. 1.2 in Mo et al. (2010).

2000).

As the virial temperature increases with halo mass and cooling rates decrease above $T > 10^6 K$, cooling of hot halo gas in hydrostatic equilibrium can become inefficient for halo masses greater than that expected for a MW-like galaxy ($M_{\rm vir} > 10^{12} M_\odot$) (Binney, 1977; Silk, 1977; Rees & Ostriker, 1977). Hydrodynamic cosmological simulations of galaxy formation during the last decade (e.g. Kereš et al., 2005; van de Voort et al., 2011) showed that for smaller halo masses, most accreting gas does not go through a stable hot phase and falls in along filaments as *cold streams* (see also Binney, 1977). Nelson et al. (2013), however, recently showed that applying different numerical techniques for the treatment of hydrodynamics yields significantly higher fractions of *hot mode* accretion.

As discussed for DM in the previous Section, baryons also gain angular momentum through tidal torques. When gas cools to the centre of a halo its rotation velocity increases due to the conservation of angular momentum. In the centre of the halo, it settles in a cold disc in centrifugal equilibrium (Fall & Efstathiou, 1980). Further cooling eventually leads to a dominance of self-gravity and catastrophic collapse. This results in cold, dense gas clouds. The clouds become molecular if self- and dust-shielding prevent the photo-dissociation of molecules by UV photons to be more efficient than molecule formation on dust grains. The typical average densities of the resulting *Giant Molecular Clouds* (GMCs) are $n \gtrsim 100 \ \rm cm^{-3}$.

GMCs are highly substructured with *cores* of $n \gtrsim 10^5 \ \rm cm^{-3}$, which are the sites of SF. Although locally all stars are observed to form from molecular gas, it is unclear whether molecules are a necessary requirement for SF (e.g. Glover & Clark, 2012). The details of SF and the *Initial Mass Function* (IMF) of stars are not well understood. Empirical determinations of the IMF (Kroupa, 2001) show that the vast majority of stars have sub-solar masses and that up to 20 $\%$ of the mass turned into stars ends up in massive stars with $M > 8 \ M_\odot$.

The high masses of SMBHs in the centres of galaxies require mechanisms for efficient growth by accretion of gas. Disc gas can lose substantial amounts of angular momentum in interactions or mergers with other galaxies or due to disc instabilities (see subsection 2.3.3) and accrete onto the BH through an accretion disc (Shakura & Sunyaev, 1976). The gravitational energy released in such accretion events is believed to power bright AGN emission (Salpeter, 1964). Spherical accretion of gas from hot atmospheres (Bondi, 1952) is significantly less efficient but is thought to take place in gas-poor massive elliptical galaxies.

2.3.2 | Feedback

A comparison of the observed luminosity function of stars and the mass function of ΛCDM haloes (see e.g. Fig. 15.2 in Mo et al., 2010) reveals very different shapes. Efficient SF at all halo masses would predict a lot more massive and a lot more dwarf galaxies. Consequently, there must be processes that significantly limit the efficiency of SF and that are dependent on halo mass.

One way to quantify these effects is through *abundance matching*. This technique combines mass functions of simulated dark-matter-only ΛCDM haloes and observed stellar galactic mass functions at various redshifts to determine the typical stellar mass $M_\star$ of a galaxy in a halo of a certain virial mass M_h under the assumption that stellar mass increases monotonically with halo mass (Guo et al., 2010; Moster et al., 2013; Behroozi et al., 2013a). Fig. 2.5 shows results from Moster et al. (2013) for the derived relation of $M_\star$ vs. M_h (left panel) at various redshifts from $z = 4$ to $z = 0$. Instead of increasing linearly with M_h, $M_\star$ increases more steeply at $M_h < 10^{11} M_\odot$ and is almost flat at $M_h > 10^{13} M_\odot$. This is true at all redshifts.

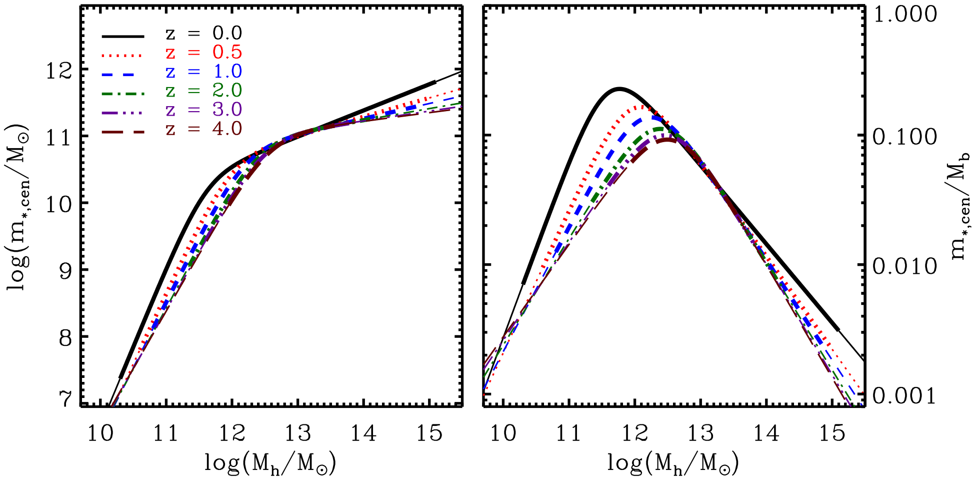

Figure 2.5: Stellar mass to halo mass relations from abundance matching at $z = 0 - 4$. Left: Stellar mass of central galaxy vs. virial mass of halo. Right: The ratio of stellar mass to baryonic halo mass (i.e. halo mass multiplied by $\Omega_{\mathrm{baryons}}/\Omega_{\mathrm{matter}}$) vs. virial mass of halo. This figure was adapted from Moster et al. (2013).

Only the halo mass at which the slope changes evolves with redshift to significantly lower values.

The right panel shows the fraction of the *available baryons* for a given halo, $M_h \times \Omega_{\mathrm{baryons}}/\Omega_{\mathrm{matter}}$, that has been turned into stars. At $z = 0$, the highest *baryon conversion efficiencies* of ~ 20 per cent are found for halo masses close to $10^{12} M_\odot$. For low mass haloes $M_h \sim 10^{10} M_\odot$ and cluster mass haloes $M_h \sim 10^{15} M_\odot$, conversion efficiencies are only a few 10^{-3}. Behroozi et al. (2013b) showed that, when abundance matching is used to calculate typical SFRs for a certain halo or stellar mass, SF efficiencies (SFR per available gas mass) are at all times $z < 4$ highest in haloes with $M_h(z) \sim 10^{11.7} M_\odot$ and most stars formed in galaxies that at the time of SF have $M_\star$ in the range between $10^{9.9} - 10^{10.8} M_\odot$. Various dynamical and statistical considerations indicate that the dynamical mass of the MW is of the order $10^{12} M_\odot$ (e.g. Barber et al., 2013 and references therein). Considering its stellar mass of $M_\star \sim 6 \times 10^{10} M_\odot$, the MW has been very efficient in forming stars.

From these considerations, we learn that there must be at least two processes which keep gas from collapsing to dense clouds and forming stars and/or are capable of removing gas from a galaxy by driving galactic winds. Possible processes are represented by the arrows in the left half of Fig. 2.4. For low mass haloes, feedback from stars and supernovae (SNe) is considered important (Larson, 1974), whereas for high mass haloes feedback from SMBHs has been suggested (Silk & Rees, 1998). The structure of disc galaxies requires that feedback processes preferentially remove low angular momentum gas (Dutton & van den Bosch, 2009; Brook et al., 2011). Independent of what their origin may be, galactic winds are also needed to explain the metal enrichment of the IGM (e.g. Oppenheimer & Davé, 2006) and to explain the observed mass-metallicity relation of galaxies (e.g. Erb et al., 2006b).

Stellar evolution offers a variety of sources for mass, metal, momentum and energy feedback. As Big Bang nucleosynthesis only produces H, He and Li, all heavy elements in the universe are believed to have formed in nuclear reactions in stellar interiors or in explosions of massive stars or white dwarfs as SNe (Burbidge et al., 1957). Metals are returned to the gas phase in stellar winds and SNe explosions. Via these channels, a population of stars loses $\sim 50\%$ of its mass to the gas phase during ~ 10 Gyr. Metals increase gas cooling rates and provide material for the formation of dust grains.

SN explosions have long been considered as a significant source of energy and momentum feedback (Larson, 1974). They are known to play a key role in regulating the inhomogeneous multi-phase structure of the ISM (McKee & Ostriker, 1977). The typical kinetic energy carried by mass ejected in core-collapse *and* thermonuclear SNe is initially $\sim 10^{51}\mathrm{erg}$, the ejecta velocities can be as high as $10^4\mathrm{kms}^{-1}$. However, due to shock heating and subsequent radiative losses, the energy input into the ISM in kinetic or thermal form is only ~ 10 per cent of the initial kinetic energy of the ejecta (e.g. Thornton et al., 1998). These losses can be reduced if several SNe explode on timescales smaller than the radiative cooling timescale. Their explosions can create overlapping shocks which are thermalized and heat the gas. Such events are known to create super-bubbles of hot, $T \sim 10^6\mathrm{K}$ gas with radii of 100 pc or more (McCray & Kafatos, 1987). If the shell of cool material swept up by the expanding super-bubble breaks up, the hot medium, the thermal velocity of which is higher than the local escape speed, can leave the bubble, expand freely and possibly leave the galactic gas disc creating a galactic wind (e.g. Lehnert & Heckman, 1996).

A different source for winds associated with SNe is the pressure due to cosmic rays accelerated in SN shocks, which has been shown to be a possible source for galactic winds in low mass galaxies (e.g. Uhlig et al., 2012).

Apart from SN explosions, massive ($M > 8\ M_\odot$) young stars, which will finally explode as core-collapse SNe (SNII), are also an important source for feedback (see e.g. Agertz et al., 2013 for an overview). The most massive stars can have luminosities up to $10^6 L_\odot$ and can drive stellar winds with velocities up to $2000\ \mathrm{kms}^{-1}$. The total energy emitted in radiation by a young stellar population until the end of SNII explosions is two orders of magnitude higher than the total energy released in SNe. In addition, ionizing radiation from massive stars has been shown to be capable of dispersing molecular clouds (Walch et al., 2012).

Moreover, the momentum injection by radiation pressure (RP) is comparable to that by winds and that by SNe. The effect of RP can be significantly enhanced by the absorption of UV photons by dust grains, which subsequently re-radiate the energy in the infrared. This process can increase the momentum injection proportional to the IR optical depth (Murray et al., 2005, 2010), which can be of the order 10-100 in dusty star forming regions. Under the assumption, that momentum injection is boosted by such factors, Agertz et al. (2013) found RP to have the strongest effect of all feedback mechanisms on the ISM. However, the validity of this IR boosting assumption is disputed (Krumholz & Thompson, 2013).

Unlike for low mass galaxies, for which the efficiency of SF increases as they grow in mass, SF in massive galaxies is *quenched* when their stellar mass approaches $\sim 10^{11} M_\odot$. As such galaxies are typically ellipticals and thus contain SMBHs with masses of $10^8 M_\odot$ or higher (Magorrian et al., 1998), the energy released during the accretion of matter onto these objects is considered an important source of feedback (Silk & Rees, 1998; Croton et al., 2006). Feedback is usually divided into *quasar mode*, when the BH is accreting material from an accretion disc with rates close to the Eddington limit, and *radio mode*, when accretion rates are low (see e.g. Fabian, 2012 for a review). The former is supposed to ionize and heat cold gas through UV and X-ray photons and may drive winds due to RP leading to a shutdown of accretion onto the BH. The latter can heat surrounding hot halo gas through mechanical feedback from relativistic jets of plasma emerging from the SMBH and thus shut down cooling and accretion onto the galaxy.

2.3.3 | Mergers and secular evolution

As described for DM haloes in Section 2.2, the hierarchical nature of structure formation makes mergers of galaxies an important process in the evolution of galaxies, However, as for DM, the baryonic mass assembly is dominated by smooth accretion of gas (van de Voort et al., 2011). The ratio of stars that were formed within the galaxy (*in-situ* stars) to stars that were accreted during mergers (*ex-situ* stars) is thought to depend sensitively on the $z = 0$ mass of a galaxy (Moster et al., 2013; Behroozi et al., 2013a). The more massive a galaxy, the higher the fraction of ex-situ stars. For a galaxy with a mass similar to that of the MW, in-situ fractions of > 90 per cent are expected, whereas in haloes with $M_h > 10^{14} M_\odot$ ex-situ stars are supposed to be dominant at $z = 0$.

During a major merger, violent relaxation transfers the orbital energy of the merging dark haloes into internal binding energy of the merged system. Hot halo gas undergoes shocks and is heated to the virial temperature of the new system. The main galaxies in the centres of the halo also merge. During a minor merger, the two dominant processes for collisionless components are *dynamical friction*, which gradually transfers orbital energy to the halo and results in an inspiral process of the smaller system, and *tidal forces* from the halo and the central galaxy of the more massive system which remove less-bound material from the outskirts of the infalling system. The efficiency of dynamical friction is smaller for high mass ratios, so that low-mass satellite galaxies can orbit their host galaxies for timescales exceeding the age of the universe. We refer to Binney & Tremaine (2008) for in-depth discussions of the processes.

These processes leave signatures in the distribution of stars over the various components of $z = 0$ galaxies. Streams of stars in galactic haloes are thought to have been tidally stripped from infalling galaxies (Helmi et al., 1999) and stellar haloes are consequently believed to consist mainly of debris from interactions during the hierarchical assembly process (Cooper et al., 2010). The fraction of accreted stars in models is highest in the outer haloes ($\gtrsim 80\%$) and substantial in the inner haloes ($\sim 50\%$) and bulges ($\sim 20\%$), but negligible in discs (Tissera et al., 2012).

The gas component of an infalling galaxy can also be exposed to a drag force from a hot halo atmosphere due to the relative motions of the fluids. This can lead to the ablation of gas from the galaxy, a process that is referred to as *ram pressure stripping*. This process is considered important for the environmental quenching of SF in galaxies within a galaxy cluster (e.g. Balogh et al., 2000).

The rapid and strong changes in the gravitational potential during major mergers of central galaxies lead to significant changes in their morphologies, such as the destruction of thin stellar discs (Toomre, 1977). Interactions and mergers have been shown to be responsible for peculiar morphologies such as rings (Lynds & Toomre, 1976) or tidal tails and bridges (Toomre & Toomre, 1972). Interactions can also excite bars and spiral structure.

Remnants of binary mergers of stellar discs have been shown to have morphologies reminiscent of elliptical galaxies (e.g. Bois et al., 2011), but these events are hard to bring into agreement with detailed properties of giant ellipticals (Naab & Ostriker, 2009). Formation scenarios relying on the continuous addition of stars to the outskirts of the central galaxy by minor mergers have been shown to yield better agreement (Naab et al., 2009).

The presence of a significant gas disc notably changes the morphology of a galaxy after a major merger (Cox et al., 2006). On the one hand, tidal perturbations lead to severe angular momentum loss of the gas and thus to strong inflows to the centre (Barnes & Hernquist, 1996), which can trigger starbursts and/or power AGN (Hopkins et al., 2006). On the other hand, gas-rich mergers can harbour enough high angular momentum disc and halo gas to efficiently (re)grow a substantial galactic disc (Barnes, 2002). Classical bulges in disc galaxies are thought to result from mergers which subsequently regrow a disc around the bulge.

As most of the gas accreting onto galaxies is not associated with merging galaxies, changes in the orientation of the angular momentum vector of infalling gas, which are expected on timescales of several Gyr (Quinn & Binney, 1992), can have significant effects on the evolution of disc galaxies. Such *misaligned infall* has been connected to the excitation of warps (Roškar et al., 2010) and the formation of polar ring galaxies (Brook et al., 2008).

Apart from the processes connected to infall of matter, dynamical processes internal to the galaxies can lead to substantial changes in the mass and angular momentum distributions of stars and thus to changes in the galactic morphology. These are often referred to as *secular evolution*.

A differentially rotating disc is unstable to the growth of local perturbations and thus to fragmentation if gravity surpasses the combined stabilizing effects of pressure (dynamical or thermal) and shear (Toomre, 1964). Unstable discs fragment into dense clumps, within which SF can occur. Violently unstable discs can fragment into a few giant clumps, which, in turn, can migrate to the centre of the galaxy due to dynamical friction and contribute to the formation of bulges (Noguchi, 1999).

An important global instability of galactic discs is the *bar instability* (see Chapter 6 in Binney & Tremaine, 2008). This instability occurs in self-gravitating discs if most kinetic energy is in rotational motion. Discs can be stabilized against bar formation by high velocity dispersions or by an additional spheroidal mass component such as a bulge or a dark halo. Interactions of bars with gas discs can lead to gas flows resulting in ring-like structures or central concentrations (Athanassoula, 1992). The latter can power starbursts and/or AGN. Bars can become unstable to a vertical bending instability which increases the vertical velocity dispersion and thickens the bar (Combes et al., 1990) leading to a peanut-shaped triaxial bulge structure as observed for pseudo-bulges. Recent simulations have shown that pseudo-bulges can also form on dynamical timescales at high redshift in complex processes involving interactions, reorientations of discs and disc instabilities (Okamoto, 2013; Guedes et al., 2013).

Spiral structures can also be the result of secular processes (see Chapter 6 in Binney & Tremaine, 2008). Flocculent spiral structure is thought to originate from locally unstable, extended perturbations that are sheared into a short-lived, transient spiral arm due to differential rotation. Grand-design spiral patterns were explained by Lin & Shu (1964) as spiral-shaped density waves which propagate through the disc with a certain pattern speed, so that gas and stars continuously pass through the spirals. Spiral waves can e.g. be excited by companion galaxies or bars, but there is not yet a comprehensive theory explaining the full variety of observed properties of spiral patterns.

Another secular process is *disc heating*, i.e. the gradual increase of the stellar velocity dispersions of stars in discs. Disc heating can be caused by substructure in the gravitational potential constituted by e.g. GMCs or transient spirals (Jenkins & Binney, 1990). The same effect could possibly also be caused by the continuous infall of satellite galaxies (Kazantzidis et al., 2008).

2.4 | Numerical methods

Due to the complex and highly nonlinear nature of structure formation involving many physical processes on a multitude of scales, numerical N-body simulations are the best tool to study galaxy formation. Given the primordial density fluctuations and their initial linear evolution, simulations constitute an ab-initio method for calculations of the evolution of cosmic structures. All simulations for this thesis were performed with the simulation code GADGET-3. Details on the applied numerical methods can be found in Springel (2005).

2.4.1 | Gravity

Gravitational N-body methods rely on the assumption that the gravitational dynamics of the system in consideration can be calculated by dividing the system into N discrete, collisionless elements, which sample its density distribution, and by calculating the gravitational forces between these *particles*. This assumption is e.g. justified for galaxies, for which the two-body relaxation times of stars are orders of magnitude larger than the age of the universe (see e.g. Binney & Tremaine, 2008) and dynamics are thus dominated by rather long-range forces within a smoothed density distribution. CDM is also modelled as a collisionless fluid, which is justified by the success of such calculations in explaining structure formation in our universe.

In a cosmological context, the expansion of space has to be taken into account in addition to the gravitational interactions of the particles. As the modifications do, however, not change the nature of the problem significantly (see e.g. Appendix C in Mo et al., 2010), we here describe the Newtonian case.

The simplest way to calculate the gravitational force on a particle i is by direct summation of contributions F_{ij} over all other particles j (particle-particle method, PP). For close particles, the force diverges as $F_{ij} \propto r_{ij}^{-2}$. This divergence is unrealistic for an N-body representation of a smooth density distribution and has to be considered a numerical artifact. Therefore *gravitational softening* is usually applied. This method modifies the force for close encounters of particles at the resolution limit of the simulation. A widely used form for the modified gravitational force from particle j on particle i is

$$\mathbf{F}_{ij} = \frac{G m_i m_j \left(\mathbf{x}_j - \mathbf{x}_i\right)}{\left(\epsilon^2 + |\mathbf{x}_j - \mathbf{x}_i|^2\right)^{3/2}}, \tag{2.8}$$

where ϵ is referred to as *softening length*. Below a certain distance scale, a particle is thus treated as an extended object with the density distribution of a *Plummer* sphere (see Binney & Tremaine, 2008). However, convergence to the Newtonian result for larger distances is slow. Consequently, in GADGET-3, a more sophisticated form is used. The single particle Dirac-δ density function $\delta(\mathbf{x})$ is replaced by a convolution of $\delta(\mathbf{x})$ with a spline kernel, so that $\tilde{\delta}(\mathbf{x}) = W(|\mathbf{x}|, 2.8\epsilon)$, where

$$W(r,h) = \frac{8}{\pi h^3} \begin{cases} 1 - 6\left(\frac{r}{h}\right)^2 + 6\left(\frac{r}{h}\right)^3, & 0 \le \frac{r}{h} \le \frac{1}{2}, \\ 2\left(1 - \frac{r}{h}\right)^3, & \frac{1}{2} \le \frac{r}{h} \le 1, \\ 0 & \frac{r}{h} > 1. \end{cases} \tag{2.9}$$

The force is then Newtonian for $r > h$.

The computational cost for the PP-method is of the order $\mathcal{O}\left(N^2\right)$, which makes simulations with $N > 10^5$ particles very slow. In the so-called *Tree* method of Barnes & Hut (1996) small range forces are calculated by direct summation, whereas distant particles are *smeared out* by combining two or more particles and treating them as a pseudo-particle. The method has a computational cost of the order $\mathcal{O}\left(N \log N\right)$. At each timestep, the D-dimensional simulation space is divided into 2^D cells. Subsequent hierarchical subdivision of cells with more than one particle continues until only cells with zero or one particle exist.

The cells are treated as the nodes of a tree structure, which is used for calculating the forces. For the force calculation, the tree is *walked* starting at the largest cell size and a smaller cell size is considered only if $s/d > \theta$, where s is the cell size, d is the distance of the particle in consideration from the centre-of-mass of the cell and θ is a tolerance parameter.

In addition to these methods, GADGET-3 relies on a *particle mesh* (PM) method to calculate long-range forces. The computational box is divided into a grid of Cartesian mesh cells and a density is assigned to each cell based on a smoothed mass distribution. The Poisson equation is then solved on the grid and the forces at the positions of the particles are interpolated from the forces on the grid points.

Positions $\mathbf{r}_i^n$ and velocities $\mathbf{v}_i^n$ of particles i at time-step n are forwarded to time-step $n+1$ (time interval Δt) with a so-called *kick-drift-kick leapfrog* integration scheme, which is defined by the following equations:

$$\begin{aligned}
\mathbf{v}_i^{n+1/2} &= \mathbf{v}_i^n + \mathbf{a}_i(\mathbf{r}^n, \mathbf{v}^n)\frac{\Delta t_i^n}{2} \\
\mathbf{r}_i^{n+1} &= \mathbf{r}_i^n + \mathbf{v}_i^{n+1/2}\Delta t_i^n \\
\mathbf{v}_i^{n+1} &= \mathbf{v}_i^{n+1/2} + \mathbf{a}_i(\mathbf{r}^{n+1}, \mathbf{v}^{n+1/2})\frac{\Delta t_i^n}{2}.
\end{aligned} \tag{2.10}$$

Here positions and velocities are updated with an offset of $\Delta t/2$. The dependence of the accelerations $\mathbf{a}_i^n$ on velocities is irrelevant for gravitational forces, but important for hydrodynamics, as will become clear in the next section.

Time-steps Δt_i^n can vary with time and particle. For collisionless systems, they are calculated as functions of accelerations $\mathbf{a}_i^n$ and softening lengths ϵ_i, which define the typical length-scale. GADGET-3 assumes $\Delta t_i^n \propto \sqrt{\epsilon_i / |\mathbf{a}_i^n|}$.

2.4.2 | Smoothed Particle Hydrodynamics

To simulate hydrodynamics, one of two competing concepts is usually applied. *Eulerian* codes discretize space and represent fluid variables on a mesh, whereas *Lagrangian* codes discretize mass and use tracer particles to model the flow. Only very recently, hybrid methods in the forms of moving-mesh codes have become popular (Springel, 2010).

For the Lagrangian method, the resolution increases automatically for dense structures, the gravitational force can be computed in the same way as for collisionless particles and there are no restrictions on the geometry of the system. These advantages make the method well-suited for galaxy formation.

Smoothed Particle Hydrodynamics (SPH, Lucy, 1977; Gingold & Monaghan, 1977) is a Lagrangian scheme, in which thermodynamic quantities A are defined via an interpolation method that *smoothes* over the values A_k for a set of disordered neighbour particles k (see Monaghan et al., 1992 for a review). The field $A(\mathbf{r})$ at the arbitrary position $\mathbf{r}$ can be expressed as

$$A(\mathbf{r}) = \sum_k m_k \frac{A_k}{\rho_k} W(\mathbf{r} - \mathbf{r}_k, h), \tag{2.11}$$

where m_k are particle masses, ρ_k are particle densities and $W(r,h)$ is a *smoothing kernel*. Equation 2.9 gives one possible functional form for the kernel. The *smoothing length* h is adaptive and for each particle determined by demanding that the mass in the kernel volume with $W(r,h) > 0$ is approximately constant.

The spatial derivative of the field is

$$\nabla A(\mathbf{r}) = \sum_k m_k \frac{A_k}{\rho_k} \nabla W(\mathbf{r} - \mathbf{r}_k, h). \tag{2.12}$$

Using Equations 2.11 and 2.12, hydrodynamical equations can be expressed within the concepts of SPH. The continuity equation, $d\rho/dt + \rho\nabla \cdot \mathbf{v} = 0$, can be represented as

$$\frac{d\rho_i}{dt} = \sum_k m_k (\mathbf{v}_i - \mathbf{v}_k) \nabla_i W(\mathbf{r}_i - \mathbf{r}_k, h). \tag{2.13}$$

Here, the time derivative d/dt denotes the Lagrangian derivative following the motion of the particle.

The pressure P is determined via an equation of state $P = (\gamma - 1)\rho u$, where γ is the adiabatic index and u is the thermal energy per unit mass. The thermal energy equation, $du/dt = -(P/\rho)\nabla \cdot \mathbf{v}$, can correspondingly be expressed as

$$\frac{du_i}{dt} = \frac{1}{2} \sum_k m_k \left(\frac{P_i}{\rho_i^2} + \frac{P_k}{\rho_k^2} \right) (\mathbf{v}_i - \mathbf{v}_k) \nabla_i W(\mathbf{r}_i - \mathbf{r}_k, h). \tag{2.14}$$

In astrophysical applications, a cooling term is usually added to the equation to capture radiative cooling processes as described in Section 2.3. Cooling rates are usually tabulated as a function of element abundances and temperatures. Additionally, a heating term due to UV and/or X-ray background radiation is often applied (see e.g. Wiersma et al., 2009b for an overview).

To assure that shock fronts are properly captured in SPH, an artificial viscous force term has to be applied. The equation of motion in the absence of self-gravity, $d\mathbf{v}/dt = -\nabla P/\rho$, can then be expressed as

$$\frac{d\mathbf{v}_i}{dt} = -\sum_k m_k \left(\frac{P_k}{\rho_k^2} + \frac{P_i}{\rho_i^2} + \Pi_{ik} \right) \nabla_i W(\mathbf{r}_i - \mathbf{r}_k, h). \tag{2.15}$$

Here Π_{ik} is the viscous contribution to the pressure gradient, which is zero when particles are not approaching each other, and otherwise can e.g. be defined as

$$\Pi_{ik} = \frac{-\alpha c_{ik} \mu_{ik} + \beta \mu_{ik}^2}{\rho_{ik}}, \tag{2.16}$$

(Balsara, 1995). Here $\alpha \sim 0.5 - 1$ and $\beta \sim 2\alpha$ are parameters, c is the speed of sound, quantities sub-scripted ik are arithmetic means over the values for i and k and $\mu_{ik} = [h_{ik}(\mathbf{v}_i - \mathbf{v}_k) \cdot (\mathbf{r}_i - \mathbf{r}_k)]/(\mathbf{r}_i - \mathbf{r}_k)^2$. Thus a linear term in velocity differences, which causes a shear and bulk viscosity, and a quadratic term, which handles high Mach number shocks, are introduced. A corresponding heating term, which transfers kinetic into thermal energy, is added to the energy equation.

Due to the presence of spatial derivatives in the hydrodynamical equations of motions, the time-step criterion has a slightly more complex form. Typically a *Courant* criterion of the form

$$\Delta t_i = \frac{\kappa h_i}{h_i \left|(\nabla \cdot \mathbf{v}_i)\right| + \max(c_i, |\mathbf{v}_i|)}, \tag{2.17}$$

where κ is a tolerance parameter, is applied.

As any numerical method, SPH is not free of problems. Agertz et al. (2007) showed that e.g. gas-dynamical fluid mixing instabilities, such as the Kelvin-Helmholtz instability, are poorly resolved by SPH codes. Moreover, shocks are not captured with high accuracy. Recently, modifications to SPH have been presented that successfully prevent some of these problems (Wadsley et al., 2008; Hopkins, 2013). Such modifications are, however, not applied in our work.

SPH is well suited for implementing models of physical processes on scales that are not resolved (see e.g. Katz, 1992 for pioneering work). These models are usually referred to as *sub-grid*. SF can, for example, be treated by converting gas particles above a certain density threshold stochastically into collisionless star particles on an appropriate timescale. Mass loss, as well as kinetic and thermal feedback can be treated by adding mass, thermal energy and/or velocity kicks to gas particles in the neighbourhood of the star particle. Magnetohydrodynamics can also be implemented in SPH codes (Dolag & Stasyszyn, 2009), but is not treated in this thesis.

2.4.3 | Initial conditions for cosmological simulations

The initial conditions (ICs) we apply in this work were taken from the studies by Springel et al. (2008) and Oser et al. (2010). We here briefly sketch how such ICs are created. As discussed in Section 2.2, the parameters for a ΛCDM universe as determined from CMB and other observations determine the ICs for structure formation in the universe.

Typically, a representative patch of the universe with a scale of ~ 100 comoving Mpc or larger is simulated. A cubic box with periodic boundary conditions on opposite faces is applied to assure that the mean comoving density remains at the value determined by the desired cosmology. First, an unperturbed, uniform distribution of particles is established in the form of a regular cubic grid or a glass-like distribution (White, 1994).

The initial Gaussian density field is represented by a direct summation of plane waves. The minimum size of perturbations is determined by the resolution of the simulation (i.e. the spacing of particles) and the maximum size is determined by the box size. Perturbations are evolved in time to $z \sim 100$ applying linear Lagrangian perturbation theory and the particle positions and velocities are adjusted accordingly.

From $z \sim 100$ to $z = 0$, the ICs are then evolved using gravitational N-body techniques as described above, usually ignoring baryonic physics (DM-only). To simulate the formation and evolution of individual galaxies, suitable DM haloes are selected at $z = 0$ and *zoom-in* ICs for individual haloes are created. Particles within several times the virial radius of the object are traced back to the initial redshift and this volume is being sampled with a much higher number of particles. Short wavelength perturbations are added in the high resolution volume. The resolution far away from the high-resolution volume is reduced in a way which assures that long range tidal forces are captured properly.

In the zoom-in volume, gas is added by splitting each particle into a gas and a DM particle with a mass ratio of $\Omega_{\rm bar}$ to $\Omega_{\rm dm}$. Their separation is chosen as 0.5 of the local mean particle separation and positions and velocities are adjusted to assure the conservation of mass and momentum. The temperature is set to the CMB temperature at the given redshift.

2.5 | (Disc) Galaxies in simulated universes

Over the last three decades, cosmological simulations, whether DM-only or hydrodynamic, have become the prime tool to study structure and galaxy formation. Collisionless simulations of cosmological boxes with various sizes up to several Gpc using up to several times 10^{11} particles have demonstrated that the results on resolved scales are converged (e.g. the *Millennium* runs: Springel et al., 2005b; Boylan-Kolchin et al., 2009; Angulo et al., 2012). The same is true for the structure of individual ΛCDM haloes, as demonstrated by the *Aquarius* project (Springel et al., 2008). Hydrodynamical galaxy formation simulations of cosmological boxes at resolutions that allow a reasonable direct treatment of baryonic physics have only recently become feasible (Schaye et al., 2010; Vogelsberger et al., 2013).

DM-only simulations have demonstrated that a ΛCDM universe agrees very well with observations of large scale structure (Springel et al., 2006). To simulate the formation and evolution of the galaxy population, the so-called *semi-analytic* method (White & Frenk, 1991) has been widely applied. This method relies on the formation, evolution and merging of (sub-)haloes from DM-only simulations and models the physics of the baryons associated with the (sub-)haloes, such as cooling, SF and feedback (see Fig. 2.4), by applying analytical prescriptions which are tuned to reproduce the observed phenomenology of galaxies. Such models have been quite successful in reproducing detailed population properties (Guo et al., 2011; Henriques et al., 2013).

To properly model the complex dynamical interplay between gas, DM and stars and thus the complex structure of galaxies, hydrodynamical simulations of the formation and evolution of individual galaxies are needed. Despite two decades of such simulations, they are still far from convergence. They have, however, made significant contributions to our understanding of the physics of galaxy formation. Specifically, the formation of MW-like disc galaxies has been a problem ever since.

The first attempts to simulate (disc) galaxy formation in a cosmological context were undertaken by Katz & Gunn (1991) and Navarro & Benz (1991). They still ignored SF and SN feedback, which were first introduced by Katz (1992) and Navarro & White (1993). Although disc-like galaxies could form from the idealized ICs of isolated constant-density perturbations, which were applied by Katz (1992), severe problems were recognized for galaxies that form hierarchically (Navarro & Benz, 1991), as in a CDM universe (Navarro & White, 1994). Gas cooling was found to be very efficient in small haloes in the early universe and SF proceeded rapidly yielding dense stellar cores (the *overcooling* problem). Moreover, during merger events, most of the baryonic angular momentum was transferred to the DM haloes due to dynamical friction and gravitational torques (the *angular momentum catastrophe*). The resulting galaxies were compact, ellipsoidal in shape and showed peaked rotation curves.

The solutions proposed for these problems can be summarized in three categories: better treatment of baryonic physics, higher resolution or different cosmology. In terms of cosmology, Sommer-Larsen & Dolgov (2001) considered disc formation in WDM cosmologies and found that due to the reduced number of low mass haloes the amount of angular momentum lost to the DM was reduced, which yielded more extended discs. In terms of resolution, spurious numerical two-body relaxation introduced by noise due to low particle numbers, as well as SPH artificial viscosity, lead to artificial dissipation and artificial angular transfer to the halo (Governato et al., 2004; Kaufmann et al., 2007).

Most work has focused on the improvement of models for physical processes, predominantly feedback processes which prevent gas from cooling and condensing in dense cores. Weil et al. (1998) demonstrated that if cooling is prevented in cosmological simulations until rather late times $z \sim$1-2, the angular momentum loss is suppressed and extended discs can form.

The source for energy and momentum feedback considered most often are SN explosions, as first conceptually introduced to galaxy formation by Larson (1974). Other sources that have been considered are SMBHs (e.g. Springel et al., 2005a) and cosmic ray pressure (e.g. Uhlig et al., 2012). The sub-grid nature of the involved physics, however, complicates the modelling. To assure that SN feedback is efficient in heating gas and driving galactic winds, models have to assume that a high fraction of the energy released by SNe is channeled into outflows. In SPH sub-grid models, this can be achieved by temporarily turning off cooling for gas affected by feedback (Stinson et al., 2006), giving high-velocity kicks to gas particles and temporarily decoupling them from hydrodynamics (e.g. Oppenheimer et al., 2010) or by including an explicit multiphase gas treatment and requiring SNe to feed the hot phase (Scannapieco et al., 2006). All these *tricks* have physical motivations, but are potentially overestimating the effect of SNe.

However, these galactic wind models have not only increased the disc fraction found in $z = 0$ simulated galaxies, but have e.g. also been successful in reproducing observations of metals in the IGM and the CGM (Oppenheimer & Davé, 2006; Shen et al., 2010) and of the structure of massive $z \sim 2$ disc galaxies (Genel et al., 2012). These simulations have thus underlined the need of efficient winds in galaxy formation. Moreover, simulations have demonstrated that winds have to preferentially remove low angular momentum gas in order to form discs with realistic surface density profiles (Brook et al., 2011).

Continuous improvement in the modelling of baryonic physics and increased resolution have led to slow, but steady improvement for cosmological simulations of disc galaxies (among many others: Navarro & Steinmetz, 1997; Abadi et al., 2003; Governato et al., 2007; Scannapieco et al., 2009; Agertz et al., 2011; Sales et al., 2011). The high number of attempts has also yielded other interesting results. Okamoto et al. (2005) demonstrated that the resulting $z = 0$ galaxy depends sensitively on the feedback model. For a specific IC simulated with the same numerical technique, they showed that mild adjustments in the models of baryonic physics can yield an elliptical instead of a disc galaxy. The *Aquila* comparison project (Scannapieco et al., 2012), for which one specific halo was simulated with 15 different models applying different physics, as well as different numerical techniques, underlined that the treatment of physics has a stronger effect than the numerical method. There are, however, also important differences caused by numerical effects, as was recently demonstrated by Nelson et al. (2013) for the thermal properties of accreting gas.

Interestingly, models with weak feedback prescriptions have been shown to be successful in reproducing observational properties of elliptical galaxies (Oser et al., 2010; Johansson et al., 2012b). Other models have demonstrated that even for haloes with very quiescent merger histories, galactic discs can be destroyed by the accretion of gas with misaligned angular momentum (Scannapieco et al., 2009) or by the reorientation of the stellar disc (this work, Okamoto, 2013). In this context, Bailin et al. (2005) showed that the rotation axis of disc galaxies preferentially aligns with the minor axis of the triaxial halo and Sales et al. (2011) demonstrated that disc fractions in $z = 0$ galaxies are higher when the gas accreted over the cosmic history shows coherent alignment of angular momentum.

Despite the partial successes of models relying on SN feedback driven winds, until recently, all of these simulations predicted overly high baryon conversion efficiencies (Guo et al., 2010; Sawala et al., 2011). Especially at high-z, SFRs are often too high by an order of magnitude (Moster et al., 2013).

One solution to this problem, which has been considered, is feedback from massive stars before their explosion as SNe. Hopkins et al. (2011) presented a model that included the effects of stellar winds and of radiation pressure (RP) on dust grains and concluded that momentum input from RP plays a key role in regulating SF (see also Agertz et al., 2013). Moreover, Stinson et al. (2013) applied a model for thermal feedback from young stars and were able to significantly improve the agreement of high-z star formation histories (SFHs) with observations.

A more sophisticated modelling of SF and ISM physics has also been shown to be of help in producing more realistic galaxies. Governato et al. (2010) suggested that a high density threshold for SF in high resolution simulations, which are capable of resolving star forming clumps, can boost the effect of SN feedback due to an increase in the coupling efficiency. For correspondingly high resolution, Christensen et al. (2012) demonstrated that an explicit modelling of the formation of molecular hydrogen and of SF in the molecular phase can also amplify the effect of feedback.

Only very recently, cosmological simulations have reached a stage, where the galaxies at $z = 0$ contain discs which agree reasonably with a variety of observables such as sizes, stellar masses, rotation curves and metallicities (Guedes et al., 2011; Brook et al., 2012) and that finally contain more stars in the disc than in the bulge component (this work, Marinacci et al., 2013).

2.6 | Aims and structure of the thesis

As has been explained in the previous Section, fully cosmological hydrodynamical simulations of the formation of MW-like disc galaxies in a ΛCDM universe have been plagued by severe problems throughout the last twenty years. In this thesis, we intend to make a contribution to this field by investigating whether the failure of these models to produce realistic disc galaxies is caused by coarse resolution or inappropriate modelling of physics or if it actually constitutes a problem for the ΛCDM cosmogony.

We build on the work by Scannapieco et al. (2009), who presented fully cosmological simulations of disc galaxy formation in eight of the well-studied *Aquarius* haloes, and the work by Scannapieco et al. (2012) who compared the results of various numerical methods and implementations of baryonic physics. We would like to learn from the limited success of these models and try to understand why none of them yielded realistic MW-like disc galaxies at $z = 0$, although the studied haloes had been selected to be prime candidates for hosting such galaxies according to semi-analytic models.

For our studies, we apply the Tree-PM SPH code GADGET-3, last described in Springel (2005). We use and improve the models for baryonic galaxy formation physics by Scannapieco et al. (2005, 2006). On the one hand, we use idealized, semi-cosmological simulations of discs forming from the cooling and condensation of rotating gas in the centres of fully cosmological ΛCDM haloes. On the other hand, we perform fully cosmological hydrodynamical zoom-in (re)simulations of a sample of 17 haloes with varying masses and assembly histories.

We intend to better understand the conditions under which thin, extended stellar discs can form and survive in triaxial, substructured and evolving ΛCDM haloes. We would like to understand, how the modelling of baryonic physics can be improved to yield a better agreement of early SFHs with observations. We aim to use comparisons of our sample of simulated galaxies with observations of the galaxy population at various redshifts to constrain the modelling. We try to improve our models in order to be capable of producing truly disc dominated galaxies in cosmological simulations.

In Chapter 3 we discuss our idealized models for galactic disc formation and evolution in realistic ΛCDM haloes. These controlled numerical experiments, which apply simplified prescriptions for baryonic physics, are used to learn about the complex dynamical interactions of gas, stars and DM which affect galaxy formation. The idealized models are compared to cosmological hydrodynamical simulations in the same haloes to better understand their failure to produce discs.

In Chapter 4 we present an update to the multiphase-SPH galaxy formation code by Scannapieco et al. (2005, 2006) and its application in cosmological simulations of our sample of haloes. The models for baryonic physics are calibrated to produce SFHs in agreement with predictions from abundance matching. It is shown, how improved modelling of physics can lead to more realistic discs. The simulated sample is compared to a variety of observations to identify remaining shortcomings.

In Chapter 5 we compare the models of Chapter 4 in detail to recent observational studies of the structural formation histories of disc galaxies. In Chapter 6 we perform a similar comparison with recent observations of the structure of galactic neutral hydrogen discs at $z = 0$. These comparisons give further insights into the problems of our models, but also underline that the models are capable of improving our understanding of physical processes important for the formation and evolution of disc galaxies in a ΛCDM universe.

Finally, in Chapter 7 we sum up, conclude and present questions and problems that should be studied in more detail in the future.

3 | Idealized models for galactic disc formation and evolution in ‘realistic’ ΛCDM haloes [1]

3.1 | Abstract

We study the dynamics of galactic disc formation and evolution in ‘realistic’ Λ cold dark matter haloes with idealized baryonic initial conditions. We add rotating spheres of hot gas at $z = 1.3$ to two fully cosmological dark-matter-only halo (re)simulations. The gas cools according to an artificial and adjustable cooling function to form a rotationally supported galaxy. The simulations evolve in the full cosmological context until z=0. We vary the angular momentum and density profiles of the initial gas sphere, the cooling time and the orientation of the angular momentum vector to study the effects on the formation and evolution of the disc. The final discs show exponential radial and (double-)exponential vertical stellar density profiles and stellar velocity dispersions that increase with age of the stars, as in real disc galaxies. The slower the cooling/accretion processes, the higher the kinematic disc-to-bulge (D/B) ratio of the resulting system. We find that the initial orientation of the baryonic angular momentum with respect to the halo has a major effect on the resulting D/B. The most stable systems result from orientations parallel to the halo minor axis. Despite the spherical and coherently rotating initial gas distribution, the orientation of the central disc and of the outer gas components and the relative angle between the components can all change by more than 90 degrees over several billion years. Initial orientations perpendicular to the major axis tend to align with the minor axis during their evolution, but the *sign of the spin* can have a strong effect. Discs can form from initial conditions oriented parallel to the major axis, but there is often strong misalignment between inner and outer material. The more the orientation of the baryonic angular momentum changes during the evolution, the lower the final D/B. The behaviour varies strongly from halo to halo. Even our very simple initial conditions can lead to strong bars, dominant bulges, massive, misaligned rings and counter-rotating components. We discuss how our results may relate to the failure or success of fully cosmological disc formation simulations.

---

[1] The results of this Chapter were published in almost identical form as Aumer & White (2013)

3.2 | Introduction

The majority of galaxies in the local Universe with masses similar to that of the Milky Way are disc-dominated (e.g. Delgado-Serrano et al., 2010). In the standard paradigm, these discs formed through cooling and condensation of gas within cold dark matter (CDM) haloes (White & Rees, 1978; Fall & Efstathiou, 1980). Disc size is a consequence of the angular momentum of the gas, which had previously been acquired through tidal torques from neighboring structures (e.g. Peebles, 1969; White, 1984).

Numerical hydrodynamical simulations of this formation scenario have been carried out in great number (e.g. Navarro & White, 1994; Navarro & Steinmetz, 1997; Abadi et al., 2003; Governato et al., 2007; Scannapieco et al., 2009). Despite recent progress (e.g. Guedes et al., 2011; Agertz et al., 2011; Sales et al., 2011), these simulations have in general suffered from a range of problems, including angular momentum loss leading to overly small discs (Navarro & Benz, 1991), production of overly massive galaxies (Guo et al., 2010), and too much early and too little late star formation (Scannapieco et al., 2009). Even if extended discs form, they are often destroyed by infalling satellites (Toth & Ostriker, 1992) or the accretion of misaligned gas (Scannapieco et al., 2009; Sales et al., 2011). Moreover, different numerical schemes can yield very different galaxies for the same initial conditions (Scannapieco et al., 2012; Kereš et al., 2012). In particular, the angular momentum content and thus the structure of the discs depends strongly on the numerical method applied (Torrey et al., 2012a). Overall, the galaxy population predicted by cosmological gas dynamical simulations disagrees in major ways with observations. Since detailed population properties are reproduced quite well in the standard Λ cold dark matter (ΛCDM) paradigm by simple semi-analytic simulations (e.g. Guo et al., 2011), it has been argued that the relevant star formation and feedback processes are still inadequately represented in hydrodynamical simulations. Such semi-analytic models are however not capable of properly capturing the complex dynamical interactions between gas, stars and dark matter found to be important in the above-mentioned simulations.

In contrast, there is general agreement on the formation and structure of dark matter haloes in ΛCDM (e.g. Springel et al., 2008), and on the observational side, a detailed picture of the structure of disc galaxies has been assembled over the last decades (see van der Kruit & Freeman, 2011 for a recent review). In this Chapter, we therefore study whether the detailed output of simulations of dark matter halo formation and our detailed knowledge of disc galaxies can be brought into agreement if the fully cosmological treatment of baryon physics is replaced by idealized models.

Previous attempts in this direction include the models of Weil et al. (1998), who showed that the prevention of radiative gas cooling in cosmological hydrodynamical simulations until $z = 1$ allows the formation of a disc galaxy population with realistic angular momentum content. Kaufmann et al. (2006, 2007) simulated disc formation by allowing a rotating gas distribution to cool inside idealized (mostly spherical) equilibrium haloes. This enabled them to examine numerical effects as well as some physical processes related to disc simulations.

ΛCDM haloes, however, show substructure, are triaxial and are continuously accreting (Frenk et al., 1988). The impact of halo shape is still an open issue. Disc galaxies in cosmological hydrodynamical simulations are typically aligned with the halo minor axis (Bailin et al., 2005). Moreover, it has been argued that the interaction of the forming disc galaxy with the dark matter tends to make the haloes axisymmetric (e.g. Berentzen & Shlosman, 2006; Kazantzidis et al., 2010). Berentzen & Shlosman (2006) introduced a disc galaxy within a cosmological triaxial halo by gradually adding stellar disc particles according to an axisymmetric analytical disc model with growing mass and size, to the simulation. They were thus able to analyze the interplay between a galactic disc and a triaxial halo. A similar study was undertaken for the same dark matter haloes we use here by DeBuhr et al. (2012).

For our study, we perform a set of controlled numerical experiments using simplified prescriptions for the physics of gas accretion and star formation in order to gain insight into the dynamical processes that affect the formation of galaxy discs within ΛCDM haloes . We use fully cosmological, triaxial haloes as initial conditions, but simulate disc formation and evolution by the cooling of a rotating gas sphere starting at redshift $z = 1.3$. Our idealized treatment allows us to study how the formation of a galactic disc is affected by the rapidity of gas cooling and by the angular momentum and mass of the gas and by the orientation of its angular momentum with respect to the principal axes of the dark halo. We compare our results to the direct output of fully cosmological hydrodynamical simulations carried out for the same haloes, so that we can better understand why they fail to produce substantial discs.

In Section 3.3 we describe the setup and numerical methods of this Chapter. In Section 3.4 we describe the formation, evolution and structure of one particular disc model. In Section 3.5 we analyze the dependence of the disc growth on our model parameters. In Section 3.6 we discuss the influence of initial spin orientation and the stability of the orientation of the resulting discs. In Section 3.7 we compare our models to the fully cosmological galaxy formation simulations of Scannapieco et al. (2009) (CS09 hereafter). Finally, in Section 3.8 we summarize and conclude.

3.3 | Simulation setup

To mimic the formation of galactic discs within fully-cosmological dark-matter-only simulations of haloes expected to host Milky-Way type galaxies, we make use of the Aquarius simulations (Springel et al., 2008), a suite of high resolution zoom-in resimulations of six dark matter haloes. These haloes were chosen from a simulation of a cosmological box with a side-length of $137\ \mathrm{Mpc}$, and were simulated from $z = 127$ assuming a ΛCDM universe with the following parameters: $\Omega_\Lambda = 0.75$, $\Omega_m = 0.25$, $\Omega_b = 0.04$, $\sigma_8 = 0.9$ and $H_0 = 73\,\mathrm{kms^{-1}Mpc^{-1}}$. For details we refer to Springel et al. (2008).

We select two haloes, named A and C, both at resolution level 5, which corresponds to dark matter particle masses of $m_{\mathrm{dm}} \approx 3 \times 10^6 M_\odot$ and a gravitational softening length of $\epsilon_{\mathrm{dm}} = 685\ \mathrm{pc}$. These haloes have (dark-matter-only) $z = 0$ virial masses of $M_{200} = 1.853$ and $1.793 \times 10^{12} M_\odot$ and have been studied in the fully cosmological galaxy formation simulations of CS09. We selected halo A as it has a very quiescent merger history after redshift $z \sim 1$ and has been identified as a prime candidate for hosting a disc galaxy by semi-analytical modelling. However, CS09 did not find a significant disc component in their simulations at $z = 0$. Halo C, in contrast, showed the highest (yet still unrealistically low) disc-to-bulge ratio, $D/B \sim 1/4$, of all 8 haloes studied in this work. Halo C was also studied in the *Aquila Comparison Project* (Scannapieco et al., 2012), which compared the results of various cosmological gas-dynamical codes.

For our simulations we apply the TreeSPH-code GADGET-3, last described in Springel (2005), an extended version of which was used by CS09.

As initial conditions for our numerical experiments we use the simulation outputs of Springel et al. (2008) at $z = 1.3$. We choose this time, as it falls after the epoch of major mergers. Disc galaxies have very likely been in place and continuously forming since before $z = 1.3$. For example, age estimates for the solar neighbourhood exceed $10\ \mathrm{Gyr}$ (see Aumer & Binney, 2009 and references therein), making our choice appear problematic. It has been argued that the ages of thin disc stars are consistent with formation after $z \sim 1.5$ (e.g. Reddy et al., 2006), but it is not clear, if a two-component-division of the Milky Way disc into thin and thick components is sensible (e.g. Schönrich & Binney, 2009b). Our goal is not, however, to model the entire formation and evolution of disc galaxies, but to study the ability of realistic dark matter haloes with evolving substructure to host thin disc galaxies over cosmological times.

To simulate the formation of a disc galaxy within the dark matter halo, we insert a rotating sphere of gas into the inner halo and evolve the combined system until $z = 0$. In our models, the gas component is initially hot ($T \sim 10^6\mathrm{K}$), with an internal energy structure determined by the assumption of approximate hydrostatic equilibrium (cf. Kaufmann et al., 2006; Aumer et al., 2010). The pressure profile is thus

$$p(R) = \int_R^\infty \rho_{gas} \, \frac{G \, M_{\mathrm{tot}}(r)}{r^2} \, dr, \tag{3.1}$$

where $M_{\mathrm{tot}}(r)$ is the spherically averaged mass of dark matter and gas within spherical radius r. The gas sphere has a density profile $\rho(r) \propto r^{-1}$ (e.g. Navarro & White, 1993) and its total mass is $M_{\mathrm{tot}} = 5.0 - 7.5 \times 10^{10} M_\odot$, in the range of estimated stellar masses for the Milky Way (McMillan, 2011) and of galaxy masses expected for this halo mass range by abundance matching techniques (e.g. Guo et al., 2010). We choose this profile as tests of various other profiles yielded undesired artifacts. A Navarro-Frenk-White-like profile, as used by Aumer et al. (2010), leads to more prominent dispersion-dominated populations forming from the initially greater central gas mass, which adjusts to the triaxial potential of the central halo before transition to a disc-like configuration. For a constant density sphere, however, the central build-up of baryonic mass is initially too slow, delaying the transition from triaxial to disc-like potential relative to the baryonic mass build-up.

The gas sphere is truncated at radius $R_{\mathrm{gas}} = 60 - 100\ \mathrm{kpc}$. We assume zero pressure outside the gas sphere when determining the pressure profile according to equation 3.1. This leads to an initial expansion phase for the outermost gas layers due to the finite temperatures assigned to the smoothed particle hydrodynamics (SPH) particles. However, this effect is negligible compared to the adjustment of the initially spherical gas distribution to the triaxial and substructured gravitational potential of the dark halo, which prevents the setup of idealized equilibrium initial conditions. The effects of this adjustment are discussed in Sections 3.4 and 3.5. Still, as we also show in these sections, this simple setup is justified by the fact that it leads to disc galaxy models with realistic properties.

We use a baryonic particle mass of $m_{\mathrm{bar}} \approx 10^5 M_\odot$ and a gravitational softening $\epsilon_{\mathrm{bar}} = 205\ \mathrm{pc}$. Kaufmann et al. (2007) found that the angular momentum content and morphology of forming discs depend on resolution. Our resolution is similar to their highest resolution, for which they found significantly reduced angular momentum losses. In Section 3.5, we show that angular momentum losses due to lack of resolution are negligible in our simulations. The gas is set to rotate with a rotation velocity profile $V_{\mathrm{rot}}(r)$, which is either constant or changing linearly from central to outer spherical radii r. These profiles yield realistic disc mass profiles as is shown in the following sections. The angular momentum vector of the gas is aligned either with one of the principal axes of the halo or with its angular momentum in order to study how this affects the final orientation of the disc (see Section 3.6).

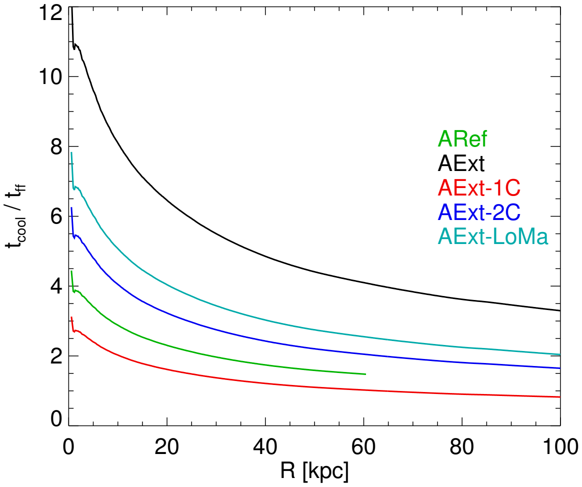

Figure 3.1: The ratio of the cooling time to the free-fall time $t_{\rm cool}/t_{\rm ff}$ as a function of radius for several models with different initial density and cooling time parameters. AExt1C, AExt2C and AExt only differ by normalization of the cooling time profile $t_{\rm cool,0}$. AExtLoMa and AExt2C only differ in total gas mass $M_{\rm gas}$. AExtLoMa and ARef only differ in initial radius of the gas sphere $R_{\rm gas}$. For a full list of models and their properties see table 3.1.

To model the cooling of the hot gas into the centre of the halo, we apply a simple parametrized cooling function with

$$t_{\rm cool} = t_{\rm cool,0}\left(\frac{\rho}{\rho_{\rm cool,0}}\right)^{-\alpha}, \tag{3.2}$$

where the normalization $t_{\rm cool,0}$ determines the rapidity of cooling. We choose $t_{\rm cool,0} = 0.5 - 2.0\ {\rm Gyr}$ for $\rho_{\rm cool,0} = 10^4 M_\odot\ {\rm kpc}^{-3} \approx 4 \times 10^{-4} {\rm m_H\ cm}^{-3}$ and $\alpha = 0.56$. These values were chosen to combine a simple dependence of the cooling time on the density with cooling time values which initially are a few times the free fall time $t_{\rm ff}$ at all radii. Moreover, $t_{\rm cool}$ increases with radius, yet the ratio $t_{\rm cool}/t_{\rm ff}$ decreases with radius. This enables an initially slow transition of the triaxial dark-matter dominated centre of the halo to a disc-dominated quasi-axisymmetric system. Ratios of $t_{\rm cool}/t_{\rm ff}$ as a function of radius for several models with different initial density and cooling time parameters are shown in Fig. 3.1 to illustrate how these parameters affect the cooling of gas in our models. The initial cooling time profiles are affected by the implications of the non-equilibrium initial conditions as discussed above on dynamical timescales and by the cooling of gas and star formation on cooling timescales. In Sections 3.4 and 3.5, we show that this cooling time setup produces gas accretion histories appropriate for our models.

A temperature floor $T_{\rm floor} = 10^5\ {\rm K}$ (Kaufmann et al., 2006) is applied to ensure that the forming disc does not fragment into a few massive clumps (Aumer et al., 2010), which would then enhance bulge formation. The high choice of $T_{\rm floor} = 10^5\ {\rm K}$ also prevents dense clumps from forming in the infalling gas via the cooling instability (Kaufmann et al., 2006).

Such a setup clearly ignores evidence from cosmological hydrodynamical simulations that steady, narrow, cold gas streams penetrating the shock-heated atmosphere of massive

Halo	Model Nr.	$R_{\rm gas}$	$M_{\rm gas}$	$V_{\rm rot}$	$N_{\rm part}$	$t_{\rm cool}$	orientation
A	ARef	60 kpc	$5.0 \times 10^{10} M_\odot$	$120 - 180 \mathrm{kms}^{-1}$	500000	2	AM300
A	ARef180	60 kpc	$5.0 \times 10^{10} M_\odot$	$120 - 180 \mathrm{kms}^{-1}$	500000	2	-AM300
A	ARef-Min	60 kpc	$5.0 \times 10^{10} M_\odot$	$120 - 180 \mathrm{kms}^{-1}$	500000	2	-Minor
A	ARef+Min	60 kpc	$5.0 \times 10^{10} M_\odot$	$120 - 180 \mathrm{kms}^{-1}$	500000	2	+Minor
A	ARef-Med	60 kpc	$5.0 \times 10^{10} M_\odot$	$120 - 180 \mathrm{kms}^{-1}$	500000	2	-Medium
A	ARef+Med	60 kpc	$5.0 \times 10^{10} M_\odot$	$120 - 180 \mathrm{kms}^{-1}$	500000	2	+Medium
A	ARefEnd	60 kpc	$5.0 \times 10^{10} M_\odot$	$120 - 180 \mathrm{kms}^{-1}$	500000	2	EndARef
A	ARef+Maj	60 kpc	$5.0 \times 10^{10} M_\odot$	$120 - 180 \mathrm{kms}^{-1}$	500000	2	+Major
A	ARef-Maj	60 kpc	$5.0 \times 10^{10} M_\odot$	$120 - 180 \mathrm{kms}^{-1}$	500000	2	-Major
A	ARef45	60 kpc	$5.0 \times 10^{10} M_\odot$	$120 - 180 \mathrm{kms}^{-1}$	500000	2	45
A	AExt	100 kpc	$7.5 \times 10^{10} M_\odot$	$120 \mathrm{kms}^{-1}$	750000	4	AM300
A	AExt1C	100 kpc	$7.5 \times 10^{10} M_\odot$	$120 \mathrm{kms}^{-1}$	500000	1	AM300
A	AExt2C	100 kpc	$7.5 \times 10^{10} M_\odot$	$120 \mathrm{kms}^{-1}$	750000	2	AM300
A	AExtMedAM	100 kpc	$7.5 \times 10^{10} M_\odot$	$80 \mathrm{kms}^{-1}$	750000	4	AM300
A	AExtLoAM	100 kpc	$7.5 \times 10^{10} M_\odot$	$40 \mathrm{kms}^{-1}$	750000	4	AM300
A	AExt-Med	100 kpc	$7.5 \times 10^{10} M_\odot$	$120 \mathrm{kms}^{-1}$	500000	4	-Medium
A	AExt180	100 kpc	$7.5 \times 10^{10} M_\odot$	$120 \mathrm{kms}^{-1}$	750000	4	-AM300
A	AExtLoMa	100 kpc	$5.0 \times 10^{10} M_\odot$	$120 \mathrm{kms}^{-1}$	500000	2	AM300
A	AExtHiMa	100 kpc	$15.0 \times 10^{10} M_\odot$	$120 \mathrm{kms}^{-1}$	750000	4	AM300
A	AMaj	60 kpc	$5.0 \times 10^{10} M_\odot$	$60 \mathrm{kms}^{-1}$	500000	4	+Major
A	AMaj2C	60 kpc	$5.0 \times 10^{10} M_\odot$	$60 \mathrm{kms}^{-1}$	500000	2	+Major
A	AMaj180	60 kpc	$5.0 \times 10^{10} M_\odot$	$60 \mathrm{kms}^{-1}$	500000	4	-Major
A	ACosmo	70 kpc	$5.0 \times 10^{10} M_\odot$	$120 \mathrm{kms}^{-1}$	500000	2	Cosmo
C	CExt+AM	100 kpc	$7.5 \times 10^{10} M_\odot$	$120 \mathrm{kms}^{-1}$	750000	4	AM300
C	CExt-AM	100 kpc	$7.5 \times 10^{10} M_\odot$	$120 \mathrm{kms}^{-1}$	750000	4	-AM300
C	CExt+Min	100 kpc	$7.5 \times 10^{10} M_\odot$	$120 \mathrm{kms}^{-1}$	750000	4	+Minor
C	CExt-Min	100 kpc	$7.5 \times 10^{10} M_\odot$	$120 \mathrm{kms}^{-1}$	750000	4	-Minor
C	CExt+Med	100 kpc	$7.5 \times 10^{10} M_\odot$	$120 \mathrm{kms}^{-1}$	750000	4	+Medium
C	CExt-Med	100 kpc	$7.5 \times 10^{10} M_\odot$	$120 \mathrm{kms}^{-1}$	750000	4	-Medium
C	CExt-Arb	100 kpc	$7.5 \times 10^{10} M_\odot$	$120 \mathrm{kms}^{-1}$	750000	4	-CArb
C	CExt+Arb	100 kpc	$7.5 \times 10^{10} M_\odot$	$120 \mathrm{kms}^{-1}$	750000	2	CArb
C	CExtEnd	100 kpc	$7.5 \times 10^{10} M_\odot$	$120 \mathrm{kms}^{-1}$	750000	4	EndCExt+Min
C	CExtCosmo	100 kpc	$7.5 \times 10^{10} M_\odot$	$120 \mathrm{kms}^{-1}$	750000	4	Cosmo
C	C+Maj	60 kpc	$5.0 \times 10^{10} M_\odot$	$60 \mathrm{kms}^{-1}$	500000	4	+Major
C	C-Maj	100 kpc	$5.0 \times 10^{10} M_\odot$	$60 \mathrm{kms}^{-1}$	500000	4	-Major

Table 3.1: **Overview over our models**
Column 1:halo A or C; *Column 2*:our model name; *Column 3*:the radius of the initial gas sphere; *Column 4*:the mass of the initial gas sphere; *Column 5*:the rotational velocity of the initial gas sphere, a single value stands for a constant $V_{\rm rot}(r)$, $a - b\ \mathrm{kms}^{-1}$ stands for a linear increase in $V_{\rm rot}(r)$ from a in the centre to b at $R_{\rm gas}$; *Column 6*:the number of baryonic particles; *Column 7*:the cooling time profile applied; the number stands for the approximate ratio $t_{\rm cool}/t_{\rm dyn}(R_{\rm gas})$ (see text and Fig. 3.1); *Column 8*:the orientation of the model. AM300 stands for the orientation of the halo angular momentum within 300 kpc, Major, Medium and Minor stand for the principal axes of the halo, '+' and '-' are arbitrarily chosen and differ by 180 degrees, EndARef stands for the $z = 0$ orientation of model ARef, 45 stands for an orientation halfing the angle between Major and Minor, Cosmo stands for the orientation of galaxy angular momentum in the cosmological runs of CS09, CArb is an arbitrary orientation in halo C, EndCExt+Min stands for the $z = 0$ orientation of model CExt+Min.

dark matter haloes, are important in feeding gas onto forming galaxies (e.g. Dekel et al., 2009). However, cold streams are only expected to be the dominant accretion mode at $z > 2$ (Faucher-Giguère et al., 2011) and even at these redshifts, there is little direct observational evidence for them (e.g. Steidel et al., 2010). The majority of the stellar mass in the Milky Way disc was formed after $z \sim 2$ (Aumer & Binney, 2009) and it may be argued that the underlying continuous star formation since $z \sim 1$ is driven by cooling of hot coronal gas in the wakes of galactic fountain clouds, which transfers gas from the virial-temperature corona to the disc (e.g. Marinacci et al., 2010). Our focus here is not on simulating a realistic assembly process, but rather on using a simplified scheme, which allows important aspects of the underlying dynamics to be clarified.

In our simulations, once the gas has reached the temperature floor and crossed a density threshold $\rho_{0,\mathrm{sfr}}$, it can form stars with

$$t_{\mathrm{sfr}} = t_{\mathrm{sfr},0} \left(\frac{\rho}{\rho_{0,\mathrm{sfr}}} \right)^{-\beta}. \tag{3.3}$$

We choose $\rho_{0,\mathrm{sfr}}$ to correspond to a hydrogen number density $n_{\mathrm{H,thresh}} = 0.1\ \mathrm{cm}^{-3}$ and we use $\beta = 0.5$ and $t_{\mathrm{sfr},0} = 10 \times t_{\mathrm{dyn}}(\rho_{0,\mathrm{sfr}})$, as often applied in simulations of this resolution (CS09). Gas particles eligible for star formation are stochastically turned into collisionless particles of the same mass (see e.g. Lia et al., 2002). In our simulation, the formation of stars is not accompanied by any kind of feedback processes. We have run tests with 50 times higher values of $\rho_{0,\mathrm{sfr}}$ and/or 10 times lower values of T_{floor} and did not find any major changes to our results. Both changes tend to produce dynamically hotter stellar discs as a lower cooling floor leads to stronger fragmentation of the disc and thus enhances disc heating by dense substructures. A higher density threshold lowers star formation rates in the later, gas-poor evolution of our disc models thus diminishing the young, cold disc component.

3.4 | Quantifying a disc model

We start the analysis of our models by discussing in detail one model in halo A, which is named ARef. We choose this model as it produces a system which has certain structural similarities to the Milky Way. The parameters applied are an initial radius of $R_{\mathrm{gas}} = 60\ \mathrm{kpc}$, a total mass of $M_{\mathrm{gas}} = 5 \times 10^{10} M_{\odot}$, a cooling time which is about twice as long as the free-fall time for the outermost gas (see Fig. 3.1), a rotational velocity which increases from $120\ \mathrm{kms}^{-1}$ in the centre to $180\ \mathrm{kms}^{-1}$ at R_{gas} and an orientation of the baryonic angular momentum vector parallel to that of the dark matter within $300\ \mathrm{kpc}$. This orientation is close to the minor axis of the potential of the inner halo. The dependence of the final disc properties on these initial parameters is discussed in the following section. We split this section into subsections that deal with disc structure, angular momentum loss, kinematics and disc heating.

3.4.1 | Structural evolution

Analyzing ARef at $z = 0$, 86% of the baryonic mass has formed stars and the remaining gas is situated mainly in a thin, extended gas disc (see top row in Fig. 3.8). This gas fraction is in reasonable agreement with $z \sim 0$ spirals (Evoli et al., 2011). As can be seen in the top left panel of Fig. 3.2, the star formation rate (SFR) rises steeply to a peak at $z \sim 1$ before falling by two orders of magnitude by $z = 0$.

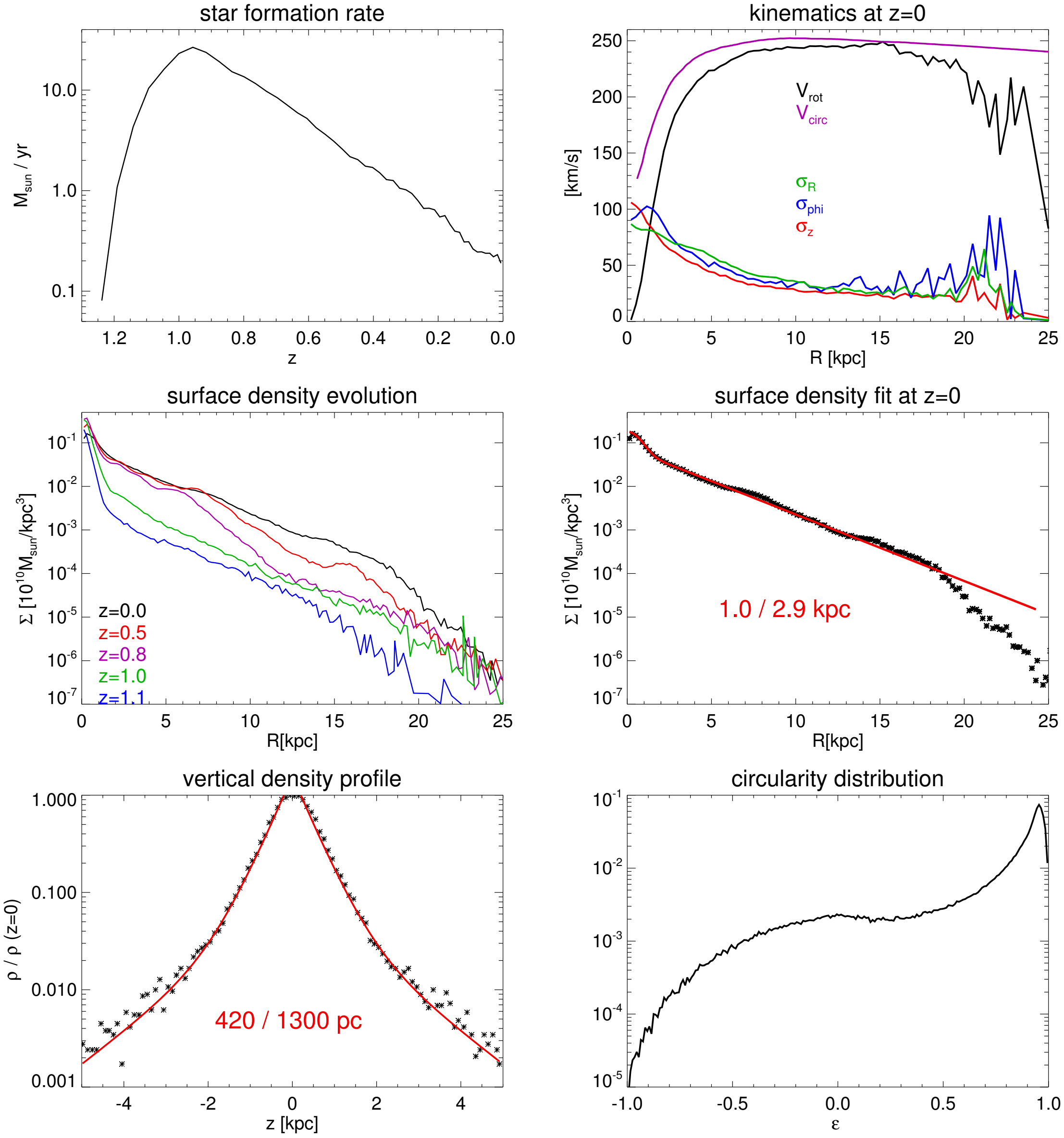

Figure 3.2: Properties of model ARef. *Top Left*: Star formation rate as a function of redshift z. *Top Right*: Stellar kinematics as a function of disc radius R at $z = 0$. Only stars within 500 pc of the midplane were taken into account. In purple we overplot the spherically-averaged circular velocity $V_{\rm circ} = \sqrt{\frac{GM(<r)}{r}}$. *Middle Left*: The evolution of the surface density profile $\Sigma(R)$ from $z = 1.1$ to $z = 0$. *Middle Right*: Surface density profile $\Sigma(R)$ at z=0 fitted with a two-component profile $\Sigma_{0,1}\ \exp\left(-\frac{R}{R_d}\right) + \Sigma_{0,2}\ \exp\left[-\left(\frac{R}{R_b}\right)^{\left(\frac{1}{n}\right)}\right]$ with scale-lengths $R_d = 2.9\ {\rm kpc}$ and $R_b = 1.0\ {\rm kpc}$ and $n = 0.47$. *Bottom Left*: Normalized $z = 0$ vertical density profile at $R = 5\ {\rm kpc}$ fitted by a double exponential with $h_{\rm thin} = 420\ {\rm pc}$ and $h_{\rm thick} = 1300\ {\rm pc}$. *Bottom Right*: Circularity distribution for all stars at $z = 0$.

In the middle left panel of Fig. 3.2 we show the evolution of the stellar surface density profile $\Sigma(R)$ of model ARef from $z = 1.1$ until $z = 0$. It can be seen that the first stars form in a concentrated bulge-like structure at $R < 2$ kpc. This structure is actually triaxial because the infalling gas adjusts to the potential imposed by the halo. Its surface density only increases by a factor of ~ 2 until $z = 0$. The surface density profile outside the bulge region is already exponential in this early phase. Once most of the baryons have cooled, the infalling gas and the forming stars settle in a well-defined disc, which grows transforming the central potential into an axisymmetric configuration. The disc grows inside-out showing a truncation at a radius $R_{\rm max}(z)$ as observed in disc galaxies (van der Kruit & Searle, 1981). This is a consequence of high-angular-momentum gas living initially at greater radii, lower densities and thus longer cooling times. Moreover, according to our assumed star formation law, star formation timescales are longer at lower surface densities. The break in $\Sigma(R)$ moves outward with time to around $R \sim 19$ kpc at $z = 0$. There is observational evidence for inside-out formation of real disc galaxies (Wang et al., 2011b) and for outward-movement of their truncations (Azzolini et al., 2008).

Due to the numerically imposed cooling floor $T_{\rm floor}$ and the density threshold $\rho_{\rm thresh}$, there is an imposed star formation threshold surface density $\Sigma_{\rm thresh}$. As is shown in the first row of Fig. 3.8 the gas disc at $z = 0$ extends to larger radii, where this threshold is not reached. This also indicates that the truncation of the initial spherical distribution does not play a role here. The extended gas disc is also slightly warped, as in real disc galaxies (Sancisi, 1976). The warp is a result of a slight misalignment between the disc and the late-infall gas (see Sections 3.6 and 3.8 for a discussion of misalignments).

Exponential disc profiles with central concentrations are common in real galaxies (de Vaucouleurs, 1958) and also in simulations (Katz & Gunn, 1991), although most simulations significantly over-predict the mass in the central bulge component (CS09, Scannapieco et al., 2010, but see Brook et al., 2012 for simulations of lower mass (nearly) bulge-less discs). The $\Sigma(R)$ profile at $z = 0$ as displayed in the middle right panel of Fig. 3.2 is well-fitted by a profile of the form $\Sigma_{0,1}\ \exp\left(-\frac{R}{R_d}\right) + \Sigma_{0,2}\ \exp\left[-\left(\frac{R}{R_b}\right)^{\left(\frac{1}{n}\right)}\right]$, which combines an exponential disc with a Sersic profile. The Sersic indices found for our disc models are $n \sim 0.5{-}2.$, similar to observed pseudo-bulges. The scale-lengths for ARef are $R_b = 1.0$ kpc and $R_d = 2.9$ kpc. Calculating a disc-to-bulge mass ratio from this profile alone yields $D/B \sim 12$.

In the bottom left panel of Fig. 3.2 we display the vertical stellar density profile $\rho(z)$ for all stars in model ARef that are located in an annulus of width 1 kpc centred around $R = 5$ kpc at $z = 0$. The profile is well fitted by a double-exponential with scale-heights 420 and 1300 pc. The vertical profile does not vary significantly within $R < 10$ kpc, but at larger radii the disc flares and the scale-height increases by a factor of ~ 2 until $R_{\rm max}$. Thus the outer vertical structure of this model is in conflict with observations of constant vertical structure within the exponential disc region (van der Kruit & Searle, 1981). In the following section we will show that this conflict is absent for some of our models. The flaring and the 'thick' disc are caused by old stellar material formed in the bulge-formation period around $z \sim 1$. From then on, the scale-heights first become smaller due to the growth of a young, cold disc before beginning to increase again due to disc heating. This increase is stronger in the inner disc as the outer disc has a younger mass-weighted age. The ARef disc thus has similar structural characteristics to the Milky Way disc (Jurić et al., 2008; McMillan, 2011), although the model disc is ~ 40 % thicker.

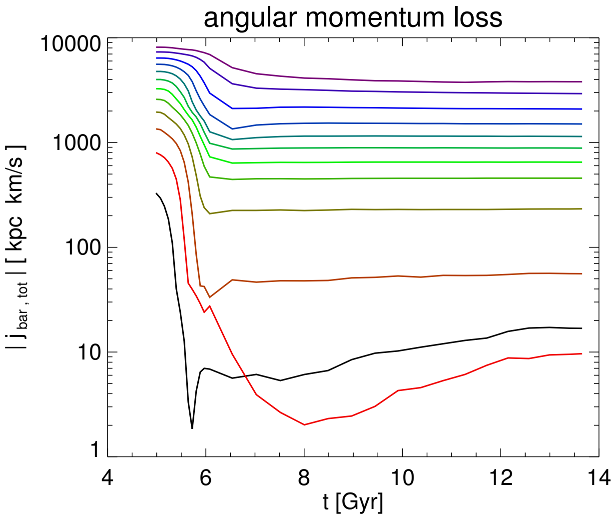

Figure 3.3: Angular momentum loss as a function of time for model ARef. The initial gas sphere has been divided into 12 spherical shells of 5 kpc width each. For each shell the absolute of the total angular momentum vector $\mathbf{j_i}$ of all particles initially in shell *i* is calculated at each output.

3.4.2 | Angular momentum loss of infalling gas

The radial structure of the disc discussed above is determined by the potential and the angular momentum content of the stellar population. The concentrated peak in $\Sigma(r)$ produced in the early stages of star formation indicates an unexpectedly high amount of low angular momentum material and thus angular momentum losses. We investigate this in Fig. 3.3, in which we plot the evolution of the total specific angular momentum of populations of baryons initially located in concentric shells of 5 kpc width. The material initially located at $R < 10$ kpc loses $\gtrsim 99\%$ of its angular momentum within the first 500 Myr. The material in the next two shells still loses $\gtrsim 90\%$, the outermost material $\sim 50\%$. The strongest losses occur in the phase when the central potential is transformed from a triaxial to a disc-like configuration, in the process of which the bulge forms. Moreover, the losses are subsequently delayed for outer shells, indicating that the angular momentum is lost as the gas cools and moves to the centre.

3.4.3 | Kinematical properties

We move on to analyze the kinematics of ARef. The top right panel of Fig. 3.2 depicts the rotation velocity $V_{\rm rot}$ and the velocity dispersions σ_R, σ_ϕ and σ_z of the disc stars and the spherically averaged circular velocity $V_{\rm circ}(r) = \sqrt{GM(r)/r}$ profile at $z = 0$. $V_{\rm circ}$ peaks at $\sim 250\ {\rm kms}^{-1}$ at $R \sim 10$ kpc and gently decreases outside. The stellar rotation curve shows a broad peak at $7 < R/{\rm kpc} < 15$ at $V_{\rm rot} \sim 240\ {\rm kms}^{-1}$. For velocity dispersions, we find a decreasing profile out to $R \sim 12$ kpc and $\sigma_R > \sigma_\phi > \sigma_z$ in the rotation-dominated region. The kinematical properties of the ARef disc are thus also similar to, but slightly hotter than the Milky Way disc (Aumer & Binney, 2009; Schönrich, 2012).

As a tool to quantify disc-to-bulge ratios, the circularity $\epsilon = V_{\rm rot}/V_{\rm rot,max}(E)$ for a stellar particle at energy E has been widely used (Abadi et al., 2003). Particles on a perfect circular orbit have $\epsilon = 1$ and thus a disc will show a peak close to $\epsilon = 1$, whereas a non-rotating bulge will have a peak at $\epsilon = 0$. The bottom right panel of Fig. 3.2 depicts the ϵ-histogram for ARef, which shows a distinct peak at $\epsilon = 0.95$ and only a shallow peak at $\epsilon = 0$, corresponding to $D/B \sim 4$. Thus the kinematic estimate for D/B is significantly lower than the one from $\Sigma(R)$-fitting, consistent with e.g. the results of Scannapieco et al. (2010) for simulations of disc formation from cosmological initial conditions.

However, this analysis is not capable of distinguishing between old and young stars and is also not good at quantifying how thin and dynamically cold a disc is. In the top panel of Fig. 3.4 we therefore employ a plot of the rotation-to-dispersion ratio $V_{\rm rot}/\sigma_z$ as a function of the age of the stars. We define a disc plane perpendicular to the total stellar angular momentum at each output time t. $V_{\rm rot}$ is calculated as the mean tangential velocity and σ_z as the rms velocity in the direction of the rotation axis of all stars in a certain age bin. Keep in mind that the Milky Way young thin disc has $V_{\rm rot}/\sigma_z >\sim 20$, the older thin disc has ~ 10 (Aumer & Binney, 2009), whereas the thick disc shows ~ 5 (Reddy et al., 2006). To be able to compare different models better, we sort the stars according to their age, bin them in equal mass bins, and sort those according to the fraction of the $z = 0$ stellar mass that has formed up to the time in consideration. We do this for five different redshifts. The black $z = 0$ line shows that $V_{\rm rot}/\sigma_z$ monotonically decreases with increasing age. Only the youngest stars are compatible with thin disc kinematics. The oldest $\sim 1/5$ is dispersion dominated and corresponds to the bulge peak seen in the bottom left panel of Fig. 3.2. Most of the galaxy thus has thick disc kinematics. Considering the evolution of $V_{\rm rot}/\sigma_z$ over time, we can see that the bulge kinematics do not change from $z = 0.9$ to $z = 0.0$, whereas the disc populations show decreasing $V_{\rm rot}/\sigma_z$ ratios over time, i.e. the disc populations are heated, indicating that at least $1/3$ of the stellar particles are born with thin-disc-like kinematics.

3.4.4 | Disc heating

In order to analyze disc heating as it occurs in ARef in more detail, we plot the evolution of σ_z for several coeval populations through time in the bottom panel of Fig. 3.4. The stars that form earliest and most centrally (see middle left panel in Fig. 3.2) show high, almost isotropic velocity dispersion (top right panel in Fig. 3.2). These stars are strongly heated within a few 10^8 years (black line) or born hot (red line). Within ~ 1 Gyr after the first star formation in the models, the initial σ_z has already become significantly lower, indicating the transition from bulge to disc formation. Within another ~ 0.5 Gyr, σ_z at birth has dropped below $20\ {\rm kms}^{-1}$. Only the stars that form latest, are born with a smaller $\sigma_z \sim 10\ {\rm kms}^{-1}$. As will be shown below, the high initial velocity dispersions of the first stars in this model are an effect of the structure of the dark halo. Test simulations in spherically symmetric haloes do not show this effect, but a significantly reduced initial velocity dispersion of the stars that form first, of the order $\sim 10 - 20\ {\rm kms}^{-1}$, as seen for the young populations in model ARef. The velocity dispersion of stellar particles in numerical simulations is limited by the applied star formation threshold, resolution and modelling of gas physics (House et al., 2011) and the formation of a realistically cold young thin disc population is thus not possible in our current models.

All the discy coeval populations show an increase of σ_z over time. Such continuous disc heating has been inferred for solar neighbourhood stars (Holmberg et al., 2009) and is usually linked to scattering of stars off disc substructure such as transient spirals and/or giant

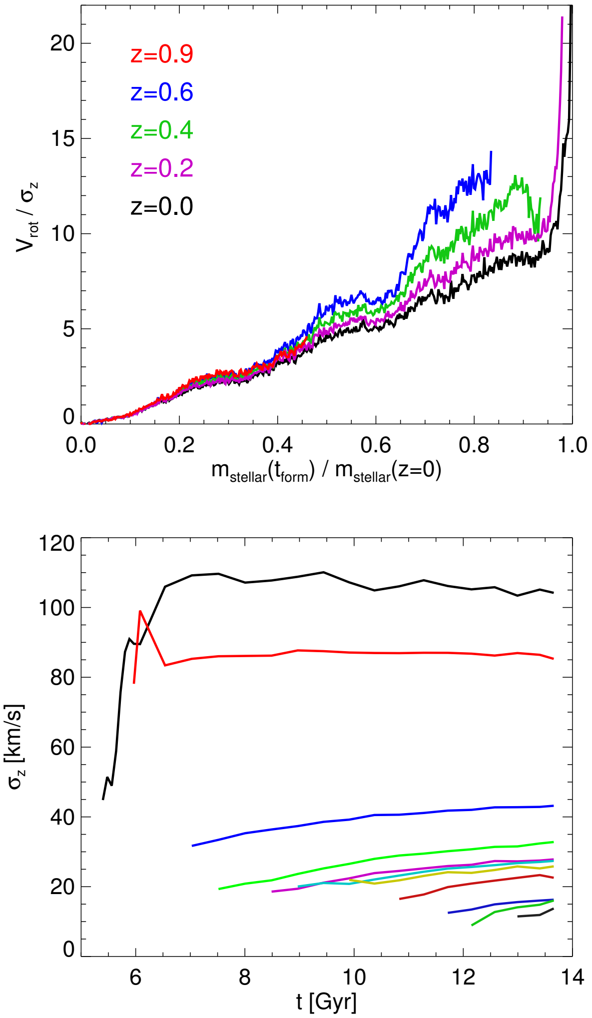

Figure 3.4: Disc Heating in model ARef: *Top*: The ratio of the rotation velocity of stars to their vertical velocity dispersion $V_{\rm rot}/\sigma_z$ as a function of the fraction of stellar mass that has formed until the formation time $t_{\rm form}$ of a star particle relative to the total stellar mass at z=0 for model ARef. The first stars are found at x-value 0, the ones formed at $z = 0$ at x-value 1. Curves are plotted for redshifts $z =$ 0.9, 0.6, 0.4, 0.2 and 0. The endpoints of curves indicate the fraction of stellar mass that has formed until the given redshift, e.g. 82 % for $z = 0.6$. The evolution of $V_{\rm rot}/\sigma_z$ over time can be inferred by considering the various coloured lines at one specific x-value. At each output redshift z we define a disc plane perpendicular to the total stellar angular momentum. $V_{\rm rot}$ is then calculated as the mean tangential velocity and σ_z as the rms velocity in the direction of the rotation axis of all stars in a certain age bin. *Bottom*: Vertical velocity dispersion $\sigma_z(t)$ as a function of time for coeval populations in model ARef. The stellar population is binned into 50 equally spaced bins in redshift z, a representative selection of which is depicted by the various colours in the figure. The starting point of a line indicates the formation time of the population in consideration.

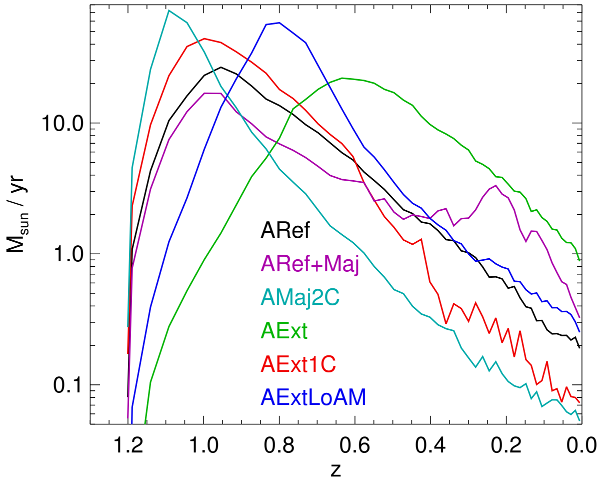

Figure 3.5: Star formation rates as a function of redshift z for various models.

molecular clouds (Jenkins & Binney, 1990). For our models we cannot, however, exclude that this effect is partly due to numerical heating (e.g. Steinmetz & White, 1997). A closer analysis of the phenomenon over all of our models reveals that the strongest heating always occurs when distinct substructure in the form of a bar or spirals is present. A look at the evolution of σ_z at different disc radii R over time reveals that due to the combined effect of the heating of coeval populations and the inside-out formation of our models, in the inner disc regions, σ_z first drops due to the formation of a thin disc and then increases due to disc heating, whereas at outer radii the formation phase lasts longer and σ_z remains almost constant after an initial drop.

3.4.5 | Summary

In conclusion, our setup is capable of producing disc galaxy models with realistic structural and kinematic properties. Disc formation proceeds inside-out and follows an early bulge-formation episode, during which the central halo potential is transformed into a disc-like configuration. This transformation is connected to angular momentum losses for the infalling gas. Moreover, a thick disc component in the vertical profiles originates from this epoch. We confirm that for a disc/bulge decomposition, a kinematic analysis is superior to a surface-density decomposition. However, circularity distributions alone, as often applied, are not ideally suited to distinguish properly between thin and thick disc components, which is why $V_{\rm rot}/\sigma_z$ ratios should be used in addition. Our model does show a significant thin disc component, however its $V_{\rm rot}/\sigma_z$ is limited to values ~ 10 compared to 20 for real young thin discs, due to the numerical lower limit we impose on σ_z. The disc undergoes secular disc heating and shows a significant decline of zero-age velocity dispersion of stars.

3.5 | How to make better discs

In this and the next section we discuss the dependencies of our models on the parameters that define them:

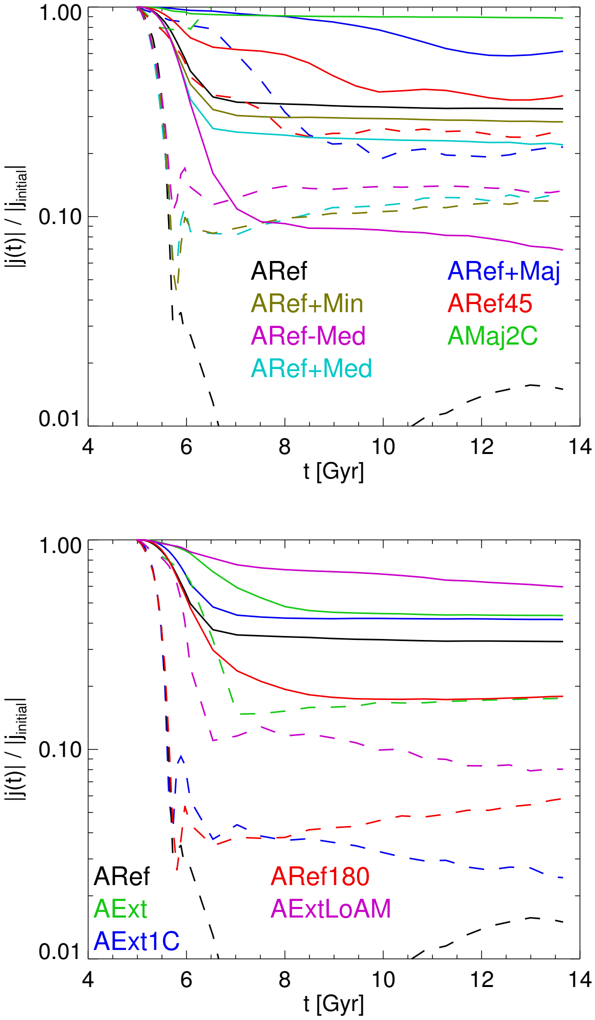

Figure 3.6: Angular momentum loss for different models. The top panel features different orientations with otherwise constant parameters, whereas the bottom panel focuses on different representations of physics at the same orientation. The definition of angular momentum loss is as in Fig. 3.3. The solid lines represent all baryonic particles in the simulations, the dashed lines only the particles that initially reside at $R < 0.2\ R_{\mathrm{gas}}$.

1. The mass of the model $M_{\rm gas}$, the initial radius $R_{\rm gas}$ and thus the initial density profile $\rho(R)$
2. The rapidity of cooling and thus accretion of gas onto the forming galaxy represented by the cooling time normalization $t_{\rm cool,0}$
3. The initial angular momentum distribution of the gas represented by the rotation velocity profile $V_{\rm rot}(R)$
4. The orientation of the angular momentum vector of the gas (see also the following section)

Our goal is to understand which physical conditions favor thin disc formation in ΛCDM haloes. An overview over our models and their parameters can be found in Table 3.1. In this section, we will mainly focus on halo A. For the parameters $M_{\rm gas}$, $R_{\rm gas}$, $t_{\rm cool,0}$ and $V_{\rm rot}(R)$ we could not find significant halo-to-halo differences. Most differences because of orientations are discussed in Section 3.6. As in the previous section, we split our analysis into subsections that deal with star formation, angular momentum loss, disc structure, kinematics and disc heating.

3.5.1 | Gas infall and star formation

We begin with a discussion of how the model parameters influence the formation histories of our models. The star formation rates of the models displayed in Fig. 3.5 reveal that the process of gas inflow depends mainly on $t_{\rm cool,0}$ and the loss of angular momentum, which is put into the initial models via $V_{\rm rot}(R)$. Models ARef (black line), ARef+Maj (purple) and AMaj2C (turquoise) share the initial density profile and cooling time. All models show a steep rise followed by a softer decrease in SFR. ARef+Maj and ARef differ only in orientation, consequently they show qualitatively similar SFRs. ARef+Maj loses a smaller amount of angular momentum (see below), thus forms a more extended structure with lower densities and has longer star formation timescales, a lower peak SFR and a higher late-time SFR. The second peak for ARef+Maj corresponds to star formation in a ring structure (see the following section). ARef+Maj and AMaj2C differ only in $V_{\rm rot}(R)$ with AMaj2C having significantly less angular momentum, which leads to a much more concentrated object, higher densities, higher cooling rates, higher SFRs, an earlier peak and a steeper decrease in SFR. The same is true for a comparison of AExt1C (red line), AExt (green) and AExtLoAM (blue). They are all more extended with a higher initial gas mass than the models mentioned so far and thus represent a different initial density profile. AExt1C cools 4 times faster than AExt and AExtLoAM has 3 times less angular momentum than AExt. In both cases this results in a higher and earlier peak in SFR.

Directly connected to the SFR is the remaining gas fraction in the discs. At $z = 0$ these are almost independent of cooling time, as the cooling and star formation timescales are small compared to the simulation time and the gas disc outside $R_{\rm max}$ contains a negligible amount of mass. Thus AExt1C and AExt both show a final gas fraction of 18%. Angular momentum variation can significantly alter the mass in the outer gas disc with very long cooling and SF timescales. Thus, ARef+Maj (36%) and AExt (18%) have much higher gas fractions than AMaj2C (3%) and AExtLoAM (4%). Realistic gas ratios are 5 to 25% (Evoli et al., 2011), so that only our most extreme models are inconsistent with observations.

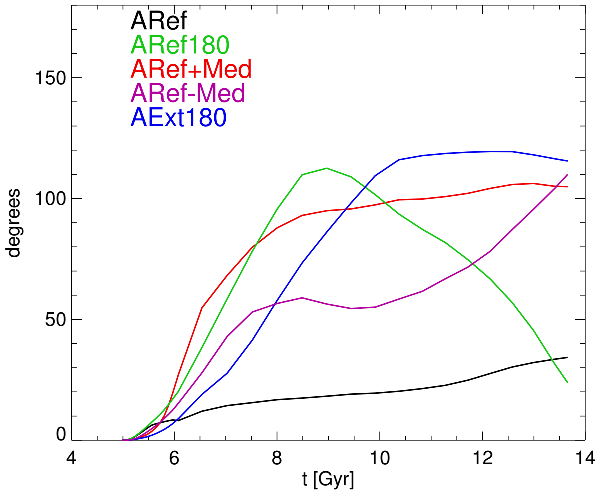

Figure 3.7: Mass-weighted reorientation angle of all baryons as a function of time for models ARef-Med, ARef+Med, ARef, ARef180, AExt180. The angle is measured in a fixed coordinate system between the initial angular momentum vector orientation at $z = 1.3$ and its given orientation at time t.

3.5.2 | Why does infalling gas lose angular momentum?

As we have shown in Section 3.4, gas in our models loses angular momentum as it falls to the centre. Fig. 3.6 allows a closer inspection of angular momentum loss in several models. For each model, the solid line represents the absolute value of the total specific angular momentum of all baryonic particles, whereas the dashed line represents only the particles that initially live within $R < 0.2\ R_{\rm gas}$. The top panel focuses on models which differ only in orientation and, apart from AMaj2C, share the same density and velocity profiles and cooling times. Apart from ARef-Med and AMaj2C, the central parts show higher angular momentum losses. The difference between central and total mass is biggest for model ARef as discussed above. Focusing on total angular momentum losses, the models aligned with the major halo axis (ARef+Maj and AMaj2C) show the lowest losses. They are about 10% at $t = 8\ \rm Gyr$ and subsequently only increase for ARef+Maj which develops strong misalignments between inner and outer galaxy, leading to higher losses than in AMaj2C, which forms a well-aligned disc. ARef45, which starts with its orientation 45 degrees offset, has lost 40% of its total angular momentum at $t = 8\ \rm Gyr$. The rest of the models, which all started oriented perpendicularly to the major axis, show losses well in excess of 50%. Only a small part of these losses, perhaps of the order of 10%, can be of numerical origin. Kaufmann et al. (2007) reported 10% losses for their highest resolution model in a spherical halo, the resolution of which is similar to our models.

As halo A has an approximately prolate shape (Vera-Ciro et al., 2011), the axis ratio of the halo potential in the plane perpendicular to the major axis is close to 1, i.e. almost axisymmetric, whereas it is ~ 0.7 if the disc axis is perpendicular to the major axis. Thus the formation of a disc in the former case requires a less severe transition of the central halo potential into an oblate, axisymmetric, disc potential, than is the case for the latter models. The strongest angular momentum losses in our models occur in these initial transformation

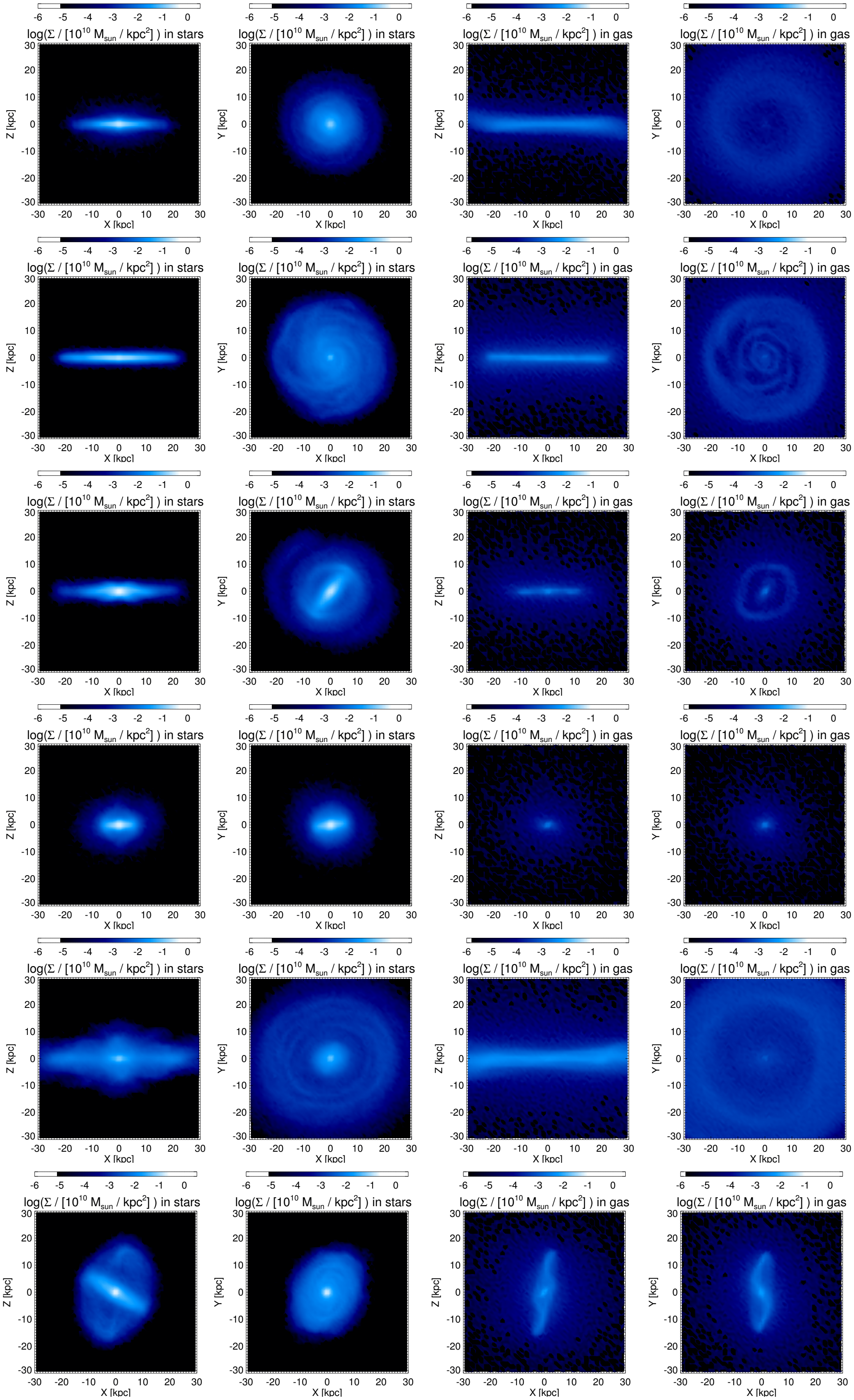

Figure 3.8: Edge-on and face-on surface density projections for stars (left panels) and gas (right panels) at $z = 0$ for models (top to bottom): ARef, CExtCosmo, AExtLoAM, ARef-Min, CExt+AM and C-Maj.

phases. As our spherical initial gas distributions are not in equilibrium with the gravitational potential of the halo, the gas, which is significantly less dense than the dark matter in the region in consideration, adjusts to the triaxial potential in the early phases of our simulations. Due to its rotation, the shape of the gas distribution becomes offset from the shape of the potential if the halo symmetry axis and the axis of rotation do not agree. Gravitational torques then lead to the transfer of angular momentum to the halo. This explains the initial loss of angular momentum in all models, except those oriented parallel to the major axis, as seen in Fig. 3.6. The differences in the evolution of models at the same orientation or with orientations perpendicular to major, which all show similar axis ratios of the equipotential ellipses in the plane defined by their initial orientation, appear at later times (after $\sim 0.5-1$ Gyrs) and coincide with phases of reorientation of the angular momentum vector (see below).

In Fig. 3.7 we illustrate this reorientation of the total baryonic angular momentum vector in models ARef-Med, ARef+Med and ARef. Strong reorientation starts to develop after $\sim 0.5-1$ Gyrs. At these times, the assembly of baryons in the centre of the halo has led to a transformation of the central halo potential shape, which apparently can induce strong reorientation of the baryonic angular momentum vector. ARef shows the lowest amount of reorientation and has the lowest losses of angular momentum. ARef-Med shows continuous reorientation, whereas ARef+Med settles into a new orientation relatively quickly. Consequently, ARef-Med loses the most angular momentum (see Fig. 3.6).

In the bottom panel of Fig. 3.6 we focus on models with the same rotation axis. ARef180, which differs in orientation by 180 degrees from ARef, loses more angular momentum, as it shows strong reorientation (Fig. 3.7). However, the losses are smaller than in ARef-Med, showing that angular momentum losses depend not only on reorientation and on the shape of the potential in the disc plane, but also on the complex details of the interaction of hot gas, dark halo and stellar component. AExt1C, which is more extended, more massive and has a higher total angular momentum content, shows a smaller total angular momentum loss. AExt, which differs from AExt1C only by a 4 times longer cooling time, loses approximately the same amount of angular momentum, but on a longer timescale, illustrating again that the loss occurs as the gas cools to the centre. AExtLoAM, which has the lowest amount of angular momentum and goes bar unstable (see Fig. 3.8), shows smaller losses than AExt, which only differs in $V_{\rm rot}(R)$.

For fixed values of other parameters, shorter cooling timescales, stronger reorientation and higher initial densities lead to increased angular momentum loss. Higher initial angular momentum also leads to greater fractional losses.

3.5.3 | Structural properties

We continue with a study of the influence of the model parameters on the structure of the disc models. In Fig. 3.9 we analyze $\Sigma(r)$ profiles for several models in halo A. Here we focus on the models that produce the strongest discs. The others are discussed in the following section. Model AExt1C, which has more initial angular momentum, a higher mass and a larger initial radius than ARef (see bottom left panel in Fig. 3.2), produces a more extended disc with a disc scale-length $R_d = 5.3$ kpc and no truncation out to 30 kpc. The four times longer cooling time of AExt mildly extends the scale-length to 6.1 kpc, but produces a truncation around 20 kpc, as the outermost material cools too slowly to form stars. The bulge profiles are very similar in the two models, showing that the formation of a centrally concentrated component due to transformation of the central halo potential depends little on

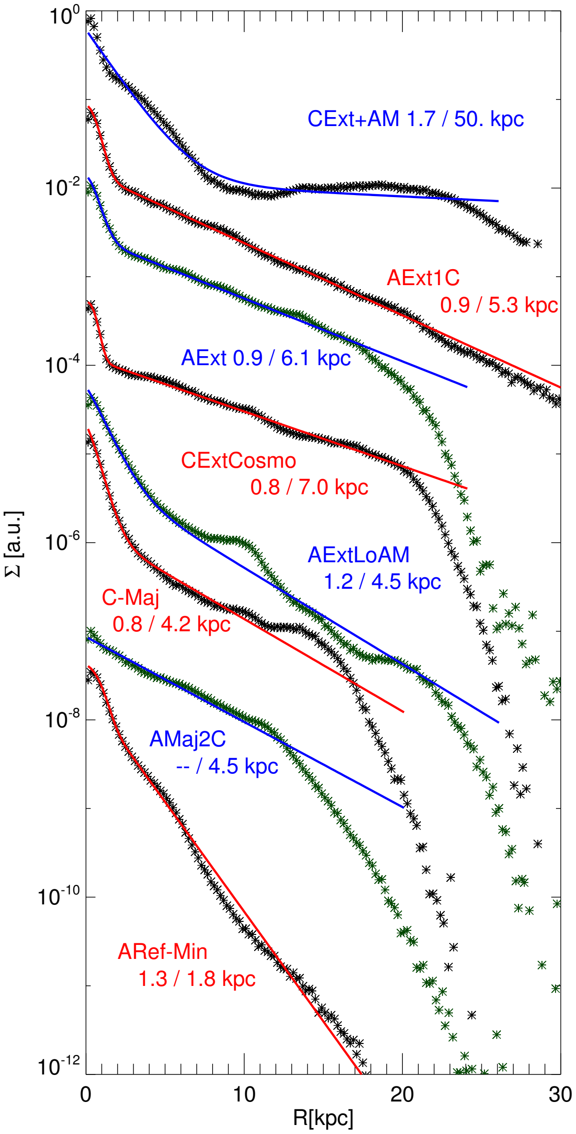

Figure 3.9: Radial stellar surface density profiles $\Sigma(R)$ at $z = 0$ for models CExt+AM, AExt1C, AExt, CExtCosmo, AExtLoAM, C-Maj, AMaj2C and ARef-Min. Overplotted are fits of the type $\Sigma_{0,1}\ \exp\left(-\frac{R}{R_d}\right)+\Sigma_{0,2}\ \exp\left[-\left(\frac{R}{R_b}\right)^{\left(\frac{1}{n}\right)}\right]$. The numbers indicate the scale-lengths of the two components.

cooling time.

Model AExtLoAM goes bar unstable and thus shows a much stronger central component with a longer scale-length (1.2 vs 0.9 kpc). The bulge profile extends to 8 kpc. The profile outside can be approximated by an exponential disc, but clearly shows a ring structure, which is also visible in Fig. 3.8, both in stars and in gas. Pseudo-bulge and ring are results of bar-induced gas flows as discussed e.g. in Athanassoula (1992).

In model AMaj2C there is no severe initial central transformation. The profile can be fitted by a single exponential, which, because of the very low angular momentum losses, has a larger scale-length than ARef (4.5 vs 2.9 kpc), despite the low initial angular momentum content. The low angular momentum also leads to a small truncation radius $R_{\max} \sim 12\ \mathrm{kpc}$.

The coldest discs form in AExt and CExtCosmo, which share initial density and angular momentum profiles, as well as cooling timescales, and which both undergo little reorientation. They show small halo-to-halo differences in terms of $\Sigma(R)$. AExt has a more massive bulge component, a slightly less extended disc ($R_d = 6.1$ versus $7.0\ \mathrm{kpc}$) and a slightly smaller truncation radius. This underlines that the effects of the parameters discussed in this section are very similar in the two cases.

In Fig. 3.10 we compare vertical profiles of several models at $R = 5\ \mathrm{kpc}$. In contrast to the double-exponential of ARef (see Fig. 3.2), AExt shows a single exponential profile with a slightly reduced exponential scale-height $h_z = 400\ \mathrm{pc}$ (compared to 420 pc for ARef). We also present the profile of CExtCosmo. It has an even thinner disc with $h_z = 330\ \mathrm{pc}$, consistent with the reduced bulge fraction discussed above. Moreover, the flaring of these discs is significantly reduced compared to ARef. Scale-heights for CExtCosmo are $h_z < 400\ \mathrm{pc}$ at $R < 10\ \mathrm{kpc}$ and $h_z < 550\ \mathrm{pc}$ out to $R \sim 20\ \mathrm{kpc}$.

The edge-on and face-on surface density projections in gas and stars of Fig. 3.8 (second row) nicely reveal that CExtCosmo sustains spiral substructure in the stellar and gas disc until $z = 0$, unlike ARef, which at this time has a significantly lower SFR. A comparison to ARef also highlights the less prominent bulge structure and the lack of an underlying thick component. A longer cooling time and a higher angular momentum content result in a prolonged star formation in the disc of CExtCosmo. Together with a small amount of reorientation of the angular momentum vector, this leads to the continuous existence of a relatively thin stellar disc preventing the formation of a thick component.

In comparison to these extended discs, the low angular momentum model AExtLoAM, which goes bar unstable, shows a thick vertical profile at $R = 5\ \mathrm{kpc}$ (in the bar region), which is fit neither by an exponential nor by an isothermal profile. In the edge-on view in the third row of Fig. 3.8, the peanut-shape of the stellar system is clearly visible.

3.5.4 | Kinematical properties

The significant parameter dependencies found above are also reflected in the stellar kinematics of our models. In terms of the circularity distribution, longer cooling times and the resulting thinner and more extended discs result in a slightly enhanced disc peak and a reduced bulge peak as may be seen by comparing AExt and ARef in Fig. 3.11. The massive bar in AExtLoAM significantly diminishes the $\epsilon \sim 1$ peak and shifts material into a wide, asymmetric distribution at $-1 < \epsilon < 0.8$.

The parameter dependence of the discs is summarized in the rotation-to-dispersion-ratio plots of Fig. 3.12. In the upper panel we compare models ARef, AExtLoMa and AExt2C. Compared to ARef, AExtLoMa is more extended ($R_{\mathrm{gas}} = 100$ vs 60 kpc). This leads to an

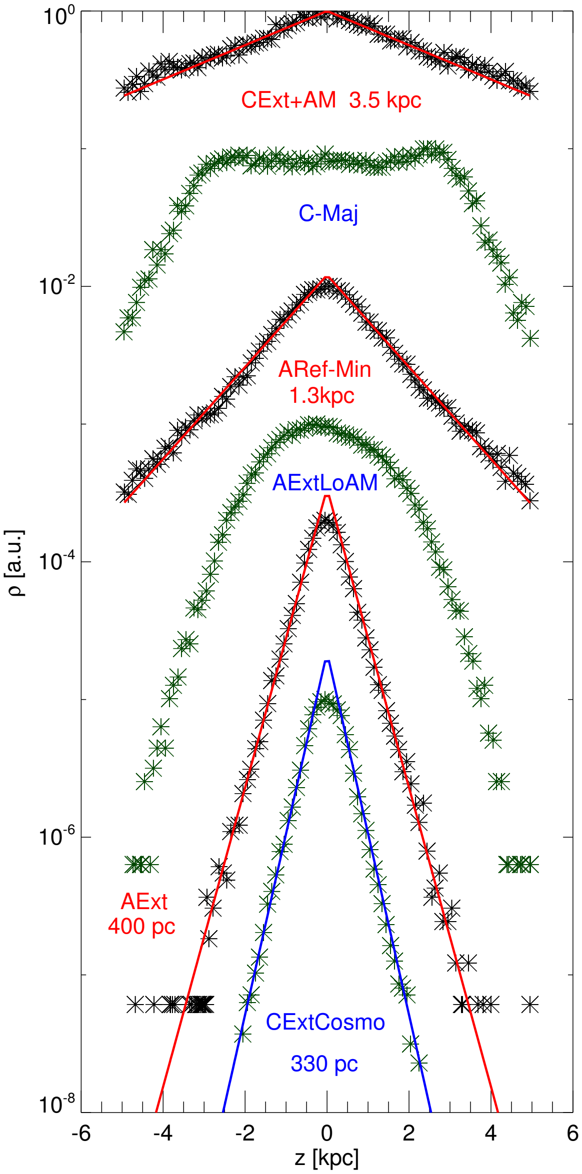

Figure 3.10: Vertical density profiles of models CExt+AM, C-Maj, ARef-Min, AExtLoAM, AExt and CExtCosmo. If sensible, exponential fits are overplotted and the scale-heights are noted.

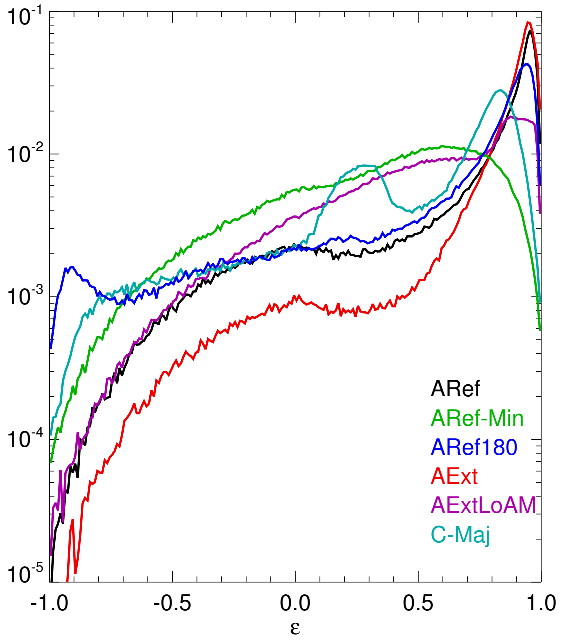

Figure 3.11: Circularity distributions for models ARef, ARef-Min, AExt, AExtLoAM, ARef180 and C-Maj.

increase of $V_{\rm rot}/\sigma_z$ for all generations of stars, a reduction of the bulge-fraction, but no significant increase in the thin disc population. A lower density, which already results in slower cooling (cf. Fig. 3.1), thus helps reduce the impact of initial bulge formation. An increase in mass by 50% has little impact, as may be seen by comparing AExt2C to AExtLoMa. It leads to more $z = 0$ thin disc stars as it increases the surface density and thus prolongs star formation in the disc outskirts. Increasing the mass again by a factor of 2, as in AExtHiMa, reduces the rotation-to-dispersion-ratio significantly. The bulge fraction is reduced due to the longer cooling time applied (see middle panel). The disc goes bar unstable, however, and the bar subsequently heats the disc.

The second panel compares the models AExt1C, AExt2C and AExt and thus reveals the impact of the cooling time. Clearly, a longer cooling time leads to an increase of $V_{\rm rot}/\sigma_z$ for all generations of stars. The increase is especially significant for the old population. AExt only shows $\sim 5\%$ bulge stars. From Fig. 3.4 we know that $V_{\rm rot}/\sigma_z$ decreases due to disc heating as stellar populations age. As we know from Fig. 3.5 that AExt has a much younger population than AExt1C, the difference for the disc stars can be attributed mainly to the younger ages of the population. $V_{\rm rot}/\sigma_z$ for the thin disc population is similar for all models, confirming that this is mainly determined by resolution and by the prescriptions for star formation and for cooling.

The bottom panel of Fig. 3.12 concerns the initial angular momentum content of the models. Compared to AExt, $V_{\rm rot}(R)$ in AExtMedAM has been reduced by $1/3$ and by $2/3$ in AExtLoAM. Interestingly, AExtMedAM shows a slightly smaller dispersion-dominated component. This indicates that the transfer of angular momentum from baryons to the dark halo plays a crucial role in the initial phase of bulge formation/transformation of the central poten-

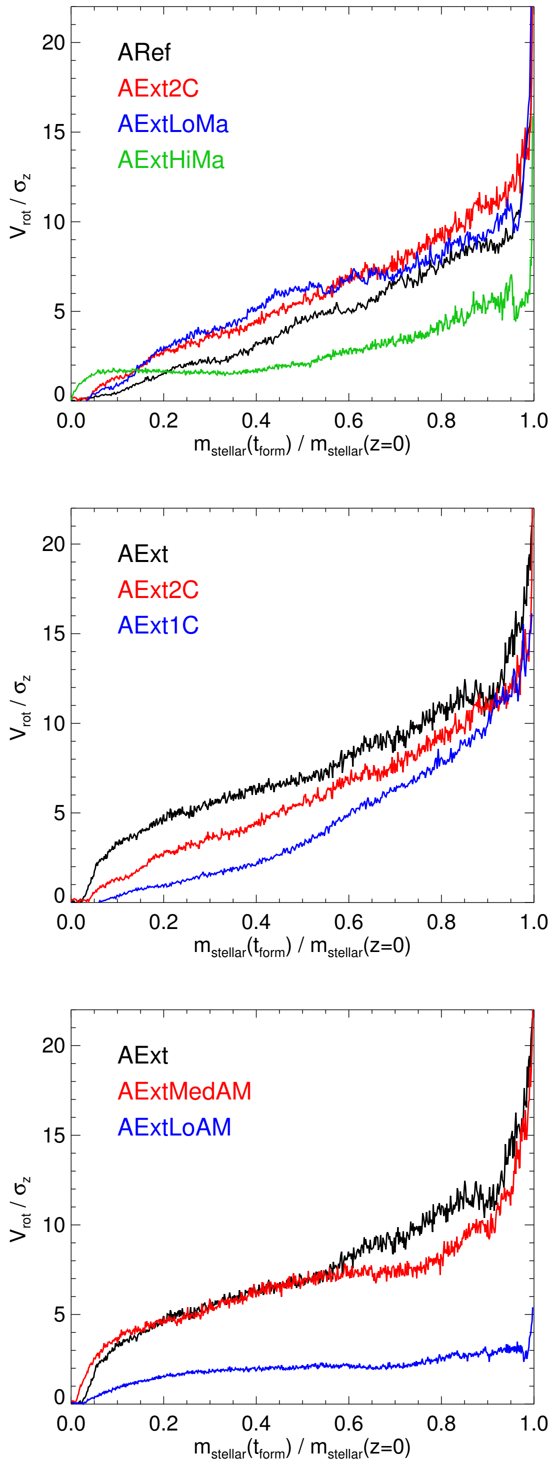

Figure 3.12: Rotation-to-dispersion ratio as in Fig. 3.4, but now for different models at $z = 0$. *Top*: The effect of the initial radius $R_{\rm gas}$ and mass $M_{\rm gas}$ illustrated by models ARef, AExtLoMa, AExt2C and AExtHiMa. *Middle*: The effect of the normalization of the cooling time $t_{\rm cool,0}$ illustrated by models AExt1C, AExt2C and AExt. *Bottom*: The effect of the angular momentum content / rotation velocity profile $V_{\rm rot}(r)$ illustrated by models AExt, AExtMedAM and AExtLoAM.

tial. For the younger population, AExt is colder than AExtMedAM, as it is more extended and thus has longer star formation timescales for the outer populations. AExtLoAM has been discussed above and shown to go massively bar unstable. The consequence is a drastic reduction of $V_{\rm rot}/\sigma_z$ for all ages.

3.5.5 | Disc heating

To illustrate differences in disc heating, we depict in Fig. 3.13 the evolution of $\sigma_z(t)$ for several coeval populations of stars in models AExtLoAM and CExtCosmo. Compared to model ARef, presented in Fig. 3.4, they both have lower initial densities and slower cooling times. Like ARef they show continuous disc heating for all populations. Moreover, the oldest populations undergo strong heating in the first several 10^8 years, but, unlike ARef, the slower initial transformation of the central potential prevents hot initial dispersions $\sigma_{z,\rm ini} > 50\ {\rm kms}^{-1}$.

The low angular momentum model AExtLoAM shows the strongest heating of old components (to $\sigma_z \sim 120\ {\rm kms}^{-1}$) due to the most concentrated surface density profile. At $t \sim 11\ {\rm Gyr}$, after the massive bar has developed (cf. Fig. 3.8), a strong enhancement in the heating of disc populations is visible. In less than a Gyr, $\sigma_z(t)$ increases by about 50% for all populations except the oldest, which are dispersion-dominated and are hardly affected by the bar. An inspection of radial velocity dispersion $\sigma_R(t)$ reveals that in-plane heating is already enhanced at $t \sim 9\ {\rm Gyr}$, when the bar starts to form. The bar also increases the birth velocity dispersions of stars by about 50%. The final bar/disc populations are heated more efficiently and are thus significantly hotter than in ARef. Analyzing $\sigma_z(t)$ for radial bins shows that the increase occurs at all radii less than $\sim 8\ {\rm kpc}$ and also in the central kpc. The stellar populations outside $R \gtrsim 10\ {\rm kpc}$ (outside the bar region) are, however, not affected.

For the disc populations in the high angular momentum model CExtCosmo, $\sigma_z(t)$ behaves as for the corresponding populations in ARef, continuously increasing with the birth dispersions decreasing with time. The initial heating for the oldest populations is, however, significantly reduced compared to ARef. Consequently, the transition between the oldest and the subsequent populations is not as strong as in the other models. This is reflected by the increase in D/B for disc models with longer assembly timescales. Still, CExtCosmo and all other disc models show a decrease in the birth velocity dispersions with time. This behaviour is a consequence of the triaxial halo and its substructure, and does not occur in simulations within idealized spherical haloes.

3.5.6 | Summary

In this section, we have studied the influence of cooling timescales, angular momentum content, initial density profile and mass on our models. We show that the formation timescale increases with increasing cooling time and increasing angular momentum content. The angular momentum loss in our models increases mainly with increasing initial ellipticity of the dark matter potential in the disc plane. If reorientation of the baryonic angular momentum vector occurs in a model, it adds to the loss of angular momentum. A slower formation process and thus a slower transformation of the central potential yields thinner and more dominant final discs and weakens the formation of prominent bulge and thick disc components. Massive bulges can only be avoided if the initial potential contours in the disc plane are almost circular. Double-exponential vertical disc profiles are suppressed by a slow formation timescale. All our discs show continuous secular heating due to (spiral) substructure

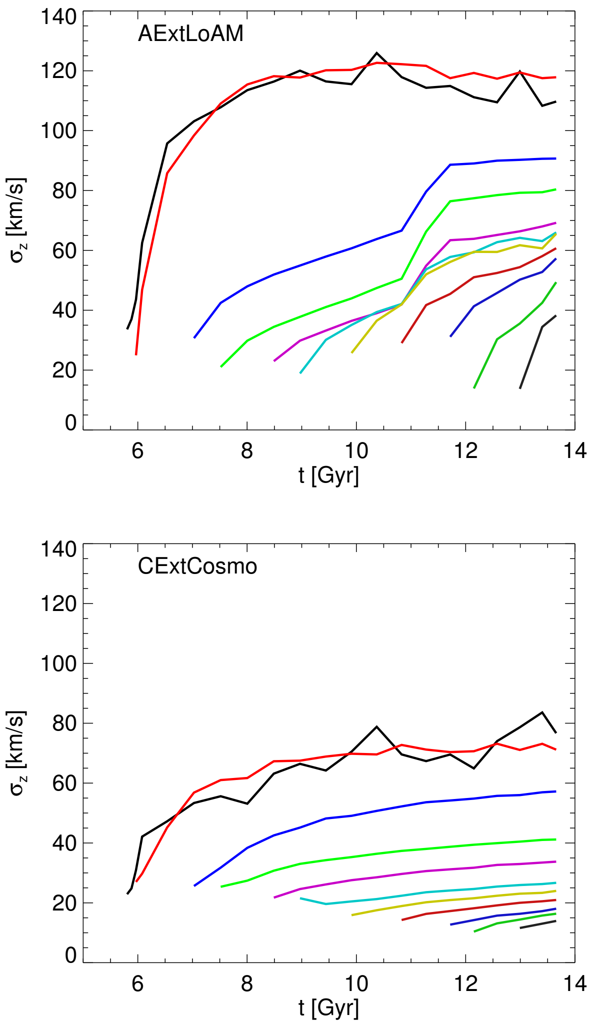

Figure 3.13: Vertical velocity dispersions $\sigma_z(t)$ as a function of time for coeval populations in models AExtLoAM (top) and CExtCosmo (bottom). See Fig. 3.4 for an explanation of how these plots are constructed.

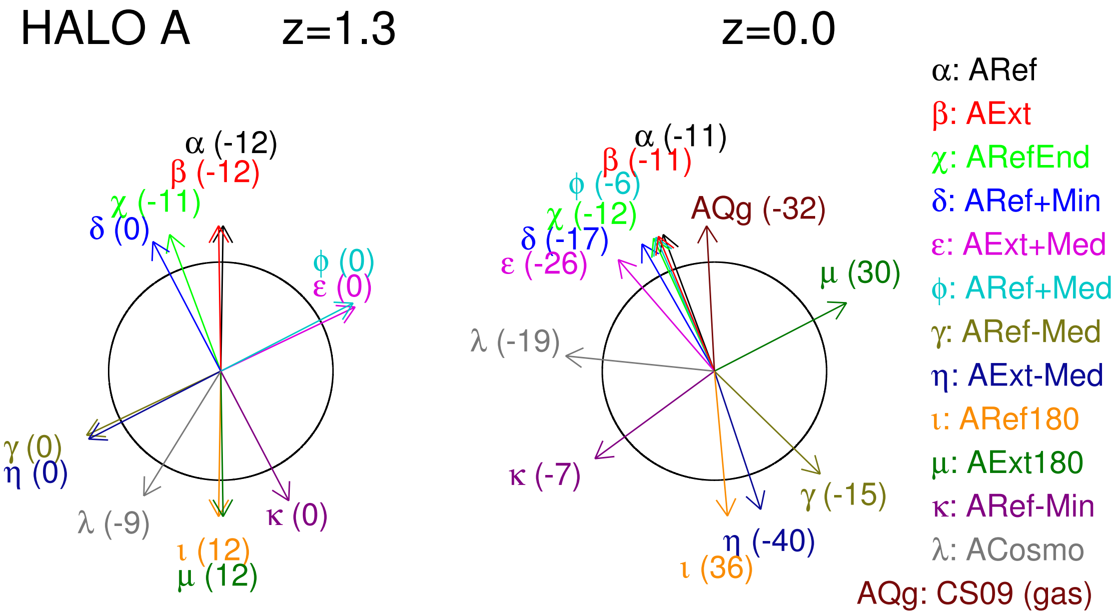

Figure 3.14: Visualization of reorientation in halo A for models with initial orientations (approximately) in the plane perpendicular to the major axis of the halo potential. Left are initial orientations at $z = 1.3$, right are mass-weighted mean orientations of the stellar systems at $z = 0$. The coordinate system is static and was fixed to be perpendicular to the major axis of the halo potential at $z = 1.3$ and to have the initial orientation of model ARef at 0 degrees. The Greek letters and colours code the models and the numbers in brackets indicate the angle between the orientation and the plane in degrees. AQg stands for the orientation of the angular momentum of the gas at $R = 30 - 100\,\mathrm{kpc}$ at $z = 0$ in the simulation of CS09.

(e.g. Jenkins & Binney, 1990), so that younger discs are thinner. Disc heating is strongly enhanced by bars, as was recently also discussed by Saha et al. (2010). Additionally, heating is strongest for the old bulge populations and the birth velocity dispersion of stars in our simulations always decreases with time, which adds to the age-velocity dispersion relation (see also House et al., 2011). Higher angular momentum content leads to more extended discs and larger truncation radii. The latter also increase with faster cooling. Bars form, if, at fixed other parameters, the mass exceeds or the angular momentum falls below (due to loss or initial lack) a stability limit consistent with standard stability criterions for bar formation (see Binney & Tremaine, 2008 §6.3). (Pseudo-)Bulges are enhanced by bar-induced gas inflows.

3.6 | (Re)Orientations of discs

So far we have paid relatively little attention to the influence of the initial orientation of the angular momentum vector of the rotating gas sphere. We have shown that it plays a crucial role in angular momentum loss of the infalling gas (Fig. 3.6). Moreover, Fig. 3.7 revealed that this orientation is not fixed, rather different models can undergo very different amounts of reorientation. Model ARef and many others, which we used to study the influence of

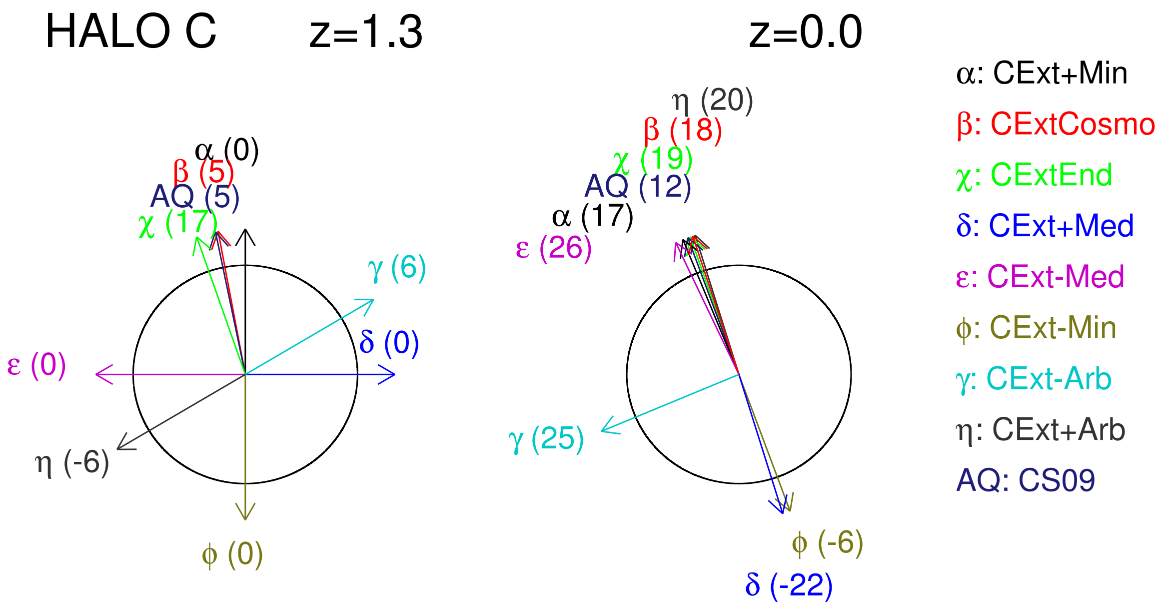

Figure 3.15: As Fig. 3.14, but for models in halo C. The initial orientation of model CExt+Min is at 0 degrees. AQ stands for the disc in halo C of CS09.

parameters, were initially oriented parallel to the angular momentum vector of the dark matter within 300 kpc. This orientation was chosen as it yielded the coldest discs in several test simulations and showed an amount of reorientation that is similar to that of the dark halo itself from $z = 1.3$ to $z = 0.0$. In terms of the principal axes of the triaxial potential ellipsoid, the orientation of ARef is close to the minor axis, but produces slightly better results than an exact alignment with this axis.

In halo C, this setup failed. The dark matter angular momentum is poorly aligned with the principal axes and thus the plane defined by this orientation contains strong variations of the vertical gravitational force, preventing quiescent disc formation. However, orientations close to the minor axis proved to work well, underlining that the influence of the shape of the halo potential is stronger than the influence of its angular momentum. This finding is consistent with previous findings that discs in cosmological simulations preferentially align with the minor axis of the halo (Bailin et al., 2005). In this section, we therefore explore which orientations in haloes A and C are capable of producing thin discs. We do so in subsections, first discussing (re)orientations in minor and medium orientation models and the effects of reorientation on kinematics. Then we discuss major/intermediate orientation models, the structure of peculiar models and how reorientation shapes the potential.

3.6.1 | Models with orientations perpendicular to the major axis

As both haloes are close to prolate at $z = 1.3$, we start by exploring orientations which lie in or close to the plane perpendicular to the major axis of the halo potential. We illustrate the findings for halo A in Fig. 3.14, where in the left half we show the initial orientations of the angular momentum of the gas sphere and in the right half we show the orientations of the angular momentum of all the stars that have formed by $z = 0$. The coordinate system is fixed and identical in both halves. Zero degrees is defined by the initial orientation of ARef and the numbers in brackets behind the model numbers indicate the angles by which the orientations are offset from the plane in degrees. Initially, all these models are within 12 degrees of this plane. We show models aligned with the dark angular momentum within 300 kpc (ARef, AExt), 180 degrees offset from this (ARef180, AExt180), aligned with the minor axis (ARef+Min, ARef-Min) and with the medium axis (ARef+Med, AExt+Med, ARef-Med, AExt-Med) and aligned with the final orientation of model ARef (ARefEnd).

The final orientations of the galaxies in halo A show a clear crowding of models around the minor axis. All models with orientations between ARef+Min and ARef+Med end up within ~ 20 degrees from the reference model ARef and close to the plane perpendicular to the initial potential major axis. Fig. 3.7 shows a continuous reorientation of a total of 30 degrees for ARef. ARef+Med, however, first turns by ~ 90 degrees before also showing a small, continuous reorientation. Thus these models all seem to adjust to the ‘correct’ orientation and then evolve rather quiescently. Models with different parameters sharing the same initial orientation show very similar final orientations as illustrated by models ARef/AExt and ARef+Med/AExt+Med.

All the other models, however, end up with significantly different orientations, and there is no clear correlation between their initial and final orientation. ARef180 seems to end up close to its original orientation, but it flips by almost 120 degrees before slowly returning. If dark matter influenced the evolution only through its global potential, there should be no difference between two orientations differing by 180 degrees, which is clearly not the case, so that halo rotation and transfer of angular momentum between the baryons and the dark matter must play a role in the described processes. Comparing AExt180 and ARef180, which share initial orientation, we detect a final offset of more than 90 degrees. A smaller, but significant difference exists also between AExt-Med and ARef-Med. In Fig. 3.7, one can see that the initial turn of ARef180 by ~ 120 degrees is also seen in AExt180, where this process takes longer. The model then stabilizes in this orientation. Model ARef-Med, which starts from a medium orientation, shows continual and strong reorientation.

In Fig. 3.15, we illustrate the situation in halo C. Zero degrees is defined by the initial orientation of CExt+Min, which was aligned with the halo minor axis. CExt-Min is 180 degrees offset, CExt-Med and CExt+Med are aligned with the medium axis and CExtEnd is the final orientation of CExt+Min. CExt+Arb and CExt-Arb resulted from an error in the setup but are useful for this analysis, AQ marks the orientation of the disc in the cosmological galaxy formation simulations of CS09. Finally, CExtCosmo uses the $z = 1.3$ cosmological orientation as an initial condition. We see that the cosmological disc is well aligned with the minor axis, around which many models again crowd at $z = 0$, in this case all models with orientations between those of CExt+Arb and CExt+Min in the initial conditions. CExt-Min and CExt+Med indicate that, for halo C, the direction 180 degrees offset from the ‘best disc’ orientation is also a preferred orientation at $z = 0$. Among the models presented, only CExt-Arb ends up in a significantly different orientation.

3.6.2 | How reorientation affects kinematics

In the previous subsection we have shown that the orientation of the angular momentum of infalling gas can undergo significant changes. In the previous section we have already shown

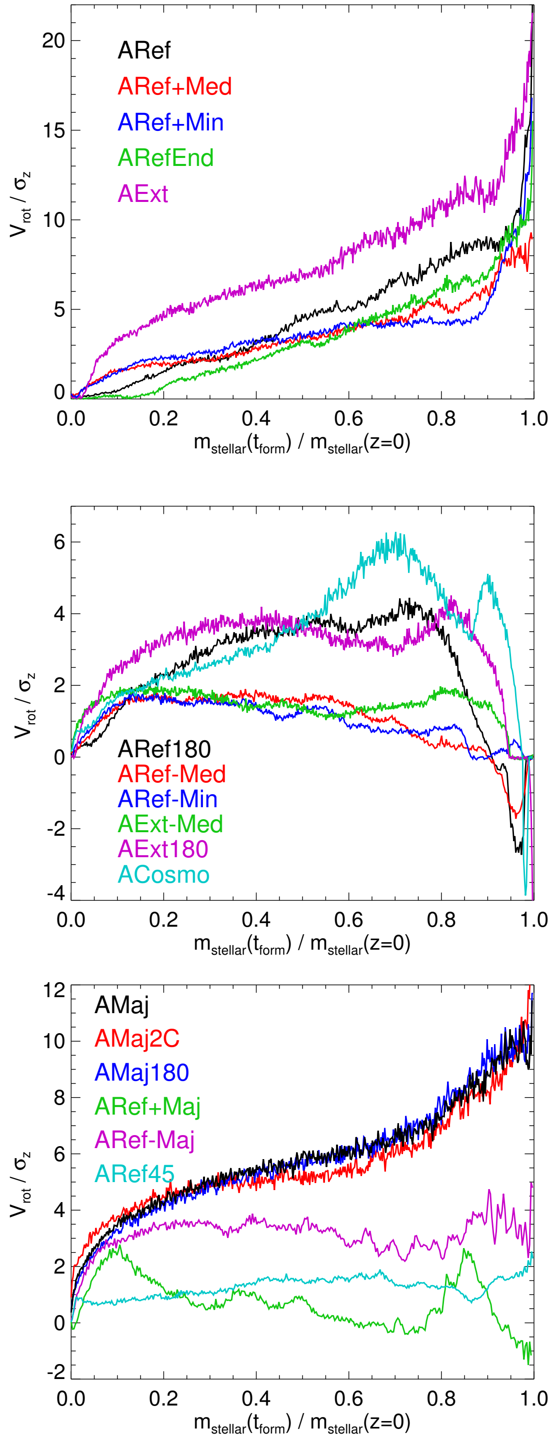

Figure 3.16: Rotation-to dispersion ratios as defined in Fig. 3.4, but now for models with different orientation. A negative ratio indicates a component that is counter-rotating with respect to the total stellar angular momentum. *Top panel*: Models perpendicular to the major axis ending up in 'disc orientation' and disc-like rotation: ARef+Med, ARef, ARef+Min, ARefEnd and AExt. *Middle panel*: Models perpendicular to the major axis not showing a continuous disc formation, but all showing significant reorientation and developing counter-rotating components: ARef-Med, ARef180, ARef-Min, AExt-Med, AExt180. *Bottom panel*: Models parallel to the major axis: ARef+Maj, ARef-Maj, AMaj2C, AMaj, AMaj180 and model ARef45.

that this leads to loss of angular momentum. Here we study the effects of these processes on the kinematics of the models.

In Fig. 3.16 we show rotation-to-dispersion ratios for the halo A models ending up close to the ARef final orientation (top panel) and for the other models of Fig. 3.14 (middle panel). In both panels, the models with longer cooling times show higher $V_{\rm rot}/\sigma_z$ for the discy populations, as was discussed in the previous section. There is, however, a clear dichotomy between the two panels. All models in the upper panel show a monotonic increase in $V_{\rm rot}/\sigma_z$ from old to young stars, indicating that these are continuously forming discs. It also shows that ARef has the coldest disc population of the models sharing the same parameters, presumably because it also shows the smallest amount of reorientation. However, ARef+Min and ARef+Med, which start exactly in the plane perpendicular to the major axis show a smaller bulge population than ARef and ARefEnd, which start with a small misalignment to this plane.

The models depicted in the middle panel do not end up close to the preferred disc orientation and all show counter-rotating young populations indicating the infall of gas misaligned with the rotation of the stellar object at late times and none of these objects show thin disc populations of stars.

Circularity distributions for ARef180 and ARef-Min are shown in Fig. 3.11. The compact, barred disc of ARef-Min has lost its $\epsilon \sim 1$ peak and shows a wide, asymmetric distribution peaking at $\epsilon \sim 0.6$. It has a strongly enhanced counter-rotating population compared to ARef. ARef180, in contrast, shows only a mildly diminished disc peak compared to ARef, but features a distinct, small counter-rotating disc peak at $\epsilon \sim (-1)$.

In Fig. 3.17 we analyze the radial profiles of vertical velocity dispersion $\sigma_z(R)$ for several of the models just discussed. Unlike ARef, which shows a realistically declining $\sigma_z(R)$, there are several models showing an outward increase in $\sigma_z(R)$ after a drop at inner radii, most strikingly ARef180. According to Fig. 3.7, ARef180 shows the strongest reorientation during its evolution and according to Fig. 3.6 also the strongest losses of angular momentum of all models, whereas ARef shows only weak reorientation. This trend is confirmed by AExt180 and ARef+Med, which are intermediate between ARef and ARef180 in terms of $\sigma_z(R)$ flaring and reorientation. ARef-Med, which shows the strongest angular momentum losses and continuously strong reorientation, displays very high $\sigma_z(R)$ at all radii and mild flaring. This also strengthens the conclusion that these two processes lead to high velocity dispersions in the final systems, especially in the outskirts.

In the top panel of Fig. 3.18 we plot rotation-to-dispersion ratios for all models in halo C that end up with a thin disc population of stars ($V/\sigma_z > 5$ and V/σ_z decreasing monotonically with age). CExtEnd and CExtCosmo, the orientations motivated by the cosmological model and the final orientation of CExt+Min, produce the coldest discs. Similarly to AExt in halo A, these models are slightly offset from the minor orientation. CExt+Min, the minor orientation run, still has a better disc than CExt-Min, which starts and ends at an angle of 180 degrees. Unlike in halo A, this orientation still produces a disc. The medium orientation runs CExt-Med and CExt+Med, which also start and end up at an angle of 180 degrees, produce slightly worse discs due to the effects of reorientation. CExt+Arb, which starts from an orientation about 120 degrees offset from CExt+Min, also produces a disc in the preferred final direction. CExt-Arb is the only model not following the trend. The orientation changes strongly and the model results in a thick disc surrounded by misaligned components, each resulting from a different formation phase, as indicated in the lower panel of Fig. 3.18.

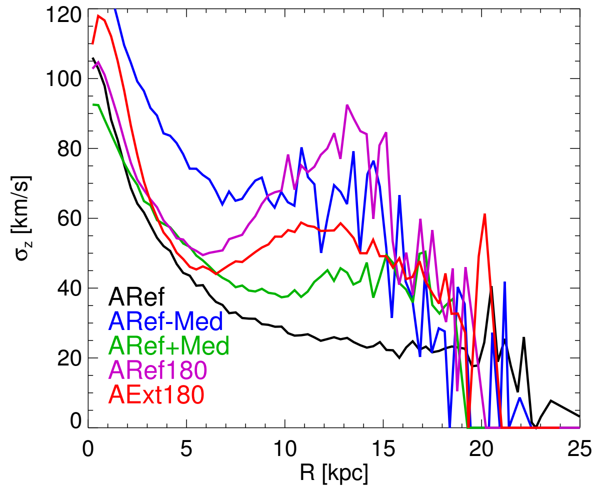

Figure 3.17: Vertical velocity dispersions $\sigma_z(R)$ as a function of disc radius R in the models ARef+Med, ARef, ARef180, ARef+Min, ARefEnd.

3.6.3 | Models with major and intermediate initial orientations

Until now, we have focused only on models that start (nearly) perpendicular to the major axis. As already discussed in the previous section, AMaj2C, which starts aligned with the major axis, also produces a relatively small, thin and exponential disc. As can be seen in the bottom panel of Fig. 3.16, the same is true for AMaj, which employs slower cooling, but produces only a slightly colder disc. It was shown in Fig. 3.5 that the infall and star formation timescales are determined by angular momentum and cooling time. For these models with low angular momentum, star formation is shifted to earlier times, and consequently the stellar populations are subject to disc heating over a longer period. As a result the final difference in σ_z is small. AMaj180, which uses the same parameters as AMaj, but is initially 180 degrees offset, produces a disc with almost the same characteristics as AMaj. All these models reorient away from the initial major axis, but by different amounts, ~ 50 degrees for AMaj2C and AMaj, which end up only ~ 5 degrees offset, and ~ 100 degrees for AMaj180. They do not end up near the minor axis, but do not seem to be affected much by reorientation. Probably this is because their formation timescales are small and they are compact. Misalignments typically happen for material that comes in late at large radii and is thus hardly affected by the potential of the inner disc.

As alluded to in the previous section, the plane defined by the major axis orientation in almost prolate systems has an almost axisymmetric potential and is thus advantageous for our models compared to the minor axis orientation. However, models ARef+Maj and ARef-Maj, which start with significantly more angular momentum than AMaj/AMaj180 do not produce disc-like objects. This is also true for ARef45, which starts from an unfavorable orientation half-way between minor and major axes, as can be seen in the bottom panel of Fig. 3.16. The reason for this failure is misalignments that develop between gas infall at early and late times, destroying an initial disc.

In halo C, the situation is similar. C+Maj, which starts in major axis orientation with the same parameters as AMaj, also produces a disc. It also undergoes reorientation away from

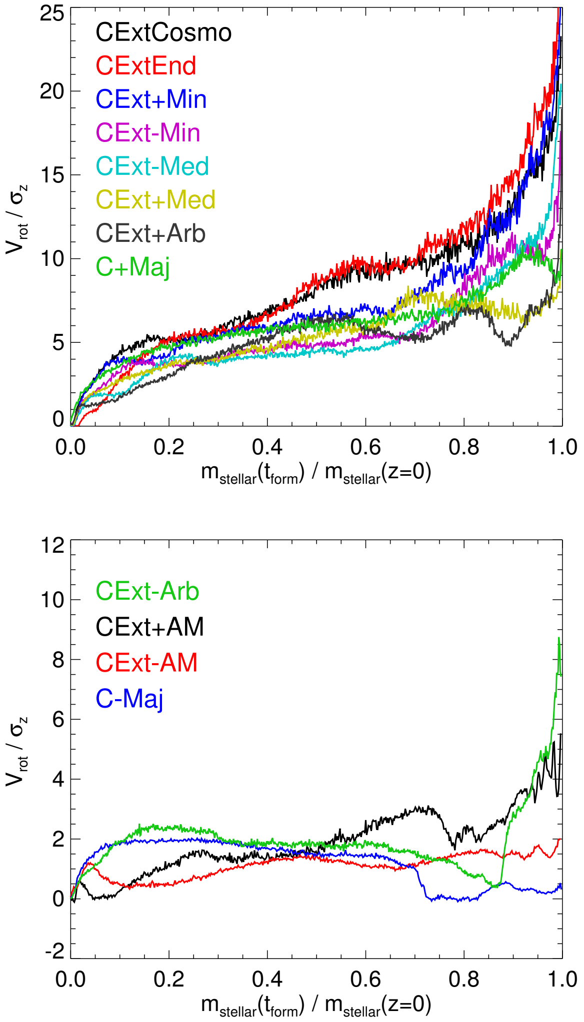

Figure 3.18: Rotation-to dispersion ratios as defined in Fig. 3.4, but now for models in halo C. *Top panel*: Models producing discs: CExt+Min, C+Maj, CExt-Min, CExt-Med, CExt+Med, CExtEnd, CExtCosmo, CExt+Arb. *Bottom panel*: Other models in halo C: CExt+AM, CExt-AM, C-Maj, CExt-Arb.

the major axis and ends up at an angle ~ 30 degrees from the final orientation of CExt+Min. However, C-Maj, which has an initial gas angular momentum orientation 180 degrees apart from C+Maj and a more extended initial radius and thus higher angular momentum, does not produce a nice disc, showing outer misalignments as in ARef+Maj. This model shows that misalignments are common for initial orientations parallel to the major halo axis, also for medium angular momentum content.

The model CExt+AM is initially aligned with the angular momentum of the halo at $R < 300\ \mathrm{kpc}$, which is at an angle of ~ 45 degrees to the major axis. This is why the model experiences problems similar to that in ARef45. The same is true for CExt-AM, which starts at an angle of 180 degrees to CExt+AM.

3.6.4 | The structure of peculiar models

Although our models were designed to produce discs, not all of them end up as such, as we have shown above. Here we briefly analyze the structure of three of those models in more detail.

ARef-Min is one of the models, which start oriented perpendicular to the major axis and show continuous, strong reorientation, which leads to strong angular momentum losses and high velocity dispersion (see middle panel in Fig. 3.16). We have included surface density projections of ARef-Min in Fig. 3.8 (fourth row). Due to the angular momentum losses the resulting disc is compact, barred and thick with an exponential scale-height of $h_z = 1.3\ \mathrm{kpc}$ (see Fig. 3.10). Its exponential-like radial profile is very steep with $R_d \sim 1.8\ \mathrm{kpc}$ as shown in Fig. 3.9. The galaxy has a high bulge fraction, $D/B \sim 1$. Even at $z = 0$ the remaining gas is concentrated in the central bulge and does not show a disc structure. Also the stellar disc structure is mostly bar-like and is surrounded by a spheroidal star distribution. Its circularity distribution (Fig. 3.11) shows a wide, asymmetric peak at $\epsilon \sim 0.6$. The system might be classified as a barred, fast rotating early-type galaxy applying a classification scheme as used for the ATLAS^{3D} survey (Emsellem et al., 2011).

CExt+AM represents the models starting with intermediate initial orientations. In the fifth row of Fig. 3.8, we show its $z = 0$ surface density projections. The gas lives in a perfect disc, whereas the stellar disc shows two regions: a dominant bulge-like central structure, which is elongated perpendicular to the gas disc, and outer regions dominated by rings and separated from the centre by a drop in surface density around $R \sim 9\ \mathrm{kpc}$ (see Fig. 3.9). The vertical profile at $R = 5\ \mathrm{kpc}$ can be fit by a thick exponential with $h_z \sim 3.5\ \mathrm{kpc}$ (Fig. 3.10). Fig. 3.18 reveals several dips and peaks in $V_{\mathrm{rot}}/\sigma_z$ during the formation of the object indicating several misaligned populations, which prevent the formation of a cold disc. The system bears some resemblance with polar bulge galaxies (see e.g. Corsini et al., 2012).

Models starting in major orientations and developing strong misalignments are represented by C-Maj, the surface density projections of which are shown in the bottom row of Fig. 3.8. Two stellar components at an angle ~ 60 degrees are clearly visible. Consequently, the circularity distribution in Fig. 3.11 shows two distinct peaks at $\epsilon \sim 0.85$ and ~ 0.25. The latter represents the ring which forms at late times (see Fig. 3.18). In the gas surface density projections, flows are visible, which channel the material to the centre. The vertical profile at $R = 5\ \mathrm{kpc}$ (Fig. 3.10) is flat for $|z| < 3.7\ \mathrm{kpc}$ before dropping exponentially, whereas the radial profile (Fig. 3.9) resembles a double-exponential with a dominant central component at $R < 5\ \mathrm{kpc}$ and rings at $R > 10\ \mathrm{kpc}$. These properties of the model reveal a similarity to polar ring galaxies (Whitmore et al., 1990).

3.6.5 | How reorientation affects the shape of the potential

In the context of the results already presented in this section, the question arises, how the shape of the final gravitational potential differs between models. Clearly, in central regions dominated by a disc, the potential is found to be oblate. Due to the interaction with the forming disc, the dark matter halo becomes less triaxial, in agreement with the results of Kazantzidis et al. (2010). Moreover, the initial triaxiality of the halo, which in the dark-matter-only simulations shows little reorientation, is still imprinted at outer, halo-dominated radii. Consequently, for models such as AExt or CExtCosmo, the gas angular momentum of which was initially aligned with the minor potential axis, the final disc axis is well aligned with the final minor axis of the potential at all radii. For disc models which end up in preferred disc orientation, but started with a different initial orientation, such as ARef+Med or CExt+Arb, the situation is similar, yet the potential contours are less flattened, consistent with the fact that these discs are thicker. For models, where the final stellar angular momentum does not align with the preferred disc orientation, such as ARef-Med or CExt-Arb, there is also no alignment between the final potential ellipsoids at inner and outer radii. This is also true for compact disc models, which formed from gas which was initially aligned with the major axis. The discs, which are finally closest to an alignment with the major axis of the outer potential are AMaj and AMaj2C with an offset angle of ~ 30 degrees.

3.6.6 | Summary

In conclusion, we have shown that each of the two haloes we studied shows a preferred orientation for discs, which roughly agrees with the minor axis of the inner halo potential, in agreement with the results of Bailin et al. (2005) for fully cosmological simulations. However, a flip of the initial angular momentum vector by 180 degrees produces a slightly worse (halo C) or unsuitable (halo A) orientation for a forming disc. This shows that it is not the shape of the potential alone that determines the preferred orientation. Models with initial non-preferred angular momentum orientations tend to reorient to a preferred axis, producing thickened and flaring discs. In some cases, they fail to settle to a stable orientation and do not end up with significant discs. There is no obvious simple criterion to explain this dichotomy. Models starting with angular momentum parallel to the major halo axis also do not show a stable orientation. They form stable discs only if their angular momentum content is low, so that they rapidly form compact objects, which cannot be destroyed by reorientation, which misaligns inner and outer components. Realistic thin discs with continuously forming populations are thus only possible for initial orientations close to the halo minor axis. Models with initial orientations in between these cases are not capable of producing cold discs. Taking results of the previous sections into account, we have also shown that the orientations both of the central disc and of the outer gas can change by more than 90 degrees, despite the simple and coherent initial distributions of our gas components. This is also true for the angle between the components.

3.7 | Comparison to cosmological simulations

Until now, we have shown that, with our method, we are capable of introducing discs into Aquarius haloes A and C. Using the cosmological orientations of the discs at $z = 1.3$ in the simulations of CS09, we showed that for halo C the disc is in the ‘right place’, meaning that

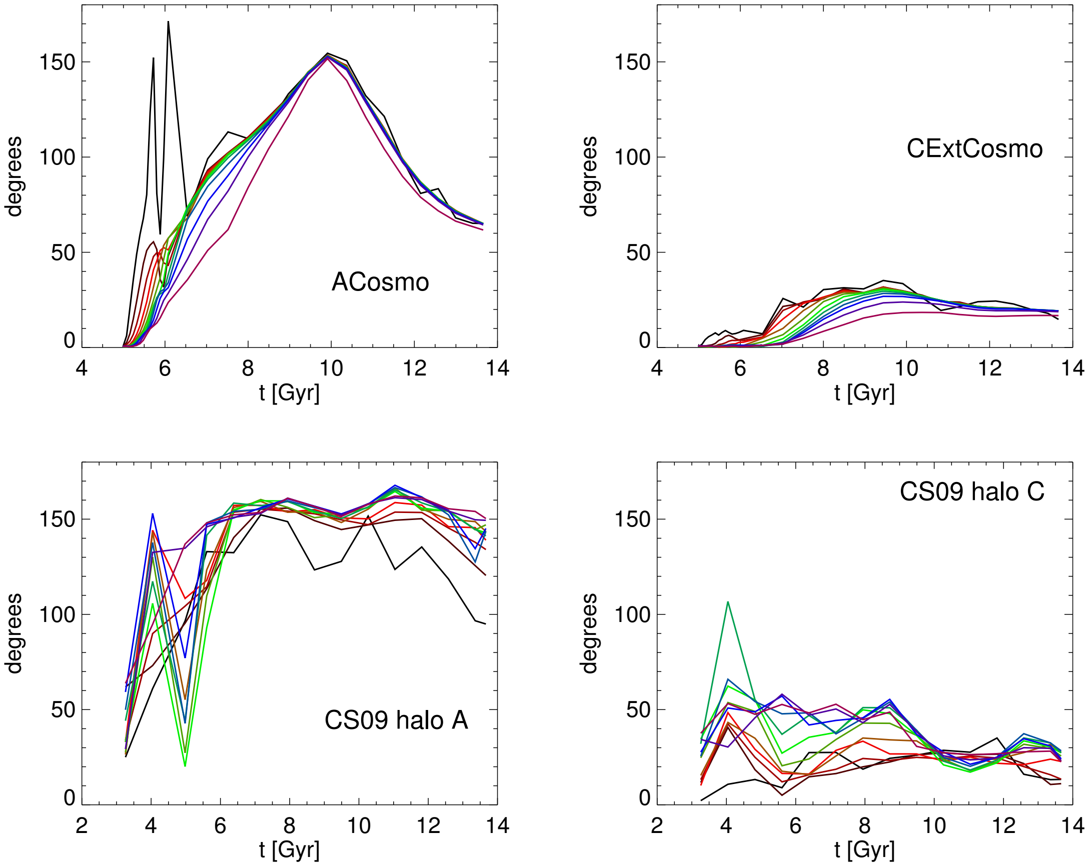

Figure 3.19: Orientation angle as a function of time for models ACosmo (top left) and CExtCosmo (top right). The initial gas sphere has been divided into 12 radial shells of $R_{\rm gas}/12$ width each. For each shell, the angle of the angular momentum vector $\mathbf{j_i}$(t) of all particles initially in shell *i* to the initial orientation is calculated at each output time t. The panels in the bottom row show the spin orientation in the same coordinate system for the gas content of 12 spatially *fixed* concentric shells of 10 kpc width for the A and C runs of CS09.

our model CExtCosmo, which starts with this orientation, produces a nice disc at $z = 0$. In halo A, the cosmological disc is in the ‘wrong place’, i.e. our model ACosmo, starting in the corresponding orientation, fails to produce a nice disc. We have identified reorientation of the angular momentum of infalling material and the angular momentum losses and misalignments connected to this phenomenon as the key factors in the failure of many of our models to build substantial discs. CS09 also identified misaligned infall of gas as the problem destroying the existing disc structure in their resimulation of halo A.

In this section we would therefore like to analyze the reorientation of gas in the runs of CS09 and compare them to our own. In these cosmological simulations, the inflow of gas is continuous and more complex than in ours, it is not desirable to define fixed gas populations by their radial position at a certain time. It is more instructive to follow, how the angular momentum of gas evolves in fixed radial shells of 10 kpc width as is shown in Fig. 3.19, where we compare the reorientation in models ACosmo and CExtCosmo to the reorientation in models A and C from CS09.

ACosmo, as depicted in the top left panel of Fig. 3.19, shows strong and continuous reorientation for all baryons, gaseous and stellar. Reorientation is slightly delayed for the outer shells compared to the inner, but the resulting misalignments are small compared to the models discussed in the previous section. After $t \sim 9~\mathrm{Gyr}$, there is no overall detectable misalignment among the initially defined shells, although there is a small counter-rotating component as shown in Fig. 3.16, which originates from temporary misalignments and continuous reorientation. As shown in Fig. 3.14, ACosmo is ~ 45 degrees offset from the orientation of most of the disc models in halo A at $z = 0$. During its evolution, it evolves towards this orientation until $t \sim 11~\mathrm{Gyr}$, when it is only ~ 20 degrees offset and then starts to turn away again.

For the fully cosmological model we start the analysis at $z = 2$ (lower left panel). The reference orientation is the one of the stars within $R < 10~\mathrm{kpc}$ at $z = 1.3$, which is the initial orientation of ACosmo. At $z = 2$, the orientation of the stellar angular momentum differs by less than 10 degrees. Even at $z = 2$ the gas out to $R = 120~\mathrm{kpc}$ is not well aligned with the galaxy. Until $z \sim 1$, there is a clear misaligning process. From then on, gas in all shells shows an orientation ~ 150 degrees offset from that of the galaxy at $z = 1.3$. The new orientation is also depicted in Fig. 3.14. It only differs by ~ 20 degrees from the initial orientation of model ARef, which explains why this orientation yielded the best results. The offset is caused by a stronger misalignment with the plane perpendicular to the major axis.

The strong reorientation of the gas is also depicted in Fig. 10 of CS09, where the evolution of the angle between the stellar and the gas components within 27 comoving kpc is plotted. The fact that the components become aligned again at $z = 0$ indicates that the inner stellar component reorients to the same direction, but with a delay. Moreover, the central gas components (black lines in Fig. 3.19) are also offset from the outer gas by up to ~ 50 degrees.

The new orientation of the (outer) gas is also within ~ 20 degrees of the orientation that model ACosmo shows at $t \sim 10.5~\mathrm{Gyr}$, but at $z = 0$ the orientations differ by ~ 70 degrees. This is due to the continual reorientation in model ACosmo. While the reorientation process is qualitatively similar in these models, the final orientation of the galaxy is also dependent on the details of its assembly, as seen above for non-disc models with identical initial orientation but otherwise different parameters such as ARef180 and AExt180.

For halo C the situation is less complicated. The orientation of the gas in the CS09 model, which was used as an initial condition for our model CExtCosmo at $z = 1.3$, behaves

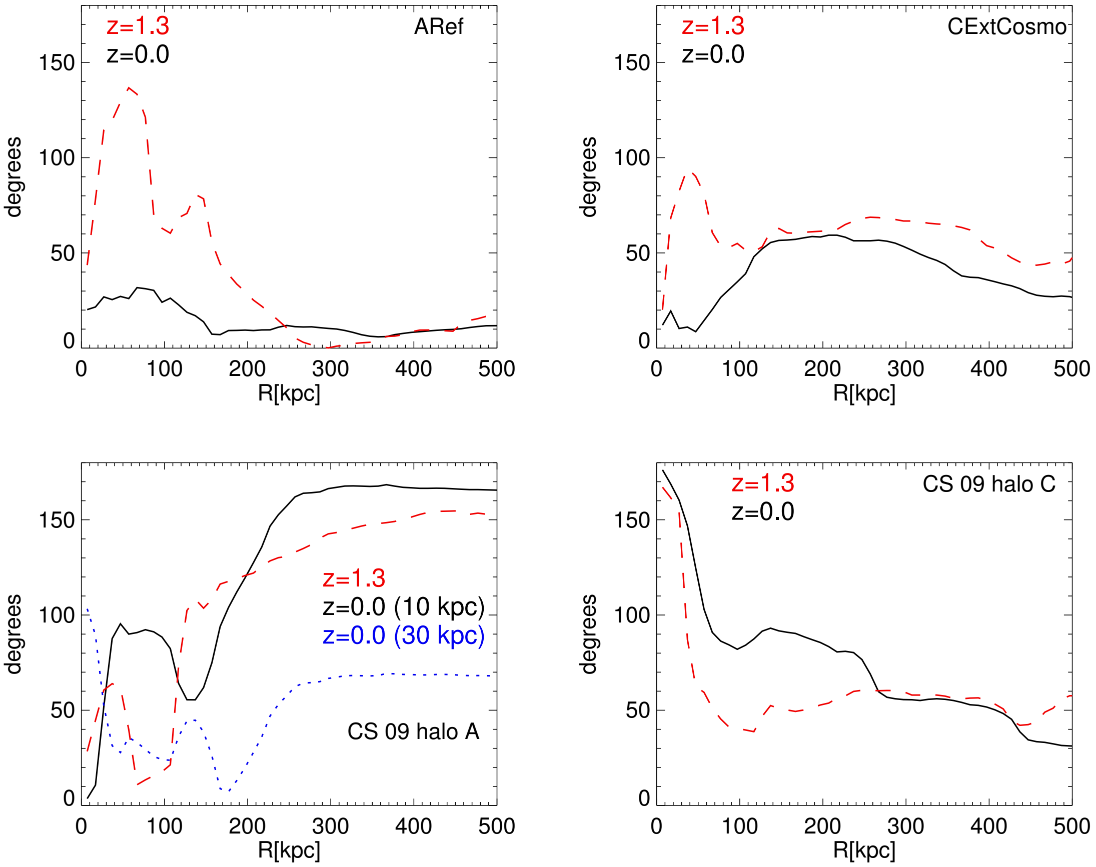

Figure 3.20: The angle between the angular momentum vector of all stars within $R < 10\,\mathrm{kpc}$ and the angular momentum vector of all dark matter within R as a function of R at $z = 1.3$ and $z = 0.0$ for models ARef (top left), CExtCosmo (top right) and the results of CS09 for haloes A (bottom left) and C (bottom right). The effect of varying the radius that defines the galaxy for halo A is indicated in the bottom left panel, where the blue line is for a 30 kpc galaxy radius. For all other models this radius definition plays a minor role.

very similarly to CExtCosmo. It shows an overall reorientation by the same amount (~ 20 degrees) and comparatively small misalignments, < 45 degrees.

In Fig. 3.20 we compare the orientation of the galaxy (all stars within 10 kpc) in a given model to the orientation of the angular momentum of the dark matter (including subhaloes) within R as a function of radius R. Model ARef is initially set up to be aligned with the dark matter within 300 kpc. As can be seen, this orientation is not, however, aligned with the dark matter within 200 kpc, but the stars and dark matter become aligned by $z = 0$ where the alignment is, in fact, better than 30 degrees for all radii $R < 500\ \mathrm{kpc}$.

In the fully cosmological halo A model, the galaxy is aligned with the dark matter within $R \sim 100\ \mathrm{kpc}$ at $z = 1.3$, but is strongly misaligned otherwise, especially at $R > 150\ \mathrm{kpc}$, where the angle reaches ~ 150 degrees. At $z = 0$, there is no disc and thus the orientation of the galaxy is not well defined. Considering stars within 10 or 30 kpc yields different results as indicated by the black and blue lines. The stars at $R < 10\ \mathrm{kpc}$ are well-aligned with the central dark halo, whereas the stars at $10 < R/\mathrm{kpc} < 30$ are not. Both populations are misaligned with the dark matter outside $R \sim 50\ \mathrm{kpc}$, but the misalignment is significantly smaller for the stars at $10 < R/\mathrm{kpc} < 30$.

For halo C the picture is different. Model CExtCosmo is initially misaligned with the dark matter angular momentum by an angle of ~ 50 degrees. This hardly changes by $z = 0$, when the inner 100 kpc have become more aligned, but the outer parts remain unchanged. In the fully cosmological run the situation is strikingly different. In the inner $\sim 50\ \mathrm{kpc}$, the dark matter both at $z = 1.3$ and at $z = 0.0$ is strongly misaligned with the galaxy, almost 180 degrees near the centre. This explains why there is no clear correlation between dark matter and galaxy angular momenta in our models based on halo C.

In summary, there are no large discrepancies between our models and fully cosmological galaxy formation simulations within the same haloes. In the absence of any destructive events, such as major mergers, a disc will survive over cosmological timescales if it has formed in the preferred orientation for its halo. As we showed, this orientation does not depend on the potential alone (Section 3.6), nor is there a clear correlation with the angular momentum of the halo (this section). The orientations of the halo principal axes and the halo spin axis can change with time (see Vera-Ciro et al., 2011 and Bett & Frenk, 2012 respectively) and so, apparently, can the preferred disc orientation, as is clear from the halo A run of CS09, where a disc is destroyed by inflowing matter oriented in a new preferred direction. Despite this, we were able to find initial gas setups which lead to thin discs in this halo. For halo C there is no such orientation change and thus both our own and the fully cosmological models produce surviving discs.

3.8 | Conclusions

We have presented a series of simulations of idealized SPH models for the formation and evolution of galactic discs within fully-cosmological ΛCDM haloes. At $z = 1.3$, we add rotating spheres of hot gas in approximate hydrostatic equilibrium to two dark matter haloes from the Aquarius Project (Springel et al., 2008). A parametrized cooling law and standard prescriptions for star formation allow us to study the evolution of the combined baryon+CDM systems until $z = 0$. We study models with different orientations and amounts of baryonic initial angular momentum, different cooling timescales and different density profiles. This allows us to determine favorable and non-favorable conditions for the formation and survival of discs.

Clearly, such simulations are not full models for the formation of disc galaxies. However, they allow us to study processes relevant to the formation of discs within triaxial and realistically evolving dark matter haloes, and hence explore the conditions under which massive discs can exist in ΛCDM haloes. This should help us understand the failure or success of various fully cosmological simulations of disc galaxy formation, which still suffer from a multitude of uncertainties (e.g. Governato et al., 2007; Guedes et al., 2011, CS09, Scannapieco et al., 2012). A particular problem may be that these simulations tend to produce overly old stellar populations (see the discussion in Aumer & Binney, 2009) and thus to under-predict the stellar mass formed since $z \sim 1$, the epoch generally thought to be best suited for disc formation due to the absence of major mergers at such late times. Our models are unable to reproduce full star formation histories, but yield interesting insights into galaxy formation at relatively recent times.

Our setup has an inherent initial discrepancy between the triaxial, substructured and dynamically growing halo and the rotating quasi-equilibrium gas sphere. This leads to an initial phase in which the gas adjusts to the potential. Thereafter, it loses angular momentum to the dark matter as it cools to the centre and transforms the total central potential, and thus also the halo, into a more axisymmetric configuration capable of hosting a stable disc. We show that the shorter the timescale of this transformation, the more destructive the effect on the forming disc, and thus the more dominant the resulting bulge and thick disc components. Haloes are expected to be near prolate after major mergers (e.g. Romano-Díaz et al., 2009), before most of the stellar mass assembles into discs, so this process of bulge formation during halo transformation is not unrealistic. Romano-Diaz et al. also report the initial formation of an asymmetric, bar-unstable disc in their fully cosmological simulations. Only if we align the initial angular momentum of the gas sphere with the major axis of the potential, can we suppress this destructive process. However, the transformation from a prolate potential to an oblate disc potential triggers misalignments between inner and outer baryonic components, which hinders disc survival.

We have shown that our models are capable of producing, and thus that the haloes in consideration are capable of hosting, discs with realistic structural and kinematic properties, which unlike in most cosmological simulations show realistic disc-to-bulge mass ratios $D/B > 4$. As has been shown previously (Scannapieco et al., 2010), structural and kinematic decompositions yield strongly differing results, with structural values exceeding kinematic ones by factors of a few. We show that our discs have rotation-to-dispersion ratios $V_{\rm rot}/\sigma_z$ monotonically decreasing with increasing age, which arises from continuous disc heating due to substructures and a monotonic decrease in birth velocity dispersion connected to the transformation of the central potential. Due to limitations in resolution, our simulations are not capable of producing realistic young thin stellar discs with $\sigma_z < 10{\rm kms}^{-1}$ (see also House et al., 2011), but they agree qualitatively with age-velocity dispersion relations for the solar neighborhood (Holmberg et al., 2009; Aumer & Binney, 2009). Our discs show truncations, which move outward with time and the radius of which increases with decreasing formation timescale and increasing angular momentum content.

We find that the slower the formation of a model galaxy, the colder and more dominant is the final disc. This is the result of the combined effects of the suppression of bulge formation during potential sphericalization and of continuous disc heating being less efficient for younger populations. Bars develop in our model discs if their surface density is enhanced by a higher total mass or lower total angular momentum. They strongly increase disc heating (see Saha et al., 2010), enhance the bulge fraction and produce prominent ring structures outside the bar regions (see Athanassoula, 1992), thus lowering the resulting $V_{\rm rot}/\sigma_z$ by factors of a few.

We show that the most stable, most extended and coldest discs form from a gas angular momentum orientation that is aligned with the minor axis of the inner halo, as had been previously found in cosmological simulations by Bailin et al. (2005). Out of the two such orientations given by the halo (180 degrees apart), one is clearly preferred. For one of our two haloes, the preferred direction is determined by the angular momentum of the outer halo in the initial conditions. By the end of the simulation,all regions are (marginally) aligned with the central disc. The counter-rotating orientation is strongly disfavored and does not produce stable discs. For the second halo, there is no alignment between halo angular momentum and shape. The non-preferred minor axis orientation of the gas angular momentum is the one which makes the larger angle with the halo spin axis. Models with this initial orientation are able to host stable, yet thicker discs. In each halo we find a certain range of initial gas angular momentum orientations perpendicular to the halo major axis for which a reorientation of the baryonic spin vector to one of the stable orientations occurs with the disc thickening, but surviving. Models, where the gas angular momentum is initially aligned with the halo major axis can produce discs, but their orientation is not stable. Intermediate models cannot produce stable discs. Reorientation especially heats the outer, lower surface density parts of discs, where self-gravity is unable to keep the stellar orbits aligned. Compact, high surface density discs are significantly less heated by orientation changes.

As reorientation is common both for halo shapes (Vera-Ciro et al., 2011) and for halo angular momenta (Bett & Frenk, 2012), the preferred orientation will evolve with time in ΛCDM haloes. This is directly connected to the well-known phenomenon of misaligned matter infall during the assembly of haloes and galaxies (e.g. Quinn & Binney, 1992). However, in our models, the initial gas distribution is spherically symmetric and its angular momentum is aligned at all radii. Despite this, the orientations of outer and inner gas and of stellar discs and also the angle between these components change by more than 90 degrees in many cases. Misalignment is thus a consequence of strongly nonlinear dynamical interactions in the final stages of galaxy assembly, not just of evolving asymmetries in the cosmological context, which feeds halo growth.

Misaligned components are common in observed galaxies in the form of warps (Sancisi, 1976), polar rings (Whitmore et al., 1990), polar bulges (Corsini et al., 2012) or counter-rotating components in early-type galaxies (Krajnović et al., 2008). Misaligned cosmological infall has been identified as a cause for a variety of phenomena, such as the destruction of discs (CS09), the formation of polar discs (Brook et al., 2008) and the excitation of warps (Roškar et al., 2010). Interestingly, all of these phenomena also occur in our models. We qualitatively reproduce the misaligned infall found in the cosmological resimulation of halo A by CS09 starting from a spherical and coherently rotating gas distribution. The torques acting in our simulation must originate in the nonlinear structure of the dark halo, suggesting a mechanism different from the conclusions of Roškar et al. (2010), who found negligible influence of the dark halo torques in comparison to anisotropic cosmological infall.

All these processes of misalignment are associated with the loss of angular momentum (see also Roškar et al., 2010) and produce more compact, hotter objects. Thin extended discs can thus only form in stable orientations and thus in haloes for which the preferred disc orientation undergoes little temporal evolution. This conclusion is similar to that of Sales et al.

(2011), who found that discs form from the continuous accretion of material with coherently aligned angular momentum orientation and that misaligned accretion of gas tends to produce spheroids. The question arises, whether ΛCDM offers enough haloes which fulfill these conditions to explain the observed abundance of disc galaxies in the Universe. Sales et al. (2011) find a significant fraction of such disc-dominated systems in their model sample of galaxies, but the limitations of their simulations do not allow a full comparison with the statistical properties of observed samples. Semi-analytic models of galaxy formation (e.g. Guo et al., 2011) are helpful for studying galaxy populations, but they do not capture the role of misalignments and other dynamical details that, as we have shown, play a major role in galaxy evolution. It would be desirable to add proper treatment of these processes to the models, however, we are not able to offer straightforward prescriptions, as we are not capable of drawing general conclusions from the presented study of two haloes.

Considering our work and recent improvements in cosmological resimulations of individual galaxies (e.g. Guedes et al., 2011; Brook et al., 2012), realistic ΛCDM haloes appear to be capable of hosting realistic disc galaxies. However, more work is needed to understand whether the population of ΛCDM haloes agrees in detail with the observed population of galaxies.

4 | Towards a more realistic population of bright spiral galaxies in cosmological simulations [1]

4.1 | Abstract

We present an update to the multiphase smoothed particle hydrodynamics galaxy formation code by Scannapieco et al. We include a more elaborate treatment of the production of metals, cooling rates based on individual element abundances, and a scheme for the turbulent diffusion of metals. Our supernova feedback model now transfers energy to the inter-stellar medium (ISM) in kinetic and thermal form, and we include a prescription for the effects of radiation pressure from massive young stars on the ISM. We calibrate our new code on the well studied Aquarius haloes and then use it to simulate a sample of 16 galaxies with halo masses between 1×10^{11} and $3 \times 10^{12} M_{\odot}$. In general, the stellar masses of the sample agree well with the stellar mass to halo mass relation inferred from abundance matching techniques for redshifts $z = 0 - 4$. There is however a tendency to overproduce stars at $z > 4$ and to underproduce them at $z < 0.5$ in the least massive haloes. Overly high star formation rates (SFRs) at $z < 1$ for the most massive haloes are likely connected to the lack of active galactic nuclei feedback in our model. The simulated sample also shows reasonable agreement with observed SFRs, sizes, gas fractions and gas-phase metallicities at $z = 0 - 3$. Remaining discrepancies can be connected to deviations from predictions for star formation histories from abundance matching. At $z = 0$, the model galaxies show realistic morphologies, stellar surface density profiles, circular velocity curves and stellar metallicities, but overly flat metallicity gradients. 15 out of 16 of our galaxies contain disc components with kinematic disc fraction ranging between 15 and 65 $\%$. The disc fraction depends on the time of the last destructive merger or misaligned infall event. Considering the remaining shortcomings of our simulations we conclude that even higher kinematic disc fractions may be possible for Λ cold dark matter haloes with quiet merger histories, such as the Aquarius haloes.

---

[1] The results of this Chapter were published in almost identical form as Aumer et al. (2013a)

4.2 | Introduction

In the standard paradigm of cosmic structure formation, galaxies form through cooling and condensation of gas within dark matter (DM) haloes (White & Rees, 1978; Fall & Efstathiou, 1980). Collisionless N-body simulations of the DM component have been able to reproduce the observed large-scale structure of the Universe with high accuracy in the Λ cold dark matter (ΛCDM) version of this paradigm (Springel et al., 2006). Semi-analytic models relying on these simulations and simple analytical prescriptions for the baryonic component are capable of reproducing the detailed systematics of the galaxy population (Guo et al., 2011). To properly understand the complex dynamical interactions between gas, stars and DM in galaxies requires, however, cosmological hydrodynamical simulations.

The complexity of properly modelling the many baryonic astrophysical processes which play a role in the formation of galaxies has led to a long list of models over the last two decades (e.g. Navarro & White, 1994; Navarro & Steinmetz, 1997; Abadi et al., 2003; Governato et al., 2007; Scannapieco et al., 2009; Agertz et al., 2011). Despite significant recent progress (e.g. Sales et al., 2011; Guedes et al., 2011; Brook et al., 2012), these simulations continue to be plagued by a range of problems, with different codes often producing very different galaxies for the same initial conditions (Okamoto et al., 2005; Kereš et al., 2012; Scannapieco et al., 2012).

The formation of realistic disc galaxies has been shown to be especially problematic. The cooling and condensation of too much low-angular momentum gas (overcooling) and the loss of angular momentum from baryons to the DM have been a problem since the first efforts to simulate cosmological galaxy formation (Navarro & Benz, 1991). Once discs have formed, they have been shown to be susceptible to destruction by major mergers (Toomre & Toomre, 1972), by the infall of satellite galaxies (Toth & Ostriker, 1992) and by accretion of misaligned gas (Scannapieco et al., 2009)(CS09 hereafter). Moreover, the reorientation of discs (Chapter 3, Okamoto, 2013) and disc instabilities (e.g. Noguchi, 1999; Aumer et al., 2010) can enhance the bulge-to-disc ratio.

In addition to these problems, stellar mass to halo mass relations from abundance matching techniques have shown that the majority of simulations over-produce stars (Guo et al., 2010; Sawala et al., 2011), especially at high z (CS09, Moster et al., 2013).

Modelling the injection of energy from supernova (SN) explosions into the surrounding gas (e.g. Scannapieco et al., 2006; Stinson et al., 2006) has been shown to be a possible mechanism to prevent overly efficient gas cooling, for driving large-scale outflows, for removing low angular momentum material and thus for producing more realistic disc galaxies (e.g. Scannapieco et al., 2008; Brook et al., 2011). Interestingly, simulations applying rather weak feedback have been shown to be more successful in reproducing early-type galaxies (Naab et al., 2007; Oser et al., 2010; Johansson et al., 2012b). Apart from SNe, active galactic nuclei (AGN, e.g. Springel et al., 2005a) and cosmic rays (Uhlig et al., 2012) have been considered as possible sources of feedback.

Simulations including empirical models of momentum-driven winds have been shown to improve the agreement with observed properties of the galaxy population and the intergalactic medium (IGM, Oppenheimer & Davé, 2006; Oppenheimer et al., 2010). Recently, the input of momentum and energy from massive young stars in form of stellar winds and radiation pressure (RP) prior to their explosion as SNe has been studied in more detail. Hopkins et al. (2011) showed that momentum input into the inter-stellar medium (ISM) from RP may play a key role in regulating star formation (SF). Stinson et al. (2013) included thermal feedback from young stars and thus were able to achieve significantly better agreement of star formation histories (SFHs) with observations. Agertz et al. (2013) presented the most complete model so far of mass, momentum and energy feedback from stars during all stages of their evolution, and concluded that RP from young stars has the strongest effect on the ISM.

Apart from feedback, a more realistic modelling of SF and the ISM has been shown to help in making simulated galaxies with more realistic properties. Governato et al. (2010) found that increasing the threshold density used in the modelling of SF to more realistic values leads to more concentrated SF, more efficient feedback energy input into the ISM, and the formation of galaxies with higher disc fraction (see also Guedes et al., 2011). Christensen et al. (2012) have shown that the implementation of a model for the formation of molecular hydrogen (see Gnedin et al., 2009) can amplify the effect of higher threshold densities.

In Chapter 3 we have shown that it is possible to form a realistic disc galaxy within a triaxial, substructured and growing cold dark matter halo, as long as the disc forms predominantly at late times ($z < 1$), the angular momentum vector of the infalling gas has a roughly constant and appropriate orientation and there are no major mergers or other significant changes in the configuration of the halo. In the *Aquila Code Comparison Project* (Scannapieco et al., 2012, CS12 hereafter) one of the haloes considered in Chapter 3 was simulated with 15 different galaxy formation codes yielding 15 model galaxies with widely varying properties. Although several models compared well to a subset of the observations considered, none of the models yielded a fully realistic disc galaxy. In this Chapter we intend to show, how modifications to the models of CS09, motivated by the findings of CS12 and some of the recently discussed solutions to problems discussed above, can lead to the formation of significantly more realistic disc galaxies. We also use our model to study a sample of haloes which has been previously studied by Oser et al. (2010) in the context of the formation of massive, early-type galaxies. The combined sample comprises haloes with very quiet merger histories, as well as low-z mergers, and is thus well suited to be compared to a range of objects in the observed galaxy population.

This Chapter is organized as follows: In Section 4.3 we describe the updates we applied to our code. In Section 4.4 we introduce the sample of initial conditions we use. In Section 4.5 we discuss the star formation histories of our galaxies. In Section 4.6 we analyze their kinematical and structural properties. In Section 4.7 we compare our sample to observed scaling relations. Finally, we conclude in Section 4.8.

4.3 | The code

For our simulations, we use the TREESPH code GADGET-3, last described in Springel (2005). Scannapieco et al. (2005, 2006) introduced models for stellar metal production, metal line cooling, star formation, SN feedback and a multiphase gas treatment to be used with GADGET-3, which we use as the basis for our code update.

4.3.1 | Multiphase model and star formation

We begin with a description of the parts of the model, which have remained unchanged. The code is unique in decoupling smoothed particle hydrodynamics (SPH) particles with very different thermodynamic properties by preventing them from being SPH neighbours. Particle

i decouples from particle j if

$$A_i > 50. \times A_j \qquad \text{and} \qquad \mu_{\rm ij} < {\rm c_{ij}}. \tag{4.1}$$

Here A is the entropic function (Springel & Hernquist, 2002), c_{ij} is the pair-averaged sound-speed and μ_{ij} is the relative velocity of the particles projected onto their separation vector. Marri & White (2003) showed that the second condition is needed to avoid decoupling in shock waves, which can lead to unphysical effects. This multiphase gas treatment has been implemented to make a realistic co-existence of hot and cold phase gas (as observed in the ISM) possible in SPH. It has also been shown to allow a more realistic modelling of energy and metal injection from stars to the distinct components of the ISM.

To model the formation of stars, we assume that gas particles are eligible for this process, if their density is above a threshold density $n_{\rm th}$. Whereas CS09 used $n_{\rm th} \sim 0.03~{\rm cm}^{-3}$, Governato et al. (2010) have argued that significantly higher threshold densities are needed to form realistic galaxies. While we can confirm their conclusions, we caution that the effect of varying this parameter depends significantly on the details of the applied feedback and ISM model. For the model and the resolution applied in this work, we use a value of $n_{\rm th} \sim 3~{\rm cm}^{-3}$, for which we find the best results. As argued by Guedes et al. (2011), a significantly lower value leads to less efficient feedback and higher bulge fraction. However, a significantly higher threshold in our model leads to the formation of bound stellar clumps, which can sink to the centre because of dynamical friction and thus also enhances the bulge fraction. Our value lies between the value of $1~{\rm cm}^{-3}$ applied for the Gasoline model for halo Aq-C-5 in CS12 and $5~{\rm cm}^{-3}$ applied by Guedes et al. (2011) in a higher resolution simulation. We note that these values are still two orders of magnitude below the average density of molecular clouds and at least four orders of magnitude below the density of molecular cores within which stars are observed to form. Our resolution is, however, too coarse to model these high densities.

For particles with $n > n_{\rm th}$ and an overdensity $\rho/\bar{\rho} > 2000$ (where $\bar{\rho}$ is the cosmic mean density), which lie in a convergent flow, a SFR of

$$\frac{{\rm d}\rho_\star}{\rm dt} = \eta \, \frac{\rho_{\rm gas}}{t_{\rm dyn}} \tag{4.2}$$

is assumed. Here stellar and gas densities are represented by $\rho_\star$ and $\rho_{\rm gas}$ and $t_{\rm dyn} = 1/\sqrt{4\pi G \rho_{\rm gas}}$ is the local dynamical time for the gas particle. We choose a SF efficiency $\eta = 0.04$, in the range of values typically used (see e.g. various models in CS12). The typical timescale for SF is thus $t_{\rm sf} = 1/\eta \; t_{\rm dyn}$. Star particles are created stochastically with one gas particle being turned into one star particle of the same mass.

4.3.2 | Metal production and cooling

To account for metals, we explicitly trace the mass in the elements H, He, C, N, O, Ne, Mg, Si, S, Ca and Fe for all gas and star particles. Our model includes chemical enrichment from Type II SNe (SNII), Type Ia SNe (SNIa) and asymptotic giant branch (AGB) stars. Each star particle represents a stellar population characterized by a Kroupa (2001) initial mass function (IMF) with lower and upper mass limits of 0.1 and $100~M_\odot$.

We assume that stars more massive than $8~M_\odot$ explode as SNII. All SNII are modelled in one event at an age $\tau_{\rm SNII}$ (see Section 4.3.4). For the calculation of the mass returned to the ISM in the various elements, we use the metal-dependent yields provided by Chieffi & Limongi (2004). The uncertainties in yields and thus in the predictions of simulations are significant, as was for example discussed by Wiersma et al. (2009a). It has been argued by Portinari et al. (1998) that adjustments by factors of 2 for certain elements can help improve the agreement with observations. Indeed, we find that halving the iron yield following their findings leads to a qualitatively better agreement of metallicities, as discussed in the following sections, which is why we apply their suggested corrections. We note that apart from this, we have not studied the variation of our results with different yield sets, IMFs etc. to optimize our results.

For the element production by SNIa, we assume the model W7 presented by Iwamoto et al. (1999). We apply a delay time distribution, which declines with age τ of a stellar population as τ^{-1}, as proposed by Maoz & Mannucci (2012). We also adopt their suggested normalization of 2 SNIa per 1000 $M_{\odot}$ of stars formed and that the first SNIa explode at $\tau = 50\ \mathrm{Myr}$. The corresponding masses of elements are returned to the ISM in $50\ \mathrm{Myr}$ time-steps in our model.

To account for the mass recycling in the winds of AGB stars, we use the metal-dependent yields of Karakas (2010). Together with the assumed IMF and using lifetimes dependent on stellar mass and metallicity, we can thus calculate the mass of the considered elements released during the time intervals considered for the SNIa enrichment.

Chemical elements are distributed to the gaseous neighbours of the star particles, where neighbours are weighted according to their distance from the star particle using an SPH kernel. To account for our multiphase treatment of the gas component, the returned (metal) mass is split between 10 hot and 10 cold neighbours. We give 50 per cent to the hot and cold phase each for all three different types of metal production sites. We have tested making this fraction dependent on the age of the stellar particle, but found that observed abundance ratios are best reproduced by our simple choice. For this purpose, the cold phase gas is defined by $T < 8 \times 10^{4}\ \mathrm{K}$ and $n > 4. \times 10^{-5}\ \mathrm{cm}^{-3}$. Note, that we have reduced this density limit by a factor of ~ 100 compared to Scannapieco et al. (2006), as we found that a higher value can have a destructive effect on extended, low-density gas discs due to energetic feedback (see below).

The metallicities of the SPH particles are used to calculate the cooling rates of the gas. We apply the rates presented by Wiersma et al. (2009b) for optically thin gas in ionization equilibrium. These rates are calculated on an element-by-element basis and take into account the effects of photo-ionization from a uniform redshift-dependent ionizing background (Haardt & Madau, 2001). The rates thus depend on redshift, gas density, temperature and chemical composition.

4.3.3 | Metal diffusion

In many standard implementations of chemical enrichment in SPH (also true for Scannapieco et al., 2005), the metallicity of a particle can only change by enrichment. This can lead to situations, where gas particles with similar thermodynamic properties, but very different metallicities live next to each other. This occurs e.g. when a galactic wind particle travels through unenriched IGM. Wiersma et al. (2009a) suggested that smoothed metallicities should be used to get rid of these situations. Although this improves the modelling by smoothing out differences, it also leads to fluctuating metallicities for individual particles for the IGM situation discussed above.

In the ISM, once metals have been released from stars, turbulent motions of gas are responsible for their spreading. Including a corresponding model for the turbulent diffusion of metals was already suggested by Groom (1997), but until recently, most galaxy formation SPH codes did not consider this process. Recent implementations were presented in Martínez-Serrano et al. (2008), Greif et al. (2009) and Shen et al. (2010).

The diffusion equation for a metal concentration c (metal mass per total mass) of a fluid element with density ρ and a diffusion coefficient D is

$$\frac{\mathrm{d}c}{\mathrm{d}t} = \frac{1}{\rho}\nabla\cdot(D\nabla c), \tag{4.3}$$

where d/dt is the Lagrangian derivative. Cleary & Monaghan (1999) gave the SPH formulation of the diffusion equation as

$$\frac{\mathrm{d}c_i}{\mathrm{d}t} = \sum_j K_{ij}\left(c_i - c_j\right), \tag{4.4}$$

where

$$K_{ij} = \frac{m_j}{\rho_i\rho_j}\frac{4D_iD_j}{(D_i+D_j)}\frac{\mathbf{r}_{ij}\cdot\nabla_i W_{ij}}{r_{ij}^2}. \tag{4.5}$$

Here quantities with subscripts i and j correspond to neighbour particles, m is the particle mass, W_{ij} is the SPH kernel and $\mathbf{r}_{ij}$ is the separation vector with absolute r_{ij}.

Greif et al. (2009) argued for the use of an integrated equation assuming that the change in c is small over Δt:

$$c_i(t_0+\Delta t) = c_i(t_o)e^{A\Delta t} + \frac{B}{A}(1-e^{A\Delta t}) \tag{4.6}$$

with

$$A = \sum_j K_{ij} \quad \text{and} \quad B = \sum_j K_{ij}c_j. \tag{4.7}$$

As we want to conserve the total metal mass, we modify the equation for a pairwise exchange of metals. For the metal mass $\mu_i = c_i m_i$ we get

$$\Delta\mu_i = \sum_j \mu_{ij} = \sum_j \left[\frac{1}{2}m_i\left(1-e^{A\Delta t}\right)\frac{1}{A}K_{ij}\left(c_j-c_i\right)\right], \tag{4.8}$$

where the factor 1/2 was included to account for the fact that most pairs of neighbours are considered twice and μ_{ij} is correspondingly subtracted from particle j. To avoid dependence on the ordering of particles, all changes $\Delta\mu_{ij}$ are calculated for all pairs of neighbours before the metal masses of all particles are updated. This procedure is applied at every time-step for all active particles using the standard SPH neighbour searches. A neighbour particle j can be inactive, so that the corresponding pair of particles only appears once. Should the particles still be neighbours at the next active time-step of j, the larger Δt compensates for that. Clearly this formalism includes a number of approximations, but applied to tests as discussed in Greif et al. (2009), we find a similar accuracy.

This leaves the determination of the diffusion coefficient D. Greif et al. (2009) argued for $D_i = 2\rho_i\sigma_i h_i$, where σ is the velocity dispersion of gas particles within its smoothing kernel characterized by the smoothing length h_i. Shen et al. (2010) argued that $D_i = 0.05\rho_i\left|S_{kl}\right|h_i^2$, based on the trace-free velocity shear tensor S_{kl} (for details see their paper) is a better choice, as it yields no diffusion for purely rotating or compressive flows. We have tested both ideas and found that for a fixed test setup, the main difference is the strength of the diffusion coefficient with Greif et al. (2009) predicting values higher by a factor ~ 20. For cosmological simulations, we find that the Shen et al. configuration yields better results when comparing to observations. As was noticed by Shen et al. (2010), diffusion leads to outflowing particles losing metals to the circumgalactic medium and subsequently also to higher gaseous and stellar metallicities in the galaxy. For the Greif et al. value for D, this effect is much stronger than for the Shen et al. value and makes galaxies lie above the mass-metallicity relation. However, when we use $D_i = 0.1\rho_i\sigma_i h_i$ this criterion loses significance. For consistency, we use D as suggested by Shen et al. in the simulations presented in this Chapter.

4.3.4 | Thermal and kinetic feedback

As in Scannapieco et al. (2006) we assume that each SN ejects an energy of $\sim 10^{51}\mathrm{erg}$ into the surrounding ISM. As for the metals, we split this energy in halves and give those to the 10 nearest hot and cold gas neighbour particles as defined above. However, we now split the energy between a kinetic and a thermal part (see also Agertz et al., 2013).

To determine the kinetic part, we consider the conservation of momentum $\Delta p = \Delta m\ v_{\mathrm{out}}$ contained in the initial SN ejecta and assume that this is characterized by a typical outflow velocity v_{out}. We use $v_{\mathrm{out}} = 3000\ \mathrm{kms}^{-1}$, a typical velocity of outflowing material in SNe in the Sedov expansion phase. Note that the kinetic energy carried by $\Delta m = 10\ M_{\odot}$ at this velocity is $0.9 \times 10^{51}\mathrm{erg}$, the average over all SNII according to our choice of IMF and SNII mass interval is $\sim 1.5 \times 10^{51}\mathrm{erg}$. With this assumption, the momentum transferred from a star particle to one of the 20 gas neighbour particles i receiving feedback is determined by Δm_i, the mass transferred to particle i, which we know from the considerations of Section 4.3.2 for each particle i at a given feedback time-step. The momentum transferred to particle i is simply $\Delta p_i = \Delta m_i\ v_{\mathrm{out}}$. The direction of the momentum change vector is modelled as pointing radially away from the star particle towards gas particle i. Our choices of parameters lead to a typical change in radial velocity component of a gas particle i receiving feedback of $\Delta v_i = 20 - 30\ \mathrm{kms}^{-1}$. As Δm is not spread equally among particles, in extreme cases $\Delta v_i \sim 100\ \mathrm{kms}^{-1}$ is possible.

We also know how many SN events are represented and thus the total energy that is available to be released, ΔE_{tot}, under the assumption that per SN an average of $1.0\times10^{51}\mathrm{erg}$ is transferred to the ISM. The transfer of momentum leads to a change in kinetic energy of the gas particle ΔE_{kin}. The remaining energy is considered to be thermalized, $\Delta E_{\mathrm{therm}} = \Delta E_{\mathrm{tot}} - \Delta E_{\mathrm{kin}}$. For this energy, we follow the ideas of Scannapieco et al. (2006). The fraction transferred to a hot particle is instantly added to its thermal energy. Instead, for cold particles, we accumulate the energy from SNe events in a reservoir. Only when the accumulated energy is high enough, so that it can become a hot particle, the energy is released (‘promotion’). To define ‘hot’ in this context, we search for neighbour particles with entropies high enough to be decoupled from the cold particle in our multiphase scheme and calculate their mean entropy A_{hot}. If a particle has less than 5 such neighbours within 10 smoothing lengths, we set $A_{\mathrm{hot}} = A_{\mathrm{th}}$, where A_{th} corresponds to $T = 1.6 \times 10^5\ \mathrm{K}$ and $n = 2\times10^{-3}\mathrm{cm}^{-3}$ (‘seeding’, see Sawala et al., 2011). Moreover, $A_{\mathrm{hot}} = A_{\mathrm{th}}$ is also assumed if $A_{\mathrm{hot}} < A_{\mathrm{th}}$, so that A_{th} acts as a minimum promotion entropy.

As $\Delta E_{\mathrm{therm}} > \Delta E_{\mathrm{kin}}$ for the considered situation, the thermal feedback is only mildly weakened. The kinetic feedback, however, helps breaking up dense clumps of gas and thus lowers the cooling rates and the SF efficiency in a star-forming disc. Gas fractions increase and so does the efficiency of the thermal feedback. Momentum is also transferred when mass is released from AGB stars, but masses and velocities are much smaller than in SN explosions, which is why this effect is negligible.

For the age of star particles at which we input SN energy, we choose $\tau_{\rm SNII} = 3$ Myr. Clearly this choice is not unproblematic, as most SNII explode after that, but the energy release from SNII peaks at this time and the most massive stars are supposed to have the strongest effect on the ISM. When not using feedback from massive stars before their explosion as SNe, as described in the following section, we find less realistic SFHs for a later choice of $\tau_{\rm SNII}$. When adding an additional source of feedback, this effect becomes less significant. SFRs for individual haloes can go up or down by up to a factor of 2 at a given epoch for a given halo when $\tau_{\rm SNII}$ is increased, but cumulative effects are weaker. From these test, we conclude that the choice of $\tau_{\rm SNII}$ does not significantly impact the results of our work.

4.3.5 | Radiation pressure

Hopkins et al. (2011) used high-resolution simulations to test the idea that the inclusion of feedback from radiation pressure (RP) of young massive stars has a comparable or possibly even stronger effect on the ISM than SN feedback (for the underlying ideas see e.g. Murray et al., 2005). They developed a model for high resolution simulations, in which they identify star-forming regions and can thus use their properties to calculate the effect of RP as a function of these local properties. Stinson et al. (2013) have introduced a model, where, instead of a momentum transfer, a thermal energy transfer is modelled, assuming that 10 per cent of the radiated energy from massive young stars is thermalized in the surrounding ISM. Agertz et al. (2013) presented a model for RP, which assumes that each star particle represents a sample of star-forming clusters. The effect is however then dependent on their choice of the maximum cluster mass.

We parametrize the rate of momentum deposition to the gas as

$$\dot{p}_{\rm rp} = (1 + \tau_{\rm IR})\frac{L(t)}{c}, \tag{4.9}$$

where $\tau_{\rm IR}$ is the infrared (IR) optical depth and $L(t)$ is the UV-luminosity of the stellar population and we have set additional efficiency parameters to 1 (see Agertz et al., 2013). This equation states that all UV photons are scattered or absorbed by dust, which subsequently re-radiates the energy in the IR. The IR photons are then scattered multiple times before leaving the star-forming cloud. We construct $L(t)$ by using the stellar evolution models for massive stars by Ekström et al. (2012) and assuming a Kroupa (2001) IMF.

More problematic is the estimation of $\tau_{\rm IR}$. If we follow Hopkins et al. (2011), $\tau_{\rm IR} = \Sigma_{\rm clump}\kappa_{\rm IR}$ with $\kappa_{\rm IR} \sim 5\ {\rm cm^2 g^{-1}}$, we effectively have to know the surface density of the star-forming gas clump. Due to our coarse resolution, we do not resolve such clumps. We therefore use the following model:

$$\tau_{\rm IR} = \tau_0 f(\rho, Z) g(\sigma). \tag{4.10}$$

Each gas particle is characterized by its density and metallicity through $f(\rho, Z)$, whereas the environment of the star particle is characterized by $g(\sigma)$. $f(\rho, Z)$ basically models the dependence on the dust surface density represented by a particle:

$$f(\rho, Z) = max\left[1, \left(\frac{\rho h}{\rho_{\rm th} h_{\rm th}}\right)\right]\left(\frac{Z}{Z_\odot}\right) \tag{4.11}$$

Here we use ρh with the smoothing length h as a measure for the surface density represented by a particle and limit the effect of this factor at the SF density threshold. We also assume a linear dependence of dust on metallicity Z. If we set $g = 1$, we gain insight into how our model works. If we choose $\tau_0 = 25$, which is a value in the range of values 10-100 found by Hopkins et al. (2011) in their models of star-forming high-z discs, we find that indeed RP significantly reduces high-z SFRs and brings them into better agreement with abundance matching results, similar to the findings of Stinson et al. (2013). However, the low-z SF efficiencies become too low and the final galaxy masses are too small, indicating that RP is too strong at later times (see Fig. 4.1 and discussion in Section 4.5.1).

However low-z discs show significantly lower gas velocity dispersions than gas-rich, turbulent high-z discs (Genzel et al., 2008). For a typical Milky-Way-type halo, we find the average gas velocity dispersion σ is $\sim 40\ \mathrm{kms}^{-1}$ at $z \sim 2$, which is in agreement with observed galaxies at that time (Förster Schreiber et al., 2009), and at low redshift $\sigma \sim 15 - 20\ \mathrm{kms}^{-1}$, which is too high, but explained by our coarse resolution. Star-forming regions, and thus the values of $\tau_{\rm IR}$, are thus much larger at high z. If we assume that the Jeans mass is a valid estimator for clump mass, then the mass scales as $M_{\rm cl} \propto \sigma^3$ (we ignore the dependence on density as we are not modelling densities above the SF threshold properly). As is pointed out in the review of observed star-forming clouds in Agertz et al. (2013), the final radius of clusters depends weakly on mass, which leads to our crude estimation

$$g(\sigma) = \left(\frac{\sigma}{\sigma_0}\right)^3. \tag{4.12}$$

To estimate σ in the environment of the star particle, we determine the velocity dispersion $\sigma_{\rm kernel}$ of gas particles within the smoothing kernel for each gas particle. Then we average over the values $\sigma_{\rm kernel}$ of all the neighbour gas particles to a young star particle to avoid strong fluctuations.

We acknowledge that this line of estimation is not particularly stringent, but it qualitatively assures that the effect of RP is stronger in galaxies with higher gas velocity dispersions and thus larger star-forming regions.

In our simulations, we model the momentum change $\Delta p = \dot{p}_{\rm rp}\Delta t$, where Δt is the time-step of the star particle, as a continuous force acting on the 10 nearest cold neighbour particles during the first 30 Myr in the life of a star particle. We use $\tau_0 = 25$ for $\sigma_0 = 40\ \mathrm{kms}^{-1}$, so that the effect at high z reduces SFRs and is weak at low z. We also limit $g(\sigma)$ at a value of 4 to avoid overly strong forces. By construction, we thus find values of $\tau_{\rm IR} \sim 20$ at $z \sim 2$ with extreme values going up to 100, whereas we find significantly lower values of the order of $1 - 5$ at low redshift. We discuss the choice of parameters in Section 4.5.1.

4.4 | The sample

As initial conditions for our cosmological zoom-in simulations we use haloes from the Aquarius Project (Springel et al., 2008, CS09), one of which was also used for the *Aquila Project* (CS12). In addition, we use a selection of haloes from Oser et al. (2010).

Halo	$M_{\rm vir}$ $[10^{10}M_{\odot}]$	$m_{\rm dm}$ $[10^{6}M_{\odot}]$	$m_{\rm gas}$ $[10^{5}M_{\odot}]$	Origin
6782-4x	17.03	3.62	7.37	LO
4323-4x	29.50	3.62	7.37	LO
4349-4x	30.28	3.62	7.37	LO
2283-4x	49.65	3.62	7.37	LO
Aq-B-5	70.35	1.50	2.87	CS
1646-4x	81.61	3.62	7.37	LO
1192-4x	100.03	3.62	7.37	LO
1196-4x	113.81	3.62	7.37	LO
0977-4x	129.56	3.62	7.37	LO
Aq-D-5	150.43	2.31	4.40	CS
Aq-C-5	151.28	2.16	4.11	CS
Aq-A-5	164.49	2.64	5.03	CS
0959-4x	164.54	3.62	7.37	LO
0858-4x	182.44	3.62	7.37	LO
0664-4x	213.74	3.62	7.37	LO
0616-4x	235.77	3.62	7.37	LO

Table 4.1: Overview over the haloes studied in this chapter, including the name of the halo, its virial mass $M_{\rm vir}$, the DM particle mass $m_{\rm dm}$ and the initial gas particle mass $m_{\rm gas}$. Under 'Origin' we distinguish between haloes from 'CS' (CS09) and 'LO' (Oser et al., 2010).

The Aquarius haloes are a suite of high resolution zoom-in resimulations of regions chosen from the Millenium II simulation (Boylan-Kolchin et al., 2009) which follows a cosmological box of a side-length $137\ {\rm Mpc}$. They were simulated from $z = 127$ assuming a ΛCDM universe with the following parameters: $\Omega_{\Lambda} = 0.75$, $\Omega_m = 0.25$,$\Omega_b = 0.040$, $\sigma_8 = 0.9$ and $H_0 = 73\ {\rm kms}^{-1}{\rm Mpc}^{-1}$. The haloes were selected to have a similar mass to that inferred for the Milky Way dark halo and to have no neighbour exceeding half of their mass within $1.4\ {\rm Mpc}$. For details we refer to Springel et al. (2008) and CS09. Because of the second criterion, the haloes have a relatively quiet low-z merger history. They are thus expected to host galaxies with high disc fractions at $z = 0$. Discs were indeed found to form in these haloes by CS09 and CS12, but with low disc-to-bulge ratios and several other properties that do not compare well to observations.

The haloes from Oser et al. (2010) were selected from a simulation of a cosmological box with a side-length of $100\ {\rm Mpc}$, and were simulated from $z = 43$ assuming a ΛCDM universe with the following parameters: $\Omega_{\Lambda} = 0.74$, $\Omega_m = 0.26$, $\Omega_b = 0.044$, $\sigma_8 = 0.77$ and $H_0 = 72\ {\rm kms}^{-1}{\rm Mpc}^{-1}$. Unlike the Aquarius haloes, these haloes were not chosen specifically as candidates for disc galaxies and the sample thus also contains $z \sim 0$ mergers. For details we refer to Oser et al. (2010), who resimulated lower resolution versions of these haloes.

The haloes we selected from these two samples are listed in Table 4.1. Our combined sample comprises 16 haloes with $z = 0$ re-simulated virial masses $M_{\rm vir}$ ranging from $1.7 \times 10^{11}M_{\odot}$ to $2.4 \times 10^{12}\ M_{\odot}$. The resolutions of the simulations are characterized by the initial gas particle masses, which lie between 2.87 and $7.37 \times 10^{5}\ M_{\odot}$ and DM particle masses between 1.50 and $3.62 \times 10^{6}\ M_{\odot}$. For our re-simulations, we applied comoving gravitational

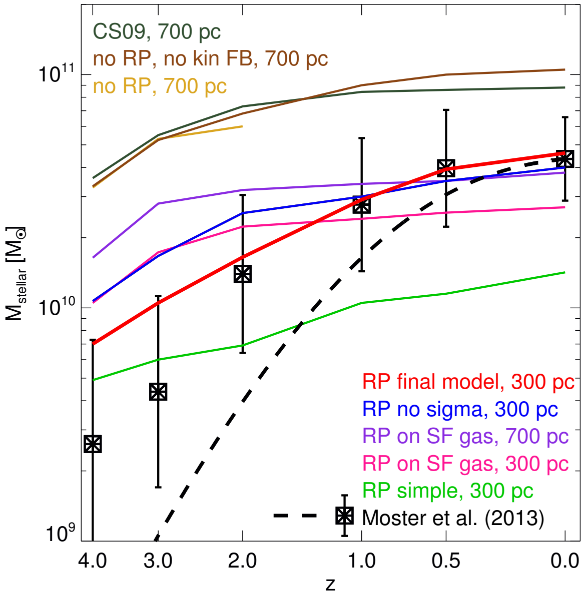

Figure 4.1: The evolution of the stellar galaxy mass $M_{\rm stellar}$ vs. redshift z in halo AqC for various code configurations (coloured lines). Overplotted are the predictions of MNW13 in two ways: a) The predicted mass evolution of a typical halo with the $z = 0$ mass of AqC (black dashed line) and b) the predicted evolution taking into account the actual halo mass of AqC at six redshifts (points with 1 σ error-bars).

softening lengths of $h_{\rm bar} \sim 300$ pc for gas and stars, and of $h_{\rm dm} \sim 650$ pc for DM. We thus use shorter softening lengths than in CS09.

4.5 | Star formation histories

We begin to analyze the outcome of our simulations by considering the star formation history (SFH) of the model galaxies. As has been shown by Moster et al. (2013) (MNW13 hereafter), the majority of simulations predicts stellar galaxy masses that are significantly higher than abundance matching results suggest at all redshifts $z = 0 - 4$ with overproduction being stronger at high redshift (for exceptions see e.g. Stinson et al., 2013; Kannan et al., 2013). As real disc galaxies form most of their stars at low z, when destructive mergers are rare, it is crucial for simulations to produce reasonable SFHs in order to get galaxy structural properties right.

4.5.1 | The effect of changing feedback models on the SFH of AqC

Halo AqC has been studied in CS12 with a variety of different simulation codes. Although some of these codes produce realistic $z = 0$ masses, none produced a good match to abundance matching results for the SFH at all $z = 0 - 4$. Compared to haloes of similar $z = 0$ mass, AqC is among the ones which assemble their dark mass earliest (see Fig. A1 in Scannapieco et al., 2011). When developing our feedback models, we found that AqC is particularly sensitive to the choice of model details, which we demonstrate in this section. We caution that the effects we discuss here can vary from halo to halo and not all conclusions drawn from AqC are true for all haloes. Moreover, abundance matching gives statistical properties for a galaxy sample and AqC could well be an outlier. As we will show below, our calibration method is justified by the fact that the feedback model that works best for AqC produces a sample of galaxies with reasonable properties.

In Fig. 4.1 we plot the evolution of the stellar mass M_{stellar} from $z = 4 - 0$ for various runs of the same initial conditions. We compare it to the evolution predicted by the abundance matching results of MNW13, who provide two different ways of comparison. On the one hand, fitting formulae for typical SF and accretion histories are presented as a function of $z = 0$ halo mass M_{200}. We represent these predictions by the dashed line in Fig. 4.1. On the other hand, we know the halo mass at each redshift z and can thus make use of the fitting formulae for $M_{\mathrm{stellar}}/M_{200}(z)$. We represent these by six data-points with corresponding error-bars from $z = 4$ to 0. This method yields significantly higher predictions for M_{stellar} at high z, which reflects the early assembly of halo AqC. Clearly the latter predictions should be used as a guideline for model calibration.

The original model by CS09 produces a stellar mass at $z = 4$ that is about an order of magnitude too high compared to the MNW13 value. It remains more than 1σ above predictions at all redshifts. If we add our updated metal production and metal cooling rates (*no RP, no kin FB*), the changes are negligible. Changing to our new thermal and kinetic feedback (*no RP*) also does not improve the SFH at high redshifts (the run was stopped at $z = 2$). We note that the change from the CS09 thermal feedback to our new thermal and kinetic feedback can produce significant changes in SFHs in other haloes.

Stinson et al. (2013) argued that adding feedback from young stars before their explosion as SNe would significantly shift SF to later times. Kannan et al. (2013) tested this idea on a simulation of a cosmological volume and found good agreement with the results of MNW13 at high z. We tested various models of feedback from RP. First we consider a simple model for RP (*simple RP*), where all affected gas particles are treated equally, independent of density, metallicity and gas velocity dispersion (assuming an effective optical depth $\tau_0 = 25$, see Equation 10). For this model, we achieve a reduction of the early SFR so that the $z = 4$ stellar mass matches predictions. However, the feedback is too strong later on and SFRs are drastically reduced so that the $z = 0$ stellar mass is more than 2σ low. When modifying our model so that the force is only acting on star-forming particles with $\rho > \rho_{\mathrm{th}}$ (*RP on SF gas*), the strength of feedback is reduced especially at high z, so that the SFR is high at $z > 4$, but the agreement at $z = 0$ is significantly better, however with low-z SFRs being still too low. A model which includes a metallicity and density dependence to account for the dust surface density of each gas particle as described in Section 4.3.5 (*RP no sigma*) lowers the effect of RP at low z when metallicities are higher, but the densities of the affected gas particles are on average lower, as the systems have lower gas fractions. Our full model including the dependence on the gas velocity dispersion σ (*RP final model*) models the dependence of RP on the size of star-forming regions. As σ is higher in high-z galaxies, the effect of RP is strengthened at high and weakened at low z leading to a significant change in the shape of the $M_{\star} - z$ curve and bringing it within 1σ of the predictions of MNW13 at all $z < 4$.

Krumholz & Thompson (2013) have argued that the efficiency of the coupling between the radiation field and the dusty gas is significantly lower than assumed in the approach of Hopkins et al. (2011), which is the basis of our model here. This would imply that RP is less efficient in reducing the problem of overly high SFRs in simulated galaxies at high z. We thus caution that the uncertainties in the modelled processes remain high and we take the

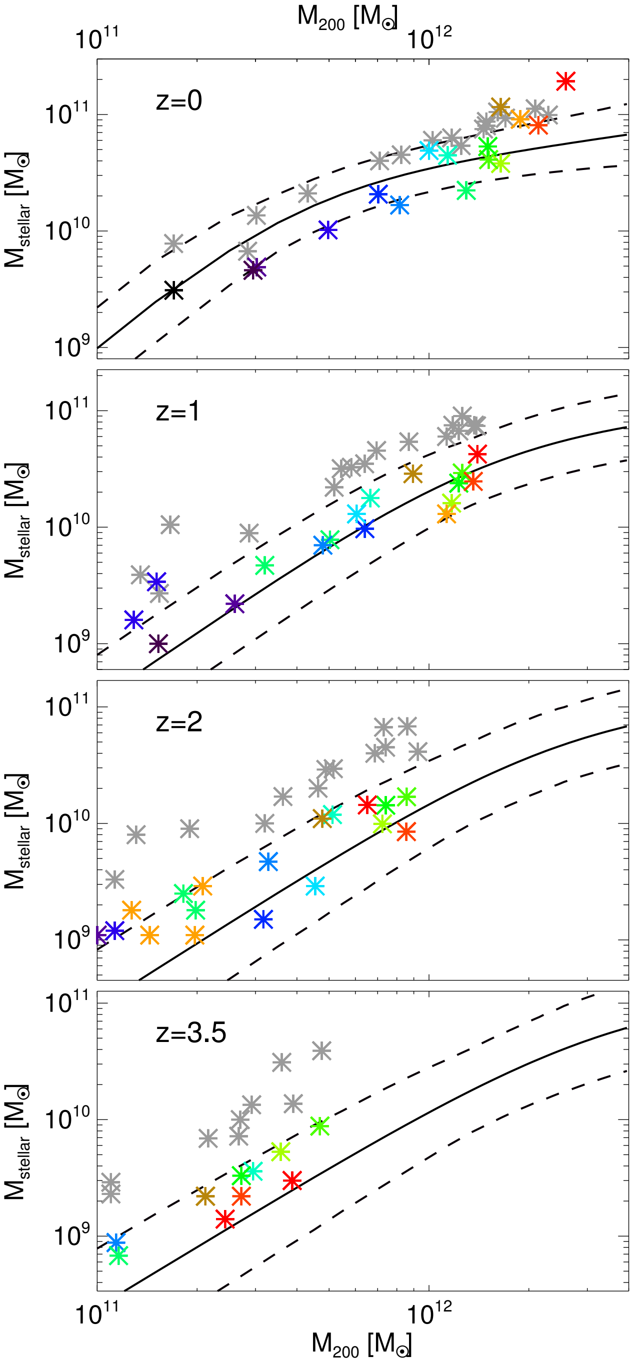

Figure 4.2: Stellar galactic mass $M_{\rm stellar}$ plotted against halo virial mass M_{200} at redshifts $z = 0, 1, 2$ and 3.5. The coloured points are the models discussed in this Chapter. Each colour represents a simulation. A colour can appear more than once at high z representing progenitor haloes. This colour coding is used for figures throughout the chapter. The gray points are models of the same set of haloes run with the code used in CS09. The black lines are the abundance matching results of MNW13 with 1σ regions indicated by the dashed lines.

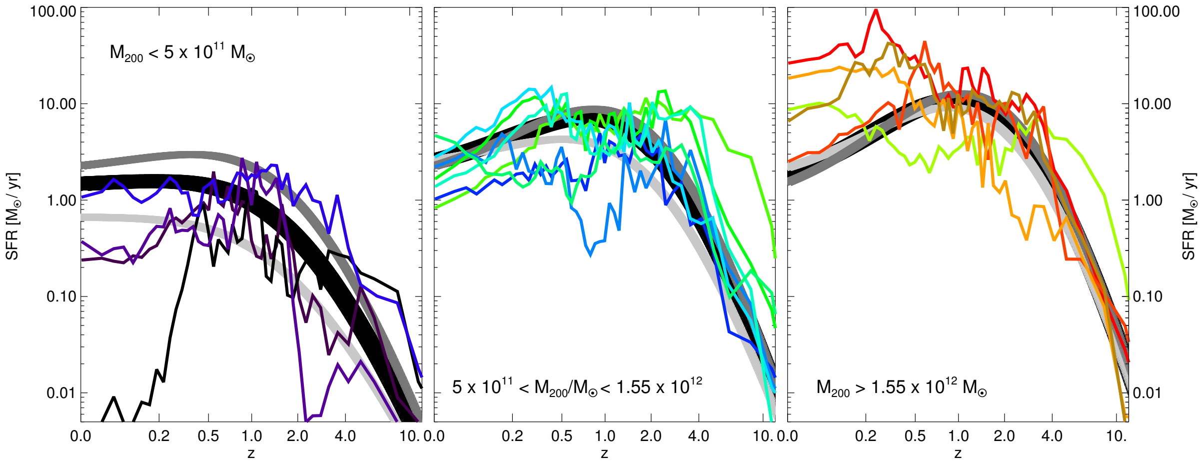

Figure 4.3: Star formation rates SFR as a function of redshift z for all our models. The haloes are split into $M_{200} < 5 \times 10^{11} M_{\odot}$ (left), $5 \times 10^{11} M_{\odot} < M_{200} < 1.55 \times 10^{12} M_{\odot}$ (middle) and $M_{200} > 1.55 \times 10^{12} M_{\odot}$ (right). Overplotted are predicted SFRs for typical haloes given by MNW13 for the mean, lowest and highest halo mass per panel.

agreement of simulated SFH with the results of MNW13 as a justification for the model we apply.

We also use Fig. 4.1 to show a dependence of our feedback on the gravitational softening length ϵ. Going from 700 to 300 pc baryonic comoving softening length significantly reduces the high-z SFRs, as shown by two versions of our *RP on SF gas* model. This seems to originate in a higher feedback efficiency due to denser structures in the very early stages of galaxy formation. Because of this effect, we apply $\epsilon_{\rm baryons} = 300 \ {\rm pc}$ for our simulations, a significantly lower value than in CS09. We note that reducing the softening length has no significant effect on the high-z SFR in the absence of a model for RP.

We conclude that the inclusion of a parametrized model for feedback from young stars in the from of radiation pressure is indeed an efficient way to bring star formation histories into better agreement with results from abundance matching techniques. We caution that details of the modelling have a significant effect on the outcome and that these effects vary from halo to halo. It is crucial to test the model on a set of haloes, as we describe in the next subsection.

4.5.2 | Applying the model to all haloes

We now apply our updated galaxy formation code to the full sample of haloes described in Section 4.4 and examine if the resulting SFHs agree with observations of the real galaxy population.

We start by discussing stellar masses $M_{\rm stellar}$ as a function of their halo masses M_{200} at redshifts $z = 3.5, 2, 1$ and 0 in Fig. 4.2. $M_{\rm stellar}$ is defined as the mass of stars within a radius $r_{\rm gal}$ defined by visually analyzing the spherical stellar mass profile $M_{\rm stellar}(< r)$ and determining where its radial growth saturates. The coloured points in this figure are for the models with our updated code, whereas the gray points are for a sample of simulations run on the same set of initial conditions with the code version and model parameters applied in

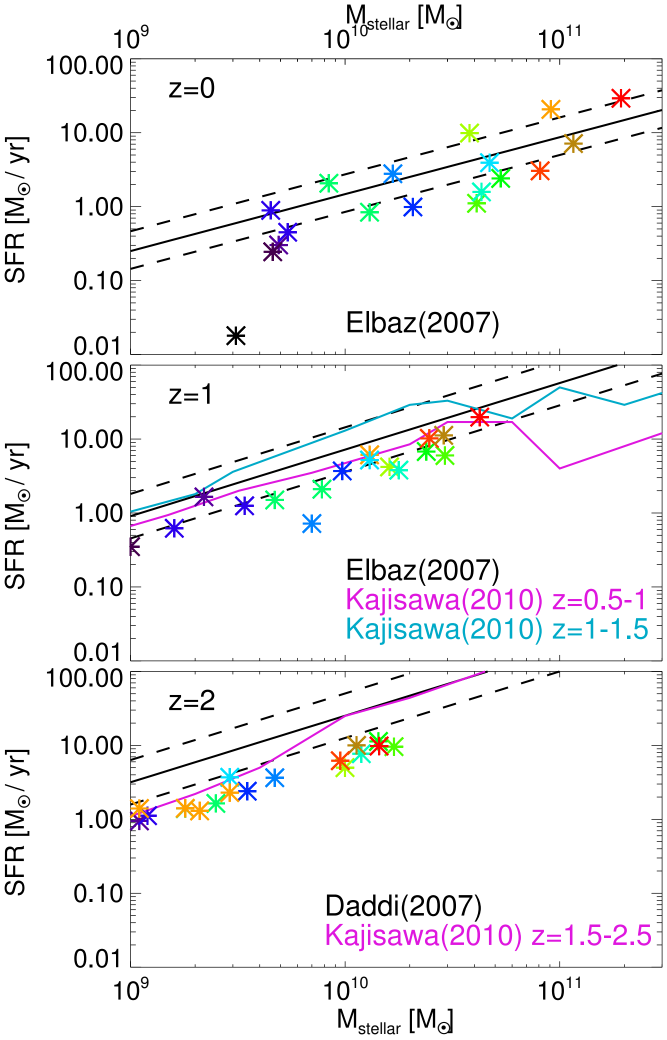

Figure 4.4: Star formation rates SFR at $z = 0$, $z = 1$ and $z = 2$ (averaged over 1 Gyr each) vs. stellar galactic mass $M_{\rm stellar}$ compared to the observed relations found by Elbaz et al. (2007) ($z = 0, 1$, black), Daddi et al. (2007) ($z = 2$, black) with 1σ errors represented by dashed lines and to median relations found by Kajisawa et al. (2010) (z=1,2, magenta and cyan).

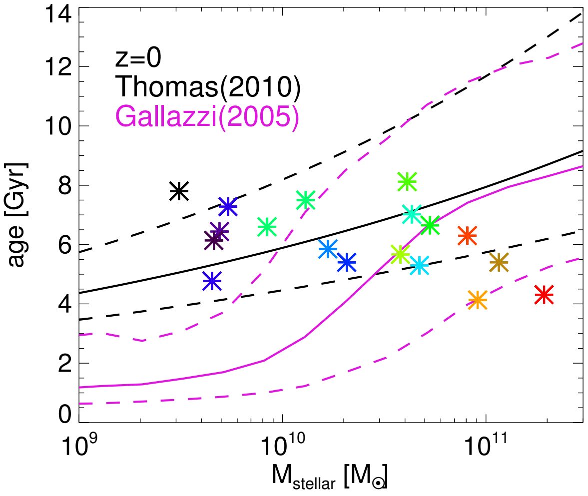

Figure 4.5: Mean mass-weighted $z = 0$ age of stars within 3 stellar half-mass radii R_{50} vs. stellar galactic mass M_{stellar} compared to the observed relation found by Gallazzi et al. (2005) for a magnitude-limited sample of galaxies (magenta lines). We also overplot in black the relation for the luminosity-weighted age of elliptical galaxies by Thomas et al. (2010). Dashed lines represent 1σ errors.

CS09. Note that the colour coding according to halo mass, which we apply here, is used for all appropriate figures throughout the chapter. For the haloes 2283 and 0977, which are undergoing major mergers at $z = 0$, we use the combined mass of the galaxies about to merge, as their dark haloes have already merged. At $z = 0$, the population as a whole agrees nicely with the halo occupation modelling by MNW13. However, there are trends in the sample that disagree. The four most massive haloes are $1 - 2\sigma$ high, whereas the lower mass galaxies show a tendency towards overly low mass.

The sample simulated with the CS09 code shows $z = 0$ stellar masses that are generally too high, but in reasonable agreement with MNW13 at lower halo mass. The strong discrepancy between the old code version and abundance matching results becomes better visible at higher redshifts, as in Fig. 4.1. The old code version yields stellar masses that for all haloes are more than 1σ high at $z \geq 1$, as was also shown for a large number of other codes in MNW13.

For the models simulated with our new code version, the situation at $z \geq 1$ is significantly different. Although there is still a tendency towards overly high mass at $z \geq 2$, all values are within 1σ uncertainties of the abundance matching results. At $z = 1$, our models show perfect agreement with MNW13, indicating that the problematic trends at $z = 0$ originate only at low z. We conclude that compared to the old code version and to compilations of previous simulations (e.g Guo et al., 2010; Sawala et al., 2011, CS12, MNW13), our results look promising.

We analyze the SFH problems further by separately plotting the SFHs of the most massive ($M_{200} > 1.55 \times 10^{12} M_\odot$), least massive ($M_{200} < 5. \times 10^{11} M_\odot$) and remaining haloes in Fig. 4.3. We determine SFHs by following the in-situ growth of the main progenitor of the $z = 0$ galaxy, so that accreted stars do not appear in the SFH. To be consistent with Fig.

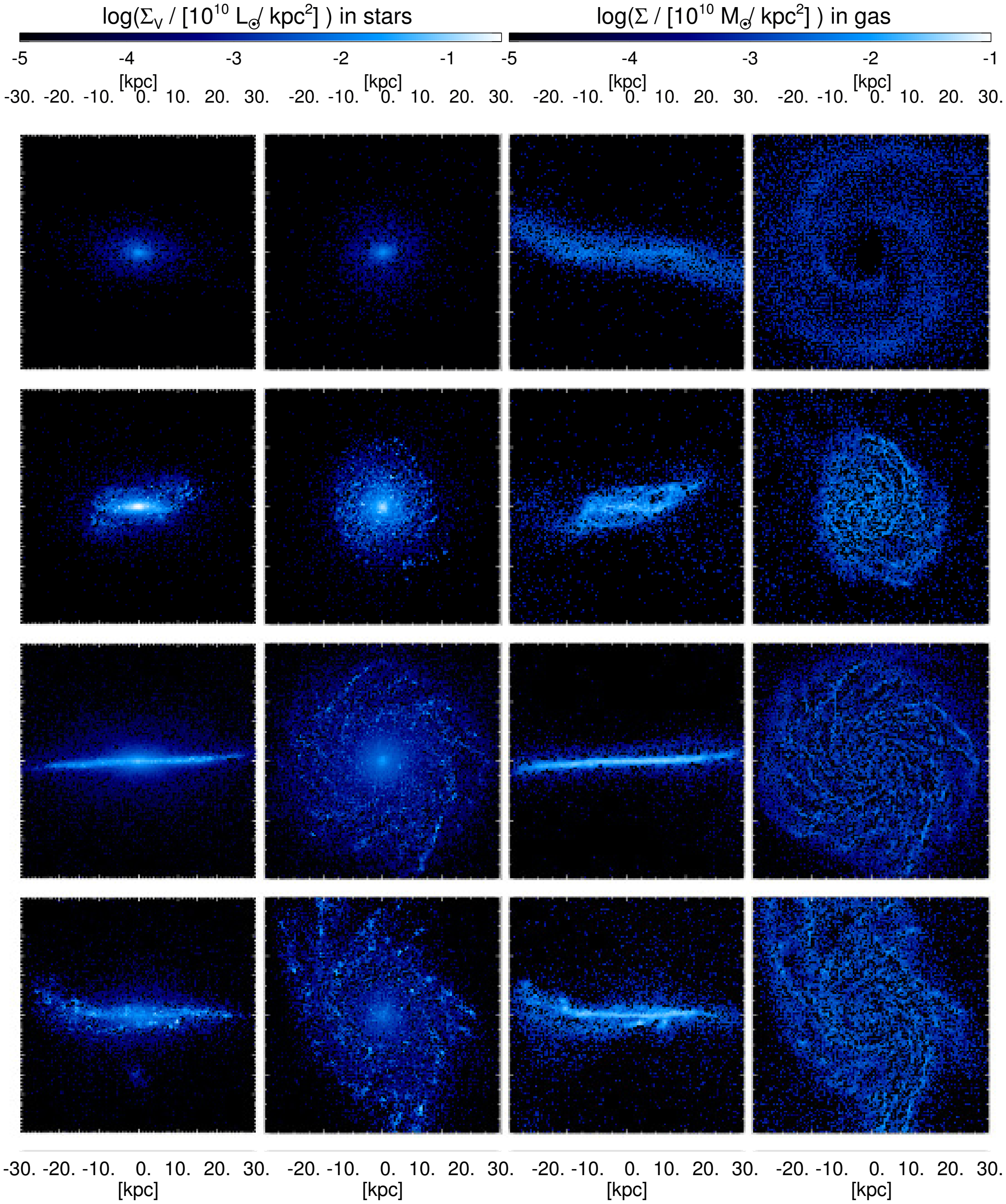

Figure 4.6: Edge- and face-on images of the $z = 0$ stellar V-band surface brightness Σ_V (left) and of the gas surface densities Σ for our model galaxies in haloes (top to bottom): 6782, 1646, AqB and one of the merging galaxies in 0977.

4.2, for the two $z = 0$ major merger haloes, we add up SFHs of the two merging galaxies. In each of the panels we overplot the predicted average SFHs for typical haloes of the lowest, mean and highest $z = 0$ halo mass in the panel as given in MNW13. These SFHs also do not include accreted stars. As discussed above, individual halo assembly histories can differ significantly from the assumed average assembly histories. The comparison can however reveal trends in the SFHs of our sample of simulated galaxies.

We start with the middle panel including AqC, which we have analyzed above. There is a trend for these haloes to overproduce stars at $z > 4$, with AqC showing the the highest SFRs, which are however mostly caused by its early assembly of mass. Otherwise this trend agrees with the slightly high stellar masses at $z \geq 2$. As a population, these haloes show reasonable later agreement, leading to the agreement found in Fig. 4.2 at $z \leq 1$. Probably due to the high-z overproduction, the predicted peak at $z = 1-2$ is not well reproduced by the models. Moreover, there is a small tendency towards underproduction at $z < 1$. Generally, the conclusions for this sub-sample are the same as for AqC alone.

For the low mass haloes in the left panel, there is hardly any overproduction at high-z, which might be connected to the lack of resolution and the consequently unresolved SF in small progenitor haloes. Tests with higher resolution indicate that high-z SFRs increase with resolution for these haloes. The sub-sample agrees with the predictions at $z \sim 0.5 - 5$, but late SFRs are low. This leads to the agreement with abundance matching at $z = 1$, but to the low $z = 0$ masses seen in Fig. 4.2.

The high-mass haloes in the right panel show a significant overproduction of stars at high redshift only for halo AqA, which has a similar mass assembly history to AqC. There is good agreement with predictions at $z \sim 0.8 - 4$. However, SFRs are significantly too high at later times and lead to high $z = 0$ stellar masses. We find that at these times there is still efficient inflow of gas onto the galaxies, but stellar feedback, as applied in our models, is too weak to efficiently remove gas from the discs, as most of the ejected gas returns in galactic fountains. AGN, which we do not model, are generally believed to stop hot halo gas from cooling onto galaxies at these redshifts in massive haloes, though typically for higher masses than in our sample (e.g. Croton et al., 2006).

To have a more direct comparison of our model SFRs to observation, we determine SFRs at $z = 0, 1$ and 2 for Fig. 4.4 by averaging over 1 Gyr of star formation each. We compare the corresponding values to the relations found by Elbaz et al. (2007) and Daddi et al. (2007) for observed SFRs vs. galaxy stellar masses. For the major merger models 2283 and 0977 we here separately include the merging galaxies. Apart from our least massive halo 6782, in which there is hardly any SF after $z \sim 0.4$, our model sample agrees well with observations and all model galaxies lie within 2σ of the observed relation at $z = 0$. The high-mass haloes do show a tendency for high SFRs, as expected, and the rest of the models show a slightly lower average than observed, as was also concluded from Fig. 4.3. It has to be noted, that the observations of Elbaz et al. (2007) and Daddi et al. (2007) only considered blue, star-forming galaxies, whereas the results of MNW13 are an average over blue and red galaxies.

At all three redshifts in consideration, the slope of the SFR vs. $M_{\rm stellar}$ relation constituted by our models is in good agreement with observation. At $z = 1$, where the different observations agree well, SFRs are typically $\sim 1\sigma$ low, which we can connect to the fact that our models do not reproduce the peak in the SFHs at $z = 1 - 2$ properly, but on average predict a flatter SFH. At $z = 2$, our model SFRs are $\sim 2\sigma$ low compared to the results of Daddi et al. (2007). Kajisawa et al. (2010) find lower SFRs at $M_{\rm stellar} < 10^{10} M_{\odot}$, which our lower mass galaxies agree with. The higher mass galaxies have significantly lower SFRs compared to

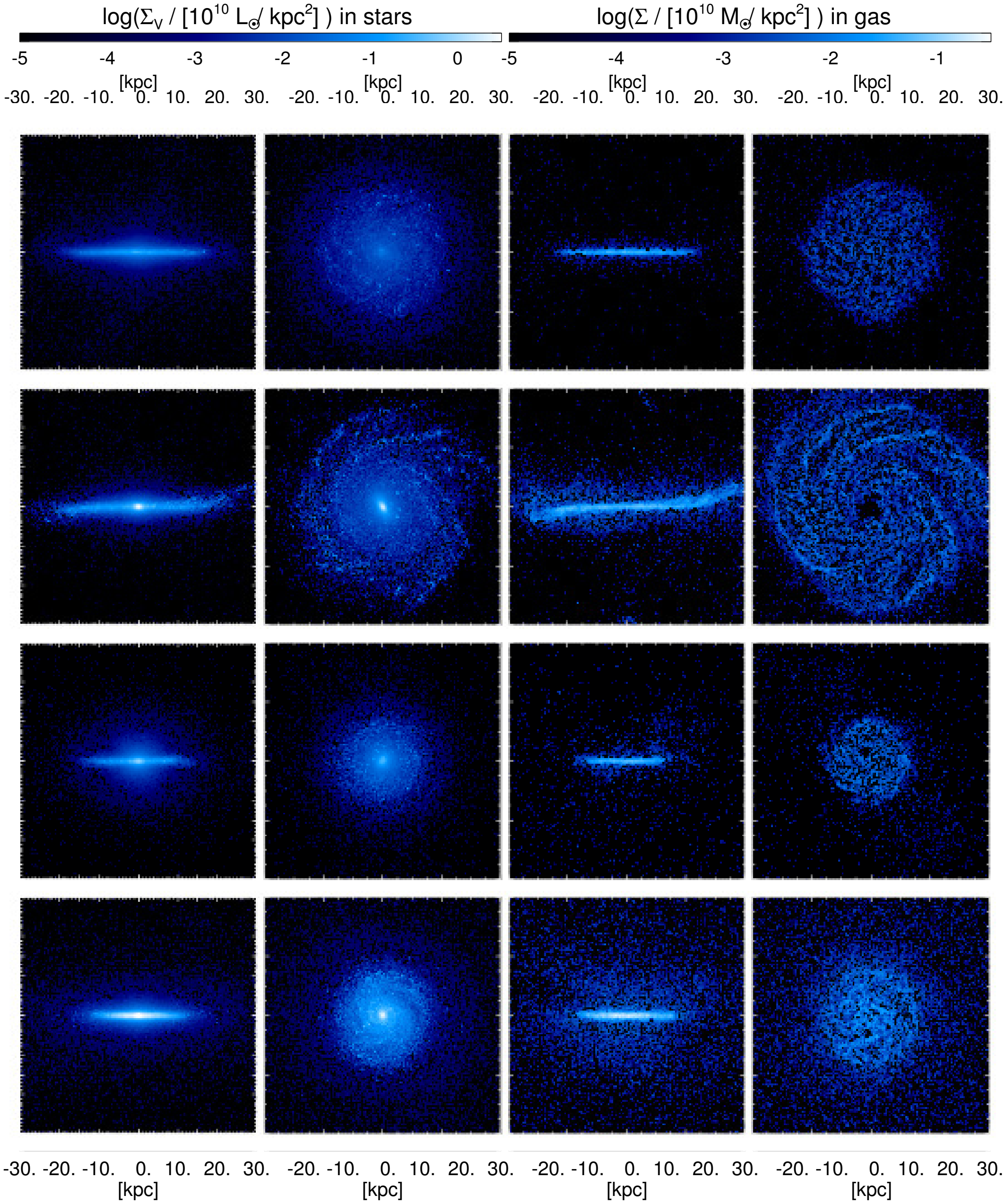

Figure 4.7: As in Fig. 4.6 for galaxies in haloes (top to bottom): AqD, 0959, 0664 and 0616.

these observations as well. This seems to disagree with the results from Fig. 4.3, where no deficiency at that time is apparent. If we take into account that the model stellar masses at $z = 2$ are slightly high, it seems reasonable to assume the measured SFRs together with stellar masses according to the MNW13 predictions from abundance matching. This can explain part of the discrepancy, but this is not enough to explain the full difference between observations and models. Interestingly, Kannan et al. (2013) found a similar discrepancy with observations for their galaxies in a simulation of a cosmological volume.

Another direct comparison to observations can be made for ages. We determine the mean age of populations within three stellar half-mass radii and compare them to two observational relations in Fig. 4.5. Gallazzi et al. (2005) provided an age-stellar-mass relation for a magnitude-limited sample of Sloan Digital Sky Survey (SDSS) galaxies, whereas Thomas et al. (2010) examined a sample of morphologically selected elliptical galaxies. This figure very clearly reveals the trends discussed above and a division of our sample in three parts. The trend of ages of all model galaxies with stellar mass is almost flat and thus disagrees with the full galaxy population. The Aquarius haloes and the other haloes with masses $\sim 10^{12} M_{\odot}$ are in reasonable agreement with both observational data-sets, which strengthens the conclusions about their well-modelled SFHs. The massive galaxies with high late SFRs only marginally agree with the youngest observed $M_{\star} \sim 10^{11} M_{\odot}$ galaxies. The lower mass galaxy models, which include the three haloes with lowest masses and the galaxies undergoing a major merger at $z = 0$, overlap with the observed elliptical galaxies, but are more than 1σ high compared to the Gallazzi et al. sample, which at these masses is dominated by discs.

In conclusion, our feedback model, calibrated on halo AqC, works well for all haloes with similar and slightly lower masses. These models show overly high SFRs only at high redshift. In the most massive haloes we studied, we find that SFRs are significantly too high at low redshift, possibly on account of the lack of a model for AGN feedback. For our lower mass galaxy models we find too low SFRs at $z < 1$, which makes the ages of their stellar populations too high for disc galaxies at these masses.

4.6 | Morphology and kinematics

After studying how the stellar mass assembles in our model galaxies, we now have a closer look at the morphology and the kinematics of their stellar components.

4.6.1 | Structural properties

We start by a visual inspection of galaxy morphologies. We use the models of Bruzual & Charlot (2003) to assign V-band luminosities to the stellar particles according to their mass, age and metallicity. We then create edge-on and face-on surface brightness Σ_V images for the stellar component without taking obscuration into account. We also create gas mass images and present the results for eight model galaxies at $z = 0$ in Figures 4.6 and 4.7 to display the variety of galaxy types produced in our simulations.

In Fig. 4.6 we present lower mass galaxies. All of these galaxies do show extended gas discs, as do observed disc galaxies (e.g. Walter et al., 2008). Moreover, the gas discs and, with the exception of 6782, also the stellar components do show warps of varying extent. Warps are also frequently observed in real galaxies (Sancisi, 1976). Considering our full

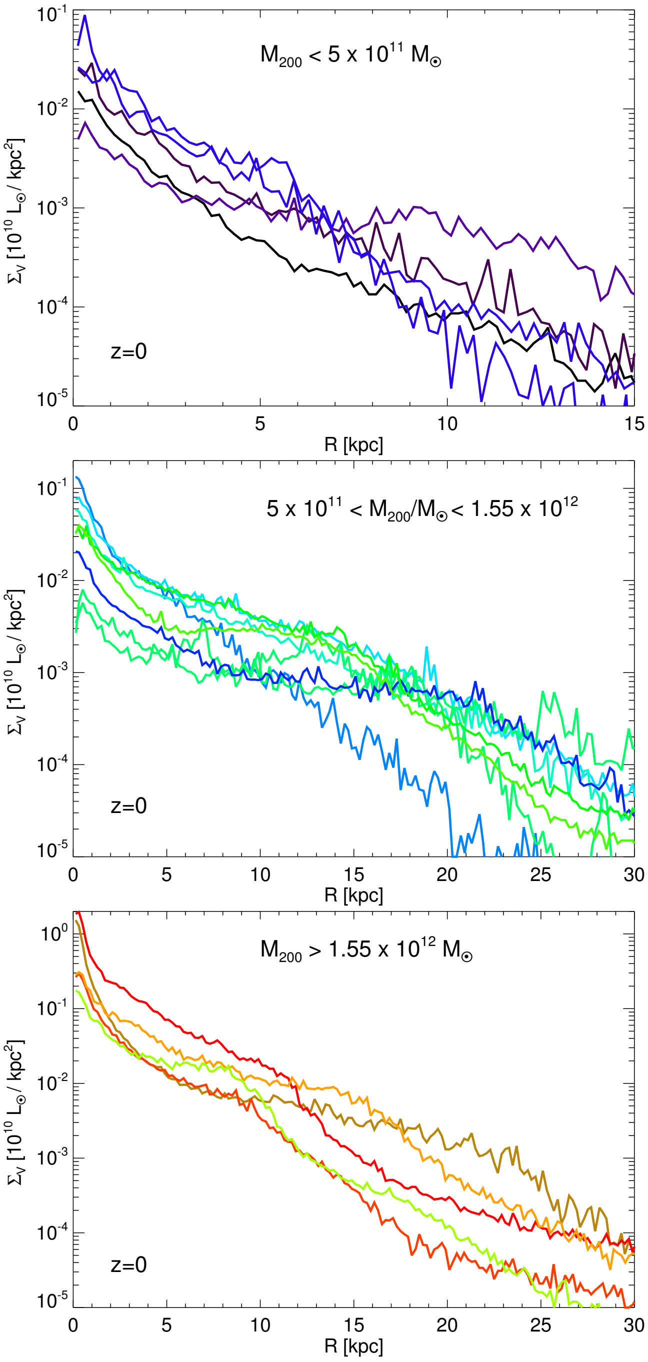

Figure 4.8: Radially averaged $z = 0$ face-on V-band surface brightness Σ_V as a function of radius R for all our model galaxies. We split the sample into three bins of halo mass: $M_{200} < 5 \times 10^{11} M_\odot$ (top), $5 \times 10^{11} M_\odot < M_{200} < 1.55 \times 10^{12} M_\odot$ (middle) and $M_{200} > 1.55 \times 10^{12} M_\odot$ (bottom).

sample of 18 galaxies in the 16 simulated haloes (2 each for 2283 and 0977), 10 galaxies show warps and 11 have gas discs that extend beyond the stellar populations.

The stars of the galaxy in our least massive halo 6782 (first row of Fig. 4.6) show an ellipsoidal distribution, which is only mildly flattened. The gas, however, lives in an extended, warped disc, which is dominated by two spiral arms. The gas disc has formed after a major merger at $z = 0.4$. Our model 1646 (second row) also shows elliptical morphology in stars, but the visible rotational flattening is higher. Moreover, there are signs of a disc and a misaligned ring. The gas displays a strongly warped, relatively compact disc with disturbed spiral structure. We will show below that this galaxy features strongly misaligned infall at $z \sim 0.1$ and a counter-rotating stellar population. Misaligned infall and reorientation of discs are frequent phenomena in our simulations. About half of the $z = 0$ discs have experienced reorientation of 40 degrees or more since they started forming.

Halo AqB (third row) hosts a very thin, extended stellar disc galaxy with flocculent spiral structure and a prominent bulge. The gas forms a very extended, slightly warped disc with spiral structure as in the stellar component. One of the discs in the major merger halo 0977 (fourth row) shows similarities to the one in AqB in terms of spiral structure and central bulge. However signs of the interaction with its neighbour are clearly visible. The system shows elongated tidal features and the stellar disc has been considerably thickened. The edge-on views reveal that the SF regions in the spiral arms do not lie in a well-defined plane as in AqB, but in projection superpose to create a thick disc.

In Fig. 4.7 we display four galaxies with higher masses. 0959 and 0616 show overly high SFRs at $z = 0$, whereas AqD and 0664 have reasonable $z = 0$ masses. For these galaxies, only 0959 (second row) shows an extended, warped gas disc. It also displays a prominent stellar bar and a multi-arm spiral pattern. Only three of our 18 $z = 0$ galaxies show clear signatures of bars, though more galaxies show bar signatures during their evolution. The $z = 0$ rate of bars is thus lower than in real galaxies (Eskridge et al., 2000). The model galaxy in halo 0664 (third row) has a low gas fraction with gas being confined to a compact, un-warped disc. The edge-on stellar morphology shows a disc and an underlying spheroidal distribution, the face-on image shows no distinct spiral structure. The morphology is thus reminiscent of S0 galaxies.

In the next subsection we will show that AqD has the highest kinematic disc fraction of all our model galaxies. The first row of Fig. 4.7 reveals a large stellar disc with a small bulge and faint spiral structure. The gas lives in a thin, un-warped disc, which is less extended than its stellar counterpart. The morphology of the galaxy in halo 0616 (fourth row) is clearly also discy and features spiral arms. However, the disc appears significantly thicker and more compact. The gas disc is also compact and thick explaining the high SFRs. Moreover, the gas distribution extends vertically beyond the disc. We find the gas to be inflowing as part of a galactic fountain.

Disc galaxies have long been known to show roughly exponential surface density profiles with central bulge concentrations (de Vaucouleurs, 1958). In the recent years, it has become clear that most of these exponentials actually consist of two or more parts which themselves are approximately exponential. Most of these breaks (or truncations) in profiles are down-bending, however a significant fraction of galaxies has up-bending profiles (see e.g. Martín-Navarro et al., 2012).

As the majority of our galaxies are discy, their profiles should show similar shapes, which indeed they do. In Fig. 4.8 we plot radially averaged face-on V-band surface brightness profiles for all our model galaxies and split them into three panels according to halo mass

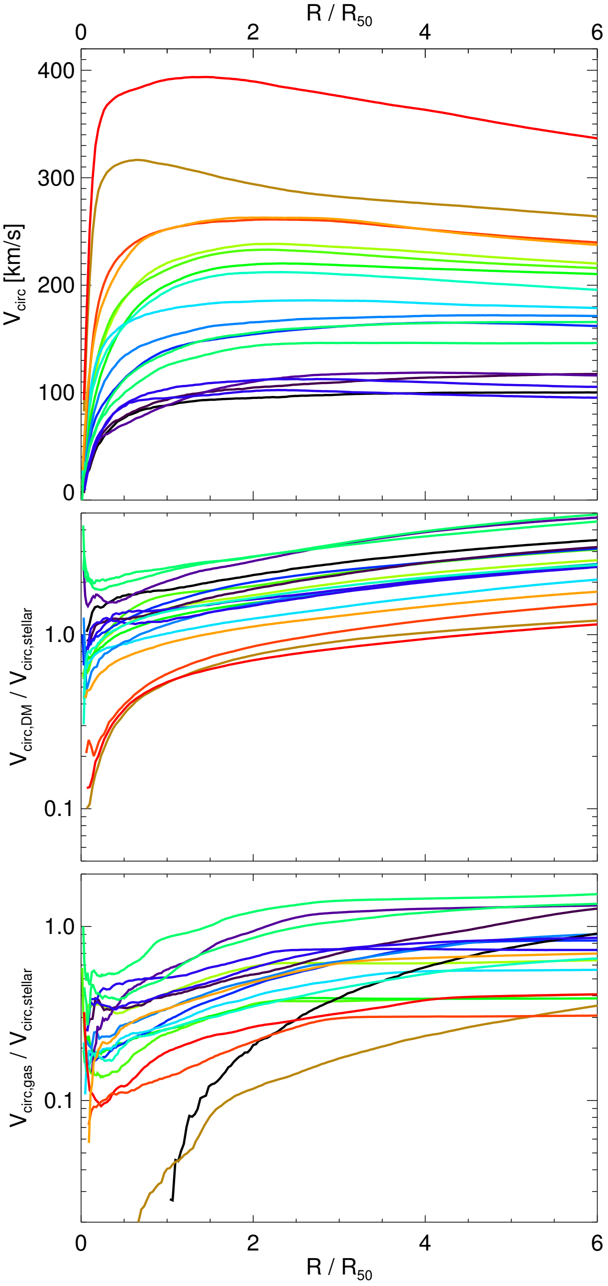

Figure 4.9: Spherically averaged $z = 0$ circular velocity $V_{\rm circ} = \sqrt{GM_{\rm tot}(< r)/r}$ for all our models (top panel). The middle panel shows the fraction of the contributions to $V_{\rm circ}$ by DM and stars $V_{\rm circ,DM}/V_{\rm circ,stellar}$, where $V_{\rm circ,i} = \sqrt{GM_i(< r)/r}$. The bottom panel depicts $V_{\rm circ,gas}/V_{\rm circ,stellar}$.

(note the different scales). We find several interesting details: The lower mass galaxies are less extended than higher mass galaxies, as observed (Courteau et al., 2007). Also most galaxies do show (almost) exponential parts in their profiles. As in real disc galaxies, the central excess is more pronounced for higher mass galaxies and there are low mass galaxies showing no or hardly any central upturn. Four out of 18 galaxies have profiles that can be fit with a single Sersic profile with $n \geq 1$, one of which could be classified as 'pure-exponential'.

Out of the galaxies with a central component, one has a single exponential outer component. In the remaining model galaxies, the disc components feature breaks. Nine of them are bulge+disc+down-bending profiles, but four of our massive galaxies (lower panel) show upturning features in their outskirts as well. So from a qualitative point of view, the distribution of surface brightness profiles is in reasonable agreement with observations.

Cosmological simulations of galaxy formation have long suffered from an over-concentration of baryons in the centres of haloes (Navarro & Benz, 1991). This is reflected by circular velocity $V_{\rm circ} = \sqrt{GM(<r)/r}$ curves that are strongly centrally peaked (see e.g. some models in CS12). Observed gas rotation curves of galaxies are, however, fairly flat or rising outwards in low mass disc galaxies (de Blok et al., 2008). To reproduce this observation, it has been shown that feedback models have to selectively remove low angular momentum gas (e.g. Brook et al., 2011).

In the top panel of Fig. 4.9 we plot circular velocity curves for all our model galaxies as a function of the radius normalized to the stellar half mass radius R/R_{50}. Only the two galaxies in 0959 and 0616, which show a strong overproduction of stars at low z and feature compact, thick gas-rich discs, show central peaks in $V_{\rm circ}$, but to a less severe extent than e.g. several models in CS12. The other galaxies indeed show very flat circular velocity curves with detailed shapes depending on the details of their formation histories. In general, our feedback mechanism is thus capable of producing realistic central mass distributions.

In the other panels of Fig. 4.9 we show the fractions of the contributions of DM, stars and gas to the $V_{\rm circ}$ curves. Clearly, the centrally peaked models are dominated by stars. It is interesting to note that there is a continuous transition in our galaxies from low-mass galaxies for which at all radii the gravitational potential is dominated by DM to more massive galaxies, which are star-dominated in the centres and for which DM becomes dominant at a radius that increases with galaxy mass. As far as gas is concerned, the baryonic contribution is dominated in the centres by stars for all galaxies. However, for low-mass, more gas-rich galaxies, the gas contribution surpasses the stellar contribution at the outskirts of the galaxies.

In summary, our model galaxies display a range of realistic morphologies in gas and stars. Unlike in many previous simulations, they are not too centrally concentrated and show no significant disagreement with observed galaxies in terms of radial surface density profiles and circular velocity curves.

4.6.2 | Circularity distributions

We now want to connect morphology to stellar kinematics. Circularity $\epsilon = j_{\rm z}/j_{\rm circ}(E)$ distributions (Abadi et al., 2003) are a tool that have been widely used to quantify stellar disks in simulations. Here $j_{\rm z}$ is the z-component of the specific angular momentum of a stellar particle in a cylindrical coordinate system with the disk axis as symmetry axis and $j_{\rm circ}(E)$ is the specific angular momentum of a particle of energy E on a circular orbit. Particles on circular orbits thus show $\epsilon = 1$ and a thin disk results in a peak close to this value. A bulge

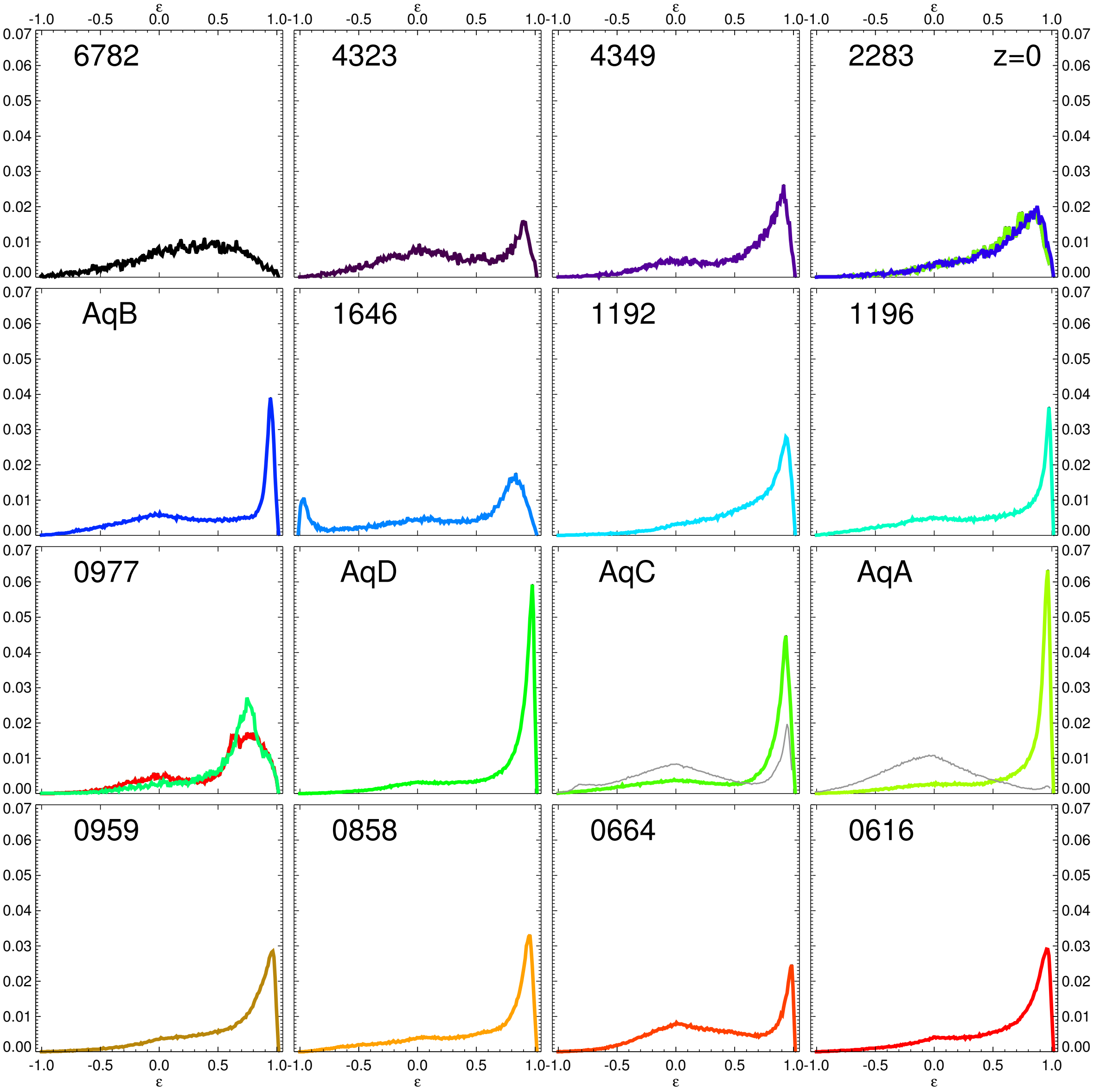

Figure 4.10: Distributions of circularity $\epsilon = j_z/j_{\rm circ}(E)$ for our model galaxies at $z = 0$. The panels for the mergers 2283 and 0977 contain distributions for both galaxies. For 2283 the two galaxies show almost indistinguishable distributions. For haloes AqA and AqC we overplot the ϵ-distributions for the corresponding models of CS09 in gray.

will results in a peak around $\epsilon = 0$. We have computed such distributions for all of our models and present them in Figure 4.10.

We notice, that apart from 6782, the lowest mass halo, all our models show distinct disc peaks. 6782 shows an asymmetric distribution indicating some rotational support, but no stellar disc, as we had observed in the first row of Fig. 4.6. The spheroid results from a major merger at $z \sim 0.4$ and a lack of SF afterwards. 4323 shows a small disc and a dominant bulge, whereas 4349 shows a broadened disc peak indicating a rather thick disc. Considering that all these haloes have overly low SFRs in the low-z era of disc formation, the lack of dominant thin discs is not surprising.

For the haloes with $z = 0$ major mergers, 2283 and 0977, we plot distributions for both galaxies. In each case they show very broad disc peaks, indicating that these are mergers of disc galaxies with similar masses. The galaxies are still separated, but the gravitational interaction has already considerably heated the stellar discs. The thickening of one of the galaxies in 0977 is clearly visible in the fourth row of Fig. 4.6.

The most peculiar distribution of circularities is exhibited by 1646. It consists of two discs with opposite directions of rotation that live on top of each other. The co-rotating disc is more massive, but is also considerably thicker than the young and relatively thin counter-rotating disc. Additionally, a distinct bulge peak is visible. This composition explains the disturbed and more elliptical morphology visible in the second row of Fig. 4.6. The model galaxy in halo 1192 shows a disc peak with a wide tail to lower values of ϵ, which is connected to a bar present throughout the evolution of the disc.

Among the most massive haloes, 0664 has the lowest low-z SFR and a correspondingly small disc peak, which has formed after a merger at $z \sim 0.7$. The circularity distribution is dominated by a broad bulge peak resulting from the merger. This explains the S0-like morphology seen in Fig. 4.7. 0959, 0858 and 0616 show dominant disc peaks with tails to lower values of ϵ indicating rather thick discs. The ϵ distribution of 0959 is shaped by the presence of a bar (see Fig. 4.7), whereas the discs in 0858 and 0616 are heated by minor mergers occurring throughout their evolutions. The bottom row of Fig. 4.7 correspondingly shows a compact and thick stellar disc in 0616.

The most dominant and thinnest disc peaks indicating high fractions of thin, star-forming discs can be found in the panels for the Aquarius haloes. Of the haloes from Oser et al. (2010), only 1196 shows a comparably thin disc peak, which however only forms after a merger at $z \sim 0.7$. This is not surprising, as the Aquarius haloes were selected to be prime candidates to host such galaxies. However, CS09 were not able to completely confirm this conception in their study of all haloes, as their highest kinematic disc fractions were $\sim 25\%$. Higher disc fractions were found for different codes for AqC in CS12, but these galaxies did not compare well to observed disc galaxies. Okamoto (2013) presented the best Aquarius cosmological disc models so far for haloes AqC and AqD, their circularity distributions are however less disc dominated than ours. Considering the idealized, semi-cosmological models in AqA and AqC from Chapter 3, our cosmological simulations produce disc fractions similar to the reference model ARef, but not as good as the best models presented there. This is not surprising, as these models ignore the evolution at $z > 1.3$, when destructive mergers occur.

To illustrate the change in circularity distributions between the models of CS09 and our models, we over-plot in Fig. 4.10 the corresponding curves for their models of AqA and AqC in gray. For AqA they found hardly any disc and correspondingly the difference between their bulge-dominated and our disc-dominated model is very prominent. For AqC they found

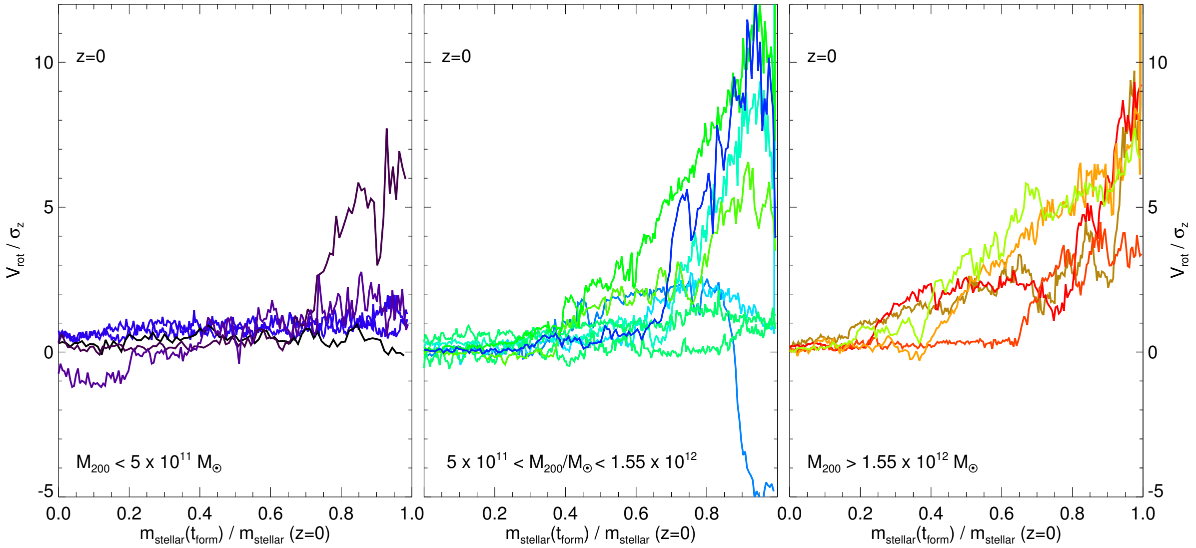

Figure 4.11: Rotation-to-dispersion ratios $V_{\rm rot}/\sigma_z$ at $z = 0$ as a function of the fraction of stellar galactic mass that has formed until the formation time $t_{\rm form}$ of a star particle relative to the stellar galactic mass at $z = 0$. Our model galaxies are split into three bins in halo mass: $M_{200} < 5 \times 10^{11} M_\odot$ (left), $5 \times 10^{11} M_\odot < M_{200} < 1.55 \times 10^{12} M_\odot$ (middle) and $M_{200} > 1.55 \times 10^{12} M_\odot$ (right).

their highest disc fraction, but the increase in disc fraction by a factor of almost 3 is still clearly visible. This comparison clearly favours the use of very efficient feedback recipes in simulations. However, we note that more conservative approaches to feedback models have also been successful in producing distinct disc peaks in circularity distributions (see e.g. Governato et al., 2007; Few et al., 2012).

In summary, our models show a large variety of kinematic properties ranging from rotating spheroids, bulge-dominated discs and counter-rotating components over discs thickened by misaligned infall, bars and mergers to compact massive discs and dominant thin discs.

4.6.3 | Disc Fractions

Disc fractions in simulations are sometimes quantified by mock photometric surface brightness decompositions (see e.g. Agertz et al., 2011; Guedes et al., 2011). Scannapieco et al. (2010) showed that this way of estimation yields significantly higher disc fractions than kinematic decompositions. In this work, we focus on kinematic disc fractions as they constitute a more fundamental characteristic of the stellar population.

To have a direct comparison to the models presented in CS12 we have calculated distributions of circularities ϵ_V according to their definition based on the local circular velocity of a stellar particle. We then determined the fraction $f_\epsilon = \epsilon_V > 0.8$. For AqC we find $f_\epsilon = 0.55$. All models in CS12 showed $f_\epsilon < 0.55$, with the highest values occurring in galaxies with centrally peaked rotation curves. Moreover, our ϵ_V distribution for AqC shows a higher ratio of disc peak to bulge peak than those galaxies. We thus conclude that our model produces a better disc than any of those models.

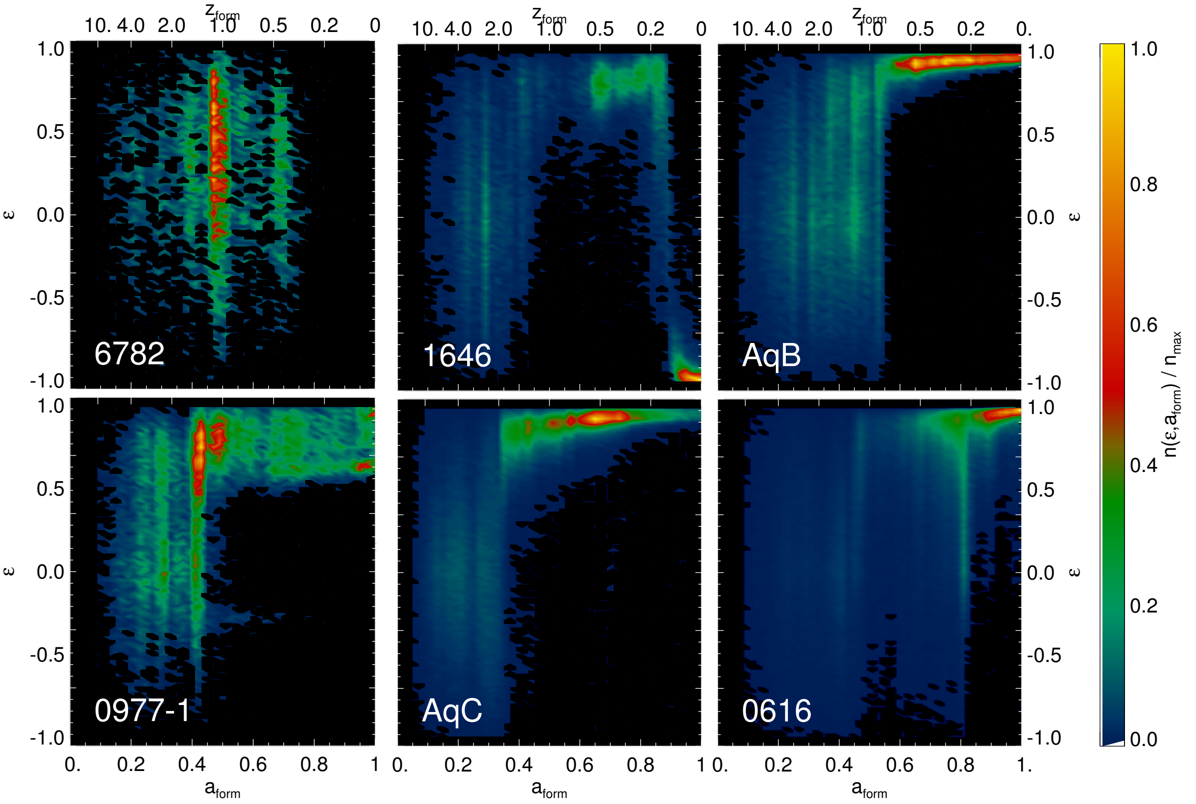

Figure 4.12: The normalized number densities of the stars in six of our galaxy models at $z = 0$ over the plane of circularity ϵ vs. formation scale factor $a_{\rm form}$, $n(\epsilon, a_{\rm form})/n_{\rm max}$. The models are from top to bottom: 6782, 1646, AqB, one of the two merging galaxies in 0977, AqC and 0616.

In Chapter 3 we argued that rotation-to-dispersion ratios are a good additional tool to characterize discs. We sort all stars in a galaxy as a function of age and bin them in equal-mass bins. We define a disc plane perpendicular to the total stellar angular momentum and calculate $V_{\rm rot}$ as the mean tangential velocity and σ_z as the rms velocity in the direction of the rotation axis for all stars in a certain age bin. In Fig. 4.11, we plot the ratio $V_{\rm rot}/\sigma_z$ as a function of the fraction of the $z = 0$ stellar mass that has formed up to the time in consideration. We again split the models into three bins according to halo mass and include two galaxies per major merger halo.

The idealized disc models from Chapter 3 showed a monotonic decrease of $V_{\rm rot}/\sigma_z$ with increasing age. However, these models did not include mergers, which for all haloes occur at high z. We thus expect an additional component with $V_{\rm rot}/\sigma_z \sim 0$ for the oldest ages. Moreover, the idealized models showed that, at the resolution in consideration, values of $V_{\rm rot}/\sigma_z >> 10$, as they are observed for the Milky Way thin disc (e.g. Aumer & Binney, 2009), are prevented by the coarse resolution and the specifics of the modelling of ISM physics (see also House et al., 2011). In general, populations of stars with $V_{\rm rot}/\sigma_z > 2$ can be interpreted as discy and the plot can thus be used to estimate disc fractions.

Significant counter-rotating components are only found for the 15 % youngest stars in

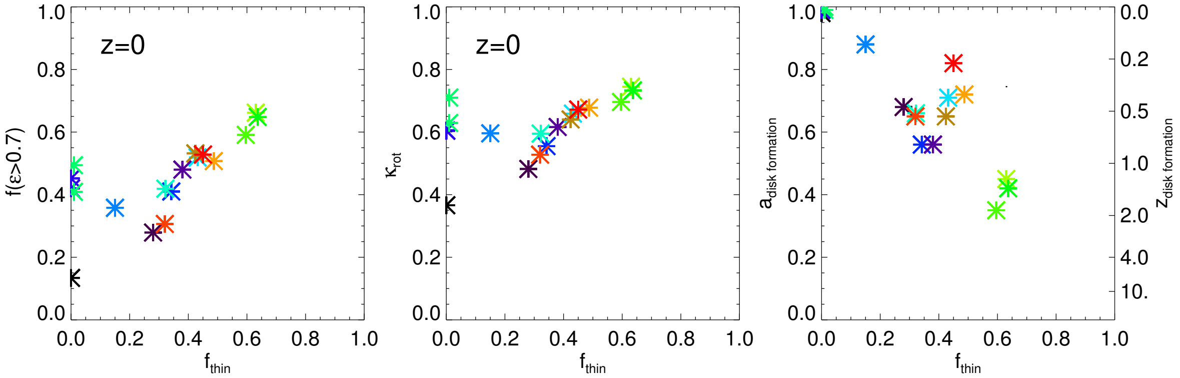

Figure 4.13: An overview of the disc fractions at $z = 0$ in our model galaxies. In all panels we compare to our definition of thin disc fraction $f_{\rm thin}$ given by the mass fraction in the 'thin disc area' of the ϵ-a plane (see Fig. 4.12). The left panel shows $f(\epsilon > 0.7)$, the fraction of stars with circularity $\epsilon > 0.7$, the middle panel the fraction of the kinetic energy in rotation $\kappa = E_{\rm rot}/E_{\rm kin}$, as defined by Sales et al. (2011) and the right panel the scale factor when disc formation starts, $a_{\rm discformation}$.

1646 as discussed above and for the mildly (counter-)rotationally supported oldest bulge component of 4323. All models show dispersion-dominated bulge populations for their oldest components, as expected. For the low mass haloes, only 4349 shows a significant 'thin' component with $V_{\rm rot}/\sigma_z > 5$. The merger-thickened discs in haloes 2283 and 0977 show $V_{\rm rot}/\sigma_z < 2$ for all populations and the disc populations of 1192 and 1646, which suffer from a bar or misaligned infall, all show $V_{\rm rot}/\sigma_z < 5$. So, as suggested in Chapter 3, misaligned infall or reorientation of the disc plane heats existing stellar populations and prevents the formation of thin discs.

All other haloes show distinct disc populations as discussed for Fig. 4.10. The highest ratios $V_{\rm rot}/\sigma_z \sim 10$ are displayed by the discs in AqB and AqD, but the massively star-forming discs in the most massive haloes also reach $V_{\rm rot}/\sigma_z \sim 8$. If discs are present, their $V_{\rm rot}/\sigma_z$ ratios decrease almost monotonically with age, a sign for continuous disc heating (e.g. Jenkins & Binney, 1990), as discussed in Chapter 3. The discs with the highest fractions of populations with $V_{\rm rot}/\sigma_z > 2$ are AqA and AqD with fractions similar to 60 %.

To gain a better understanding for the formation times of stellar disc components in our simulations, we present in Fig. 4.12 the distribution of stellar mass in the plane of circularity ϵ vs. formation scale factor $a_{\rm form}$. We present six different models to give an overview of how different evolution histories show up in this plot. The SFH of 6782 is bursty and stops at $z \sim 0.4$, when a major merger occurs. Stars of all ages show a similar distribution of circularities, which characterizes an elliptical galaxy with small net rotation.

A merger is still ongoing in halo 0977. Here we see two-stage formation. The stars that formed at $z > 1.3$ show a bulge distribution similar to 6782, whereas all younger stars live in a disc, which has been disturbed by the ongoing merger. The galaxy in 1646 shows three-stage formation. Again stars that formed at $z > 1.3$ live in a bulge, whereas stars that formed at $1.3 > z > 0.15$ make up a thick disc. In this case the disc was heated by a drastic change in the angular momentum orientation of the infalling gas starting at $z \sim 0.25$. This reorientation results in the formation of a thinner counter-rotating disc.

In 0616 the picture is more complicated. Stars at all formation times $a < 0.8$ show a broad bulge distribution. At $a = 0.8$, a last destructive merger occurs. However, there is an older disc population, formed at $0.6 < a < 0.8$, that has survived thickened by the merger. A thinner disc forms after $a = 0.8$, but there are also young stars with thick disc circularities, which are connected to ongoing interactions with satellite galaxies after $a = 0.8$.

This is not the case for the discs in AqB and AqC. For both a dominant disc population is visible at high ϵ after some well-defined time when formation starts, which for AqB is a destructive merger at $z \sim 1$. In AqC disc settling starts around $z = 2$, when mergers stop disturbing the galaxy. The disc populations widen in ϵ for older ages, again indicating continuous disc heating.

These ϵ vs. a plots provide us with a good procedure to define disc fractions. We can define a 'disc area' in this diagram, which for AqB is clearly given by $a > 0.55$ and $\epsilon > 0.8$. The lower border for ϵ is not well-defined, however $\epsilon \sim 0.75$ works well for all examples. We hereby also define a time when disc formation starts. With this definition, 6782 and 0977-1 have no discs, the latter as the stellar system has been significantly heated by the ongoing merger. We therefore refer to this definition of disc fraction as 'thin disc fraction' $f_{\rm thin}$, but caution that observed thick discs would not necessarily be excluded by this method.

For 1646, the counter-rotating disc is counted as the thin disc and for 0616 only the disc that formed at $a > 0.8$ is included. We use this procedure to determine $f_{\rm thin}$ for all model galaxies and use the values in Fig. 4.13. In the right panel we plot disc formation time $a_{\rm form}$ against $f_{\rm thin}$. The values for $f_{\rm thin}$ range between 0.15 (the counter-rotating disc in 1646) and 0.64 (AqA and AqD). We clearly see a correlation in the sense that younger discs have smaller mass fractions, which is not surprising. It is however interesting to have qualitative predictions for the connection of the time of the last destructive event and the final disc fraction. It is also interesting that the best discs in the Aquarius haloes AqA, AqC and AqD separate from the rest of the population indicating that their selection criteria indeed yielded haloes which host dominant disc galaxies.

We also compare to previously used definitions to quantify discs. CS12 used all stars with $\epsilon_V > 0.8$. We find that for our definition of the circularity $\epsilon > 0.7$ gives similar results. From the left panel in Fig. 4.13 we see a clear correlation between the two disc fractions. However, a simple ϵ cut assigns a disc fraction to the thick merging systems, as well as to the elliptical galaxy 6782. Sales et al. (2011) used the fraction of kinetic energy in rotation $\kappa = E_{\rm rot}/E_{\rm kin}$ as an indicator for disciness. κ increases with increasing $f_{\rm thin}$ except for ongoing mergers.

In conclusion, we have shown, how rotation-to-dispersion ratios and the distribution of stars in the plane of circularity vs. formation time can be used to connect the kinematics and the formation history of model galaxies. Our galaxies are not as dynamically cold as real galaxies due to numerical issues. However, they realistically show that the oldest components of galaxies are dispersion dominated and that rotational support increases with decreasing age of stars, as observed in disc galaxies. We have shown that the model disc fractions in our Aquarius galaxies are higher than in any previously published simulation for these haloes. The disc fraction in our simulations depends mostly on the time since the last destructive event, be it merger or misaligned infall.

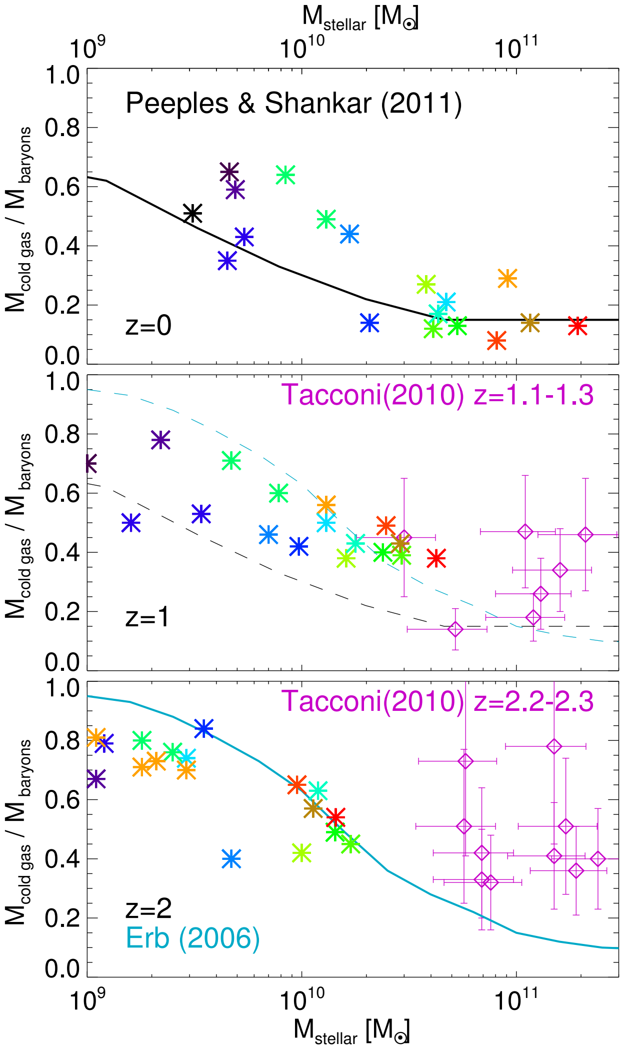

Figure 4.14: The fraction of the mass in gas with $T < 10^4$ K to total baryonic mass within 20 kpc vs. the galactic stellar mass $M_{\rm stellar}$ at redshifts $z = 0, 1$ and 2. Overplotted are the observed mean $z = 0$ relation presented by Peeples & Shankar (2011), an approximate relation for $z = 2$ obtained from the results of Erb et al. (2006a) and data from Tacconi et al. (2010).

4.7 | Scaling Relations

We continue our study of the galaxy population constituted by our models and have a look at how they compare to observed relations involving stellar and gas masses, rotation velocities, sizes and metallicities.

4.7.1 | Gas fractions

Observed gas fractions in $z = 0$ galaxies show a clear trend of higher gas fractions at lower galaxy masses (Haynes & Giovanelli, 1984, see Peeples & Shankar, 2011 for a recent compilation of data). At $z = 1 - 2$, Tacconi et al. (2010) using measurements of CO showed that gas fractions at a given stellar galactic mass are on average significantly higher. They, however, analyzed galaxies more massive than the ones in our simulations. Erb et al. (2006a) provided gas fractions for lower mass $z \sim 2$ galaxies by estimating the gas mass applying the local Kennicutt-Schmitt relation to SFR measurements. At higher masses, they found significantly lower gas fractions than those measured by Tacconi et al. (2010).

These observations provide an important test for our models of star formation and feedback in the context of cosmological gas accretion. SF uses up gas, whereas feedback can prevent gas from cooling and thus forming stars or eject gas from galaxies. Ejected gas can leave the halo if energetic enough or come back in galactic fountains. Clearly, inappropriate modelling of these processes can thus be identified from such a relation.

In Fig. 4.14 we attempt such a comparison. We determine the mass of gas with $T < 10^4$ K within 20 kpc and use it to determine the fraction of cold gas to total baryonic mass in the galaxy. At $z = 0$, our simulations reproduce the observed decrease in gas fraction with increasing stellar mass which becomes shallow or potentially flat at masses $M_\star > 10^{10.5}\ M_\odot$. For the shallow part of the relation, the gas fractions in our model galaxies scatter around ~ 15 %, as in real galaxies. For the lower mass galaxies, gas fractions can be as high as 65 % and the low-mass population in total shows a higher mean than observed. The low-mass galaxies that lie significantly above the relation all live in haloes which show low stellar masses in the $M_{\rm stellar} - M_{200}$ relation discussed in Fig. 4.2. Thus for these galaxies, the low SFRs at low z lead to an underproduction of stars despite a significant reservoir of gas in the model galaxies. This inefficient SF then leads to overly high gas fractions at $z = 0$.

As in real galaxies, the gas fractions in our model galaxies at fixed $M_{\rm stellar}$ steadily increase when going to redshifts $z = 1$ and 2. At $z = 1$, the gas fractions for $M_{\rm stellar} < 10^{10} M_\odot$ are intermediate to the $z = 0$ and $z = 2$ observational constraints. For $M_{\rm stellar} > 10^{10} M_\odot$, the gas fractions agree well with the observations of Tacconi et al. (2010). At $z = 2$, our models lie on top of the observational relation provided by Erb et al. (2006a), with only a slight discrepancy towards low gas fractions for the lowest stellar masses, consistent with the fact that these galaxies show too high stellar masses at these times. Considering the gas fractions measured by Tacconi et al. (2010) for higher mass galaxies, our gas fraction in higher mass galaxies at $z = 2$ appears too low. Narayanan et al. (2012) recently reported a similar discrepancy for the simulations of Davé et al. (2010). They argue that this discrepancy arises from an overestimation of gas fractions based on incorrect CO-to-$\rm H_2$ conversion factors.

In summary, the evolution of gas fractions in our model galaxies reproduces observed trends well. Deviations from observational data can be linked to deviations from the predicted SFH and uncertainties in high-z observations.

4.7.2 | Sizes

Another important test for galaxy formation models is the size distribution of galaxies. Galaxy sizes depend on the distribution of baryonic angular momentum and reproducing this distribution is crucial for achieving correct morphologies, and thus also SFRs, gas fractions etc. Cosmological simulations have long suffered from an over-concentration of low angular momentum material in the centres of haloes (Navarro & Benz, 1991). It has been shown that in order to reproduce observed galaxy sizes the invoked feedback mechanism has to preferentially remove gas with low angular momentum (Dutton & van den Bosch, 2009). Thus feedback modelling is effectively tested by galaxy sizes.

In Fig. 4.15 we attempt a comparison of our galaxy model sizes with observations by Shen et al. (2010) for SDSS late-type galaxies and by Nagy et al. (2011) for $z = 1.5 - 3.0$ star-forming galaxies. The half-mass radius R_{50} of observed galaxies at all redshifts increases on average with galaxy stellar mass $M_{\rm stellar}$. Nagy et al. (2011) find that galaxy sizes at a given $M_{\rm stellar}$ increase with time, being $\sim 41\%$ smaller than local galaxies at $z = 2.0 - 2.5$ and $\sim 27\%$ smaller at $z = 1.5 - 2.0$. This suggests that around $z = 1$ galaxies start to lie on the local relation (see also Barden et al., 2005).

For our model galaxies, we also detect such an increase of R_{50} with time. At $z = 2$, the sizes scatter around values similar to those found by Nagy at $z = 1.5 - 2.0$, whereas at $z = 1$ and at $z = 0$ they scatter around the $z = 0$ relation. At $z = 1 - 2$, the increase of R_{50} with stellar mass also agrees well with observations. At $z = 0$, our models lie on an overly flat relation. We already showed that the most massive haloes in our sample at $z = 0$ host compact, overly star-forming galaxies. Here these galaxies explicitly appear as too small. On the other hand, our sample also includes two major mergers. The two galaxies in halo 0977 show elongated features due to their gravitational interactions and thus are most extended relative to the observations. Ignoring these model galaxies yields a relation with reduced scatter and a clear trend of increasing size with increasing mass, which is, however, still shallower than observed.

Considering the connection of sizes and feedback modelling, we note that our prescriptions are capable of reproducing observed galaxy sizes well at $z \geq 1$, but tend to be too strong at late times in removing low angular momentum gas in haloes with $M_{200} < 0.7 \times 10^{12} M_\odot$ and too weak in haloes with $M_{200} > 1.6 \times 10^{12} M_\odot$.

4.7.3 | The baryonic Tully-Fisher relation

The luminosities and rotation velocities of disc galaxies are strongly correlated, they lie on the Tully-Fisher relation (Tully & Fisher, 1977). In recent years, it has been shown that using the total baryonic mass instead of luminosity yields a tighter correlation (McGaugh, 2012). As McGaugh gives a relation that is among the steepest and tightest found in the literature, we also consider the observational results of Avila-Reese et al. (2008) and Hall et al. (2012), who find shallower slopes and significantly more scatter. We attempt to compare to these observational relations in Fig. 4.16. We plot the mass of stars and gas within $r_{\rm gal}$ (as defined in Section 4.5.2) against the circular velocity $V_{\rm circ} = \sqrt{GM(<r)/r}$ at $r = 4\ R_{50}$. We use this radius, as McGaugh (2012) use measurements of velocities where rotation curves are flat, which is well reproduced by our choice as depicted in Fig. 4.9. Note that Avila-Reese et al. (2008) use the maximum rotation velocity and Hall et al. (2012) use the velocity at half light radius. Only for the most massive, compact galaxies in our sample, which overproduce

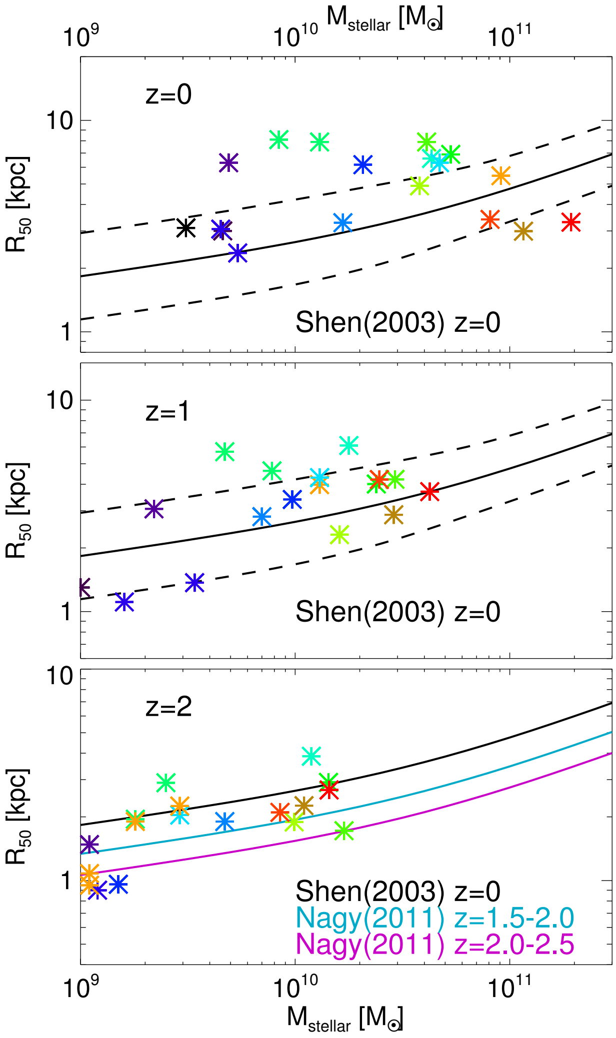

Figure 4.15: Stellar half-mass radius R_{50} vs. galactic stellar mass $M_{\rm stellar}$ at redshifts $z = 0, 1$ and 2. Overplotted in all panels is the observed relation for late-type SDSS galaxies by Shen et al. (2003) for $z = 0$ with 1σ scatter denoted by dashed lines. Nagy et al. (2011) find that galaxies at $z = 1.5 - 2.0$ are typically 27 % and galaxies at $z = 2.0 - 2.5$ typically 42 % smaller than galaxies of the same mass at $z = 0$. We overplot the corresponding lines in the $z = 2$ panel.

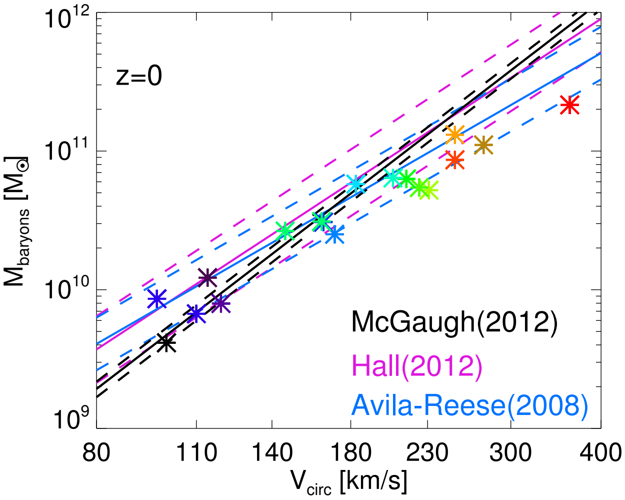

Figure 4.16: Baryonic mass within $r_{\rm gal}$ vs. circular velocity $V_{\rm circ} = \sqrt{GM(<r)/r}$ at $r = 4R_{50}$ at $z = 0$. Overplotted are the observational results from McGaugh (2012) (black), Hall et al. (2012) (magenta) and Avila-Reese et al. (2008) (cyan) for the so-called baryonic Tully-Fisher relation with 1σ deviations represented by the dashed lines.

stars at low z, would a different choice of radius alter the data-points significantly. A different choice for the radius within which we consider the baryonic mass does also not change our conclusions.

The baryonic Tully-Fisher relation is intrinsically connected to the $M_\star - M_{\rm halo}$ relation discussed in Fig. 4.2 and to the gas fractions discussed in Fig. 4.14. Moreover, as was shown e.g. in CS12, the correct distribution of matter and thus the sizes of galaxies as discussed in Fig. 4.15, also play an important role. The Tully-Fisher relation is thus a good test for the interplay of the model ingredients included in our galaxy formation code. Considering that for all the mentioned figures we found at least reasonable agreement with observations, with smaller deviations, we expect also to find this in Fig. 4.16. Compared to McGaugh (2012), this is not, however, the case. Only a minority of galaxies lies within 1σ of these observations and the power-law slope constituted by our model sample is closer to 3 as advocated by Avila-Reese et al. (2008), and not 4 as found by McGaugh (2012). Due to the greater scatter found by Hall et al. (2012), our galaxies are marginally consistent with their results, and there is good agreement with the results of Avila-Reese et al. (2008).

Considering that the power-law slope of the relation given by our model galaxies is smaller than most observations, it is interesting to discuss the trends. The most massive galaxies have too high rotation velocities for their masses. This agrees with the fact that they are too compact for their baryonic mass. There is a weaker trend for low-mass galaxies to lie above the relation, possibly connected to overly efficient feedback for these haloes preventing a further concentration of the halo.

In summary, our model galaxy sample shows a power-law slope for the baryonic Tully-Fisher relation that agrees only with the lowest in the range of values found observationally. The deviations from the relation can be connected to the remaining fine-tuning problems for the feedback mechanisms which have already been discussed in the previous sections.

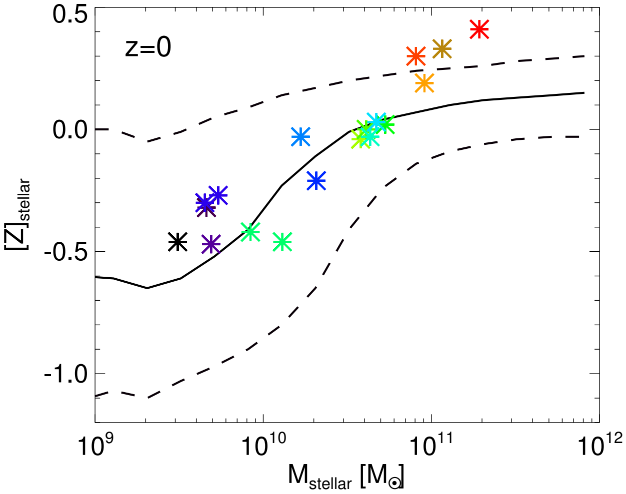

Figure 4.17: Mean mass-weighted galactic stellar metallicity within $r = 3\ R_{50}$, $[Z]$ vs. stellar galaxy mass $M_{\rm stellar}$ at $z = 0$ compared to the observational results of Gallazzi et al. (2005)

4.7.4 | Metals

Another way to test how well the complex interplay of gas accretion, star formation, galactic winds and gas recycling is modelled, is to consider the amount of metals stored in the galactic stars and gas. Metals are produced in stars and returned to the ISM in stellar explosions or winds. Thus metal production and energetic feedback are intrinsically coupled. Consequently, galactic winds are an efficient way to get metals out of galaxies. However, the metals in outflows can diffuse into hot halo gas and re-accrete, alternatively, outflowing material can return in galactic fountains, providing ways for ejected metals to re-enter the galaxy. Moreover, the metal content of galactic gas can be diluted by the accretion of pristine gas. Basically all ingredients in our galaxy formation simulations have a direct influence on the galactic metallicities.

Whereas gas metallicities probe cumulative effects over the whole evolution of galaxies, stellar metallicities contain probes from every stage in galaxy formation. In Fig. 4.17 we attempt a comparison of the mean stellar metallicities of our model galaxies to the observational data of Gallazzi et al. (2005). Apart from the overly metal-rich massive galaxies, the sample agrees well with observations and reproduces the slope of total stellar metallicity $[Z]$ with stellar mass.

The picture is different however for gas phase metallicities, which we explore in Fig. 4.18. The observed relations are quite uncertain in their calibration, which is why different authors find deviations of up to 0.3 dex in the normalization of the relation of oxygen abundance $12 + log(O/H)$ versus galaxy stellar mass. The slope also differs, but too a smaller amount. Typically, quoted 1σ errors at $z = 0$ are of the order 0.1-0.2 dex depending on mass and calibration. We include three different observed $z = 0$ relations by Tremonti et al. (2004), by Andrews & Martini (2013) and by Maiolino et al. (2008) and compare our results to them. Our galaxies follow a significantly steeper relation with higher mass galaxies ($M_\star > 2 \times 10^{10} M_\odot$) agreeing with Maiolino et al. (2008) and Tremonti et al. (2004) and the lower mass galaxies in better agreement with Andrews & Martini (2013), but on average more metal-poor than all

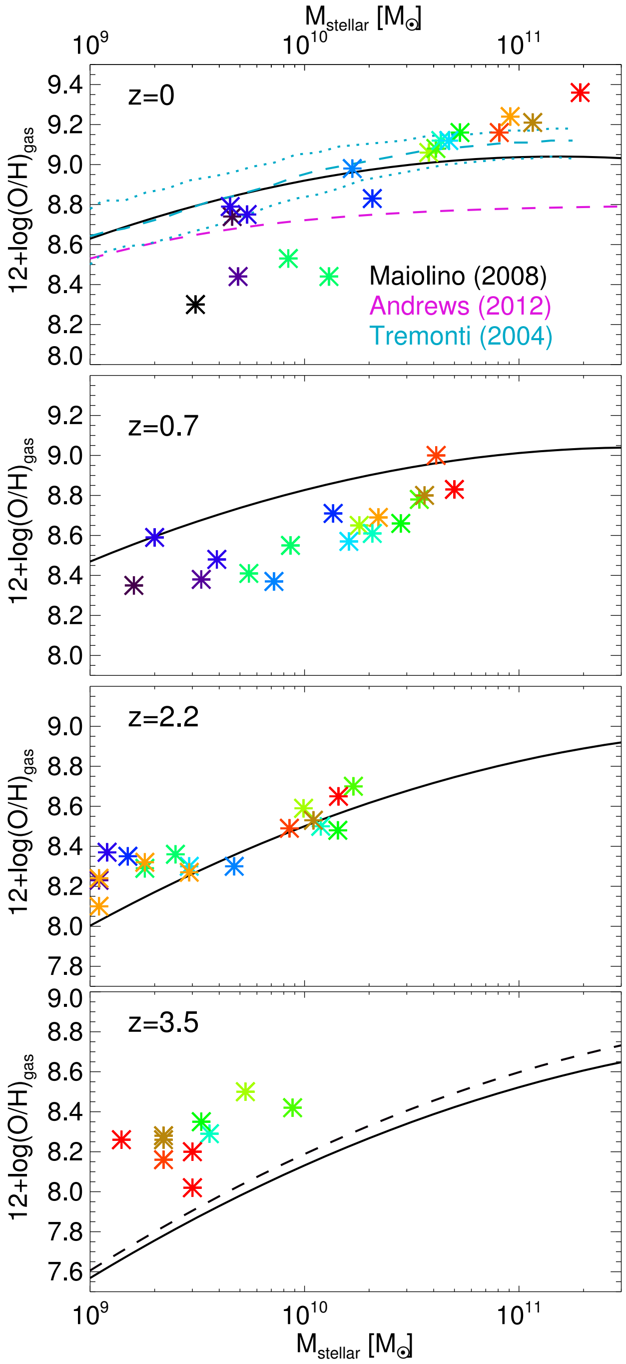

Figure 4.18: Mean galactic gas-phase oxygen abundance $12 + log(O/H)$ vs. stellar galaxy mass compared to the observational results of Maiolino et al. (2008) (black), Andrews & Martini (2013) (magenta) and Tremonti et al. (2004) (cyan, dotted lines mark 1σ regions) at $z = 0, 0.7, 2.2$ and 3.5. At $z = 3.5$, Maiolino et al. (2008) give two calibrations.

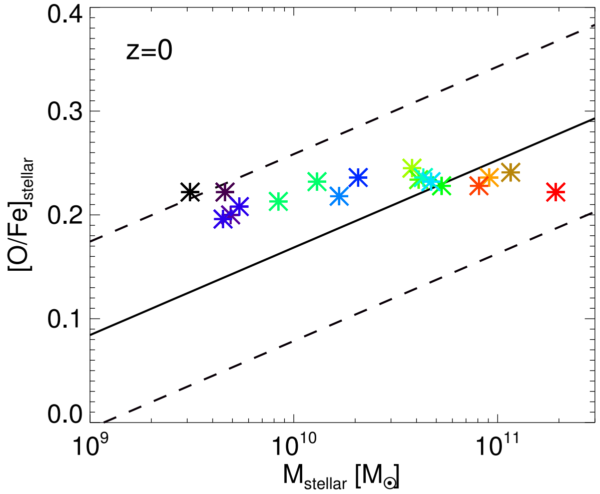

Figure 4.19: Mean luminosity-weighted galactic stellar oxygen to iron ratio $[O/Fe]$ vs stellar galaxy mass at $z = 0$ compared to the observational results of Johansson et al. (2012a) for elliptical galaxies.

three observational relations.

At higher redshifts, we do not find such a disagreement with the observational slope of the relation. When we compare to the results of Maiolino et al. (2008) at $z = 0.7-3.5$, we find reasonable agreement between our models and observations when taking into account the observational uncertainties. At $z = 3.5$, our model galaxies are slightly too metal rich, which considering the over-production of stars at $z > 4$, is not surprising. At $z = 2$, we find perfect agreement with observations, whereas at $z = 0.7$ our models are slightly metal-deficient, probably due to the small deficit in SFRs around $z = 1$. The discrepancies at $z = 0$ obviously origin at $z < 0.7$.

At late times, four lower mass galaxies are metal-deficient. They include two of the haloes with the lowest masses and the two galaxies involved in the major merger of halo 0977. We have noted that these galaxies are overly gas rich. From observed relations, we know that higher gas fractions and lower metallicities are present in lower mass galaxies. As our lower mass galaxies are deficient in SF and too gas rich, late low metallicity infalling material can dilute the metallicity and lead to even lower metallicities than the observed ones. The most massive galaxies tend to be too metal-rich, which, as discussed for stellar metallicities, can be connected to overly high low-z SFRs.

It is well known that SNII and SNIa produce different fractions of elements and explode on different timescales. Because of that, fractions of O (SNII) to Fe (SNIa) test the validity of the modelling of metal production yields, SFHs and model SN time distributions. In Fig. 4.19 we plot the mean luminosity-weighted element ratio $[O/Fe]$ in stars. We compare them to observations from Johansson et al. (2012a) for elliptical galaxies. Although the average $[O/Fe]$ in our galaxies agrees with ellipticals, these values are too high, as disc galaxies typically show lower values of $[O/Fe]$ due to the higher SFRs at late times. Compared to observed ellipticals, the increase in $[O/Fe]$ with galaxy mass is much shallower in our model galaxy sample. Clearly, higher low-z SFRs in lower mass galaxies would shift $[O/Fe]$ to lower values and the opposite is true for the highest mass galaxies which overproduce stars at low redshifts. However, to shift the normalization, a different calibration of yields and SN distributions over time is necessary. As we noted in Section 4.3.2, the metal production yields we apply were not calibrated in any way.

The modelling of turbulent diffusion of metals also has an influence on the metallicity in galaxies. We find that using higher normalizations for the diffusion coefficients yields higher metallicities in galaxies. Using the normalization proposed by Greif et al. (2009) (see Section 4.3.3) increases the metallicity of model galaxies by $\sim 0.2-0.4$ dex and would lead to significantly worse results compared to observations. The reason for this is that outflowing gas is metal-enriched and thus loses metals to the circumgalactic gas by diffusion. The halo gas can later accrete onto the galaxy (Shen et al., 2010). This effect is enhanced by stronger diffusion coefficients.

Metals in galaxies are not equally distributed. Most galaxies show gas oxygen metallicities that decrease outwards, with gradient slopes in units of dex per scale length being independent of galaxy mass (Zaritsky et al., 1994). As more massive galaxies are more extended, absolute gradients in dex/kpc are thus steeper for galaxies with lower masses and smaller sizes. Disc galaxies have steeper gradients than ellipticals and than interacting discs (Kewley et al., 2010). Zaritsky et al. (1994) found gradients ranging from -0.23 to +0.02 dex/kpc for a sample of ~ 40 disc galaxies with a mean of ~ -0.06 dex/kpc. Gradients are believed to arise from the inside-out formation of disc galaxies and the corresponding variation of SF and feedback efficiency with radius.

In Fig. 4.20 we plot the gradients which we find in the oxygen abundances in the gas discs of our model galaxies and plot them against galaxy mass. All our galaxies show clear negative gradients, but they are rather shallow ranging from -0.053 to -0.007 dex/kpc , being a factor of $\sim 3-4$ shallower than observations. We do however reproduce the fact that absolute gradients are steeper for smaller galaxies. As far as our interacting galaxies in the merger haloes 2283 and 0977 are concerned, the extended discs in halo 0977 indeed have flatter gradients than the other galaxies of similar mass. The significantly more compact galaxies in halo 2283, however, show the steepest gradients in our sample.

It is interesting that Pilkington et al. (2012a) found steeper gradients in a set of cosmological simulations with adaptive mesh refinement and SPH codes. Considering our modelling there are two ingredients which can make gradients become too flat. Turbulent diffusion of metals is modelled on the scale of the SPH smoothing kernel and thus is not independent of resolution. In test simulations, we find that stronger diffusion produces flatter metallicity gradients, as diffusion intrinsically acts against metallicity gradients. Moreover, our two-phase enrichment model, which spreads half of the metals into the hot gas phase, intrinsically yields a relatively non-local enrichment of the ISM, which also weakens gradients.

Recently, Gibson et al. (2013) compared gradients in cosmological simulations which share initial conditions, but use different feedback prescriptions. They found that models which assume efficient SN feedback and pre-SN early stellar feedback produce shallower metallicity gradients than more conservative feedback models, as they spread metals over larger scales. As our models, their stronger feedback models also do not predict a steepening of gradients at high z, a behaviour displayed by their weaker feedback models. In general, their conclusions about the interplay between feedback and gradients thus agree well with ours.

In summary, our model galaxies reproduce the observed relation of stellar metallicity vs. stellar mass well. The evolution of the gas phase oxygen abundance is also reproduced

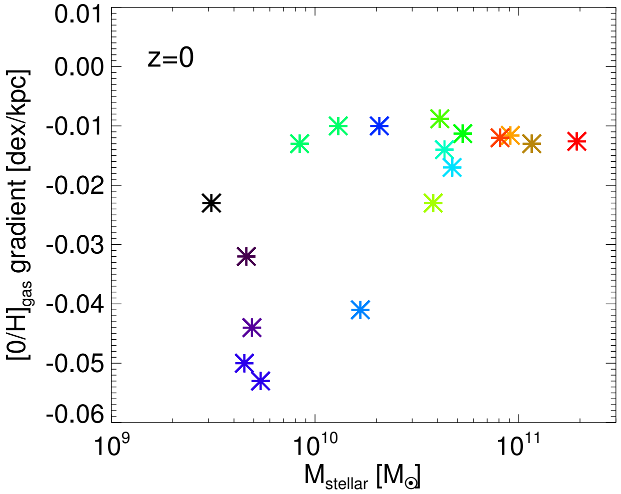

Figure 4.20: The (lack of) gas phase metallicity gradients in the galactic discs at $z = 0$. Mean gradients in $[O/H]$ are plotted against galactic stellar mass $M_{\rm stellar}$.

reasonably well at $z \geq 1$. At low z, the problems with SFHs discussed in Section 4.5.2 lead to deviations from observations. The oxygen-to-iron fractions [O/Fe] in our models are too high and the metallicity gradients in our gas discs are too shallow. This indicates that the details of our modelling of metal production, enrichment and diffusion still needs fine-tuning.

4.8 | Conclusions

We have presented an extensive update to the multiphase SPH galaxy formation code by Scannapieco et al. (2005, 2006). This includes updated metal cooling rates based on individual element abundances, a continuous modelling of metal production in SNIa and AGB stars, an increase in the star formation threshold and a model for the turbulent diffusion of gas phase metals. Moreover, we now use feedback prescriptions which spread energy in kinetic and thermal form and apply a model for the effect of RP from massive, young stars on the surrounding ISM.

We calibrate our feedback model to match the SFH of the previously well studied halo Aquarius C (CS09, CS12) predicted by results from abundance matching techniques out to $z = 4$ (MNW13). By doing so, we confirm the findings of Stinson et al. (2013) that modelling feedback from young stars can play a very important role in shifting SF to later times, in increasing the efficiency of feedback at high z and thus in improving cosmological simulations of galaxy formation. We find that in order to reproduce the inferred SFH, the influence of RP from young stars on the ISM has to be stronger at higher redshifts. We achieve this by invoking a model in which the higher gas velocity dispersions at early formation stages lead to larger star formation regions and thus to greater column densities of dust, which enhance the effect of RP. Our model still predicts an overproduction of stars at $z > 4$, however, pointing to inaccurate modelling of SF at early formation stages.

It was noted in CS12 that there is a priori no reason why this halo should not be an outlier in terms of its SFH. However, considering the many previous galaxy formation models for halo AqC from CS12, our model not only improves the shape of the SFH, but also yields the most dominant disc galaxy in this halo known to us. The galaxy properties show good agreement with a variety of observations.

The efficiency of the coupling between the radiation field and the dusty gas is uncertain and some have argued that the approach of Hopkins et al. (2011), which is similar to our modelling, overestimates the effects of RP (Krumholz & Thompson, 2013). The influence of our RP model on the SFH is, however, a key ingredient for improving the agreement of simulated galaxies with observations. We conclude that any kind of feedback process acting before the explosion of SNe with effects similar to those in our model is likely to achieve this effect (see also Stinson et al., 2013; Brook et al., 2012).

We have applied our code to a sample of 16 haloes with virial masses M_{200} ranging from $1.7 \times 10^{11} M_\odot$ to $2.4 \times 10^{12} M_\odot$, including haloes which were selected to have no recent major mergers (Springel et al., 2008) and haloes with low-z mergers (Oser et al., 2010). As a population, the resulting galaxies reproduce the observed $M_\star - M_{\rm halo}$ relation well at all redshifts $z = 0 - 4$. There are however trends of overly high stellar masses at high z, of low mass haloes under-producing stars at low z, and of high mass haloes overproducing stars at late times.

Our model galaxies also reproduce observations of gas fractions, stellar half-mass radii, SFRs and gas phase metallicities at $z = 0 - 3$ reasonably well. At $z = 0$, our sample also shows agreement with observed stellar metallicities and the galaxies provide a reasonable fit to the baryonic Tully-Fisher relation. Deviations from the observed scaling relations can mostly be connected to the problems with SFHs mentioned above. Considering these results, one could argue that our finding that reproducing the SFH helps in reproducing a range of observations to some degree validates the abundance matching methods used by MNW13.

The problems at the high mass end could well be explained by the lack of a model for AGN feedback, which could prevent the cooling of large masses of halo gas at low z, which occurs in our models (see e.g. Puchwein & Springel, 2013). The low mass haloes indicate that our model is far from perfect, as feedback in these galaxies is too efficient at preventing SF at late times. Again, the question arises whether our calibration method is appropriate. As the peak in conversion efficiency $M_\star / M_{\rm halo}$ appears to happen at slightly lower masses than that of AqC, it is justified to note that lower halo masses could be more appropriate for calibration. Brook et al. (2012) argue that calibrating their galaxy formation model at a halo mass $M_{200} < 10^{11.6} M_\odot$ enables them to produce galaxies that reproduce a range of observations up to the peak in conversion efficiency.

Compared to simulations with the previous code version (CS09), the resulting morphologies are significantly more disc-dominated. 15 out of 16 models show stellar disc components. Morphologies include spheroidal components, extended gas discs, discs that are disturbed and thickened by mergers, warped gas and stellar discs, discs suffering from reorientation and misaligned infall, barred discs, a galaxy with counter-rotating discs living on top of each other, thin extended discs with varying bulge fractions and massive discs, which are compact and thick. Radial surface brightness profiles of our galaxies show pure exponentials and bulge + exponential disc profiles, as well as up- and down-bending breaks, as found in observations (Martín-Navarro et al., 2012). Moreover, apart from two massive galaxies, all circular velocity curves are flat and none show strong central peaks of the kind encountered in many previous simulations (e.g. some models in CS12).

We show how distributions of stars over the circularity ϵ vs. formation time $a_{\rm form}$ plane can be used to visualize formation histories and extract disc populations. This tool nicely reveals mergers and misaligned infall of gas. Interestingly, if misaligned infall and/or the reorientation of existing discs occur, the signatures of these processes, which heat stellar populations, are very similar to those observed for idealized, semi-cosmological models studied in Chapter 3. These processes are of interest in the context of the formation of counter-rotating components and 2σ signatures found in several elliptical galaxies (Krajnović et al., 2008).

Most of the discs in our model sample feature a well-defined start for disc formation, defined by a merger or a misaligned infall event. The later the last destructive event occurs, the lower the disc mass. These 'disc ages' all correspond to $z < 2$. It is interesting that the age inferred for the thin disc population in the solar neighbourhood is even older (see Aumer & Binney, 2009 and references therein). It should also be noted that observational evidence in favour of a picture where a significant fraction disc galaxies (re-)formed after a destructive event since $z \sim 2$ exists (Puech et al., 2012), consistent with the idea that the Milky Way's formation history was more quiescent than that of an average disc galaxy (Hammer et al., 2007).

The disc fractions derived from the $\epsilon - a_{\rm form}$ plots range from 15 to 65 %. Some galaxies are thus disc-dominated. However, there are real galaxies with even higher disc fractions. Considering the shortcomings of our SFHs at $z > 4$, and assuming disc formation times are correctly modelled, we can estimate disc fractions for our haloes under the assumption that SFHs follow the MNW13 predictions. For our three most disc-dominated galaxies, these estimations yield an increase in disc fraction from 59-65 % to 70-77 %. We thus conclude that high disc fractions are not problematic for ΛCDM haloes with sufficiently quiet merger histories. The Aquarius haloes show the highest disc fractions and the quietest merger histories, as was expected from their selection. However, previous simulations (CS09, CS12) failed to validate these predictions.

Some of the problems of our simulations are connected to metallicities. Although our model galaxies reproduce the stellar metallicity - stellar mass relation, the $z = 0$ gas phase metallicity - stellar mass relation is too steep, our alpha-element abundances are too high and the metallicity gradients in our discs are too shallow. No optimization of yields has been attempted for our models so far, leaving room for improvement. Shallow metallicity gradients are likely to be connected to the details of our diffusion model and our two-phase enrichment scheme, which both could require modification. Another problem is that tests indicate unsatisfactory convergence of our results when increasing the resolution. Such problems are common for galaxy formation codes (see e.g. the discussion in CS12). One must take into account that important ingredients are 'sub-grid' and thus that a dependence on the lowest resolved length-scale is expected, when resolution is increased without adjusting model parameters.

In general, our simulations provide us with an interesting sample of simulated galaxies with realistic properties, at least for Milky-Way-like halo masses $M_{200} \sim 10^{12} M_{\odot}$. The simulations predict many more observables that can be compared to the real galaxy population than are touched in this Chapter.

5 | The diverse formation histories of simulated disc galaxies [1]

5.1 | Abstract

Motivated by recent observations of the evolution of structural properties of disc galaxies from z=2.5 to z=0 we analyze the formation histories of a sample of 19 galaxies from cosmological smoothed particle hydrodynamics zoom-in resimulations. By constructing mock three-colour images, we show that the models reproduce the observed trends in the evolution of galaxy colours and morphologies. Our model disc galaxies are deficient in bars and long-lived spirals. Many galaxies go through phases of central mass growth by in-situ star formation driven by gas-rich mergers or misaligned infall of gas and the associated accretion of low-angular momentum gas to the central regions. These events leave clear imprints on the distributions of $z = 0$ circularities, radii and metallicities as functions of stellar age. The galaxies with the highest $z = 0$ disc fractions, however, typically show no central mass growth after the last 'destructive' merger at $z > 1.5$ confirming the picture of inside-out growth. Mergers and misaligned infall are thus likely key ingredients driving the observed structural evolution of samples of disc galaxies, which show continuous growth at all radii. When comparing the average profiles of our simulated disc galaxies at various redshifts to the observed ones, we find good agreement at high redshifts $z \geq 1.5$, but too much growth in size at $z \leq 1$. The average central mass increases too slowly in the models, possibly due to the under-abundance of bars. The discrepancies may in part be caused by differences between the star formation histories of the simulations and those assumed for observations.

---

[1] The results of this Chapter will be submitted for publication in similar form as Aumer et al. (2013b).

5.2 | Introduction

Galaxies with masses similar to that of the Milky Way (MW) are thought to have been most efficient of all galaxies in turning available baryons into stars (Guo et al., 2010). At $z = 0$, a majority of them are dominated by discs (Delgado-Serrano et al., 2010). It is therefore a key question in astrophysics to understand the formation histories of MW-like disc galaxies.

Recently, van Dokkum et al. (2013) (D13 hereafter) and Patel et al. (2013b) (P13 hereafter) presented observational data on the growth and structural evolution of such galaxies from $z = 2.5$ to $z = 0$. To achieve this, D13 selected samples of galaxies in six disjoint redshift intervals at the same cumulative co-moving number density, assuming that this would reproduce the typical formation history of a $z = 0$ galaxy with a stellar mass of $\sim 5 \times 10^{10}\ M_{\odot}$. P13 selected samples of galaxies at six redshifts from $z = 1.3$ to $z = 0$ according to their star formation rates and masses under the assumption that a typical selected galaxy stays on the evolving main sequence of star formation (e.g. Karim et al., 2011) and has a $z = 0$ mass of $3.2 \times 10^{10}\ M_{\odot}$.

Both papers concluded that the galaxy populations under consideration grew only mildly in effective radius over the studied time. Stellar mass growth in the centre occurs at all times with outer growth being only mildly more efficient at late times. This behaviour differs strongly from the stellar mass growth as observed in massive elliptical galaxies, some of which apparently formed dense cores at high redshifts ($z > 2$), and which as a population grew strongly in outer mass and effective radius at later times (van Dokkum et al., 2010; Patel et al., 2013a). This evolutionary path has been explained as a result of the continuous accretion of stars in dry minor mergers (Naab et al., 2009; Bezanson et al., 2009; Hopkins et al., 2010; Hilz et al., 2013).

Major mergers destroy thin galactic discs (Toomre, 1977), so disc dominated galaxies are thought to form in haloes with quiescent merger histories from the cooling of gas from increasingly large radii leading to an inside-out formation (e.g. Fall & Efstathiou, 1980; Mo et al., 1998). Results from abundance matching support the idea that most stars in disc galaxies formed in-situ (Behroozi et al., 2013a; Moster et al., 2013; Yang et al., 2013). Additionally, it has been suggested that for ΛCDM haloes, feedback processes that preferentially remove low-angular momentum gas are needed to explain the observed structure of galactic discs (Dutton & van den Bosch, 2009; Brook et al., 2011).

Several processes that modify the simple inside-out formation picture for disc galaxies are, however, known and can lead to substantial star formation (SF) in the central galactic regions. These include clump migration in violently unstable discs (Noguchi, 1999), bar-induced gas inflows (Athanassoula, 1992), gas-rich minor mergers (Barnes & Hernquist, 1996), angular momentum loss due to the reorientation of the disc rotation axis (Chapter 3; Okamoto, 2013) and the infall of gas with misaligned angular momentum (Scannapieco et al., 2009). Moreover, it has also been shown that discs can (re)form after gas rich mergers (Barnes, 2002; Springel & Hernquist, 2005; Robertson et al., 2006), a process for which observational evidence has also been presented (Hammer et al., 2005; Puech et al., 2012).

In this Chapter we use the cosmological hydrodynamical simulations presented in Chapter 4 to better understand the observed structural evolution of disc galaxies. The Chapter is organized as follows: In Section 5.3 we describe the sample of simulated galaxies. In Section 5.4 we illustrate the diverse formation histories of the models. In Section 5.5 we discuss the influence of mergers and misaligned infall. In Section 5.6 we compare to recent observations. Finally, we conclude in Section 5.7.

5.3 | The simulated galaxies

For our analysis of simulated disc galaxies, we rely on the models presented in Chapter 4. These re-simulations follow the formation of galaxies in a ΛCDM universe, including dark matter and baryonic physics. The simulations were run with the TreePM-Smoothed Particle Hydrodynamics (SPH) code GADGET-3, last described in Springel (2005). Models for baryonic physics were presented in Scannapieco et al. (2005, 2006) and Chapter 4 and include a Schmidt-type star formation law above a threshold density of $n_{\rm th} \sim 3\ {\rm cm}^{-3}$, metal production by supernovae (SNe) of types II and Ia and by asymptotic giant branch stars, and metal-line cooling based on individual element abundances (Wiersma et al., 2009b). Metals can also mix by a scheme modelling their turbulent diffusion. Feedback energy ejected from SNe into the ISM is split into a kinetic and a thermal part and, additionally, a model for feedback from radiation pressure of massive young stars on the surrounding ISM is included. The application of an explicit multiphase scheme for gas particles allows the coexistence of and the exchange of material between a cold, dense phase, from which stars can form, and a diffuse, hot phase.

Our sample includes 19 $z = 0$ galaxies, 18 of which were already discussed in Chapter 4 (two of the 16 haloes hosted two galaxies of similar masses at $z = 0$) and one additional galaxy (AqE), which in all studied properties behaves very similarly to the other studied galaxies. The initial conditions originate from previous studies by Oser et al. (2010) and by Scannapieco et al. (2009) (Aquarius haloes, Springel et al., 2008). The halo mass range of the model galaxies is $1.7 \times 10^{10} < M_{200}/M_\odot < 2.4 \times 10^{12}$ and the model galaxies at $z = 0$ have stellar masses of $3 \times 10^9 < M_{\rm stellar}/M_\odot < 2 \times 10^{11}$. In Chapter 4 we showed that the star formation histories (SFHs) and the $z = 0$ stellar masses of the model galaxies are in good agreement with recent results from abundance matching by Moster et al. (2013).

As was shown in Chapter 4, all but one of the model galaxies show significant disc components and are actively star-forming at $z = 0$. They show realistic morphologies in gas and stars, realistic surface brightness profiles and flat circular velocity curves. The evolution of gas fractions, stellar and gas phase metallicities is also in good agreement with observational constraints. The model galaxies thus present an interesting sample to be compared to recent observations of structural evolution of disc galaxies.

5.4 | Structural evolution of simulated disc galaxies

We begin our analysis of simulated disc galaxies by creating mock three-colour images of galaxies at various redshifts. We therefore rotate each galaxy at each considered redshift to face-on orientation and create square pixels with side lengths of $100 - 200$ pc. Using the stellar population synthesis models of Bruzual & Charlot (2003) for a Chabrier (2003) initial mass function, we determine u, g, and r band luminosities for all pixels taking into account masses, metallicities and ages of star particles. We also take into account obscuration effects by calculating gas-phase metal mass distributions along the line-of-sight for each pixel from the masses, SPH smoothing lengths and metallicities of gas particles with $T < 15000\ {\rm K}$. We use these as a proxy for the dust mass distributions. For each star particle, we thus obtain a dust surface density according to its position along the line-of-sight, which we convert into an extinction factor following the relations presented in Pei (1992). We assume that their results for the Milky Way correspond to solar metallicity gas and replace HI mass, as used in their relation, by cold gas mass. The extinction corrected $u/g/r$ luminosities

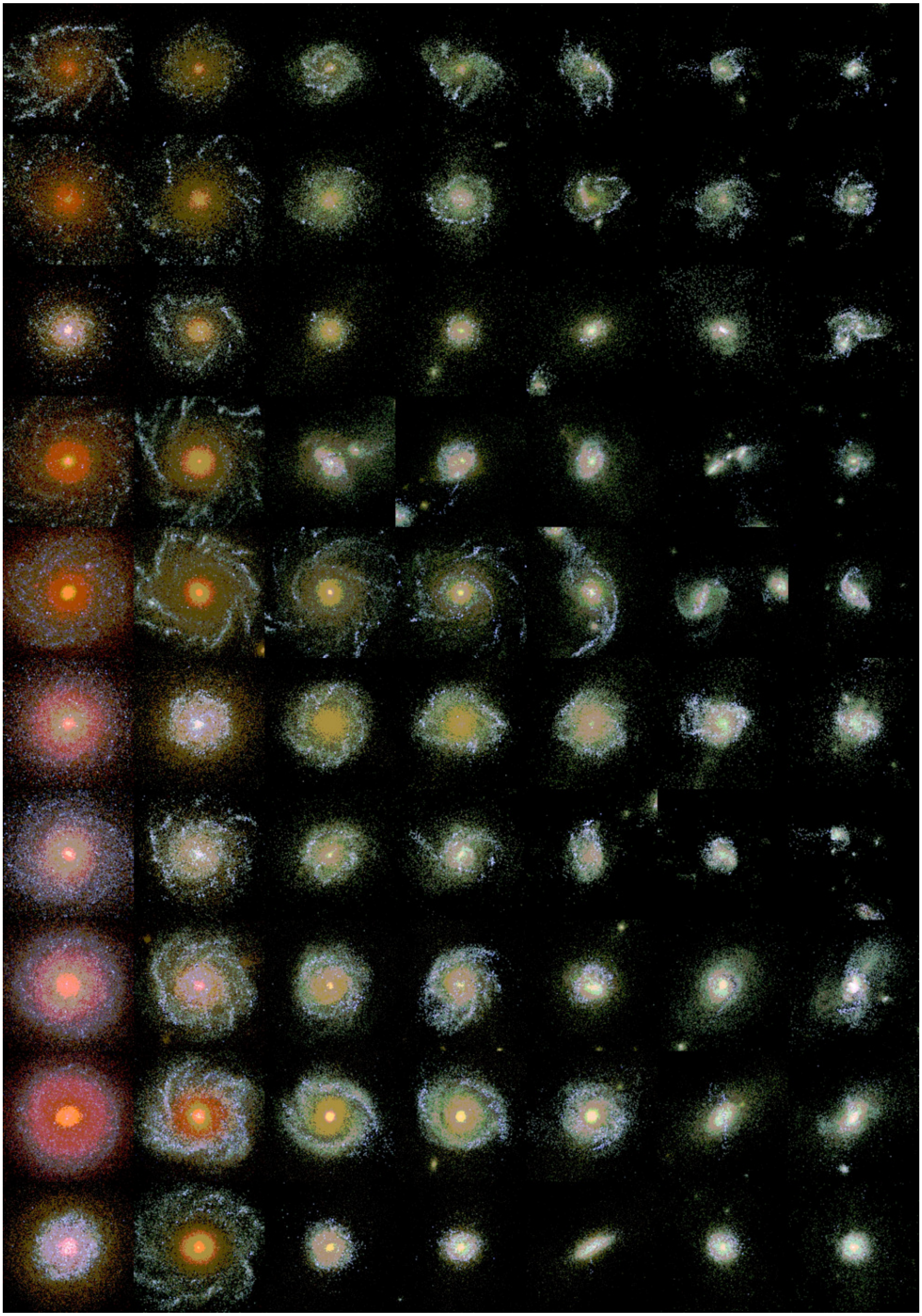

Figure 5.1: Evolution of face-on mock three-colour ugr-band images of model galaxies. From right to left redshifts $z = 2.5, 2.0, 1.5, 1.1, 0.85, 0.37, 0.0$. From top to bottom models 0997-1, 0997-2, 1646, AqB, AqE, 1196, 1192, AqD, AqC, AqA. Each image comprises 20 x 20 kpc.

are then mapped to blue/green/red colours to create three-colour images. This procedure was motivated by the images presented by Hopkins et al. (2013). Similar image series without extinction corrections were recently also presented by Marinacci et al. (2013) for their cosmological simulations of disc galaxies.

Images with sizes of 20 x 20 kpc for ten galaxies at redshifts $z =$ 2.5, 2.0, 1.5, 1.1, 0.85, 0.37 and 0.0 are presented in Fig. 5.1 (for completeness, images for the other nine galaxies can be found in Fig. 5.12). We can compare these images to the observed images presented in Fig. 2 of D13 taking into account that the observed galaxies show various orientations and are presented in two colour u/g band images. As in the observed galaxy sample, the model galaxies change markedly during their evolution and become significantly redder at redshifts $z < 1$ as specific star formation rates decrease with time. The total sizes of galaxies grow considerably.

The galaxies also undergo morphological changes with spiral structures being common at low z, but less prominent at high z. Spiral structure is typically flocculent and there are very few indications of bars. The importance of mergers is indicated by pairs, tidal structures and other irregular morphologies displayed by several galaxies, preferentially at higher redshifts.

At $z = 0$, there is a dichotomy between galaxies having red central regions, which are deficient in SF compared to the blue, actively star-forming outskirts, and galaxies with blue, actively star-forming centres. Some model galaxies display phases of disc growth around a redder centre after a phase of central SF, but typically discs do not assemble around ‘naked’ bulges. Phases of replenished central SF can also follow after inside-out growth phases. Moreover, there are galaxies which never show a strong colour gradient between inner and outer parts. We conclude, that there is considerable diversity in behaviour and good qualitative agreement between observed and mock images.

One generic problem in comparing structural properties of galaxies in observations and simulations are conversions from observed surface brightness to mass and from simulated mass to surface brightness. Moreover, D13 and P13 use different bands for their analysis of structural evolution, bands close to rest-frame g band (D13) and bands close to rest frame i band (P13) respectively. Orientations of galaxies also complicate the picture, as profiles from edge-on and face-on galaxies give different results. We attempt to address these complications in Fig. 5.2.

We create mock images in $u/g/r$ bands as detailed above. This gives us qualitative insight into the effects involved, but is less sophisticated than fully self-consistent radiative transfer post-processing (Jonsson, 2006), which would, however, also result in significant parameter uncertainties and large computational costs.

The upper panel of Fig. 5.2 compares face-on radial profiles of model 1192 at $z = 0$ for mass (black) and for $u/g/r$ band light (blue/green/red) normalized to their values at $R = 2\,\mathrm{kpc}$. We note that the mock r band profile nicely traces the mass profile. In the bluer bands, the effective scale-lengths are clearly longer, in qualitative agreement with observations that find longer disc scale-lengths at shorter wavelengths (e.g. MacArthur et al., 2003). The u band, which mainly traces young stars is also significantly less smooth than the mass profile due to the clumpy nature of SF. The asterisks in the lower panel of Fig. 5.2 give the face-on extinction factors predicted by our procedure. These are typically below 2, only for some star formation regions, there are higher values in the u band.

If we redo the exercise for edge-on views and create profiles for a slit of 1 kpc width, the results are markedly different. The mass profile shows an almost identical exponential decline outside $R \sim 5\,\mathrm{kpc}$ as in the face-on profile, but the central excess is weakened due

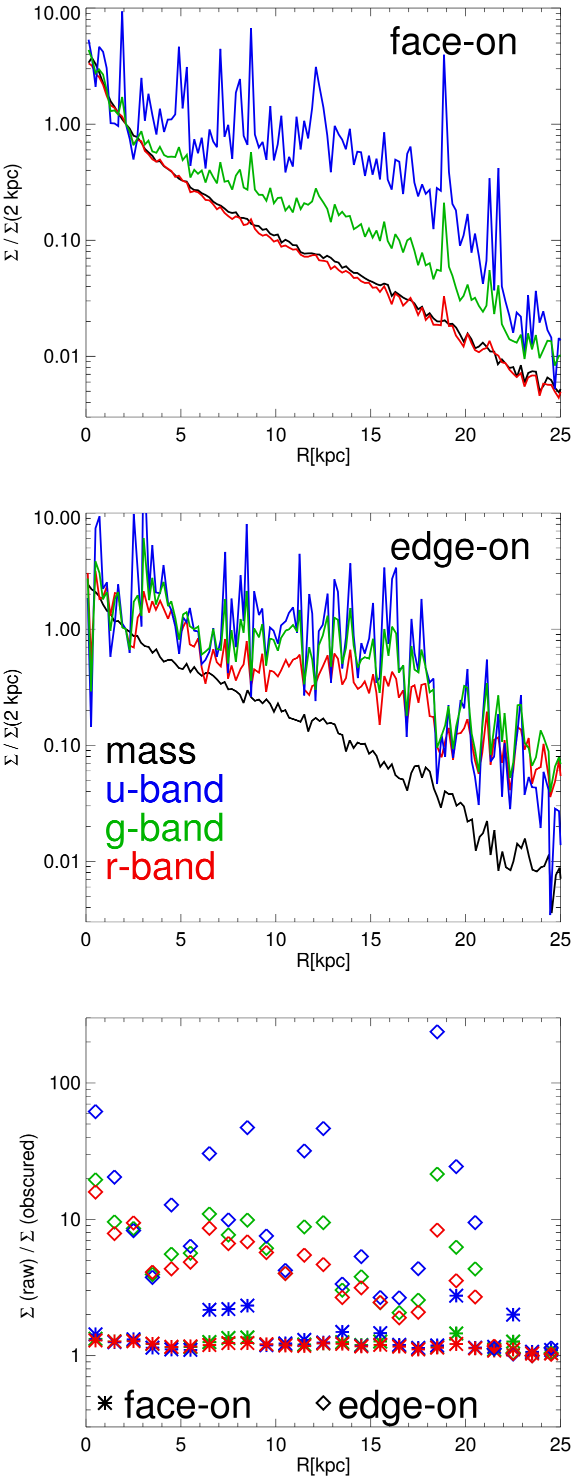

Figure 5.2: Mass and light profiles of model 1192 at $z = 0$. Top: Face-on profiles for mass (black), r band (red), g band (green) and u band (blue). Middle: As above, but for edge-on profiles. The profiles are normalized to intersect at $R = 2$ kpc. Bottom: The ratio of raw to obscured light as a function of radius R for edge-on (diamonds) and face-on (asterisks) profiles in u, g and r bands.

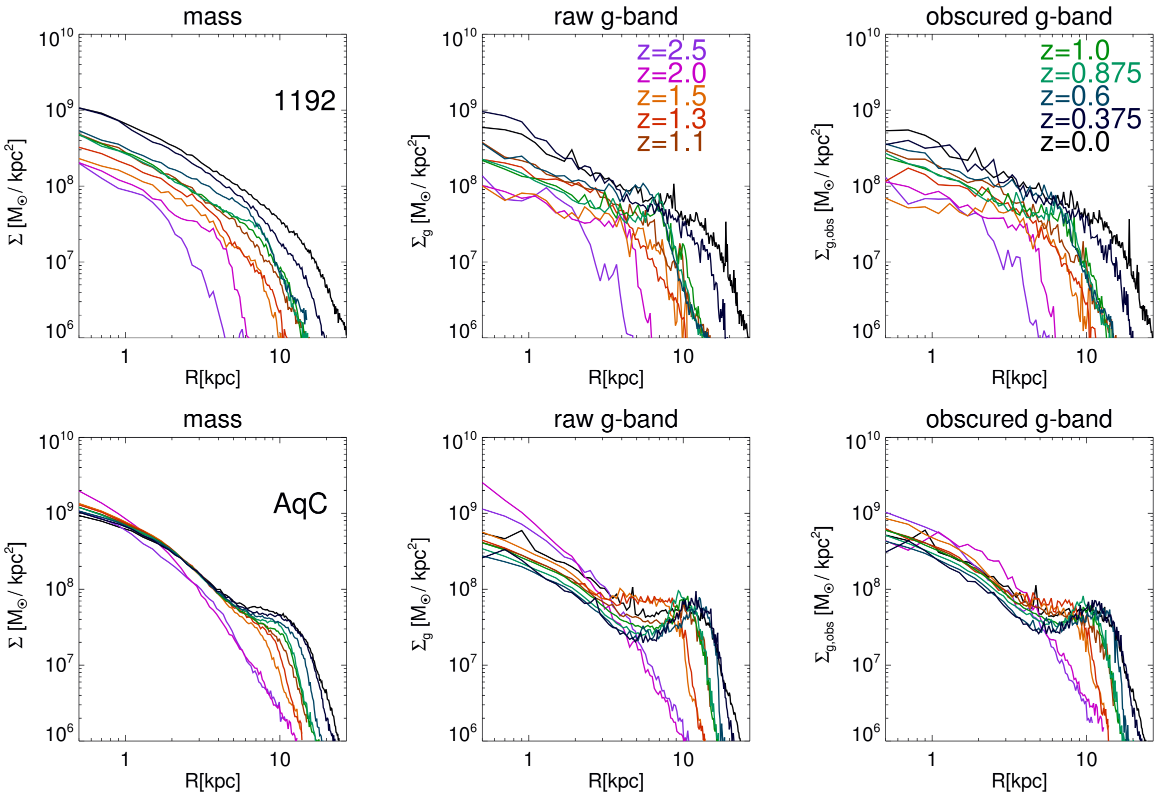

Figure 5.3: The evolution of face-on surface mass density (left) and g band surface brightness profiles (raw: middle, obscured: right) for two models: 1192 (top) and AqC (bottom).

to projection effects. However, the extinction caused by the significantly larger dust column densities severely affects the light profiles, which in all bands are shallower than the mass profile. The three bands differ primarily in variability for the reasons discussed above. The extinction factors, as shown by the diamonds in the lower panel of Fig. 5.2, are typically of the order of 3-10 but can be as high as 100 in the u band.

We conclude that both the selection of the colour band and the orientation can have a significant effect on the determination of structural properties for disc galaxies. It is interesting that D13 and P13 reach similar conclusions using bands for which our simple analysis would predict differing behaviour. In our work, we now restrict ourselves to face-on profiles and caution that the above findings should be kept in mind.

In Fig. 5.3 we depict the structural evolution of two galaxies with very different formation histories. We show profiles in mass, raw g band and obscured g band from $z = 2.5$ to $z = 0$. For the light profiles, we normalize each profile to the same total ‘mass’ as the corresponding mass profile.

The model galaxy 1192 (seventh row in Fig. 5.1) experiences its last significant merger at $z \sim 0.5$ and develops a central bar afterwards. Its stellar mass increases continuously at all radii, it does not experience classical inside-out growth. When analyzing raw and obscured g band light profiles, we notice that these are more extended (see discussion above) and less smooth, but that continuous growth at all radii remains clearly visible .

Model galaxy AqC (ninth row in Fig. 5.1) evolves very differently. Its central mass density

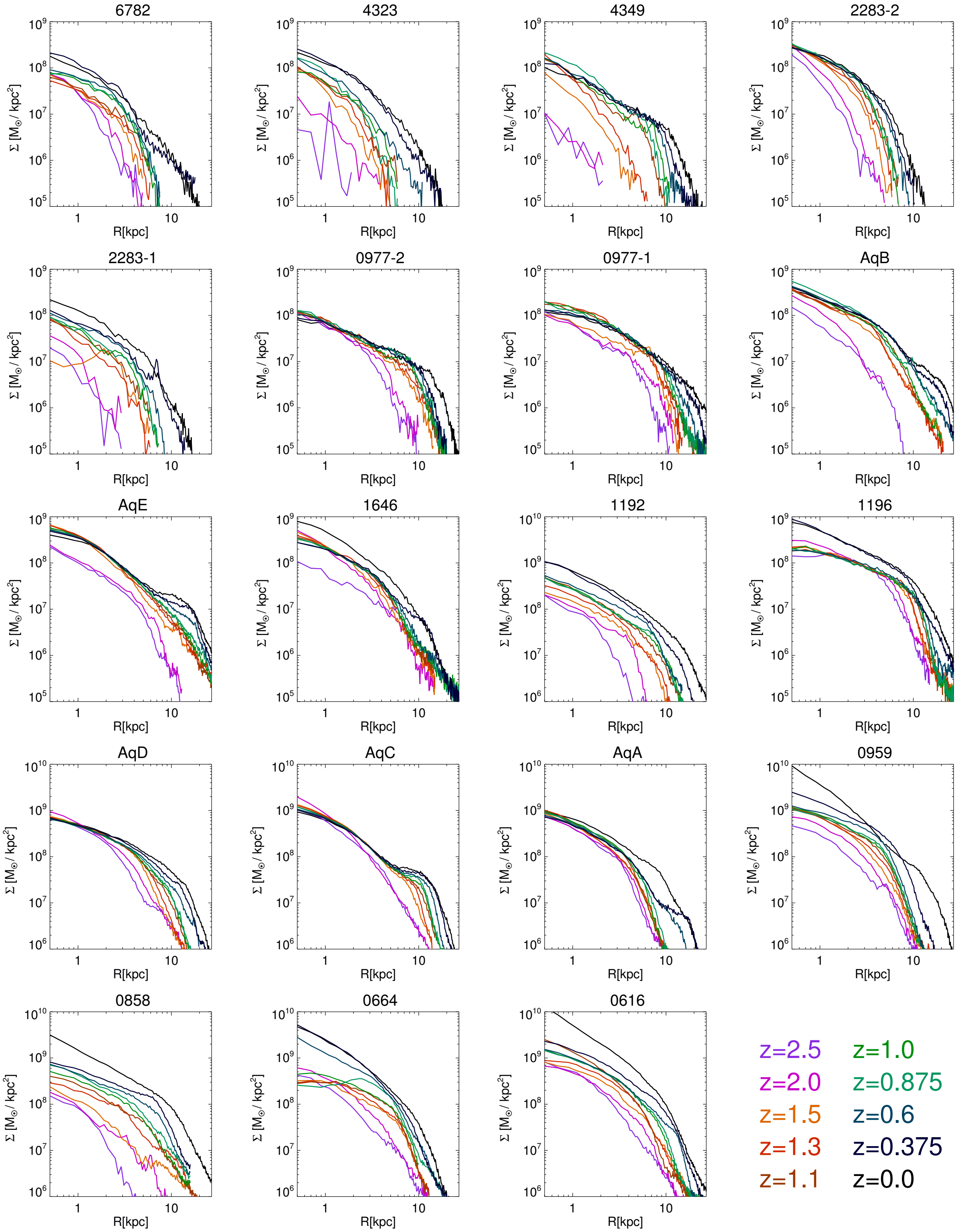

Figure 5.4: The evolution of face-on surface mass density profiles $\Sigma(R)$ from $z = 2.5$ to $z = 0$ for all 19 model galaxies. The models are sorted by $z = 0$ stellar mass. The most massive galaxy (0616) is on the bottom right.

only increases at early times and later decreases due to stellar mass loss. After $z = 2$, there is little change in surface density at $R < 5\ \mathrm{kpc}$. Mass growth happens in an extending ring around the dead central region, thus displaying inside-out formation. In raw g-band light, the evolution looks significantly different (see e.g. also the models of Naab & Ostriker, 2006). The central surface brightness decreases continuously as no new stars form and bright stars die early. Taking obscuration into account, this behaviour is still visible, but it is weaker, as galaxies are richer in gas and dust relative to stars at earlier times. As it is the site of SF, and thus of bright young stars, the ring is significantly more distinct in surface brightness than in mass surface density, constituting a local maximum in surface brightness both in the raw and in the obscured light profiles. If such effects are not accounted for, the inferred structural history would differ significantly depending on whether mass or g-band light were used.

Having studied the differences between light and mass profiles, we use Fig. 5.4 to give an overview of the structural evolution of all 19 model galaxies, restricting ourselves to face-on surface mass density profiles. In Chapter 4 we showed that the five lowest mass galaxies have below average star formation rates (SFRs) at late times, whereas the four highest mass galaxies overproduce stars at low redshifts (the models are sorted by mass in Fig. 5.4). It is interesting to see that all of these higher and lower mass models are more similar in evolution to 1192 than to AqC, as they show continuous mass growth at all radii. The detailed extent and distribution of mass growth varies significantly, but the majority of these galaxies show more complex evolution than simple inside-out growth.

All the lower and higher mass galaxies are part of the halo sample first studied by Oser et al. (2010). The remaining ten haloes are in equal parts made up of haloes from Oser et al. (2010) and of Aquarius haloes (Springel et al., 2008; Scannapieco et al., 2009). For these ten haloes, we found SFHs in good agreement with abundance matching predictions by Moster et al. (2013), as well as $z = 0$ masses which are similar to the ones of the galaxies studied by D13 and P13 (see Chapter 4). The Aquarius haloes were selected to be prime candidates for hosting disc galaxies and have rather quiescent merger histories. Four out of five of these (AqB is the exception) host galaxies with kinematic disc fractions above 50%, higher than any of the disc fractions found in non-Aquarius haloes. The structural evolution of all Aquarius haloes shows an inside-out behaviour with varying details. Interestingly, the haloes from Oser et al. (2010) which are closest to simple inside-out formation are also in this mass range (the two galaxies in halo 0977, which are however about to merge after $z = 0$).

In summary, we have shown that simulated disc galaxies exhibit a variety in morphologies and formation histories when analyzed with mock three-colour images, or through the evolution of surface brightness/density profiles. For the latter, we find evolution ranging from inside-out growth of a disc around a central stellar population which hardly evolves after $z = 2$ to continuous mass growth at all radii at all times. We find more extended discs in optical light than in mass, as in observations, and we identify complications in the interpretation of mass evolution from light profiles especially for edge-on galaxies and for galaxies that grow mainly inside-out.

5.5 | Mergers and misaligned infall

In our introduction to this Chapter we listed several mechanisms that lead to central mass growth in disc galaxies. In Chapter 4 we already noted that our models are deficient in bars. Fig. 5.1 confirmed this and also showed no examples of violently unstable, clumpy

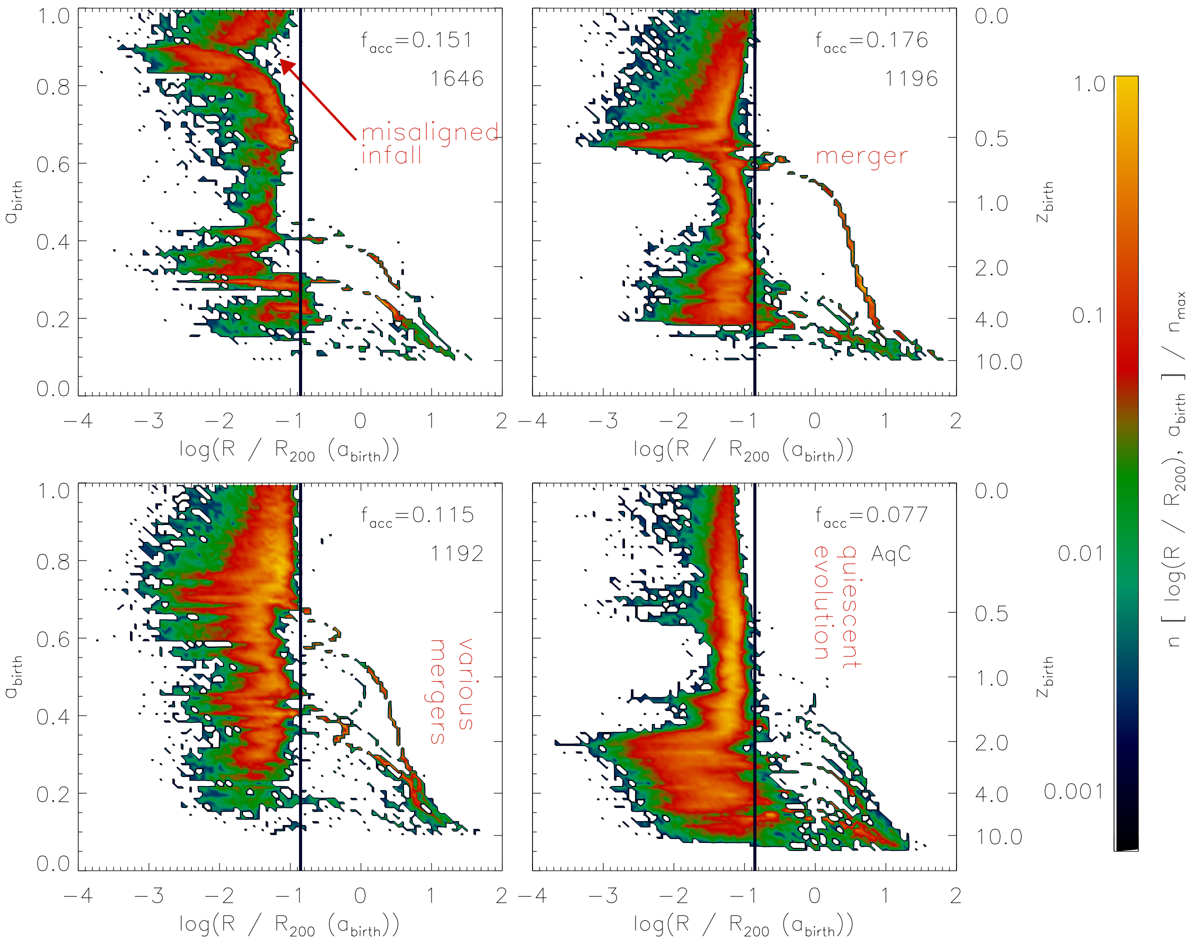

Figure 5.5: The distribution of birth radii of $z = 0$ galactic stars in units of birth virial radius $R_{200}(a_{\rm birth})$ against the formation scale factor $a_{\rm birth}$. Displayed models are 1646 (top left), 1196 (top right), 1192 (bottom left) and AqC (bottom right). For each displayed model, we give the fraction of accreted stars $f_{\rm acc}$ in the top right of the corresponding panel. The vertical black lines indicate a radius of $0.14\ R_{200}$, which we use to distinguish between in-situ and ex-situ star formation.

discs. This leaves mergers and accretion of gas with misaligned angular momentum as possible mechanisms. We have already shown that haloes selected to have more quiescent merger histories show less central mass growth. In Chapter 4, we already demonstrated that misaligned infall of gas can lead to the formation of a counter-rotating disc on top of an existing disc. In this section we study in more detail, how mergers and misaligned infall influence the structural history of our model disc galaxies. Reorientation of disc galaxies by large angles in these simulations is always connected to misaligned infall, which is why we do not analyze it separately here.

Motivated by Oser et al. (2010), we plot in Fig. 5.5 the distribution of stars in the plane of formation scale-factor $a_{\rm birth}$ versus formation radius in units of the virial radius of the main galaxy $R/R_{200}(a_{\rm form})$. Unlike Oser et al. (2010), we use 14 % of the virial radius instead of 10 % to distinguish between in-situ and ex-situ SF, as otherwise the outskirts of several of our galaxies would be ex-situ. These plots show when stellar mass was accreted in mergers, as long as the merging galaxy is gas-rich and star-forming, which is the case for all the significant merger events in our simulations.

For the four galaxies shown, we give in the upper right of each panel the fraction of stars that were accreted, i.e. which had birth radii $R_{\rm birth} > 0.14\ R_{200,\rm birth}$. The fractions are between 8 % and 18 %, in agreement with the finding of Moster et al. (2013) that galaxies of these masses should be dominated by stars formed in-situ. The values are typical for all our 19 model galaxies, which have accreted fractions ranging from 2 % to 40 %.

Comparing the panels for models 1192 and AqC, which we already studied in Fig. 5.3, again reveals striking differences. In AqC stars only form in the centre of the galaxy at $a < 0.35$, when the galaxy undergoes several merger events. Afterwards, in the absence of mergers, stars form only in a ring around the centre. Merging activity continues until $a \sim 0.7$ in 1192 and continuously triggers central SF. When merging has ended, there is a clear trend towards less centrally concentrated SF, despite the presence of a bar. The mergers with the strongest impact have baryonic mass ratios of $\sim 1:2.5$ ($a \sim 0.4$) and $\sim 1:5.5$ ($a \sim 0.67$). There are several more mergers with mass fractions of $\sim 1:10$ and smaller. The total accreted stellar mass is small (11.5 %) as all incoming galaxies have gas fractions between 50 % and 90 %.

The panel depicting model 1196 in Fig. 5.4 (see also sixth row in Fig. 5.1) reveals inside-out growth at $z > 0.5$, followed by an event of strong central growth, followed by inside-out growth at $z < 0.3$. In Fig. 5.5 we detect that a merger at $a \sim 0.65$ is the event which shapes the formation history. A closer analysis shows that the merger has a baryonic mass ratio of $\sim 1:3$ and that the involved galaxies both are gas-rich with gas fractions $M_{\rm coldgas}/M_{baryons}(< 20\ {\rm kpc})$ of 43 % and 55 %.

Model 1646 (see also third row in Fig. 5.1) does not undergo significant mergers after $a = 0.4$. However at $a \sim 0.9$ an event with similar effects on the central mass growth as displayed by the merger in model 1196 is clearly visible. The corresponding panel in Fig. 5.4 also clearly shows this event. In Chapter 4 we found that the youngest stars of this model live in a counter-rotating disc, resulting from misaligned infall of gas, which leads to the shrinking and reorientation of the gas disc, to an episode of centrally concentrated SF and to the inside-out growth of the counter-rotating disc.

In Fig. 5.6 we take an archaeological approach to these questions and analyze at $z = 0$ the radii, the circularities $\epsilon = j_{\rm z}/j_{\rm circ}(E)$, and the metallicities of stars as a function of their age. When comparing these radii to the birth radii displayed in Fig. 5.5, keep in mind that especially, but not exclusively, the accreted stars have significantly different radii at $z = 0$

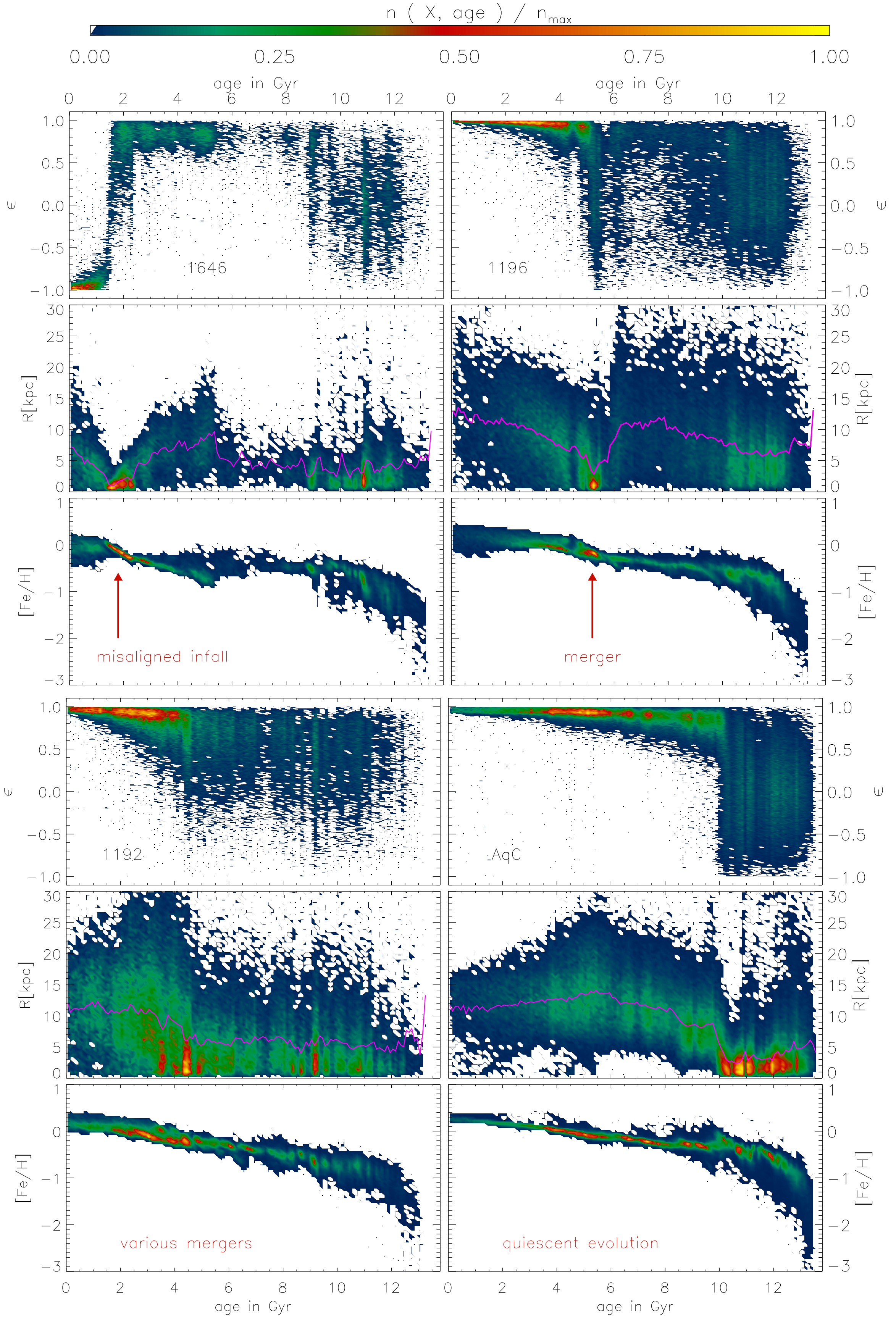

Figure 5.6: Distributions of $z = 0$ galactic stars in models 1646 (top left), 1196 (top right), 1192 (bottom left) and AqC (bottom right) in the planes of $z = 0$ circularity ϵ (top), cylindrical radius R (middle) and metallicity $[Fe/H]$ (bottom) against age. The magenta lines in the middle panels indicate the mean $z = 0$ radius of stars of a certain age.

than at birth. Note that the upturns for the $z = 0$ radii of the oldest stars are caused by accreted stars.

We start with a combined analysis of radii and circularities. In AqC all stars with ages $\tau \lesssim 10$ Gyr live in a disc, as all these stars have circularities $\epsilon > 0.75$. The circularities of older stars are centered around $\epsilon = 0$ and their radii are centrally concentrated, they form a bulge. The bulge population indicates several episodes of increased SF activity, which are connected to the various merger events visible in Fig. 5.5. After the last destructive merger, the disc formed inside-out ($6 < \tau/\mathrm{Gyr} < 10$), then SF started to decline and the disc stopped growing in size.

The situation in model 1196 is complicated by the additional late merger event at $\tau \sim 5$ Gyr, which triggers a short episode of centrally concentrated SF resulting in a dispersion-dominated component. The old bulge component with ages $\tau > 10$ Gyr is more extended than in AqC, in part due to the higher fraction of accreted stars. Between early bulge formation and the late merger ($5 < \tau/\mathrm{Gyr} < 10$), a thick, but rotationally supported component is present, which formed inside-out. The $z = 0$ thin disc component also formed inside-out over the last 5 Gyr.

As in 1196, model 1646 shows an old bulge and an intermediate-age thick disc component, which formed inside-out. However, the infall of misaligned material, which started ~ 5 Gyr ago, led to an outside-in formation process which first created a centrally-concentrated, non-rotating component and then an inside-out growing, counter-rotating disc.

The various minor mergers of model 1192 lead to a multitude of episodes of centrally-concentrated SF up until ~ 4 Gyr ago. These stellar populations are, however, mildly rotating at $z = 0$, with a mean circularity $\epsilon \sim 0.5$. At late times, the mean stellar radius increases only mildly, as the disc is barred, producing a broader ϵ distribution compared to the other young discs.

In Fig. 5.6 we also plot age-metallicity relations (AMRs) for all stars in the galaxies. Note that in simulated galaxies, this relation depends strongly on the details of the modelling of metal enrichment and diffusion, as was e.g. shown by Pilkington et al. (2012b). For comparison, the solar neighbourhood shows a very flat AMR for stars with ages $\tau \lesssim 10 - 12$ Gyr and a steep decrease for older stars (Casagrande et al., 2011).

All four depicted galaxies show a steep decrease in $[Fe/H]$ at $\tau \sim 12$ Gyr. This corresponds to the first stages of galaxy formation when the first generations of stars enriched the ISM to metallicities $[Fe/H] > -1$. The scatter at these ages is large, as the accreted fractions are high and the different progenitor galaxies show variations in enrichment history. As for the solar neighbourhood, there is a transition in the AMR of all four galaxies at $\tau \sim 10-12$ Gyr. The detailed evolution for younger stars differs between model galaxies.

We note that the phases of inside-out growth identified above are characterized by rather flat AMRs, e.g. at $5 < \tau/\mathrm{Gyr} < 10$ in 1196 or at $3 < \tau/\mathrm{Gyr} < 9$ in 1646. The merger or misaligned infall events in these models show short phases of increasing $[Fe/H]$. In AqC the metallicity is mildly increasing with time, more strongly at $\tau < 6$ Gyr, when the disc no longer increases its size and enrichment by stars dominates over accretion of less-enriched material. The numerous minor mergers in 1192 lead to a continuously increasing AMR which tends to flatten at late times after the last merger. In 1646, at the start of the outside-in evolution ($\tau \sim 5$ Gyr), the average metallicity drops and the spread in $[Fe/H]$ widens, as new, relatively metal-poor gas is accreted after a gas-poor phase with little SF.

If we, instead of all galactic stars, only consider the AMR of outer disc stars ($R > 5$ kpc), we can give a tentative statement on whether one of the metallicity features found for our

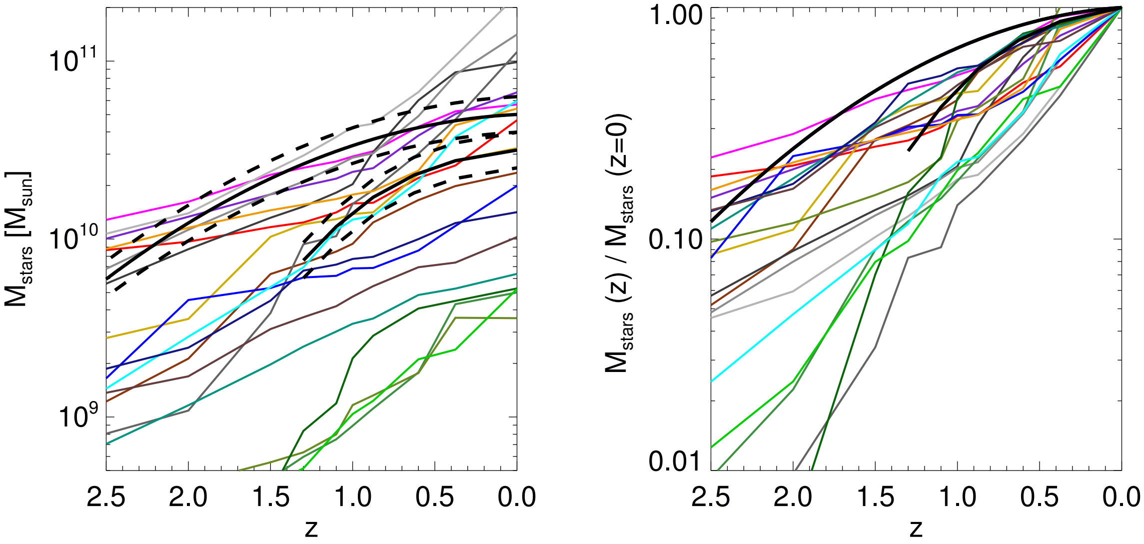

Figure 5.7: The evolution of stellar mass $M_{\rm stars}$ with redshift z for all 19 model galaxies. Left: The evolution of absolute masses $M_{\rm stars}(z)$. Right: The evolution of masses in units of the $z = 0$ mass $M_{\rm stars}(z)/M_{\rm stars}(z = 0)$ for each galaxy. We overplot in black the mean mass evolution histories adopted by D13 (final mass $5 \times 10^{10} M_{\odot}$) and P13 (final mass $3.2 \times 10^{10} M_{\odot}$). Dashed lines represent a scatter of $\pm 0.1\rm dex$.

models could also be found in a solar-neighbourhood-like environment. We find that the details of the AMR vary, but the general shape is the same in the centre and in the outer regions.

In summary, we have shown that, for our simulated disc galaxies, gas-rich mergers and misaligned infall events are the main drivers of central mass growth. Galaxies with high $z = 0$ disc fractions, which generally show no such event after $z \gtrsim 1.5$, hardly grow in central mass. For other galaxies, such events transport low angular momentum gas inwards leading to in-situ formation of dispersion-dominated stellar populations. ‘Archaeological’ investigations of stellar radii, circularities and metallicities at $z = 0$ reveal these events as centrally-concentrated, non-rotating populations of stars of a small age range, during which metallicity increases more strongly than average.

5.6 | Comparison to observations

In this section we attempt a more direct comparison of our simulations to the observations by D13 and P13. This is complicated by the variety in mass evolution histories of our galaxies, few of which agree with the selection criteria of either study. It is also unclear, how well the selection criteria used by P13 and D13 actually trace the mean evolution of galaxies at a targeted $z = 0$ mass. Leja et al. (2013) showed that the method applied by D13 worked reasonably well in tracing galaxy populations in semi-analytical models of galaxy formation. P13 showed that their selection criteria agree with predictions for galaxy populations from abundance matching. In Fig. 5.7 we plot the evolution of stellar mass of the

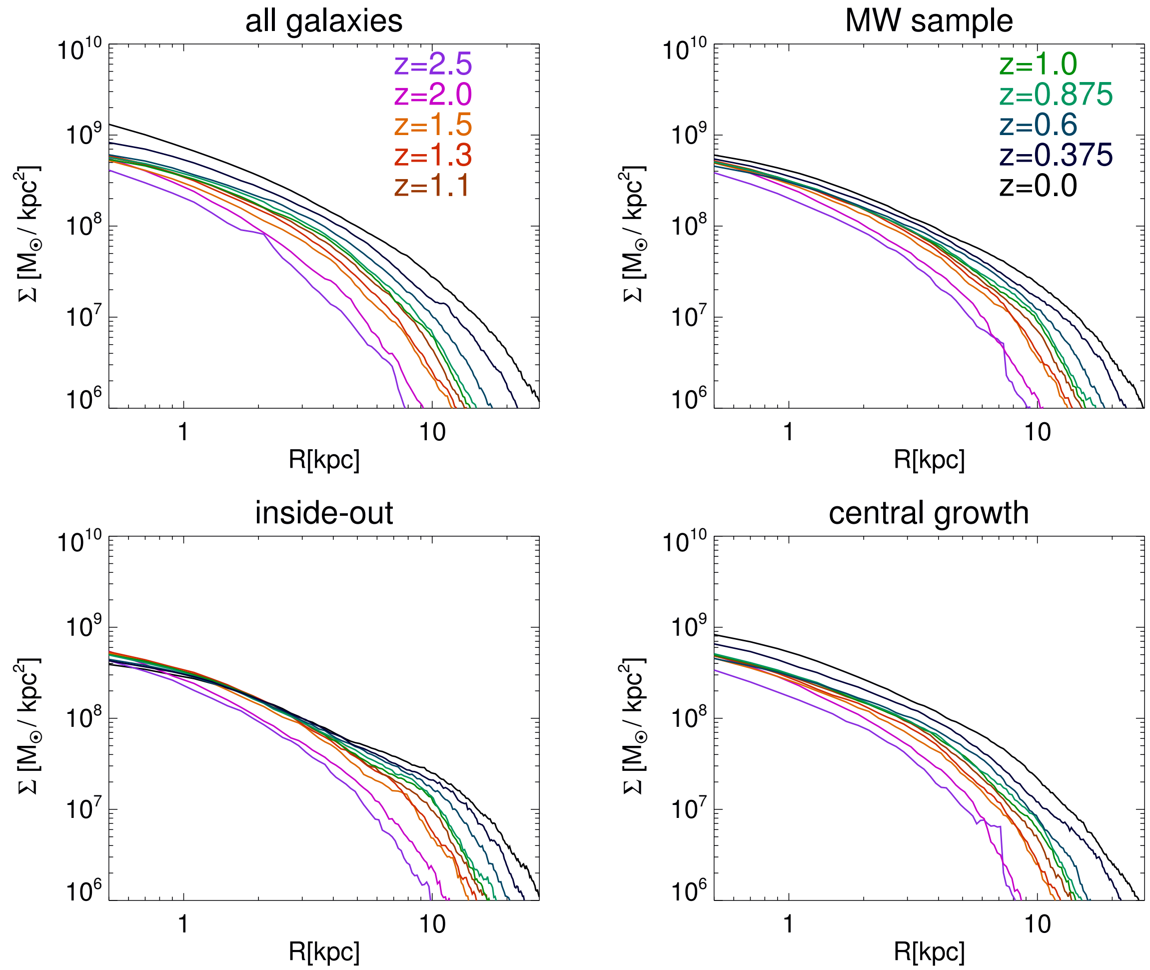

Figure 5.8: Evolution of mean number-weighted stellar mass surface density profiles from $z = 2.5$ to $z = 0$ for various samples: all galaxies (upper left), MW mass sample (upper right), inside-out sample (lower left), central growth sample (lower right). We here apply scaling in mass and radius according to the procedure detailed in the text. Masses are scaled to the mean mass evolution of the simulated samples.

model galaxies against redshift in two ways: in the left panel we show $M_{\rm stars}(z)$ to depict the variety among masses of the model galaxies at each redshift and in the right panel we show $M_{\rm stars}(z)/M_{\rm stars}(z=0)$ to highlight the variety in stellar mass assembly history. In both panels we overplot the corresponding lines for the selection criteria of D13 and P13.

The range of stellar masses of our model sample is at all times much wider than the selection intervals. Moreover, most of the galaxies that at some point in time are inside one of the intervals, fulfill this criterion only temporarily. In other words, most individual formation histories are flatter, steeper or more episodic than the smooth average formation history of a population selected by a certain $z=0$ mass. Galaxy 0858, for example, at $z=2.5$ is an order of magnitude less massive than the mass anticipated by D13, but at $z=0$ more massive than their observed galaxies. The right panel of Fig. 5.7 reveals that none of our galaxies lies close to the relative assembly history selected by D13, but several galaxies are similar to the history assumed by P13. As was shown in Fig. 4.3, the expected peak in SFH at $z\sim 1-2$ of galaxies with $z=0$ stellar masses similar to that of the MW (e.g. Moster et al., 2013) is not well reproduced by our models. The models on average show a flatter SFH(z), which contributes to the discrepancy in the right panel of Fig. 5.7.

Nevertheless, we create four test samples of galaxies to be compared to the observational results. The first sample includes all galaxies, the second sample excludes the four most massive and five least massive galaxies at $z=0$. This leaves ten galaxies with $z=0$ stellar masses $1\times 10^{10} < M_{\rm stars}/M_{\odot} < 6\times 10^{10}$, which we sloppily call 'MW mass sample'. Due to the variety of formation histories of our galaxies, we further divide the 10 galaxies in equal parts into an 'inside-out' and a 'central growth' sample according to the growth of stellar mass at $R<2$ kpc at $z<2$. We note that our general results are not affected by our selection criteria. Selecting at each z the galaxies closest to the mass evolution assumed by D13 would, for example, give results similar to that of the MW mass sample.

Due to the wide spread in masses of our models, we apply a scaling in mass and size. In terms of mass, we consider two cases: scaling the integrated total mass of each galaxy to the mean mass of the considered sample at the given z or scaling the galaxy mass to the corresponding mass selected by D13. In terms of size, Shen et al. (2003) give a mass-size relation for $z=0$. At high-z, a mass-size relation with increasing sizes for increasing stellar masses is also present (Mosleh et al., 2011; Nagy et al., 2011; Ichikawa et al., 2012), but the shape of the relation is yet uncertain. Ichikawa et al. (2012) suggested that the mean slope is independent of redshift. We therefore assume that the mean relative difference in size of galaxies at varying masses at all redshifts is given by the Shen et al. (2003) relation. Consequently, we extend or shrink the mass distribution of each galaxy in consideration by a factor that is determined by the ratio of the Shen relation radii at its actual mass and the assumed mean mass. We note that the general conclusions of this Chapter are not dependent on the details of the scaling procedure.

The evolution of the mean surface density profiles for all our four samples is presented in Fig. 5.8. For this figure, we scale each galaxy to the mean sample mass as detailed above and then stack the profiles to determine the mean number-weighted profile of the sample. Note that the mean masses at a given redshift differ significantly from sample to sample. Whereas the evolution of the outer surface density profiles ($R\gtrsim 5$ kpc) for all samples shows a continuous increase in mass and also a continuous increase in size, the samples significantly differ in the evolution of the central surface density.

The 'MW mass' sample shows significantly less central growth than the 'all galaxies' sample. Fig. 5.4 reveals that the four most massive galaxies drive central mass growth in

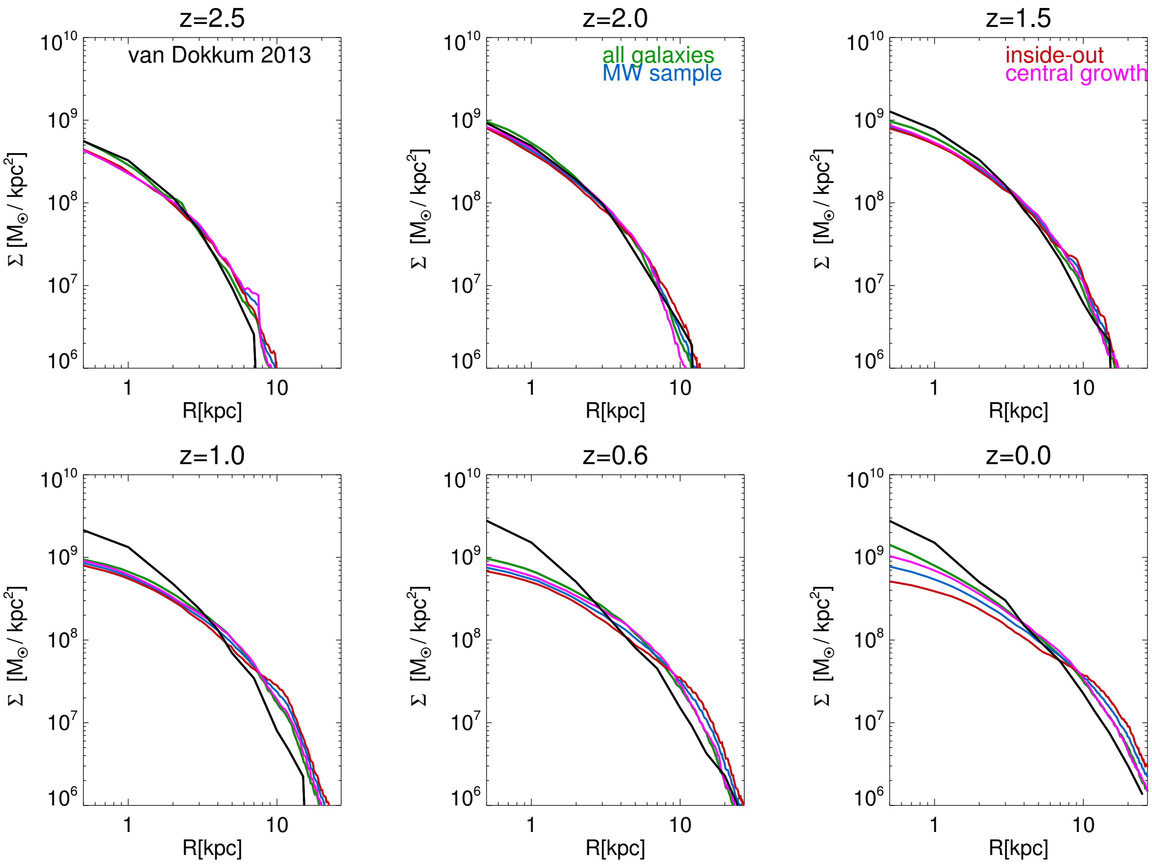

Figure 5.9: A direct comparison of simulated and observed mean profiles. In black we show the observed profiles by D13 at $z = 2.5$, 2.0, 1.5, 1.0, 0.6 and 0.0. We show mean number-weighted mass surface density profiles $\Sigma(R)$ for four sub-samples of our simulated galaxies: all galaxies (green), MW sample (blue), inside-out (red) and central growth (magenta). For our scaling in mass and radius we here assume the mass evolution selected in D13.

the all galaxies sample at late times, whereas the low-mass galaxies are responsible for the central growth at earlier times. By construction, the inside-out sample shows a decreasing mean central mass density with time due to stellar mass loss as discussed in Fig. 5.3 for model AqC. Also by construction, the central growth sample shows higher central growth rates than the MW mass sample.

In Figure 5.9 we present a direct comparison of the samples with the observations of D13 at various redshifts. As discussed above, the evolution of mean masses differs between samples and is also different from the evolution assumed in observations, which is why we restrict ourselves to profile shapes and consequently scale all profiles to the mass evolution assumed by D13.

We first note that the mean profile of all simulated galaxies is at all times more concentrated than the other three samples, which is caused by lower and higher mass galaxies, which all do not show inside-out growth, as discussed in Section 3. At $z \geq 1.5$, the differences are, however, minor and the mean profiles of all samples show a remarkably good agreement with observations. Considering the error bars presented in D13, all samples are consistent with the data at these times.

After $z = 1$, there is, however, a clear trend for all simulated galaxies to produce too shallow surface density profiles. The trend is worst for galaxies that grow inside-out with discrepancies increasing with time. At $z = 0$, their scaled mean central surface density is a factor of ~ 4 lower than in observed galaxies and the scaled mean surface density at $R \sim 5 - 20$ kpc is consequently a factor of up to ~ 3 higher. The sample of all galaxies at $z = 0$ disagrees less strongly with the data, the scaled profile at all radii agrees to within a factor of ~ 2. The other two samples fall between all galaxies and the inside-out sample. Note that the discrepancies would be smaller if no scaling in size were applied. We caution that D13 used rest-frame g band as a proxy for mass. If we used mock g band surface brightness profiles, the discrepancies would increase (see Fig. 5.3). However P13 reached similar conclusion with rest-frame i band profiles, which we do not find to be significantly different from mass profiles.

In Figure 5.10 we show the evolution of several structural parameters characterizing the profiles, which were also presented in D13 and P13. We show the quantities for both variants of scaling as explained above. In the left panels of Fig. 5.10 we plot the evolution of the total stellar mass within and outside 2 kpc. D13 found an increase at $R < 2$ kpc by a factor of ~ 3.5 from $z = 2.5$ to 0.5 and no evolution afterwards, and a mass increase by a factor of ~ 10 outside. P13, who analyzed slightly less massive galaxies, found a less flattened central mass increase at late times, which is likely connected to lower mass galaxies assembling stellar mass later (e.g. Moster et al., 2013). They otherwise found similar results.

We first discuss results for the upper left panel, where we use the mean mass evolution of each sample for the scaling procedure. When we consider all galaxies, we find an increase at $R > 2$ kpc by a factor $f_> \sim 19$, significantly higher than observed. At $R < 2$ kpc we find an increase by a factor of $f_< \sim 3.9$, which agrees with observations. However, the central mass growth does not flatten at late times. For the 'MW mass' sample, the respective growth factors are $f_> \sim 9$ and $f_< \sim 2.0$, showing that these galaxies mainly differ from observations in the lack of central growth. This discrepancy is consequently worse for the inside-out sample ($f_< \sim 1.25$, $f_> \sim 8.3$) and rather small for the central growth sample ($f_< \sim 2.9$, $f_> \sim 10.5$).

As discussed above, the samples all show evolution in total stellar mass different from the galaxy samples in the observational papers. In the lower left panel of Fig. 5.10 we

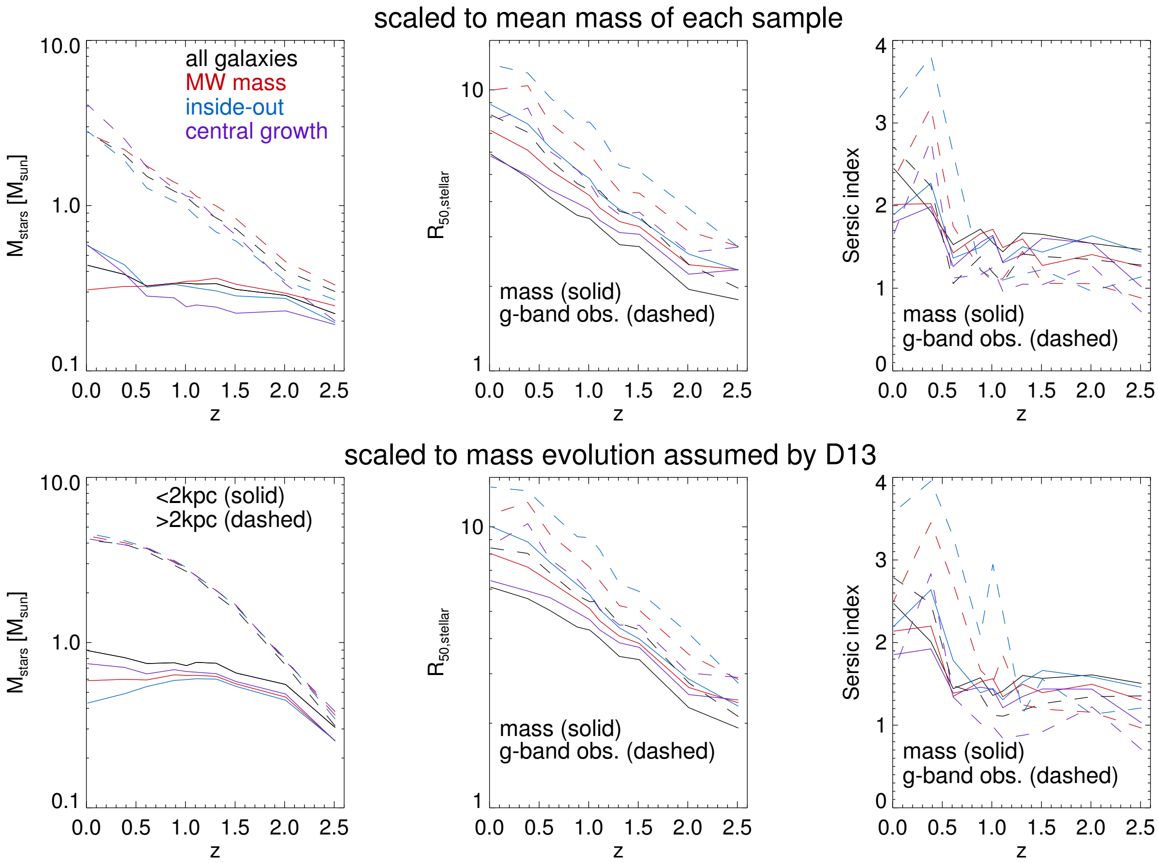

Figure 5.10: Evolution of properties characterizing the mean mass and light profiles of simulated galaxy samples: All galaxies (black), MW mass (red), inside-out (cyan) and central growth (purple). Upper panels: Galaxies scaled to the mean mass evolution of each sample. Lower panels: Galaxies scaled to the mass evolution selected by D13. Left: Evolution of the mass within $R = 2$ kpc (solid) and outside $R = 2$ kpc (dashed). Middle: Evolution of the half-mass (solid) and half g band light (dashed) radii. Right: Evolution of Sersic indices obtained by fitting the mean mass (solid) and mean g band light (dashed) profiles.

therefore show the evolution of stellar mass within and outside 2 kpc when we use the mass evolution assumed by D13 for the scaling procedure. As already noted for Fig. 5.9, the scaled $R < 2$ kpc mass at $z = 0$ is for all samples lower than in observed galaxies. D13 found $\sim 1.5 \times 10^{10}\ M_{\odot}$, whereas we find a scaled $R < 2$ kpc mass of $\sim 0.9 \times 10^{10}\ M_{\odot}$ for all galaxies and $\sim 0.6 \times 10^{10}\ M_{\odot}$ for the MW mass sample. We note that, after scaling, the factors of growth from $z = 2.5$ to $z = 0$ for all samples change in a way that yields better agreement with observed growth factors. Moreover, the evolution curves now show flattening at late times, as those found by D13, although central growth flattens too early. This exercise shows that the discrepancies are in part caused by the difference between the SFH of our model galaxies and that inferred for the observed sample, as visualized in Fig. 5.7.

Another structural property that encodes the shape of the profile is the Sersic index n_S. P13 and D13 showed that the galaxies they observed displayed an increase from $n_S \sim 1$ at high z to $n_S \sim 2.3 - 3$ at $z = 0$ for one-component fits. We also perform one-component Sersic fits to the mean profiles of the four samples introduced above and depict the results in the right panels of Fig. 5.10. Fits can depend significantly on the binning of the data or on the fitted region and the uncertainty is thus high. Independent of the assumed scaling and of sample selection, we find a mild increase of Sersic index, from $n_S \sim 1.3 - 1.6$ at $z > 2$ to $n_S \sim 1.8 - 2.4$ at $z = 0$. If we redo the procedure with g band surface brightness profiles instead of mass profiles, we find somewhat lower indices at high z and higher indices at low z. This is especially true for the inside-out sample, for which the low z profiles show clear disc and bulge regions (see AqC in Fig. 5.3 for an extreme example) and are generally not well fit by one-component profiles. Considering these trends, the agreement with observations is reasonable.

The biggest discrepancies between observations and simulations become clear in the middle panels of Fig. 5.10, where we plot the evolution of stellar half-mass radii. In Chapter 4 we already showed that the simulated galaxies tend to be too extended at $z = 0$ compared to the mass-size relation found by Shen et al. (2003) for local galaxies. This discrepancy was biggest for the galaxies with MW-like masses. From above, we have learned that this is driven by overly low central masses. D13 showed that their galaxies had half-light radii of $R_{50} \sim 2$ kpc at $z > 2$, which only increased mildly to $R_{50} \sim 3.5$ kpc at $z = 0$ with hardly any evolution after $z = 1$. The results of P13 are very similar.

Although for all our different samples of simulated disc galaxies we also find sizes $R_{50} \sim 2$ kpc at $z > 2$, the increase in size is much stronger at later times, especially at $z < 1$. Assuming the mean mass evolution of each sample for the scaling procedure, the final mean half-mass radius is $R_{50} \sim 5.8$ kpc for all galaxies, $R_{50} \sim 5.9$ kpc for the central growth sample, $R_{50} \sim 7.1$ kpc for the MW mass sample and $R_{50} \sim 8.8$ kpc for the inside-out sample. Size thus clearly anti-correlates with central mass growth. We also overplot half-light radii for our mock g band profiles which are again ~ 40 per cent more extended at $z = 0$ than the corresponding half-mass radii. When the mass evolution selected by D13 is assumed for the scaling, radii also increase by $\sim 10\%$.

In Fig. 5.11 we plot the evolution of the samples in the mass-size plane. P13 and D13 find for their observational samples relations similar to $R_{50} \propto M^{0.3}$, whereas Patel et al. (2013a) found $R_{50} \propto M^{2.0}$ for elliptical galaxies. At high z, all our samples start to evolve as predicted for observed disc galaxies, but then evolve away from this relation. We find that our all galaxies and central mass growth samples grow as $R_{50} \propto M^{0.5}$ and our inside-out sample grows as $R_{50} \propto M^{0.8}$. The growth is thus significantly stronger than for observed disc galaxies, but significantly weaker than for observed ellipticals. Scaling according to the

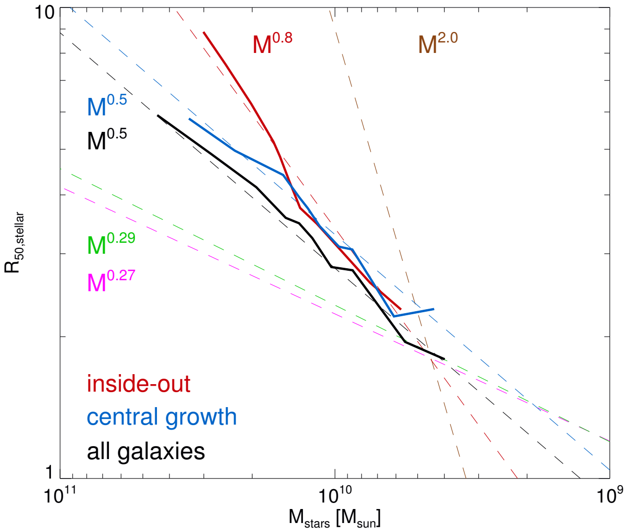

Figure 5.11: The evolution of simulated galaxies in the plane of stellar half-mass radius $R_{50,\mathrm{stellar}}$ and stellar mass M_{stellar}. The all galaxies (black) and central growth (cyan) samples follow roughly an $R \propto M^{0.5}$ growth, whereas the inside-out sample (red) follows approx. an $R \propto M^{0.8}$ growth. For comparison the results for disc galaxies by D13 (magenta $R \propto M^{0.27}$) and P13 (green $R \propto M^{0.29}$) and for elliptical galaxies by Patel et al. (2013a) (brown $R \propto M^{2.0}$) are shown. The latter was shifted to lower masses to allow a comparison between the relations. The mean mass evolution of the simulated samples is used for scaling.

mean mass evolution of the simulated samples was used for Fig. 5.11, but the slopes are independent of scaling. Hirschmann et al. (2013) recently presented this plot for a larger set of lower resolution resimulations with a very different feedback model compared to ours. Interestingly, they find a better agreement for the size evolution ($R_{50} \propto M^{0.4}$ for their WM feedback model and MW mass galaxies), although their model galaxies are at all times too compact.

In summary, we have shown that our simulated galaxies agree well in structure with observed galaxies at $z \geq 1.5$, independent of sample construction. After $z = 1$, all galaxies, especially those with $z = 0$ stellar masses around $1 - 6 \times 10^{10} M_{\odot}$, grow a factor of ~ 2 too little in central mass and consequently a factor of ~ 2 too much in size. The discrepancy with observations is strongest for inside-out growing galaxies, but also valid for other formation histories. We also find that this comparison between observations and simulations of disc galaxy evolution is complicated by the variety of SFHs of simulated discs, which often differ from the simple assumptions chosen for observations.

5.7 | Conclusions

We have presented an analysis of the evolution of the structural properties of a sample of 19 simulated disc galaxies. These are cosmological re-simulations with multiphase SPH which were presented in Chapter 4. We have created mock three-colour $u/g/r$ band images to visualize the evolution of the models. We have investigated, how the complexity of light profiles and variations with orientation could complicate the interpretation of observed data, especially if rest-frame g band is used as a proxy for mass, as in the work of D13. The model galaxies show a variety of structural evolution histories, ranging from inside-out growing discs around older, more centrally concentrated stellar populations to continuous SF at all radii.

Our models are deficient in bars and violently unstable discs, so that not all known mechanisms for central mass growth in disc galaxies are well represented. However, gas-rich mergers with mass fractions up to $1:3$ and misaligned infall of gas can be clearly linked to episodes of central mass growth. In a ΛCDM universe, these events are common and are thus likely to be major contributors to the continuous central growth observed in mean surface density profiles of samples of galaxies selected at various redshifts in order to represent the typical evolution history of galaxies with $z = 0$ masses similar to that of the MW (D13 and P13). Galaxies which do not experience such events, grow inside-out and show no or little central mass growth. We have shown that mergers or misaligned infall leave distinct features in the distributions of present-day radii, circularities and metallicities as functions of stellar age. Observational detection of such features is complicated by the fact that the timescales of these events are smaller than the typical errors in age determinations of stars.

In our simulations, metallicities effectively increase during events that drive central SF, as these events enrich the ISM. The evolution of metallicities in discs due to interactions has been studied in detail by several groups (Montuori et al., 2010; Perez et al., 2011; Torrey et al., 2012b). All these papers discuss non-cosmological simulations of mergers of pairs of disc galaxies. They all apply SPH codes without a prescription for the turbulent diffusion of metals, which is included in our fully cosmological models and has been shown to significantly change the metallicity distributions in discs (Pilkington et al., 2012b) and the circumgalactic medium (Shen et al., 2010). All these models find a strong initial dilution of central metallicities caused by the inflow of gas originating from the outer disc which, due to the metallicity gradients assumed in the set-up, is metal poor. In Chapter 4 we showed that the discs in our simulations have gradients that are shallower than observed and Gibson et al. (2013) recently showed that the details of feedback models significantly influence gradients. Because of the shallow gradients, only very weak metallicity dilution features in the form of slightly lowered metallicities at the beginning of the events can be found in Fig. 5.6. For the idealized simulations, it has, however, also been shown that enrichment due to SF in gas-rich mergers leads to an effective increase of metallicities at the end of the merger, in agreement with our findings. We conclude that events which trigger central SF are likely to leave an imprint on the age-metallicity relation of stars in that region and possibly also throughout the whole disc, but the shape of this feature is uncertain on account of modelling uncertainties.

When we compare our sample of simulated galaxies directly to observed samples, we have to take into account that the allowed scatter in the observers' selection criteria on evolution histories is much narrower than the scatter of the evolution histories displayed by our simulated galaxies. Moreover, the shapes of the SFHs of our galaxies differ significantly from that assumed by D13, although in Chapter 4 we have shown that the models with similar $z = 0$ masses as targeted by D13 agree well with abundance matching predictions for SFHs by Moster et al. (2013). Agreement with the assumptions of P13 in terms of SFH at slightly lower galaxy masses is better. Nevertheless, independent of sample selection, the mean profiles of the simulated galaxies agree well with observations at $z > 1$. At later times, galaxies show too little central mass growth and effective radii that increase too rapidly. At $z = 0$ galaxies are typically a factor of ~ 2 too extended. It is not, however, clear how much this result is influenced by the biased selection of haloes, as a significant number of galaxies with effective radii $R_{50} \sim 10$ kpc have been observed (Sargent et al., 2007).

Size growth is strongest for galaxies with masses similar to that of the MW and several of those models show strong inside-out growth. Although our full sample of galaxies shows better agreement with observations, we caution that this behaviour is driven by the high central SFRs and high central stellar mass densities at $z = 0$ of the most massive galaxies, which are likely unrealistic. Fang et al. (2013) recently showed that low-redshift galaxies with high central mass densities are preferentially quenched.

It is interesting to note that our models agree well with observations at high z, as, until recently, simulations matched observational data particularly poorly at early formation stages (e.g. Scannapieco et al., 2012; Moster et al., 2013). As already discussed in Chapter 4, our new simulations show better agreement with a variety of observations at $z \sim 1$ than at $z = 0$. One clearly identified problem is the lack of bars, which predominantly form at low z and can lead to inflow of gas to the centres of discs. The velocity dispersions in our model discs are too high (see Chapter 4), which prevents the formation of dynamically cold structures. This is partly caused by poor resolution (see e.g. House et al., 2011), but also by the strong stellar feedback in these models. The lack of disc instabilities thus prevents a mechanism for the growth of (central) surface densities, which in turn would make the discs more unstable due to the increase in surface gravity.

Marinacci et al. (2013) recently simulated five of our haloes with a different galaxy formation code. Interestingly, in these haloes, they found more massive and less extended galaxies compared to our models. On average, their sizes lie mildly above the observed mass-size relation of Shen et al. (2003). They used a very different prescription for stellar feedback and also find a higher fraction of bars.

These arguments seem to confirm the tentative conclusion of Chapter 4 that the stellar feedback applied in these simulations is too strong at low redshifts, as was also indicated by the underproduction of stars at low z in lower mass galaxies. It is interesting that the model for feedback from radiation pressure from young massive stars already invokes a significantly stronger feedback for high z gas-rich, turbulent galaxies than for quiescently star-forming discs at low z. It is possible that the calibration on galaxies similar in mass to the MW is problematic. At this halo mass, the quenching mechanism needed for high mass galaxies, be it AGN or something else, but not implemented here, probably already plays a role.

Simulations of disc galaxy formation have long been struggling with removing sufficient amounts of low angular momentum material from the inner regions and avoiding the formation of overly compact galaxies. Apparently our efforts in Chapter 4 to overcome this have led to the opposite problem. Weakening feedback seems an obvious solution, but the success of the model at high redshifts suggests that this should be done only at late times. Evidently, our models are still far from capturing all relevant astrophysical processes accurately.

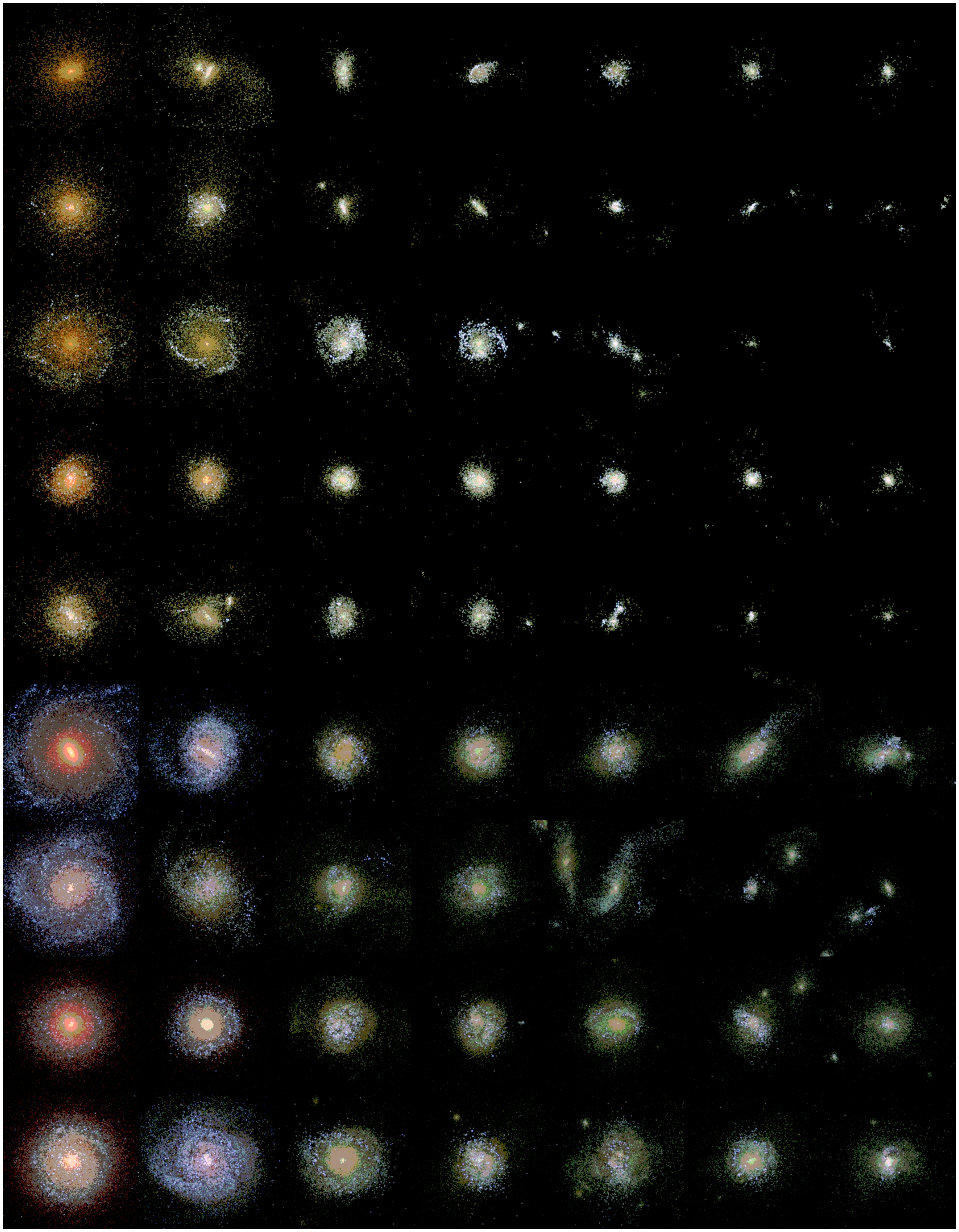

Figure 5.12: Evolution of face-on mock three-colour ugr-band images of model galaxies. From right to left redshifts $z = 2.5, 2.0, 1.5, 1.1, 0.85, 0.37, 0.0$. From top to bottom models 6782, 4323, 4349, 2283-2, 2283-1, 0959, 0858, 0664, 0616. Each image comprises 20 x 20 kpc. Different color scales were chosen for low and high mass galaxies.

6 | Comparing simulated gas discs and observed HI discs [1]

6.1 | Abstract

We attempt a comparison of neutral hydrogen (HI) surface density profiles between a sample of 19 $z = 0$ disc galaxies from cosmological zoom-in simulations and the galaxies from the Bluedisc survey recently presented by Wang et al. We apply a simple, observationally motivated model for the decomposition of simulated cold gas discs into HI and molecular hydrogen (H2). The simulated galaxies have on average higher HI mass fractions than typical observed galaxies, as have the Bluedisc galaxies. A correction for beam-smearing effects is applied to the simulated profiles. The correction significantly affects the shapes of the profiles. This is crucial for bringing observations and simulations into agreement and illustrates potential dangers for the interpretation of observed profiles. In terms of the HI mass-size relation, observed and simulated HI discs show identical slope and scatter. Profiles show flat inner parts because of the transition from HI to H2 and exponentially declining outer parts. The inner parts harbour slightly more HI mass than the outer parts, but similarity of profiles in both parts is needed to explain the mass-size relation.

---

[1] This Chapter presents first preliminary results on a comparison of the simulations presented in Chapters 4 and 5 with observations by Wang et al. (2013a).

6.2 | Introduction

Gas discs are an essential component of star-forming disc galaxies, as they provide the fuel for star formation. Although at a given galactic stellar mass, gas fractions (e.g. Tacconi et al., 2010) and star formation rates (e.g. Karim et al., 2011) are both higher at high redshift, gas depletion timescales are at high and low z significantly smaller than the age of the universe (Kennicutt, 1998; Genzel et al., 2010). Consequently, the gas reservoir has to be continuously replenished. The same conclusion can be reached by archaeological studies of the stars in the solar neighbourhood, which indicate that the disc of the Milky Way has been continuously forming stars over the last 10-13 Gyr (Aumer & Binney, 2009; Schönrich & Binney, 2009a). Unlike stellar discs, $z = 0$ gas discs thus encode primarily the current and recent epochs of galaxy formation.

Star formation in disc galaxies has been observed to occur in the molecular phase of the inter-stellar medium (ISM) (Bigiel et al., 2008, but see Glover & Clark, 2012 for why molecules might not be needed). Molecular hydrogen (H2) is confined to dense clouds which are self-shielded against dissociating radiation. The overall structure of gas discs is better traced by neutral hydrogen (HI). HI discs are often more extended than stellar discs (Walter et al., 2008) and show more complicated morphology, such as warps (Sancisi, 1976) or lopsidedness (Baldwin et al., 1980), which has been interpreted as a sign of recent gas accretion (e.g. Bournaud et al., 2005).

Galaxies that are richer in HI than average are thus good targets to improve our understanding of the mechanisms for gas accretion and thus for disc galaxy formation. Therefore Wang et al. (2013a,b) presented the 'Bluedisc' survey, which studies HI in 50 local galaxies with stellar masses similar to that of the Milky Way ($10 < log(M_{\rm stars}/M_{\odot}) < 11$), half of which were selected to be exceptionally HI-rich and half of which show normal HI fractions.

The simulations presented in Chapter 4 produce star-forming disc galaxies at redshift $z = 0$ with gas fractions ranging from average to high. They give specific predictions about the processes relevant for the accretion of gas and for the formation, the evolution and the morphologies of gas discs. The simulated sample also shares various morphological features with observed gas discs including warps and flocculent spiral structure. It thus constitutes an interesting sample of models to be compared to the observed HI discs.

In this Chapter we present first results of such a comparison and focus on HI mass surface density profiles. In Section 6.3 we describe the modelling of HI for our simulated discs. In Section 6.4 we compare them to observations. In Section 6.5 we apply a very simple model to understand, how inner and outer HI disc profiles combine to yield the HI mass-size relation. Finally, we conclude in Section 6.6.

6.3 | Simulations and modelling of HI

For our comparison to observed HI discs, we use the 19 $z = 0$ model galaxies presented in Chapters 4 and 5. These models result from cosmological zoom-in smoothed particle hydrodynamics (SPH) (re)simulations which follow the formation of galaxies in haloes with masses $1 \times 10^{11} < M_{200}/M_{\odot} < 3 \times 10^{12}$ in a Λ Cold Dark Matter universe. The simulations include models for multiphase gas treatment, star formation, metal enrichment, metal-line cooling, turbulent metal diffusion, thermal and kinetic supernova feedback, and radiation pressure from young stars. They, however, lack a model for the formation and destruction of HI and H2.

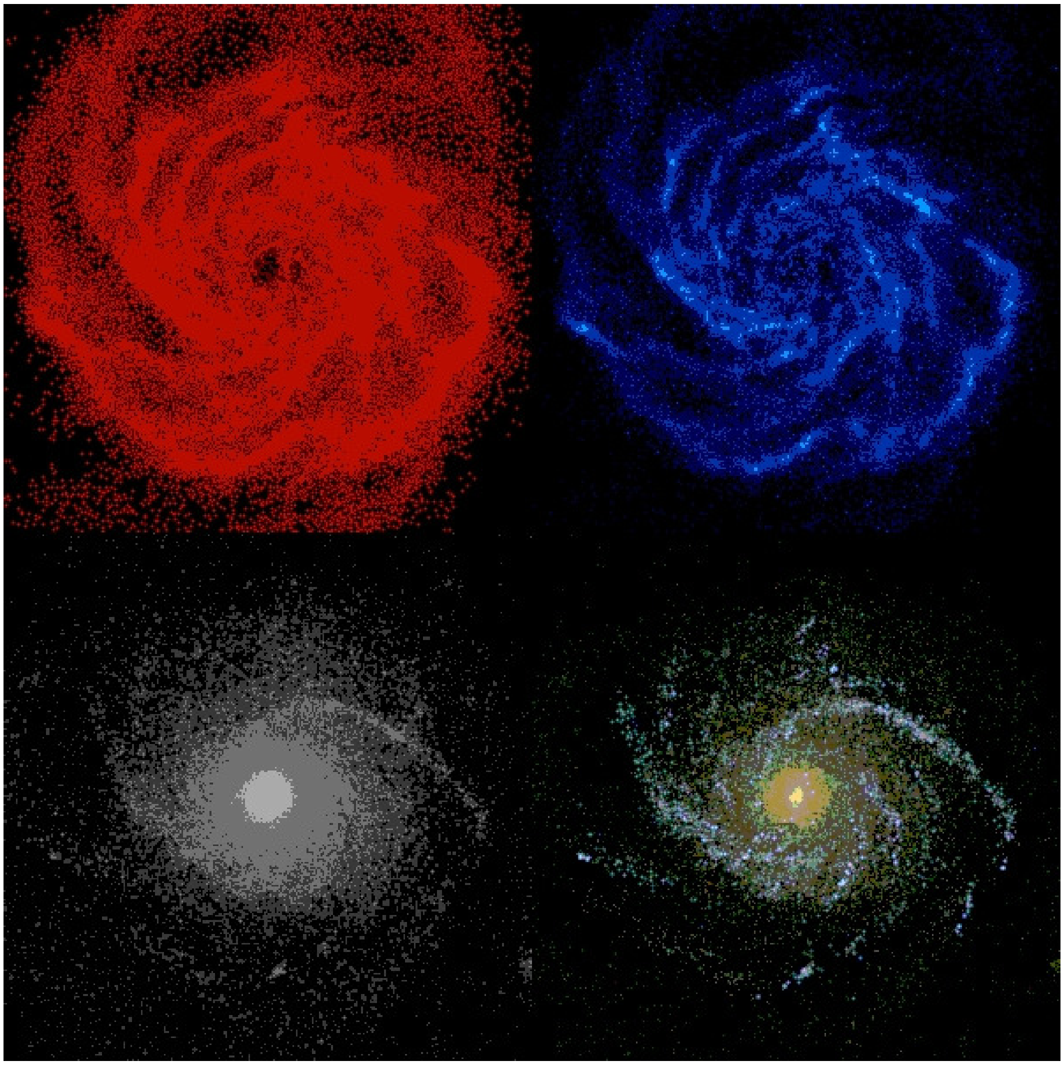

Figure 6.1: Face-on images of model galaxy AqE at $z \sim 0.5$. We show HI mass surface density in red (upper left), H2 mass surface density in blue (upper right), stellar mass surface density in gray (lower left) and a three-colour ugr band image as described in Chapter 5 (lower right). The images comprise 25 x 25 kpc.

As was shown in Chapter 4, the $z = 0$ model galaxies all contain gas discs, with gas fractions that tend to be higher than observed averages. These gas discs thus present a good comparison sample to the observed Bluedisc galaxies. To obtain HI profiles for the simulated discs, we apply a simple procedure based on the observationally motivated model by Blitz & Rosolowsky (2006) and its application in the semi-analytical models by Fu et al. (2010). We first select all gas with $T < 15000\ \mathrm{K}$ and determine its angular momentum vector to orient the galaxy in a face-on orientation. We then divide the galaxies into square pixels with $500\ \mathrm{pc}$ side-length.

According to Blitz & Rosolowsky (2006) the ratio of molecular and atomic hydrogen is

$$f_{\mathrm{mol}}(x,y) = \Sigma_{\mathrm{H}_2}(x,y)/\Sigma_{\mathrm{HI}}(x,y) = (P(x,y)/P_0)^{\alpha}\,, \tag{6.1}$$

where $\alpha = 0.92$ and $P_0 = 5.93 \times 10^{-13}\ \mathrm{Pa}$ are constants fit to observations. For the mid-plane pressure $P(x,y)$ we use the relation given by Elmegreen (1993) as

$$P(x,y) = \frac{\pi}{2} G \left[\Sigma_{\mathrm{gas}}(x,y)^2 + f_{\sigma}(x,y)\Sigma_{\mathrm{gas}}(x,y)\Sigma_{\mathrm{stars}}(x,y)\right], \tag{6.2}$$

with the ratio of gas-to-stellar velocity dispersions

$$f_{\sigma}(x,y) = \frac{\sigma_{\mathrm{gas}}(x,y)}{\sigma_{\mathrm{stars}}(x,y)}, \tag{6.3}$$

which, as the surface densities, we take directly from the simulations. To account for ionized hydrogen among the $T < 15000\ \mathrm{K}$ gas, we assume a 25% ionized fraction in stellar dominated regions and correct for the absence of stars as a source of ionization by crudely invoking a factor $\Sigma_{\mathrm{gas}}/\Sigma_{\mathrm{stars}}$ where stars are sub-dominant.

In Fig. 6.1 we visualize for one model galaxy, AqE at $z \sim 0.5$, the surface densities in HI and H2 as determined with the formalism presented above. As a contrast, we also show stellar mass and light distributions. The stellar mass (gray image) is centrally concentrated and shows the smoothest morphology. Two spiral arms are visible in the outskirts. A three-colour ugr band image, created according to the procedure detailed in Chapter 5, displays that the centre of the galaxy is redder due to lower specific star formation rates. The spiral structure in the outskirts is blue and bright due to the dominance of young stars and thus also much more distinct than in the stellar mass image.

The neutral gas (red image) is significantly more extended than the stellar mass. The morphology in the outskirts is not symmetric, indicating recent accretion. Flocculent spiral structure dominates the overall gas disc. The contrast in HI surface densities is lower than in stars and H2, as at $\Sigma \sim 5\ M_{\odot}\mathrm{pc}^{-2}$ the transition to molecular gas occurs, setting an effective upper limit for the HI surface density. H2 (blue image) is consequently significantly more clumpy, appearing mostly in dense knots along the flocculent spiral arms. A comparison with observed molecular and atomic gas in M51 (Schinnerer et al., 2013 and Walter et al., 2008 respectively) reveals good qualitative agreement in terms of general features of HI and H2 morphologies.

From the procedure detailed above, we can determine the total HI masses of the simulated disc galaxies at $z = 0$. In Fig. 6.2 we depict the HI-to-stellar mass ratio $M_{\mathrm{HI}}/M_{\mathrm{stars}}$ as a function of stellar mass M_{stars} for the simulated and observed galaxies. Note that the simulations (red) span a wider range in stellar mass ($9.5 < \log(M_{\mathrm{stars}}/M_{\odot}) < 11.3$) than the observations which were limited to $10. < \log(M_{\mathrm{stars}}/M_{\odot}) < 11$. In terms of gas-richness,

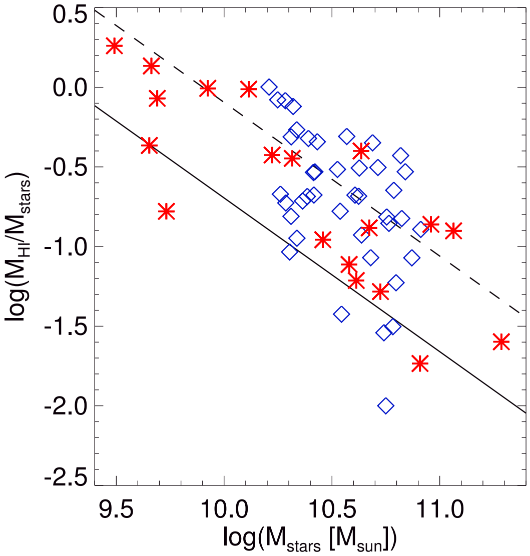

Figure 6.2: The HI-to-stellar mass ratio $M_{\rm HI}/M_{\rm stars}$ as a function of stellar mass $M_{\rm stars}$ for simulated (red stars) and observed galaxies (blue diamonds). The solid black line shows the median relation between HI mass fraction and stellar mass found by Catinella et al. (2010), the dashed black line is offset from this relation by +0.6 dex.

by construction about half of the observed galaxies lie above the black dashed line which depicts the median relation found by Catinella et al. (2010) (solid black line) shifted up by 0.6 dex. Only 4 of 19 simulated galaxies are above this line. However, the rest of the simulated galaxies shows a similar distribution of HI-mass fraction compared to the observed galaxies from the control sample with lower gas fractions. The range in relative HI-richness covered by the simulations is very similar to the range covered by the observed galaxies, which allows a meaningful comparison.

For such a comparison between simulations and observations, resolution effects have to be taken into account. In our case, the spacial resolution of observations (~ 10 kpc) is significantly larger than the 500 pc resolution of the pixels used above to determine the HI/H2 surface densities, which is slightly greater than the intrinsic resolution of the simulations (~ 300 pc). In order to model the effect of beam smearing in observations, we convolve $\Sigma_{\rm HI}(x,y)$ with an elliptical Gaussian Kernel with FWHM values of 14 and 9 kpc for major and minor axes, which mimics the observational configuration. Note that we apply this to face-on views for all model galaxies, whereas the observed galaxies show various inclinations, which were corrected for by Wang et al. (2013a).

The obtained HI un-convolved surface density $\Sigma_{\rm HI}(x,y)$ is then used to create radial face-on HI profiles $\Sigma_{\rm HI}(r)$ for all model galaxies. The characteristic HI radius $R1$ is determined as the radius, where $\Sigma_{\rm HI}(r)$ drops below $1\ M_{\odot}{\rm pc}^{-2}$, and the HI mass $M_{\rm HI}$ is determined as the total mass out to the radius, where $\Sigma_{\rm HI}(r)$ drops below $0.2\ M_{\odot}{\rm pc}^{-2}$, which mimics a realistic detection threshold. We also derive $\Sigma_{\rm HI,convolved}(r)$, $M_{\rm HI,convolved}$ and $R1_{\rm convolved}$ from the beam-convolved surface densities $\Sigma_{\rm HI,convolved}(x,y)$.

Fig. 6.3 displays the effects of convolution by depicting all 19 model HI profiles in raw

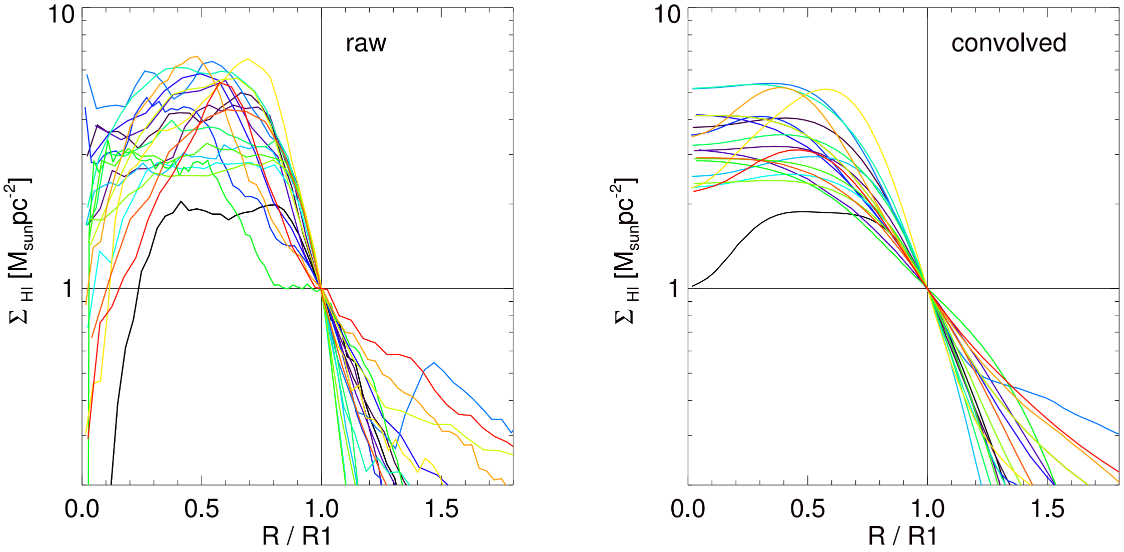

Figure 6.3: The effect of beam smearing on the HI surface density profiles. Left: Raw Profiles. Right: Profiles after convolution with an elliptical Gaussian Kernel with FWHM values of 14 and 9 kpc for major and minor axes. Surface densities are plotted against radii in units of the characteristic HI radii $R1$.

and convolved versions. The surface densities are plotted against radii in units of the characteristic radii $R1$ to eliminate dependencies on the specific size of the galaxy. Apart from the obviously significantly increased smoothness of the convolved profiles, the following aspects are interesting. Several raw profiles show holes or strong declines of surface densities in the centre (see also Fig. 6.1), which are smoothed out to only mildly centrally decreasing profiles. The declining profiles in the outer parts can be significantly steeper for the raw versions, resulting also in more extended flat parts. Moreover, the scatter at inner and outer radii is significantly reduced for convolved profiles.

In summary, we have applied a simple, observationally motivated model to determine HI and H2 surface densities from the cold gas and stellar properties of 19 model galaxies at $z = 0$. The resulting HI and H2 morphologies show reasonable agreement with observations. The HI-to-stellar mass fractions of the galaxies are on average higher than in observed galaxies, but span the same range in HI fraction as the Bluedisc galaxies. We have applied a model for the effects of beam smearing in HI observations and have shown that this correction significantly affects the structure of the HI profiles.

6.4 | A comparison with observations

In this section we compare the simulated HI surface density profiles described above to the observed HI profiles of the Bluedisc sample. We start in Fig. 6.4 with a comparison of normalized HI and cold gas profiles. The Bluedisc cold gas profiles were derived from HI data and measurements of star formation rate surface densities. The latter are converted into H2 surface densities following the observed relation by Bigiel et al. (2008) and added to the HI surface density.

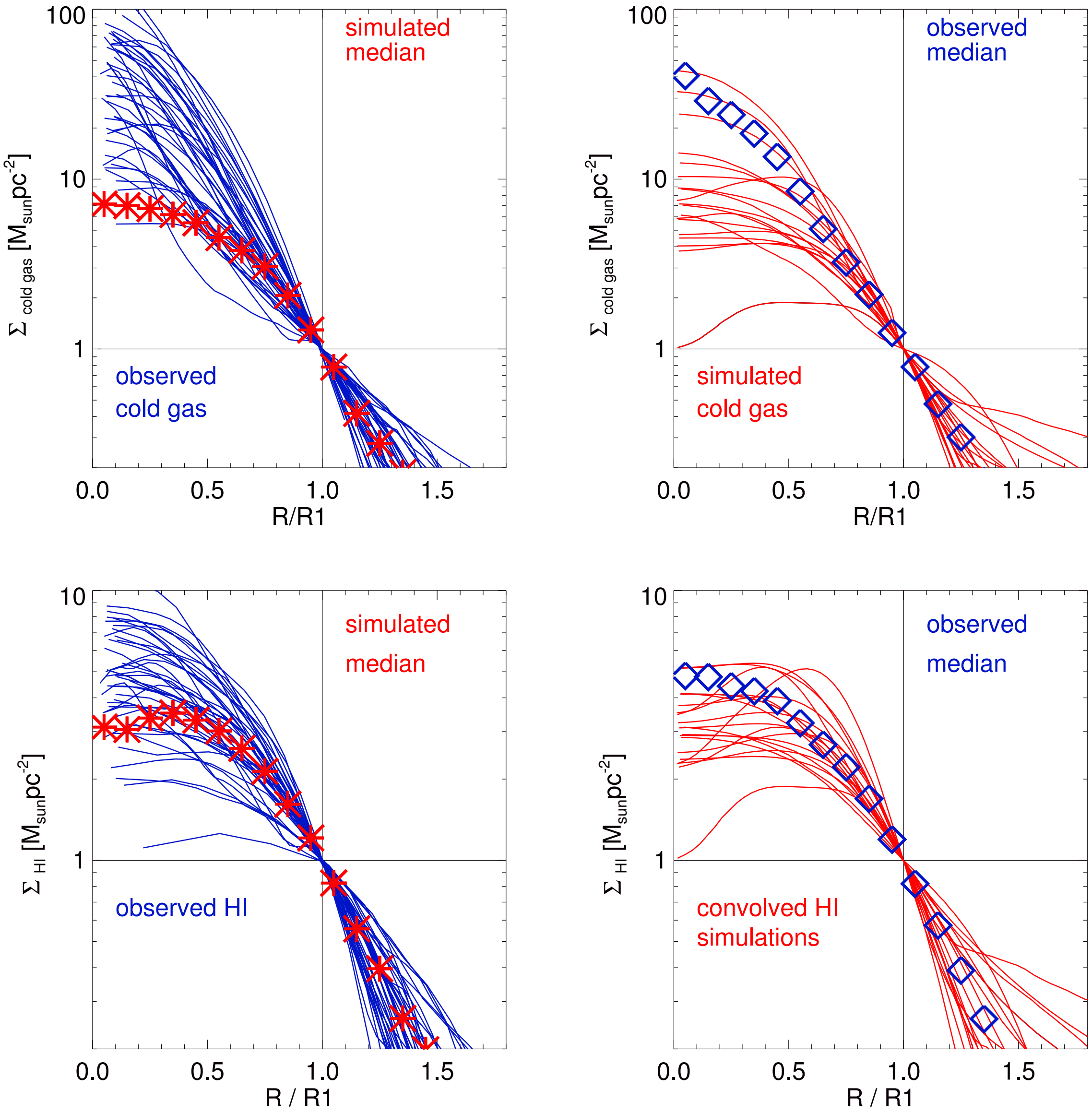

Figure 6.4: Cold gas (upper panels) and HI (lower panels) surface density profiles in simulations (beam convolved, red lines, right panels) and observations (blue lines, left panels). We overplot in corresponding colours the median profiles of simulations and observations. Surface densities are plotted against radii in units of the characteristic radii $R1$, determined independently for cold gas and HI.

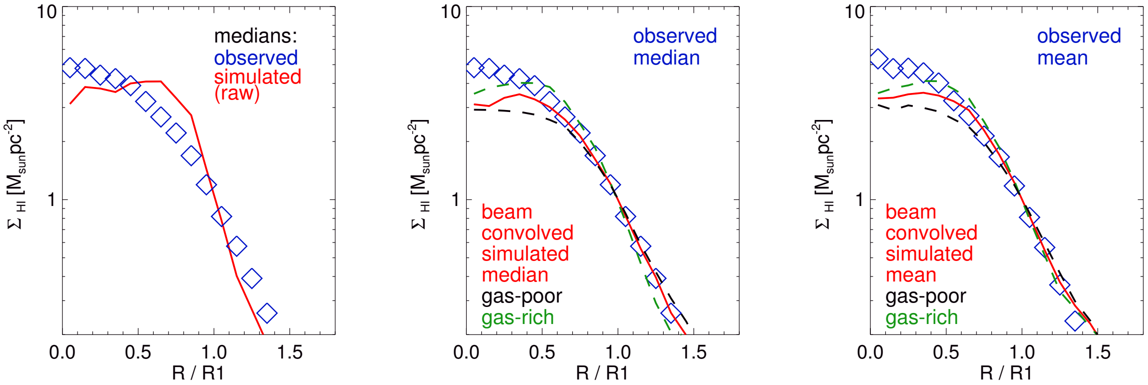

Figure 6.5: A comparison between simulated and observed median and mean HI surface density profiles. Left panel: The raw simulated median profile (red) compared to the observed median profile (blue). Middle panel: The beam convolved simulated median profile (red) compared to the observed median profile (blue). Overplotted are with dashed lines median profiles for gas-poor (gray) and gas-rich (green) sub-samples of the simulated galaxies. Right panel: As in the middle panel, but with mean profiles instead of median profiles.

In the lower right panel of Fig. 6.4 we depict a compilation of all 19 beam-convolved, simulated HI-mass profiles $\Sigma_{\mathrm{HI,convolved}}(R)$, where we use radii R in units of characteristic radii $R1$. All profiles follow a similar shape. They are rather flat in the centre and fall off exponentially at $R > 0.75\ R1$. The central surface density values scatter between 2 and 5 $M_{\odot}\mathrm{pc}^{-2}$, and for the outer exponential scale-length, we find values between 0.15 and 0.45 $R1$.

In the lower left panel we plot all observed HI profiles in the same way. To simplify a comparison, we overplot in both panels the median profiles of the sample that is shown in the respective neighbouring panel. We note that the observed central HI surface densities extend to higher values, the sample spans a range from 2 to 10 $M_{\odot}\mathrm{pc}^{-2}$. Surface densities tend to increase more steeply towards the centre than in the simulated galaxies, which might be connected to problems of the HI/H2 decomposition procedure and to the fact that half of the observed galaxies were selected to be particularly gas-rich. The observed profiles also show exponential decline at $R > 0.75\ R1$ with a similar scatter in steepness as found for the simulations.

In the upper panels of Fig. 6.4 we redo the exercise for cold gas profiles. Again the outer declining parts at $R > 0.8\ R1$ show good agreement in terms of slope and scatter. For the inner parts, there is disagreement, as observed profiles increase to significantly higher central surface densities and almost all observed central profiles lie above the simulated median profile. Possible contributors to this discrepancy are the indirect measurement of molecular surface densities and the higher average gas-richness of the observed sample.

Fig. 6.5 shows direct comparisons between median and mean profiles of the simulated and the observed samples. The left panel compares the raw simulated median profile with the observed median profile and reveals clear discrepancies. The simulated profiles are flatter in the centre and decrease more steeply outside. The middle panel shows that the application of the beam-smearing correction makes these problems disappear. The outer

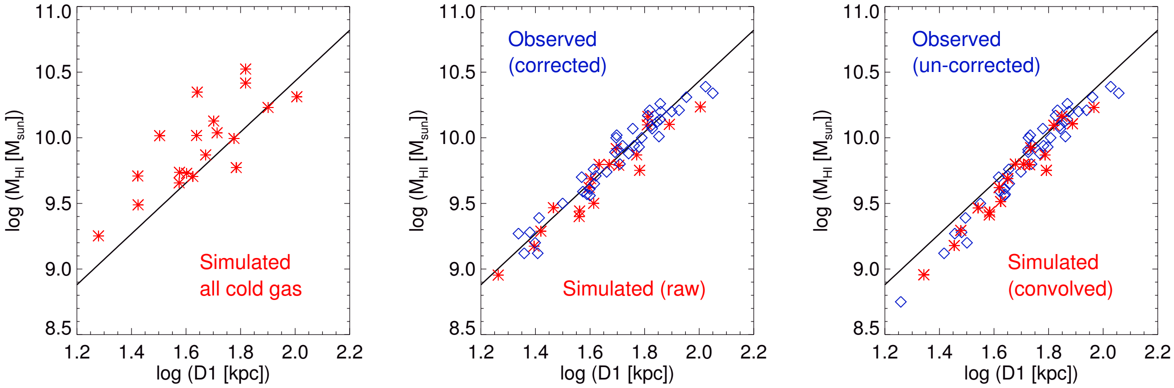

Figure 6.6: The HI mass-size relation. The relation found by Broeils & Rhee (1997) is shown by the black line in all panels. In all panels simulations are represented by red stars and observations by blue diamonds. Left: The relation of cold gas mass $M_{\rm coldgas}$ versus cold gas diameter $D1_{\rm coldgas} = 2\ R1_{\rm coldgas}$. Middle: The relation of HI mass $M_{\rm HI}$ and HI diameter $D1 = 2\ R1$ determined from the un-convolved simulations and from observations applying a beam correction for the radii. Right: Again for HI, but now for beam-convolved simulations and un-corrected observations.

flat parts are partly shifted to the declining part of the profile, which results in longer outer scale-lengths. The central surface densities in simulations are lower than in observations, as noted above. The outer profiles at $R > 0.5\ R1$ agree very well. The right panel shows that we obtain the same results if we use means instead of medians.

Wang et al. (2013b) tried to estimate the effect of beam smearing and to give corrected values for the observed exponential outer scale-length, $h_{\rm outer,intrinsic}$. On average they find $h_{\rm outer,intrinsic} \sim 0.2R1$. We find that the median outer HI scale-length of the un-convolved simulated discs is 0.17 in units of $R1$. This reasonable agreement emphasizes the importance of taking beam smearing effects into account.

Wang et al. (2013b) find that the shape of the normalized HI profile is independent of several properties of the gas discs including HI-richness, stellar mass, asymmetry of the gas disc etc. We restrict ourselves to test whether HI-richness affects the profile shapes. We therefore use the offset of the HI-to-stellar mass ratios from the observed median relation depicted in Fig. 6.2 to split our simulated sample into a gas-rich and a gas-poor sample. The median profiles of the sub-samples are shown as dashed lines in the middle panel of Fig. 6.5. We find that the gas-rich sample has slightly higher central surface densities and shows slightly steeper decline at outer radii compared to the gas-poor sample. The discrepancy between the sub-samples is more distinct than in observations. We caution, however, that we are comparing two samples with ~ 10 objects each. Considering the corresponding statistical errors, there is no significant disagreement between the profiles of the sub-samples. Moreover, if we use means instead of medians (see right panel of Fig. 6.5), the difference in outer scale-length becomes very small.

The HI masses and the characteristic HI diameters $D1 = 2\ R1$ of galaxies are known to be related as approx. $M_{\rm HI} \propto D1^2$ (Broeils & Rhee, 1997). Wang et al. (2013a) showed that in terms of this mass-size relation, their galaxies agree well with other samples of galaxies from the literature. In Fig. 6.6 we plot mass-size relations for the gas discs in our simulated galaxies. We start by analyzing this relation for cold gas instead of HI to gain better understanding of the origin of the observed relation. The left panel of Fig. 6.6 shows that cold gas masses and sizes could be fit by a $M \propto D^2$ relation with a higher mean than for observed HI. However, the scatter is large and some galaxies lie on the observed HI mass-size relation even if their total cold gas content is used.

In the middle panel we compare observed galaxies using $D1$ values corrected for beam effects and simulated galaxies using the un-convolved values. We see that both samples follow the Broeils & Rhee (1997) relation and agree very well with each other both in slope and in scatter of the relation. Note also that the range of sizes of the two samples is very similar. We find that the largest HI discs in simulations form from gas that cools and settles in a disc after merger events at $z \sim 1$. This is interesting, as in Chapter 5 we found that the sizes of the observed stellar galaxies at $z = 0$ are on average a factor two larger than in observations. Our work here shows that these galaxies are not too extended in gas size. However, it is unclear how much the selection of the observed galaxies as particularly gas-rich objects affects this. A more detailed comparison between observed and simulated ratios of characteristic HI radii and stellar half-mass radii could help in understanding why stellar discs are too extended, but gas discs appear to be in better agreement with observations. Problems with density thresholds for star formation in simulations could play a role, as they would affect centres and outskirts of galaxies differently. However, in Chapter 4 we found on average too little star formation in low surface density discs, which does not explain the overly high stellar half-mass radii.

In the right panel of Fig. 6.6 we, for comparison, depict the mass-size relations for observed profiles without a beam correction and beam-convolved simulated discs. These relations are actually tighter than the ones depicted above, as beam-convolved profiles show less scatter as seen in Fig. 6.3 . They fall below the Broeils & Rhee (1997) relation at small sizes, as $R1$ increases due to beam-smearing. The agreement between simulations and observations is even better than in Fig. 6.5.

In summary, we have presented a comparison between observed and simulated HI and cold gas surface density profiles. All profiles in observations and simulations have rather flat inner parts and decline exponentially at outer radii with similar slopes and similar scatter of slopes. We have shown that beam-smearing effects have a significant effect on these slopes as they smear mass to outer radii and thus produce shallower profiles. For the inner profiles we find slightly higher HI surface densities and significantly higher cold gas surface densities in observations than in simulations. In terms of the HI mass-size relation, observations and simulations agree very well in size range, HI mass scatter and slope of the relation. Beam-smearing effects slightly tilt the relation for smaller galaxies, but lead to reduced scatter.

6.5 | Origin of the HI mass-size relation

In the previous Subsection we showed that there is good agreement of the simulations with the observed HI mass-size relation. The relation $M \propto R1^2$ implies a geometric relationship with profiles that show little scatter around a mean profile, when HI surface density is plotted against radii in units of the characteristic radius $R1$, where the density drops below a threshold of $1\ M_{\odot}\mathrm{pc}^{-2}$. The HI profiles depicted in Fig. 6.4 show a rather flat inner part and an exponentially declining outer part. Thus the combination of a typical central surface density and a characteristic outer exponential slope leads to the observed relation. The former reflects the transition from HI to H2 above a certain density, whereas the latter is connected

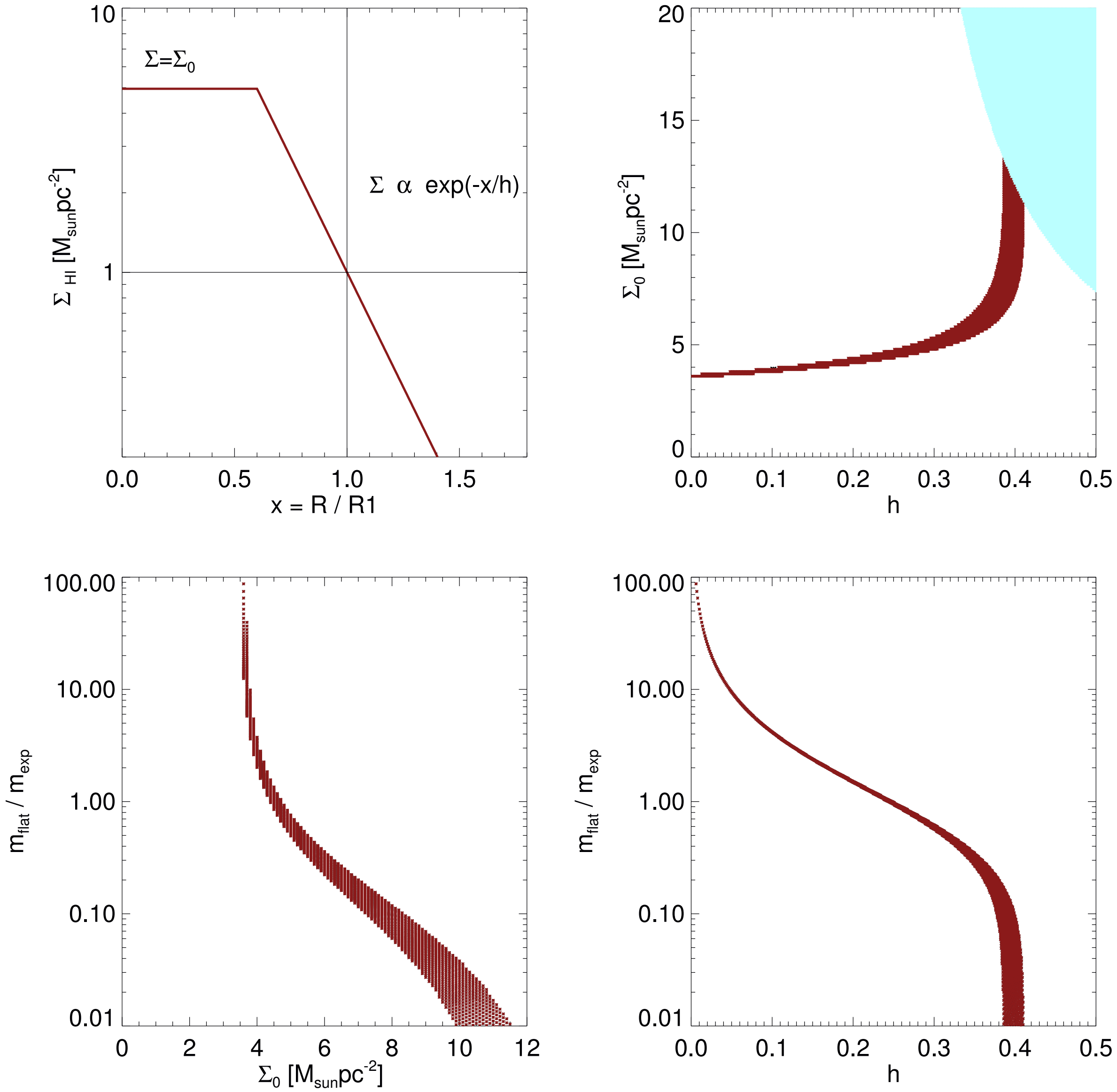

Figure 6.7: How central density and exponential outer slope combine to fit the mass-size relation. Upper left: Sketch of the simple model profile. Upper right: The parameter space searched (white area) and the region with low-χ^2 fits (red). No model is possible for the turquoise area. Lower panels: The mass ratio of the inner flat part to the outer declining part as a function of central density Σ_0 (left) and exponential outer slope h (right) for the low-χ^2 fits.

to the angular momentum distribution of the accreted gas. In this section we discuss which factor is more important for the relation.

Above, we have shown that beam-smearing effects play a crucial role in the shape of the profiles. Note that for the raw simulation profiles a break is apparent at around $R/R1 \sim 0.85$. Correspondingly $\sim 72\%$ of the HI mass is found in the flat inner part. When we analyze the convolved profiles the break can be found around $R/R1 \sim 0.62$ and the fraction of mass in the central part drops to $\sim 47\%$. For the observed median profile the break can be found around $R/R1 \sim 0.6$ and a dominance of the gas mass in the declining part was inferred. This comparison shows how vulnerable these estimates are. Consequently, one should expect that *both* the flat inner and the declining outer parts contribute significantly to the relation.

To gain a better understanding, we consider the simplest possible model in this context. Its is shown in the upper left panel of Fig. 6.7 and has a flat inner part with $\Sigma = \Sigma_0$ and an exponentially declining outer part with $\Sigma = \Sigma_1 \exp[-(R/R1)/h]$. Due to the condition that $\Sigma = 1\ M_{\odot}\mathrm{pc}^{-2}$ at $R = R1$, the relevant parameters are Σ_0 and h. We note that neither observed nor simulated HI profiles are exactly flat in the centre, but they are significantly flatter than the outer parts and Σ_0 should be viewed as a typical average inner surface density.

For all possible and sensible combinations of parameters Σ_0 and h we compute the relation between the HI mass out to $R_{0.2}$ where Σ drops below $0.2\ M_{\odot}\mathrm{pc}^{-2}$ and $R1$ for values of $R1$ between 7 and 50 kpc. In the upper right panel of Fig. 6.7 we mark in red the parameter pairs which yield good fits. Good is here defined in terms of χ^2 lower than an arbitrary threshold, which was chosen as low as possible to accept at least one parameter pair for every possible value of each parameter considering the used sampling of parameter space. In the lower panels we show, how the mass ratio between the inner and the outer region varies with parameters for acceptable parameter pairs.

In the previous sections we found that typical values of Σ_0 should be $3 - 5\ M_{\odot}\mathrm{pc}^{-2}$ and that typical values for h for profiles that are not affected by beam smearing effects should be ~ 0.2. We note that such parameter pairs are accepted for our simple model, which is thus justified. We see that for such parameter pairs the flat inner part of the profile is at least as massive and typically more massive than the mass in the declining outer part. This is reflected in the little change of possible Σ_0 values with possible h values around 0.2.

This exercise shows us that the threshold surface density for the transformation from HI to H2 is likely to play a more important role for the HI mass-size relation than the characteristic outer slope of the profile determined by the angular momentum distribution of the gas and the mass distribution of the galaxy and the dark halo. The latter however has a non-negligible effect as $\sim 1/3$ of the HI mass is contributed by the outer parts. It is likely that the ‘universal’ outer slope found in observations is connected to beam-smearing effects.

6.6 | Conclusions

We have presented a comparison of HI surface density profiles in simulations and observations. We have analyzed the 19 $z = 0$ gas discs of the cosmological zoom-in resimulations presented in Chapters 4 and 5 and ~ 50 observed galaxies from the Bluedisc survey recently presented by Wang et al. (2013a). The simulated gas discs, which are typically more extended than the stellar discs, show realistic features such as warps and flocculent spiral structure. We have applied a simple observationally motivated model for the decomposition of cold gas discs into neutral and molecular phases, which is capable of reproducing corresponding observed features.

The HI mass fractions of the simulations are on average higher than for typical observed galaxies, independent of galactic stellar mass. The simulations span a similar range in HI richness as the Bluedisc sample which features both very HI rich and normal galaxies.

We have shown that taking the effects of beam smearing into account is important, as it significantly affects the shapes of surface density profiles, which can lead to misinterpretations. These effects flatten the outer profile slopes, shrink the flat inner part, reduce the scatter between objects and produce smoother profile shapes.

When beam smearing is modelled, we find good agreement between simulated and observed profiles. If we attempt the same comparison for total cold gas profiles, the inner observed galaxies show significantly higher surface densities. It is unclear how much the indirect estimation of molecular gas masses via the observed star formation rate surface densities affects this or if overly strong feedback models prevent higher gas surface densities in simulations (see also the discussion in Chapter 5).

We also find good agreement between the observed and the simulated HI mass-size relation. Agreement in terms of slope and scatter is found if observations are corrected for beam affects and compared to raw simulation data and if a corresponding correction is applied on the simulation data and the corrected data are compared to un-corrected observations. Beam smearing reduces the scatter in the relation and tilts the mean relation for small galaxies.

The mass-size relation requires similarity of all HI profiles if surface densities are plotted against radii in units of the characteristic HI radii $R1$. The profiles feature a rather flat inner part, which results from the transition from neutral to molecular gas above a threshold surface density, and an exponentially declining outer part, which reflects the angular momentum distribution of the gas and the mass distribution of the galaxy and its dark halo. Simple models show that in order to fit the observed relation, the inner region has to harbour slightly more mass than the outer, so that similarity in both regions is required to yield the tight observed relation. The inner profiles tend to show more scatter, but this is most significant in the centres, where little mass can be found. The outer slopes seem to show less scatter between observed profiles, but beam smearing tends to reduce this scatter.

The results presented in this Chapter should be viewed as first steps in comparing our simulations to HI observations. Further questions that could be addressed include asymmetries of the gas discs as a result of recent accretion, the velocity fields of the gas discs, the origin of the slopes of outer profiles, the connection between sizes of gas and stellar discs or warps in outer gas discs.

7 | Concluding remarks

In this thesis, we have investigated the formation and evolution of disc galaxies in a ΛCDM universe. We have presented idealized semi-cosmological models for galactic disc formation within realistic ΛCDM haloes, as well as a sample of fully cosmological hydrodynamical simulations of individual disc galaxies. We have demonstrated that triaxial, substructured and evolving ΛCDM haloes are capable of hosting thin disc galaxies over several billion years. We have also shown that disc dominated galaxies can form in cosmological simulations. Comparisons with a variety of observations at high and low z have yielded good agreement for a variety of observables. However, we have also identified substantial remaining problems, from which we can learn, how to improve our models and thus our understanding of galaxy formation.

In Chapter 3, we presented idealized models for galactic disc formation in fully cosmological ΛCDM haloes. For these models, rotating hot gas spheres are added to high resolution dark-matter-only simulations of individual haloes at $z = 1.3$. Gas cooling and star formation are modelled with simplified prescriptions and the evolution of the forming galaxies is studied in the full cosmological context. We are thus able to better understand the complex dynamical processes relevant for the formation of discs in triaxial and substructured dark matter haloes. These models yield thin discs with realistic structure and kinematics preferentially if gas cooling times are sufficiently slow and allow a continuous growth of the disc, if the initial orientation of the gas angular momentum vector is aligned with the minor axis of the halo and if the orientation of the disc normal does not change significantly during its evolution.

It is very interesting that, despite the simple baryonic initial conditions (ICs) of coherently rotating gas spheres, the orientations of the angular momentum of the forming disc, the hot outer gas layers and the relative angles between different components can all change by more than 90 degrees over several Gyr. These orientation changes can not only lead to angular momentum loss, but also to peculiar structures, such as dominant bulges, warps, polar rings and counter-rotating components, which all have counterparts in the real universe. Clearly, the idealized ICs, which contain an inherent discrepancy between the spherical hot gas and the triaxial halo, play a role here. Misaligned infall of material (e.g. Quinn & Binney, 1992) and changes in the orientations of the angular momentum (Bett & Frenk, 2012) and of the shape of ΛCDM haloes (Vera-Ciro et al., 2011) are, however, common phenomena in a ΛCDM universe.

A question to pursue is thus, how important strongly non-linear dynamical interactions in the final stages of galaxy assembly, as seen in our idealized models, are for the formation of real galaxies, especially for observed multi-spin structures. Interestingly, similar processes were recently reported for semi-cosmological disc evolution models by DeBuhr et al. (2012) and by Debattista et al. (2013). Our fully cosmological simulations of Chapter 4 clearly offer information on this topic. The most striking example is the counter-rotating disc component found in one of the simulations. A different approach would be to compare the warps, rings and counter-rotating structures of our idealized models in detail to corresponding observations in order to find similarities or discrepancies and thus to constrain the formation processes.

In Chapter 4, we presented a new version of the multiphase Smoothed Particle Hydrodynamics (SPH) galaxy formation code originally described in Scannapieco et al. (2005, 2006). We have updated the production of metals in stars and supernova (SN) explosions and the metal cooling rates. We have reworked the modelling of feedback from SNe and we have included prescriptions for the turbulent diffusion of metals and for the effects of radiation pressure from massive young stars on the inter-stellar medium (ISM). The code was applied in cosmological hydrodynamical simulations of galaxy formation within 17 ΛCDM haloes of varying masses and formation histories.

Our models are successful in reproducing star formation histories of galaxies as inferred with the abundance matching method by Moster et al. (2013). Unlike most of the previous models, they thus show realistic stellar-to-dark-halo mass ratios at all redshifts $z < 4$. Moreover, observations of the evolution of gas fractions and stellar, as well as gas-phase metallicities from $z = 3$ until today are reasonably reproduced. We were thus able to confirm the conclusions of Stinson et al. (2013) that feedback from massive stars before their explosion as SNe can play an important role in regulating star formation, especially at high redshifts.

The galaxies at $z = 0$ show realistic morphologies, stellar surface brightness profiles and circular velocity curves. All but one of the galaxies at $z = 0$ contain prominent stellar disc components with kinematic disc fractions up to 65 per cent, higher than in any other published simulations. Our simulations are the first to confirm that the *Aquarius* haloes (Springel et al., 2008), which were selected to be prime candidates for hosting Milky Way (MW) like galaxies because of their relatively quiescent merger histories, on average indeed contain more prominent discs than randomly selected haloes of similar mass.

Some of the problems in our simulations are connected to metallicities. The $z = 0$ gas-phase mass-metallicity relation is too steep, the metallicity gradients in our discs are too flat and the observed abundances of α elements are not correctly reproduced. Many ingredients play a role here: metal production yields, the model for the turbulent diffusion of metals, the multiphase enrichment scheme, outflows of metals due to feedback etc. A detailed study of the interplay of the various processes is needed to constrain the involved models for physics. In our code, the enrichment of the hot phase, which, due to the diffuse nature of the hot phase, has the ability to spread metals over larger distances than the cold phase enrichment, should for example be studied more carefully. Moreover, metal diffusion models have been frequently included in recent simulations, but there is not yet a comprehensive study of its effect on the distribution of metals in the gaseous and stellar discs of galaxy models (but see Pilkington et al., 2012b and Gibson et al., 2013 for interesting effects).

The detailed distribution of metals in the various structural components of disc galaxies, such as the age-metallicity relation in the solar neighbourhood (Casagrande et al., 2011) or the metal distribution in the Galactic bulge (Ness et al., 2013) offer constraints on the formation processes and should thus be studied in more detail. Several such studies relying on cosmological simulations exist in the literature (e.g. Tissera et al., 2012), but most of them lack three important ingredients that our models have: a model for metal diffusion, dominant disc components and realistic star formation histories.

In Chapter 5, we compared our cosmological simulations in detail to recent observations

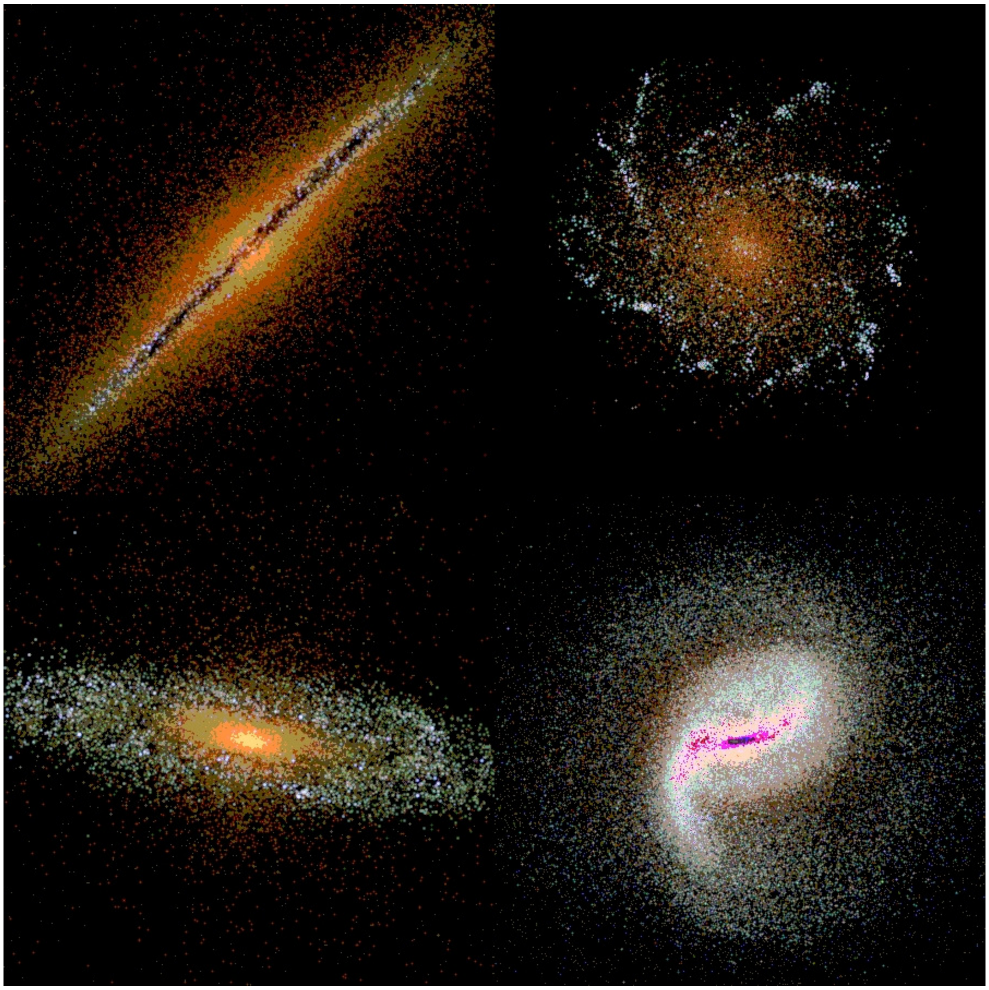

Figure 7.1: Four three-colour ugr-band images of simulated modern day disc galaxies to attempt a comparison with the images of real galaxies presented in Figure 1.1. Top left: Halo AqE, edge-on, $z = 0.12$; Top right: Halo 0977, galaxy 2, almost face-on, $z = 0.07$; Bottom left: Halo AqA, almost edge-on, $z = 0.33$; Bottom right: Halo 0616, almost face-on, short-lived bar triggered by an interaction, $z = 0.25$.

by van Dokkum et al. (2013) and Patel et al. (2013b), who analyzed the structural evolution history of disc galaxies from $z = 2.5$ to $z = 0$. When comparing average surface density profiles from observations and simulations, we find good agreement at $z > 1.5$, but increasing discrepancies at low z. Our simulated disc galaxies on average grow too much in radial extent and do not show enough central mass growth.

We find that these problems are likely connected to an under-abundance of bars in our disc galaxies, which could trigger gas flows to the centres of discs (Athanassoula, 1992) and thus sustain the growth in central stellar surface densities. Generally, the formation histories of the simulated disc galaxies are diverse. The galaxies with the highest disc fractions grow inside-out, whereas mergers and misaligned infall events can lead to episodes of central growth. Discs frequently regrow after such destructive events, which leave imprints on the distributions of stellar radii, metallicities and circularities as a function of stellar age.

In our motivating Chapter 1, we presented a compilation of images showing four disc galaxies in the real universe (Fig. 1.1). In Chapter 5 we created mock three-colour ugr-band images of our simulated disc galaxies. It is of course interesting to ask, how similar images of the simulated discs can get to the images of real discs. We attempt such a comparison with Fig. 7.1 in which we present images of four of our model galaxies, which, at low redshifts, have some resemblance to the real galaxies of Fig. 1.1.

Clearly, the limited resolution of our simulations makes a detailed comparison impossible. But if this limitation is taken into account, similarities can be found for morphologies, colour gradients and dust extinction lines for all but the barred system. The latter comes from one of the models that overproduces stars at low z and is thus clearly too blue and lacking a distinct red bulge component. The bar was triggered by an interaction with an infalling galaxy. As discussed in Chapter 5, bars are under-represented in our models. The dust lane in this model, especially its colour, is also problematic, but at least the two arm spiral plus bar morphology in stars and dust bears resemblance to the corresponding structures in the lower right panel of Fig. 1.1.

The other three images are, however, encouraging and depict what cosmological hydrodynamical simulations are capable of. We also use this concluding section to present a collection of three-colour images of the interacting spiral galaxies in our model 0977 seen from various orientations at various times in Fig. 7.2.

These images bring along topics for improvement. Increasing the resolution of simulations allows an improved understanding of the many processes that are unresolved. However, applying our models for baryonic physics at a higher resolution currently yields unsatisfactory convergence. This problem has to be investigated.

Higher resolution would be desirable for studies of secular processes in disc evolution such as disc heating (Jenkins & Binney, 1990), radial mixing (Sellwood & Binney, 2002) or bar formation. Low resolution leads to an effective lower limit for the vertical velocity dispersion σ_z (House et al., 2011), which prevents the formation of realistically thin young stellar discs. Too high velocity dispersions can also stabilize discs against bar formation and thus generally limit the significance of simulations in explaining dynamical processes in the discs.

The lack of bars in our simulations is, however, likely also connected to overly strong stellar feedback in discs after $z \sim 1$. This is also indicated by overly low star formation rates (SFRs) and overly high gas fractions in the lowest mass galaxies at these times. The situation is complicated by the fact that our simulations agree well with various constraints from high-z observations, although the feedback in our models is stronger in gas-rich, turbulent discs as found at earlier formation stages.

Evidently, there are details about our stellar feedback models that should be updated. SNe of type II should be represented by more than one event, as in the current implementation, to take into account that SNII explosions occur at a range of stellar ages 3-30 Myr. Moreover, stellar winds could explicitly be taken into account as a source for momentum feedback. However, these changes are unlikely to solve the problem. Possibly, in addition to radiation pressure from massive stars and kinetic plus thermal feedback from SNe, further feedback mechanisms have be taken into account, such as cosmic ray pressure (see e.g. Uhlig et al., 2012). In the context of such changes, simulations of dwarf galaxies (see e.g. Sawala et al., 2011, who used the original version of our galaxy formation code) could be very helpful, as additional observational constraints could be used and as computational costs would be significantly smaller than for high resolution MW analogs.

The overly high SFRs of the most massive galaxy models at low redshift indicate the lack of a quenching mechanism for galaxies above $M_\star \sim 10^{11} M_\odot$. One possible mechanism is AGN feedback (Croton et al., 2006). Under the assumption that this mechanism already plays a significant role for halo masses $M_{200} \sim 10^{12} M_\odot$, as studied in Chapter 4, a recalibration of stellar feedback would be required, which might also help in reducing the problems in lower mass galaxies discussed above. The inclusion of an AGN feedback model would allow us to study more massive haloes and thus the formation of massive, elliptical galaxies and of groups and clusters of galaxies.

In Chapter 6, we attempted a comparison of our cosmological simulations to recent observations of $z = 0$ neutral hydrogen (HI) discs (Wang et al., 2013a). We therefore apply an observationally motivated model for the decomposition of cold gas in the simulations into HI and molecular hydrogen (H2). We find that the simulated galaxies at $z = 0$ are on average too rich in HI, independent of galaxy mass. Nevertheless, the shapes of the HI mass profiles agree very well with observations when an appropriate correction for observational beam-smearing effects is taken into account. The observed HI mass-size relation is very well reproduced by the models.

Observations of gas discs offer several additional constraints on our models. Possible topics include asymmetries of gas disc as a result of accretion, the formation of warped HI discs, the velocity fields of gas discs, the connection between the sizes of gaseous and stellar discs or the origin of the exponential outer HI mass profiles. To avoid HI/H2 decomposition in post-processing, an explicit model for the formation and destruction of H2 and HI could be added to the sub-grid physics, as was e.g. presented by Christensen et al. (2012). These authors also stressed that applying a model for SF from molecular gas could significantly affect the interplay of star formation and feedback in simulations.

Further constraints on galaxy formation from observations of gas properties come from the circumgalactic medium (CGM). Recent advances in observational techniques have started providing previously inaccessible information. Among several others, Peeples et al. (2013) recently presented an inventory of metals in stars, the interstellar medium and the CGM, Anderson et al. (2013) presented constraints on the hot gas contents within 50 kpc of galaxies and Bolatto et al. (2013) presented observations of large masses of molecular gas in a galactic wind driven by a star-burst galaxy. These data provide important constraints on the modelling of galactic winds in simulations.

In general, it would be interesting to analyze in more detail the fate of galactic wind gas in simulations. Questions to be asked include: How far do winds transport metals away from galaxies? What fraction of the wind gas returns in galactic fountains? How does the angular momentum of the outflowing/inflowing gas evolve? What are the ratios of star formation rates to outflow rates? How much dependence on galaxy mass is there?

Apart from improving models for baryonic physics, improving numerical methods should also be considered. Several updates to SPH were recently presented, which improve its ability to treat fluid mixing instabilities properly (e.g. Wadsley et al., 2008; Read & Hayfield, 2012; Hopkins, 2013). One straightforward change should be to apply the *pressure-entropy* formulation of SPH presented by Hopkins. Other changes, which e.g. require the application of significantly higher numbers of neighbour particles in the smoothing kernel (Read & Hayfield, 2012), might be problematic to be combined with the multiphase gas model.

In conclusion, we have achieved significant progress in modelling the formation and evolution of disc galaxy formation in a ΛCDM universe with the help of Smoothed Particle Hydrodynamics simulations. The detailed analysis of our models has helped us in identifying a variety of remaining problems. As always in physics, these problems provide the basis for further improvements of the modelling and thus of our understanding of galaxy formation.

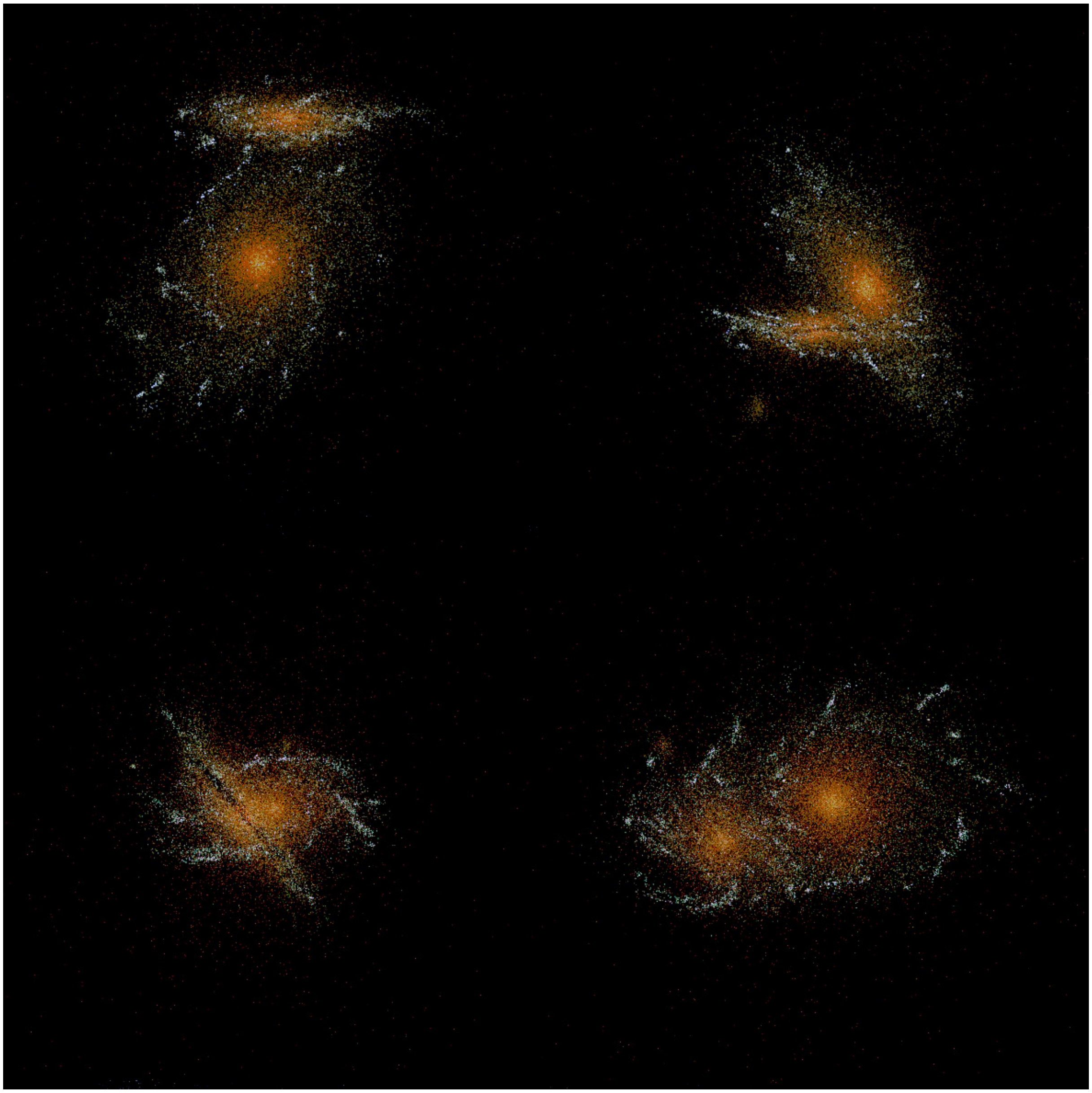

Figure 7.2: Various three-color ugr-band images of the two galaxies in halo 0977 at $z < 0.05$. Images show views from different orientations at different times.

Bibliography

Abadi M. G., Navarro J. F., Steinmetz M., Eke V. R., 2003, ApJ, 597, 21

Agertz O. et al., 2007, MNRAS, 380, 963

Agertz O., Teyssier R., Moore B., 2011, MNRAS, 410, 1391

Agertz O., Kravtsov A. V., Leitner S. N., Gnedin N. Y., 2013, ApJ, 770, 25

Alpher R. A., Herman R., 1946, Nature, 162, 774

Anderson M. E., Bregman J. N., Dai X., 2013, ApJ, 762, 106

Andrews B. H., Martini P., 2013, ApJ, 765, 140

Angulo R. E., Springel V., White S. D. M., Jenkins A., Baugh C. M., Frenk C. S., 2012, MNRAS, 426, 2046

Athanassoula E., 1990, MNRAS, 259, 345

Aumer M., Binney J. J., 2009, MNRAS, 397, 1286

Aumer M., 2010, Diplomarbeit an der LMU München

Aumer M., Burkert A., Johansson P. H., Genzel R., 2010, ApJ, 719, 1230

Aumer M., White S. D. M., 2013, MNRAS, 428, 1055

Aumer M., White S. D. M., Naab T., Scannapieco C., 2013a, MNRAS, 434, 3142

Aumer M., White S. D. M., Naab T., 2013b, in preparation

Avila-Reese V., Zavala J., Firmani C., Hernández-Toledo H. M., 2008, AJ, 136, 1340

Azzollini R., Trujillo I., Beckman J. E., 2008, ApJ, 684, 1026

Bailin J. et al., 2005, ApJ, 627, L17

Baldry I. K., Glazebrook K., Brinkmann J., Ivezić Ž., Lupton R. H., Nichol R. C., Szalay A. S., 2004, ApJ, 600, 681

Baldwin J. E., Lynden-Bell D., Sancisi R., 1980, MNRAS, 193, 313

Balogh M. L., Navarro J. F., Morris S. L., 2000, ApJ, 540, 113

Balsara D. S., 1995, Journal of Computational Physics, 121, 357

Barber C., Starkenburg E., Navarro J., McConnachie A., Fattahi A., 2013, arXiv e-prints, arXiv:1310.0466

Barden M. et al., 2005, ApJ, 635, 959

Barnes J., Hut P., 1986, Nature, 324, 446

Barnes J. E., Hernquist L., 1996, ApJ, 471, 115

Barnes J. E., 2002, MNRAS, 333, 481

Behroozi P. S., Wechsler R. H., Conroy C., 2013a, ApJ, 770, 57

Behroozi P. S., Wechsler R. H., Conroy C., 2013b, ApJ, 762, L31

Berentzen I., Shlosman I., 2006, ApJ, 648, 807

Bett P. E., Frenk C. S., 2012, MNRAS, 420, 3324

Bezanson R., van Dokkum P. G., Tal T., Marchesini D., Kriek M., Franx M., Coppi P., 2009, ApJ, 697, 1290

Bigiel F., Leroy A., Walter F., Brinks E., de Blok W. J. G., Madore B., Thornley M. D., 2008, AJ, 136, 2846

Binney J., 1977, ApJ, 215, 483

Binney J., Tremaine S., 2008, Galactic Dynamics: Second Edition, Princeton University Press, Princeton

Blitz L., Rosolowsky E., 2006, ApJ, 650, 933

Bois M. et al., 2011, MNRAS, 416, 1654

Bolatto A. D. et al., 2013, Nature, 499, 450

Bondi H., 1952, MNRAS, 112, 195

Bournaud F., Combes F., Jog C. J., Puerari I., 2005, A&A, 438, 507

Bovy J., Rix H.-W., Liu C., Hogg D. W., Beers T. C., Lee Y. S., 2012, ApJ, 753, 148

Boylan-Kolchin M., Springel V., White S. D. M., Jenkins A., Lemson G., 2009, MNRAS, 398, 1150

Broeils A. H., Rhee M.-H, 1997, A&A, 324, 877

Brook C. B., Governato F., Quinn T., Wadsley J., Brooks A. M., Willman B., Stilp A., Jonsson P., 2008, ApJ, 689, 678

Brook C. B. et al., 2011, MNRAS, 415, 1051

Brook C. B., Stinson G., Gibson B. K., Wadsley J., Quinn T., 2012, MNRAS, 424, 1275

Bruzual G., Charlot S., 2003, MNRAS, 344, 1000

Bullock J. S., Kravtsov A. V., Weinberg D. H., 2000, ApJ, 539, 517

Burbidge E. M., Burbidge G. R., Fowler W. A., Hoyle F., 1957, Reviews of Modern Physics, 29, 547

Cappellari M. et al., 2011, MNRAS, 416, 1680

Casagrande L., Schönrich R., Asplund M., Cassisi S., Ramírez I., Meléndez J., Bensby T., Feltzing S., 2011, A&A, 530, 138

Catinella B. et al., 2010, MNRAS, 403, 683

Chabrier G., 2003, PASP, 115, 763

Chieffi A., Limongi M., 2004, ApJ, 608, 405

Christensen C., Quinn T., Governato F., Stilp A., Shen S., Wadsley J., 2012, MNRAS, 425, 3058

Cleary P. W., Monaghan J. J., 1999, Journal of Computational Physics, 148(1), 227

Cole S. et al., 2005, MNRAS, 362, 505

Combes F., Debbasch F., Friedli D., Pfenniger D., 1990, A&A, 233, 82

Cooper A. P. et al., 2012, MNRAS, 406, 744

Corsini E.M., Méndez-Abreu J., Pastorello N., Dalla Bontà E., Morelli L., Beifiori A., Pizzella A., Bertola F., 2012, MNRAS, 423, 79

Courteau S., Dutton A. A., van den Bosch F. C., MacArthur L. A., Dekel A., McIntosh D. H., Dale D. A., 2007, ApJ, 671, 203

Cox T. J., Dutta S. N., Di Matteo T., Hernquist L., Hopkins P. F., Robertson B., Springel V., 2006, ApJ, 650, 791

Croton D. J. et al., 2006, MNRAS, 365, 11

Daddi E. et al., 2007, ApJ, 670, 156

Davé R. et al., 2001, ApJ, 552, 473

Davé R., Finlator K., Oppenheimer B. D., Fardal M., Katz N., Kereš D., Weinberg D. H., 2010, MNRAS, 404, 1355

Davis M., Efstathiou G., Frenk C. S., White S. D. M., 1985, ApJ, 292, 371

Debattista V. P., Roškar R., Valluri M., Quinn T., Moore B., Wadsley J., 2013, MNRAS, 434, 2971

de Blok W. J. G., Walter F., Brinks E., Trachternach C., Oh S.-H., Kennicutt Jr. R. C., 2008, AJ, 136, 2648

DeBuhr J., Ma C.-P., White S. D. M., 2012, MNRAS, 426, 983

Dekel A. et al., 2009, Nature, 457, 451

Delgado-Serrano R., Hammer F., Yang Y. B., Puech M., Flores H., Rodrigues M., 2010, A&A, 509, A78

de Vaucouleurs G., 1958, ApJ, 128, 465

Dolag K., Stasyszyn F., 2009, MNRAS, 398, 1678

Dutton A. A., van den Bosch F. C., 2009, MNRAS, 396, 141

Einstein A., 1916, Annalen der Physik, 354, 769

Efstathiou G., Sutherland W. J., Maddox S. J., 1990, Nature, 348, 705

Ekström S. et al., 2012, A&A, 537, A146

Elbaz D. et al., 2007, A&A, 468, 33

Elmegreen B. G., 1993, ApJ, 411, 170

Emsellem E. et al., 2011, MNRAS, 414, 888

Erb D. K., Steidel C. C., Shapley A. E., Pettini M., Reddy N. A., Adelberger K. L., 2006a, ApJ, 646, 107

Erb D. K., Shapley A. E., Pettini M., Steidel C. C., Reddy N. A., Adelberger K. L., 2006b, ApJ, 644, 813

Eskridge P. B. et al., 2000, AJ, 119, 536

Evoli C., Salucci P., Lapi A., Danese L., 2011, ApJ, 743, 45

Fabian A. C., 2012, ARAA, 50, 455

Fall S. M., Efstathiou G., 1980, MNRAS, 193, 189

Fang J. J., Faber S. M., Koo D. C., Dekel A., 2013, ApJ, 776, 63

Faucher-Giguère C.-A., Kereš D., Ma C.-P., 2011, MNRAS, 417, 2982

Feng J. L., 2010, ARAA, 48, 495

Fermani F., Schönrich R., 2013, MNRAS, 432, 2402

Few C. G., Gibson B. K., Courty S., Michel-Dansac L., Brook C. B., Stinson G. S., 2012, A&A, 547, A63

Förster Schreiber N. M. et al., 2009, ApJ, 706, 1364

Fraternali F., van Moorsel G., Sancisi R., Oosterloo T., 2002, AJ, 123, 3124

Freeman K. C., 1970, ApJ, 160, 811

Frenk C. S., White S. D. M., Davis M., Efstathiou G., 1988, ApJ, 327, 507

Friedmann A., 1922, Z. Phys., 10, 377

Fu J., Guo Q., Kauffmann G., Krumholz M. R., 2010, MNRAS, 409, 515

Gallazzi A., Charlot S., Brinchmann J., White S. D. M., Tremonti C. A., 2005, MNRAS, 362, 41

Gamow G., Teller E., 1939, Physical Review, 55, 654

Gamow G., 1946, Physical Review, 70, 572

Genel S., Bouché N., Naab T., Sternberg A., Genzel R., 2010, ApJ, 719, 229

Genel S. et al., 2012, ApJ, 745, 11

Genzel R. et al., 2008, ApJ, 687, 59

Genzel R. et al., 2010, MNRAS, 407, 2091

Gibson B. K., Pilkington K., Brook C. B., Stinson G. S., Bailin J., 2013, A&A, 554, A47

Gingold R. A., Monaghan J. J., 1977, MNRAS, 181, 375

Glover S. C. O., Clark P. C., 2012, MNRAS, 421, 9

Gnedin N. Y., Tassis K., Kravtsov A. V., 2009, ApJ, 697, 55

Goerdt T., Moore B., Read J. I., Stadel J., Zemp M., 2006, MNRAS, 368, 1073

Governato F. et al., 2004, ApJ, 607, 688

Governato F., Willman B., Mayer L., Brooks A., Stinson G., Valenzuela O., Wadsley J., Quinn T., 2007, MNRAS, 374, 1479

Governato F. et al., 2010, Nature, 463, 203

Greif T. H., Glover S. C. O., Bromm V., Klessen R. S., 2009, MNRAS, 392, 1381

Groom W., 1997, PhD thesis, Cambridge Univ.

Guedes J., Callegari S., Madau P., Mayer L., 2011, ApJ, 742, 76

Guedes J., Mayer L., Carollo M., Madau P., 2013, ApJ, 772, 36

Gunn J. E., Gott III J. R., 1972, ApJ, 176, 1

Guo Q., White S., Li C., Boylan-Kolchin M., 2010, MNRAS, 404, 1111

Guo Q. et al., 2011, MNRAS, 413, 101

Guth A. H., 1981, PhRvD, 23, 347

Haardt F., Madau P., 2001, in Neumann D. M., Tran J. T. V., eds, XXIst Moriond Astrophys. Meeting, Clusters of Galaxies and the High Redshift Universe Observed in X-rays, Editions Frontieres, Paris

Hall M., Courteau S., Dutton A. A., McDonald M., Zhu Y., 2012, MNRAS, 425, 2741

Hammer F., Flores H., Elbaz D., Zheng X. Z., Liang Y. C., Cesarsky C., 2005, A&A, 430, 115

Hammer F., Puech M., Chemin L., Flores H., Lehnert M. D., 2007, ApJ, 662, 322

Harrison E. R., 1970, PhRvD, 1, 2726

Haynes M. P., Giovanelli R., 1984, AJ, 89, 758

Helmi A., White S. D. M., de Zeeuw P. T., Zhao H., 1999, Nature, 402, 53

Henriques B. M. B., White S. D. M., Thomas P. A., Angulo R. E., Guo Q., Lemson G., Springel V., 2013, MNRAS, 431, 3373

Hilz M., Naab T., Ostriker J. P., 2013, MNRAS, 429, 2924

Hirschmann M. et al., 2013, arXiv e-prints, arXiv:1309.2946

Hoekstra H., Jain B., 2008, Annual Review of Nuclear and Particle Science, 58, 99

Holmberg J., Nordström B., Andersen J., 2009, A&A, 501, 941

Hopkins A. M., Beacom J. F., 2006, ApJ, 651, 142

Hopkins P. F., Hernquist L., Cox T. J., Di Matteo T., Robertson B., Springel V., 2006, ApJS, 163, 1

Hopkins P. F., Bundy K., Hernquist L., Wuyts S., Cox T. J., 2010, MNRAS, 401, 1099

Hopkins P. F., Quataert E., Murray N., 2011, MNRAS, 417, 950

Hopkins P. F., 2013, MNRAS, 428, 2840

Hopkins P. F., Cox T. J., Hernquist L., Narayanan D., Hayward C. C., Murray N., 2013, MNRAS, 430, 1901

House E. L. et al., 2011, MNRAS, 415, 2652

Hubble E., 1926, ApJ, 64, 321

Hubble E., 1929, Proceedings of the National Academy of Science, 15, 168

Ichikawa T., Kajisawa M., Akhlaghi M., 2012, MNRAS, 422, 1014

Iwamoto K., Brachwitz F., Nomoto K., Kishimoto N., Umeda H., Hix W. R., Thielemann F.-K., 1999, ApJS, 125, 435

Jeans J. H., 1902, Royal Society of London Philosophical Transactions Series A, 199, 1

Jenkins A., Binney J., 1990, MNRAS, 245, 305

Johansson J., Thomas D., Maraston C., 2012a, MNRAS, 421, 1908

Johansson P. H., Naab T., Ostriker J. P., 2012b, ApJ, 754, 115

Jonsson P., 2006, MNRAS, 372, 2

Jurić M. et al., 2008, ApJ, 673, 864

Kajisawa M., Ichikawa T., Yamada T., Uchimoto Y. K., Yoshikawa T., Akiyama M., Onodera M., 2010, ApJ, 723, 129

Kannan R., Stinson G. S., Macciò A. V., Brook C., Weinmann S. M., Wadsley J., Couchman H. M. P., 2013, arXiv e-prints, arXiv:1302.2618

Karakas A. I., 2010, MNRAS, 403, 1413

Karim A. et al., 2011, ApJ, 730, 61

Katz N., Gunn J. E., 1991, ApJ, 377, 365

Katz N., 1992, ApJ, 391, 502

Kauffmann G. et al., 2003a, MNRAS, 341, 33

Kauffmann G. et al., 2003b, MNRAS, 341, 54

Kauffmann G. et al., 2004, MNRAS, 353, 713

Kaufmann T., Mayer L., Wadsley J., Stadel J., Moore B., 2006, MNRAS, 370, 1612

Kaufmann T., Mayer L., Wadsley J., Stadel J., Moore B., 2007, MNRAS, 375, 53

Kazantzidis S., Bullock J. S., Zentner A. R., Kravtsov A. V., Moustakas L. A., 2008, ApJ, 688, 254

Kazantzidis S., Abadi M. G., Navarro J. F., 2010, ApJ, 720, L62

Kennicutt Jr. R. C., 1998, ARAA, 36, 189

Kereš D., Katz N., Weinberg D. H., Davé R., 2005, MNRAS, 363, 2

Kereš D., Vogelsberger M., Sijacki D., Springel V., Hernquist L., 2012, MNRAS, 425, 2027

Kewley L. J., Rupke D., Zahid H. J., Geller M. J., Barton E. J., 2010, ApJ, 721, L48

Krajnović D. et al., 2008, MNRAS, 390, 93

Kroupa P., 2001, MNRAS, 322, 231

Krumholz M. R., Thompson T. A., 2013, MNRAS, 434, 2329

Larson R. B., 1974, MNRAS, 169, 229

Lehnert M. D., Heckman T. M., 1996, ApJ, 462, 651

Leja J., van Dokkum P., Franx M., 2013, ApJ, 766, 33

Lemaître G., 1931, Nature, 127, 706

Lia C., Portinari L., Carraro G., 2002, MNRAS, 330, 821

Lin C. C., Shu F. H., 1964, ApJ, 140, 646

Lovell M. R et al., 2012, MNRAS, 420, 2318

Lucy L. B., 1977, AJ, 82, 1013

Lynds R., Toomre A., 1976, ApJ, 209, 382

MacArthur L. A., Courteau S., Holtzman J. A., 2003, ApJ, 582, 689

Magorrian J. et al., 1998, AJ, 115, 2285

Maiolino R. et al., 2008, A&A, 488, 463

Maoz D., Mannucci F., 2012, Publications of the Astronomical Society of Australia, Volume 29, Issue 4, pp. 447-465

Marinacci F., Binney J., Fraternali F., Nipoti C., Ciotti L., Londrillo P., 2010, MNRAS, 404, 1464

Marinacci F., Pakmor R., Springel V., 2013, arXiv e-prints, arXiv:1305.5360

Marri S., White S. D. M., 2003, MNRAS, 345, 561

Martín-Navarro I. et al., 2012, MNRAS, 427, 1102

Martínez-Serrano F. J., Serna A., Domínguez-Tenreiro R., Mollá M., 2008, MNRAS, 388, 39

McCray R., Kafatos M., 1987, ApJ, 317, 190

McGaugh S. S., 2012, AJ, 143, 40

McKee C. F., Ostriker J. P., 1977, ApJ, 218, 148

McMillan P. J., 2011, MNRAS, 414, 2446

Milgrom M., 1983, ApJ, 270, 365

Mo H. J., Mao S., White S. D. M., 1998, MNRAS, 295,319

Mo H., van den Bosch F. C., White S., 2010, Galaxy Formation and Evolution, Cambridge University Press, Cambridge

Monaghan J. J., 1992, ARAA, 30, 543

Montuori M., Di Matteo P., Lehnert M. D., Combes F., Semelin B., 2010, A&A, 518, 56

Moore B., Ghigna S., Governato F., Lake G., Quinn T., Stadel J., Tozzi P., 1999, ApJ, 524, L19

Mosleh M., Williams R. J., Franx M., Kriek M., 2011, ApJ, 727, 5

Moster B. P., Naab T., White S. D. M., 2013, MNRAS, 428, 3121

Mukhanov V. F., Chibisov, G. V., 1981, Soviet Journal of Experimental and Theoretical Physics Letters, 33, 532

Murray N., Quataert E., Thompson T. A., 2005, ApJ, 618, 569

Murray N., Quataert E., Thompson T. A., 2010, ApJ, 709, 191

Naab T., Ostriker J.P., 2006, MNRAS, 366, 899

Naab T., Johansson P. H., Ostriker J. P., Efstathiou G., 2007, ApJ, 658, 710

Naab T., Ostriker J.P., 2009, ApJ, 690, 1452

Naab T., Johansson P. H., Ostriker J. P., 2009, ApJ, 699, L178

Nagy S. R., Law D. R., Shapley A. E., Steidel C. C., 2011, ApJ, 735, L19

Narayanan D., Bothwell M., Davé R., 2012, MNRAS, 426, 1178

Navarro J. F., Benz W., 1991, ApJ, 380, 320

Navarro J. F., White S. D. M., 1993, MNRAS, 265, 271

Navarro J. F., White S. D. M., 1994, MNRAS, 267, 401

Navarro J. F., Steinmetz M., 1997, ApJ, 478, 13

Navarro J. F., Frenk C. S., White S. D. M., 1997, ApJ, 490, 493

Negroponte J,.White S. D. M., 1983, MNRAS, 205, 1009

Nelson D., Vogelsberger M., Genel S., Sijacki D., Kereš D., Springel V., Hernquist L., 2013, MNRAS, 429, 3353

Ness M. et al., 2013, MNRAS, 430, 836

Noguchi M., 1999, ApJ, 514, 77

Okamoto T., Eke V. R., Frenk C. S., Jenkins A., 2005, MNRAS, 363, 1299

Okamoto T., 2013, MNRAS, 428, 718

Oppenheimer B. D., Davé R., 2006, MNRAS, 373, 1265

Oppenheimer B. D., Davé R., Kereš D., Fardal M., Katz N., Kollmeier J. A., Weinberg D. H., 2010, MNRAS, 406, 2325

Oser L., Ostriker J. P., Naab T., Johansson P. H., Burkert A., 2010, ApJ, 725, 2312

Ostriker J. P., Peebles P. J. E., Yahil A., 1974, ApJ, 193, L1

Patel S. G. et al., 2013a, ApJ, 766, 15

Patel S. G. et al., 2013b, arXiv e-prints, arXiv:1304.2395

Pawlowski M. S., Pflamm-Altenburg J., Kroupa P., 2012, MNRAS, 423, 1109

Peebles P. J. E., 1965, ApJ, 142, 1317

Peebles P. J. E., 1969, ApJ, 155, 393

Peebles P. J. E., 1993, Principles of Physical Cosmology, Princeton University Press, Princeton

Peebles P. J., Ratra B., 2003, Reviews of Modern Physics, 75, 559

Peek J. E. G., Putman M. E., Sommer-Larsen J., 2008, ApJ, 674, 227

Peeples M. S., Shankar F., 2011, MNRAS, 417, 2962

Peeples M. S., Werk J. K., Tumlinson J., Oppenheimer B. D., Prochaska J. X., Katz N., 2013, arXiv e-prints, arXiv:1310.2253

Pei Y. C., 1992, ApJ, 395, 130

Peng Y.-j. et al., 2010, ApJ, 721, 193

Penzias A. A., Wilson R. W., 1965, ApJ, 142, 419

Percival W. J. et al., 2010, MNRAS, 401, 2148

Perez J., Michel-Dansac L., Tissera P. B., 2011, MNRAS, 417, 580

Pilkington K. et al., 2012a, A&A, 540, A56

Pilkington K. et al., 2012b, MNRAS, 425, 969

Planck Collaboration, 2013, arXiv e-prints, arXiv:1303.5076

Portinari L., Chiosi C., Bressan A., 1998, A&A, 334, 505

Press W. H., Schechter P., 1974, ApJ, 187, 425

Puchwein E., Springel V., 2013, MNRAS, 428, 2966

Puech M., Hammer F., Hopkins P. F., Athanassoula E., Flores H., Rodrigues M., Wang J. L., Yang Y. B., 2012, ApJ, 753, 128

Quinn T., Binney J., 1992, MNRAS, 255, 729

Read J. I., Hayfield T., 2012, MNRAS, 422, 3037

Reddy B. E., Lambert D. L., Allende Prieto C., 2006, MNRAS, 367, 1329

Rees M. J., Ostriker J. P., 1977, MNRAS, 179, 541

Riess A. G. et al., 1998, AJ, 116, 1009

Robertson B., Bullock J. S., Cox T. J., Di Matteo T., Hernquist L., Springel V., Yoshida N., 2006, ApJ, 645, 986

Rodighiero G. et al., 2011, ApJ, 739, L40

Romano-Díaz E., Shlosman I., Heller C., Hoffman Y., 2009, ApJ, 702, 1250

Roškar R., Debattista V. P., Brooks A. M., Quinn T. R., Brook C. B., Governato F., Dalcanton J. J., Wadsley J., 2010, MNRAS, 408, 783

Rubin V. C., Thonnard N., Ford Jr. W. K., 1978, ApJ, 225, L107

Saha K., Tseng Y.-H., Taam R. E., 2010, ApJ, 721, 1878

Sales L. V., Navarro J. F., Theuns T., Schaye J., White S. D. M., Frenk C. S., Crain R. A., Dalla Vecchia C., 2012, MNRAS, 423, 1544

Salpeter E. E., 1964, ApJ, 140, 796

Sancisi R., 1976, A&A, 53, 159

Sargent M. T. et al., 2007, ApJS, 172, 434

Sawala T., Guo Q., Scannapieco C., Jenkins A., White S., 2011, MNRAS, 413, 659

Scannapieco C., Tissera P. B., White S. D. M., Springel V., 2005, MNRAS, 364, 552

Scannapieco C., Tissera P. B., White S. D. M., Springel V., 2006, MNRAS, 371, 1125

Scannapieco C., Tissera P. B., White S. D. M., Springel V., 2008, MNRAS, 389, 1137

Scannapieco C., White S. D. M., Springel V., Tissera P. B., 2009, MNRAS, 396, 696

Scannapieco C., Gadotti D. A., Jonsson P., White S. D. M., 2010, MNRAS, 407, L41

Scannapieco C., White S. D. M., Springel V., Tissera P. B., 2011, MNRAS, 417, 154

Scannapieco C. et al., 2012, MNRAS, 423, 1726

Schaye J., Aguirre A., Kim T.-S., Theuns T., Rauch M., Sargent W. L. W., 2003, ApJ, 596, 768

Schaye J. et al., 2010, MNRAS, 402, 1536

Schinnerer E. et al., 2013, arXiv E-prints, arXiv:1304.1801

Schönrich R., Binney J. J., 2009a, MNRAS, 396, 203

Schönrich R., Binney J. J., 2009b, MNRAS, 399, 1145

Schönrich R., 2012, MNRAS, 427, 274

Seljak U., Slosar A., McDonald P., 2006, Journal of Cosmology and Astroparticle Physics, 10, 14

Sellwood J. A., Binney J. J., 2002, MNRAS, 336, 785

Sersic J. L., 1968, Atlas de galaxias australes, Cordoba

Shakura N. I., Sunyaev R. A., 1976, MNRAS, 175, 613

Shen S., Mo H. J., White S. D. M., Blanton M. R., Kauffmann G., Voges W., Brinkmann J., Csabai I., 2003, MNRAS, 343, 978

Shen S., Wadsley J., Stinson G., 2010, MNRAS, 407, 1581

Silk J., 1977, ApJ, 211, 638

Silk J., Rees M. J., 1998, A&A, 331, L1

Sommer-Larsen J., Dolgov A., 2001, ApJ, 551, 608

Springel V., Hernquist L., 2002, MNRAS, 333, 649

Springel V., 2005, MNRAS, 364, 1105

Springel V., Hernquist L., 2005, ApJ, 622, L9

Springel V., Di Matteo T., Hernquist L., 2005a, MNRAS, 361, 776

Springel V. et al., 2005b, Nature, 435, 629

Springel V., Frenk C. S., White S. D. M., 2006, Nature, 440, 1137

Springel V. et al., 2008, MNRAS, 391, 1685

Springel V., 2010, MNRAS, 401, 791

Steidel C. C., Erb D. K., Shapley A. E., Pettini M., Reddy N., Bogosavljević M., Rudie G. C., Rakic O., 2010, ApJ, 717, 289

Steinmetz M., White S. D. M., 1997, MNRAS, 288, 545

Stinson G., Seth A., Katz N., Wadsley J., Governato F., Quinn T., 2006, MNRAS, 373, 1074

Stinson G. et al., 2012, MNRAS, 425, 1270

Stinson G. S., Brook C., Macciò A. V., Wadsley J., Quinn T. R., Couchman H. M. P., 2013, MNRAS, 428, 129

Tacconi L. J. et al., 2010, Nature, 463, 781

Thomas D., Maraston C., Schawinski K., Sarzi M., Silk J., 2010, MNRAS, 404, 1775

Thornton K., Gaudlitz M., Janka H.-T., Steinmetz M., 1998, ApJ, 500, 95

Tissera P. B., White S. D. M., Scannapieco C., 2012, MNRAS, 420, 255

Toomre A., 1964, ApJ, 139, 1217

Toomre A., Toomre J., 1972, ApJ, 178, 623

Toomre A., 1977, in ‘Evolution of Galaxies and Stellar Populations’, eds. Tinsley B. M., Larson D., Campbell, R. B. G., New Haven: Yale Univ. Observatory, p. 401

Torrey P., Vogelsberger M., Sijacki D., Springel V., Hernquist L., 2012a, MNRAS, 427, 2224

Torrey P., Cox T. J., Kewley L., Hernquist L., 2012b, ApJ, 746, 108

Toth G., Ostriker J. P., 1992, ApJ, 389, 5

Tremonti C. A. et al., 2004, ApJ, 613, 898

Tully R. B., Fisher J. R., 1977, A&A, 54, 661

Uhlig M., Pfrommer C., Sharma M., Nath B. B., Enßlin T. A., Springel V., 2012, MNRAS, 423, 2374

van den Bergh S., 1976, ApJ, 206, 883

van der Kruit P. C., Searle L., 1981, A&A, 95, 105

van der Kruit P. C., Freeman K. C., 2011, ARAA, 49, 301

van de Voort F., Schaye J., Booth C. M., Haas M. R., Dalla Vecchia C., 2011, MNRAS, 414, 2458

van Dokkum P. G. et al., 2010, ApJ, 709, 1018

van Dokkum P. G. et al., 2013, ApJ, 771, L35

Veilleux S., Cecil G., Bland-Hawthorn J., 2005, ARAA, 43, 769

Vera-Ciro C. A., Sales L. V., Helmi A., Frenk C. S., Navarro J. F., Springel V., Vogelsberger M., White S. D. M., 2011, MNRAS, 416, 1377

Viel M., Becker G. D., Bolton J. S., Haehnelt M. G., 2013, PhRvD, 88, 4

Vogelsberger M., Genel S., Sijacki D., Torrey P., Springel V., Hernquist L., 2013, ArXiv e-prints, arXiv:1305.2913

Wadsley J. W., Veeravalli G., Couchman H. M. P., 2008, MNRAS, 387, 427

Walch S. K., Whitworth A. P., Bisbas T., Wünsch R., Hubber D., 2012, MNRAS, 427, 625

Walter F., Brinks E., de Blok W. J. G., Bigiel F., Kennicutt Jr. R. C., Thornley M. D., Leroy A., 2008, AJ, 136, 2536

Wang Jie et al., 2011a, MNRAS, 413, 1373

Wang Jing et al., 2011b, MNRAS, 412, 1081

Wang Jing et al., 2013a, MNRAS, 433, 270

Wang Jing et al., 2013b, in preparation

Wegg C., Gerhard O., 2013, MNRAS, 435, 1874

Weil M. L., Eke V. R., Efstathiou G., 1998, MNRAS, 300, 773

White S. D. M., Rees M. J., 1978, MNRAS, 183, 341

White S. D. M., 1984, ApJ, 286, 38

White S. D. M., Davis M., Frenk C. S., 1984, MNRAS, 209, 27

White S. D. M., Frenk C. S., 1991, ApJ, 379, 52

White S. D. M., Navarro J. F., Evrard A. E., Frenk C. S., 1993, Nature, 366, 429

White S. D. M., 1994, Formation and Evolution of Galaxies: Les Houches Lectures, arXiv:astro-ph/9410043

Whitmore B. C., Lucas R. A., McElroy D. B., Steiman-Cameron T. Y., Sackett P. D., Olling R. P., AJ, 100, 1489

Wiersma R. P. C., Schaye J., Theuns T., Dalla Vecchia C., Tornatore L., 2009a, MNRAS, 399, 574

Wiersma R. P. C., Schaye J., Smith B. D., 2009b, MNRAS, 393, 99

Willman B., Strader J., 2012, AJ, 144, 76

Wuyts S. et al., 2011, ApJ, 742, 96

Yang J., Turner M. S., Schramm D. N., Steigman G., Olive K. A., 1984, ApJ, 281, 493

Yang X., Mo H. J., van den Bosch F. C., Bonaca A., Li S., Lu Y., Lu Y., Lu Z., 2013, ApJ, 770, 115

Yoachim P., Dalcanton J. J., 2006, AJ, 131, 226

Zaritsky D., Kennicutt Jr. R. C., Huchra J. P., 1994, ApJ, 420, 87

Zel'dovich Y. B., 1970, A&A, 5, 84

Zel'dovich Y. B., 1972, MNRAS, 160, 1

Zolotov A. et al., 2012, ApJ, 761, 71

Zwicky F., 1933, Helvetica Physica Acta, 6, 110

Acknowledgements

I would like to thank ...

- Simon White for giving me the opportunity to work with him, for always letting me pursue the projects that I was interested in, and for always being positive about my work.
- Thorsten Naab for continuously trying to convince me that my results are interesting and for many helpful comments.
- Cecilia Scannapieco for providing her simulation code as well as her simulations and for valuable discussions.
- Ralph Schönrich for making me apply for a job at MPA and for being a helpful and supportive office mate.
- James Binney, Andi Burkert and Peter Johansson for their support during the earlier stages of my astrophysical career.
- Jackson DeBuhr and Chung-Pei Ma for their constructive collaboration in the idealized disc model project and Laura Sales for valuable comments on these models.
- the DFG Excellence Cluster ‘Origin and Structure of the Universe’ for financial support.
- my family for their constant support and for never asking questions about my work during my free time.

Erklärung

des Doktoranden

Michael Aumer
aus Roding

Mit der Abgabe dieser Doktorarbeit versichere ich, dass ich die Arbeit selbständig vefasst und keine anderen als die angegebenen Quellen und Hilfsmittel benutzt habe.

München, den 29.10.2013 AD